
STRUCTURAL, SPECTROSCOPIC AND CHARGE DENSITY INVESTIGATIONS OF ORGANIC MOLECULAR CRYSTALS

A Thesis
Submitted for the Degree of
Doctor of Philosophy

By
Reji Thomas



Chemistry and Physics of Materials Unit
Jawaharlal Nehru Centre for Advanced Scientific Research
(A Deemed University)
Bangalore 560064, India
November 2008

Dedicated to my parents ...

DECLARATION

I hereby declare that the matter embodied in this thesis entitled **“Structural, Spectroscopic and Experimental Charge Density Investigations of Organic Molecular Crystals”** is the result of investigations carried out by me under the supervision of *Prof. G. U. Kulkarni* at the Chemistry and Physics of Materials Unit, Jawaharlal Nehru Centre for Advanced Scientific Research, Bangalore, India, and it has not been submitted elsewhere for the award of any degree or diploma.

In keeping with the general practice of reporting scientific observations, due acknowledgement has been made whenever the work described has been based on the findings of the other investigators. Any omission that might have occurred by oversight or error of judgement is regretted.

Reji Thomas

CERTIFICATE

Certified that the work described in this thesis entitled “**Structural, Spectroscopic and Experimental Charge Density Investigations of Organic Molecular Crystals**” has been carried out by *Reji Thomas*, under my supervision at the Chemistry and Physics of Materials Unit, Jawaharlal Nehru Centre for Advanced Scientific Research, Bangalore, India.

Prof. G. U. Kulkarni
(Research Supervisor)

ACKNOWLEDGEMENTS

I express my sincere and warm gratitude to my research supervisor Prof. G. U. Kulkarni, for suggesting various research problems and for the invaluable guidance during the course of research work. His enthusiasm, curiosity and imagination made me think and to work in right direction. I specially thank him for his friendly approach and constant encouragement. I also thank him for giving me the opportunity to work on different areas of research which gave me confidence to work with different types of experiments and instruments. I also thank him for his care and concern in my personal matters.

I am grateful to the chairman of CPMU, Prof. C. N. R. Rao, FRS for suggesting me interesting problems in supramolecular chemistry and for his guidance with this work. I also thank him for his constant support and encouragement in various ways. He has been a constant source of inspiration for me with his dedication, commitment to science, boundless enthusiasm and up-to date knowledge.

I express my sincere thanks to Prof. Swapan K. Pati for various theoretical calculations and for the useful discussions with him. I also thank him for clearing my doubts related to theoretical calculations with enthusiasm.

I express my sincere thanks to various collaborators during my research work Dr. R. Srinivasa Gopalan, Dr. S. Lakshmi, Dr. Ayan Datta, Sairam, Sudipto and Shrinwantu.

I am grateful to Dr. Suresh Das and Dr. George Thomas (NIIST, Trivandrum) for their help with various photophysical property measurements and for valuable discussions. I thank Prof. Henryk Ratajczak, (University of Wroclaw, Poland) for providing crystal (melaminium tartrate) for charge density studies.

It's my pleasure to thank Dr. Anupama Ranganathan and Dr. P. Kumaradhas for teaching me crystallography and experimental charge density.

I thank all the faculty members of CPMU for their cordiality, especially my teachers, Profs. N. Chandrabhas, S. Natarajan, Dr. A. R. Raju for courses. Thanks to Dr. Govindaraj for various helps. I thank Profs. P. Balaram, T. N. Guru Row (IISC) for course work.

I thank Dr. Suresh Das for introducing me to the field of research and Dr. U. Santhosh for teaching me various experiments during my master project at NIIST Trivandrum, which helped me during my research work at JNCASR.

I also extend my thanks to Ramesh and Shinto for their help with various instruments at NIIST, Trivandrum.

I thank all my teachers who have taught me till now, especially, Sivan master (GHSS Kamballur) and K. T. Ramachandran sir (Govt. College Kasaragod) who have been a source of inspiration.

I thank Mrs. Indira Kulkarni, Tejaswin and Poorna for their warmth and hospitality.

I am grateful to my past and present labmates, Dr. Anaupama, Dr. John Thomas, Dr. Gargi, Dr. Neena, Dr. Saravanan, Dr. Ved, Dr. Angappane, Dr. Karthik, Girish, Selvi, Vijay, Bhuvana, Radha, Narendra & Ritu for discussions and cheerful atmosphere. I also thank all my crystallography labmates for various helps and cheerful atmosphere.

I am very thankful to Mr. Srinivas and Dr. Kiran Kulkarni for their invaluable, technical assistance with the diffractometer. Thanks to Mr. Srinath, Mr. Vasu, Mr. Anil, Mr. Srinivasa Rao, Ms. Usha, Mr. Basavaraj, Mr. Narasimha Moorthy and Mr. Sunil.

I thank the staffs of academic and administrative section in JNCASR for their assistance. I also thank the library staffs for their help. I am thankful to the staffs of the computer lab for their assistance.

I am very thankful to JNCASR for the invaluable financial support and the excellent accommodation.

Thanks go to all my friends Neena, Lakshmi, Vivek, Neenu, Selvi, Kalyani, Sameen, N. Vinod, Manojettan, Ujjal, Gautam, Deepak, Ved, Gomathi, Thiru, Meenakshi, Behera, Prabhakar, Harish, Raja, Venkidesh, Pranab, Rajashekhar, Guru, Sonia, Achut, Madhu, Sameer, Rakesh, Sandeep, Jithesh, Manoj, Anupama, Ramakrishna, Leela, Subramanyam, Chandu, Kanishka, Bhat, Claudy, Jyothi, Datta, Dinesh, Saikrishna, Prakash, Sudheep, Anirban and all those whom I would have missed here for a memorable and joyous JNC life.

I thank all my M. Sc. and B. Sc. class mates for their invaluable friendship.

Words cannot express my deep sense of gratitude to Kunchachan, Ammachi, Joji chettayi, Smitha chechi, Saju and Ponnukkutty. Their endless support, constant encouragement, love and prayers have been a constant source of strength for me.

Preface

The thesis pertains to investigations on several organic crystal systems employing X-ray diffraction, photophysical measurements as well as the experimental charge density method. It consists of six chapters. **Chapter 1** provides an overview on supramolecular assemblies in relation to the solid state properties with few examples from experimental charge density.

Chapter 2 deals with the supramolecular assemblies formed by pyrimidine bases, uracil and cytosine with various hydrogen bond donor and acceptor compounds. Another related molecule, 5-nitrouracil forms supramolecular assemblies with variety of compounds including solvents. The study brings out various hydrogen bonded architectures and patterns including the proton transfer interactions in these assemblies. Understanding the weak interactions present in 1,4-bis(phenylethynyl)-2,5-bis(*n*-dialkyloxy)benzenes and their influence on molecular geometry, packing as well as on the solid state fluorescence properties is the subject matter of **Chapter 3**. The molecule in the crystal structure becomes increasingly planar with longer alkyl chains. The molecules pack to form J-aggregates and the band position is observed to vary linearly with the distance between the interacting molecules in the aggregate. The quantum yield lies in the range, 0.3 – 0.8. Interestingly, the fluorescence behavior of the methoxy substituted molecule depends crucially on the method of crystallization. Melt cooled films of this molecule fluoresce in the blue region with four distinct bands, the relative intensities depending on the rate of cooling. The crystallites formed show preferred orientations sensitive to the wetting behavior of the substrate.

The experimental charge density analysis of two phenyleneethynylene prototypes- 1,2-diphenylacetylene and 1,4-diphenylbutadiyne, and the use of various charge density descriptors such as density, Laplacian and ellipticity in describing the conjugation in these molecules is the content of **Chapter 4**. The non-zero ellipticity value associated with the triple bond in 1,2-diphenylacetylene is a clear indication of the extent of conjugation present in the molecule. For 1,4-diphenylbutadiyne, the deviation from the ideal value is small. **Chapter 5** presents the results of the experimental charge density analysis of two proton transfer complexes- melaminum L-tartrate monohydrate and L-asparginium picrate. The study brings out the role of hydrogen bonding in proton transfer and also the enhancement dipole moments in the non-centrosymmetric crystal field. Experimental charge density analysis on antiepileptic drugs- carbamazepine and oxcarbazepine, is presented in **Chapter 6**. Of the two, oxcarbazepine exhibits a higher dipole moment. The study gives some insight into the improved bioavailability and specificity of oxcarbazepine over carbamazepine.

CONTENTS

Declaration.....	i
Certificate.....	ii
Acknowledgements.....	iii
Preface.....	v
Table of Contents.....	vi
List of Acronyms and Formulae.....	xi
1. ORGANIC SUPRAMOLECULAR ASSEMBLIES, SOLID STATE PROPERTIES AND EXPERIMENTAL CHARGE DENSITY: AN OVERVIEW.....	1
1.1 Hydrogen Bonded Supramolecular Architectures.....	1
1.1.1 Intermolecular interactions.....	3
1.1.2 Hydrogen bond.....	4
1.1.3 Supramolecular synthon and designer crystals.....	7
1.1.4 Engineering strategies based on strong hydrogen bonds.....	9
1.1.5 Engineering strategies based on weak hydrogen bonds.....	13
1.1.6 Co-existence of strong and weak hydrogen bonds.....	16
1.1.7 Other types of intermolecular interactions.....	18
1.2 Effect of Weak Interactions and Molecular Packing on Solid-State Properties of Organic Supramolecular Assemblies.....	19
1.2.1 Organic porous solids.....	19
1.2.2 Electronic properties of supramolecular assemblies.....	20
1.2.3 Photophysical and optical properties of organic supramolecular assemblies.....	22

1.2.4	Organic ferroelectric and magnetic materials.....	25
1.3	Experimental Charge Density Understanding of Bonding and Non-bonding Interactions and Properties.....	26
1.3.1	The electron density.....	28
1.3.2	Charge density from theoretical calculations.....	28
1.3.3	Charge density from experiment.....	29
1.3.4	Representation of the charge density and deformation densities.....	31
1.3.5	The multipole model and computer codes.....	33
1.3.6	Criteria for the use of the multipole model.....	35
1.3.7	Topology of the charge density.....	35
1.3.8	Other topological parameters.....	38
1.3.9	Understanding of molecular properties.....	41
1.3.10	Intermolecular regions - hydrogen bonds.....	44
1.4	General Experimental and Related Aspects.....	47
1.4.1	Synthesis and crystallization of the compounds.....	47
1.4.2	Single crystal X-ray diffraction.....	47
	Reference.....	55
2.	INVESTIGATION OF SUPRAMOLECULAR ASSEMBLIES FORMED BY PYRIMIDINE BASES AND DERIVATIVE.....	68
	Summary.....	68
2.1	Introduction.....	69
2.2	Scope of the Present Investigation.....	70
2.3	Experimental Section.....	73
2.3.1	Preparation of the various molecular complexes and solvates.....	73

2.3.2	Crystal data collection.....	74
2.4	Results and Discussion.....	74
2.4.1	A hydrogen-bonded channel structure formed by a complex of uracil and melamine.....	74
2.4.2	Hydrogen bonding in proton-transfer complexes of cytosine with trimesic and pyromellitic acids.....	78
2.4.3	Hydrogen bonding patterns in the cocrystals and solvates of 5-nitrouracil.....	85
2.5	Conclusions.....	107
	References.....	109
3.	UNDERSTANDING OF WEAK INTERACTIONS IN ALKYOXY SUBSTITUTED OLIGO(PHENYLENE-ETHYNYLENE)S AND THEIR EFFECT ON SOLID STATE FLUORESCENCE PROEPRITIES.....	112
	Summary.....	112
3.1	Introduction.....	113
3.2	Scope of the Present Investigation.....	114
3.3	Experimental Section.....	115
3.3.1	General method of synthesis.....	115
3.3.2	Photophysical studies.....	116
3.3.3	Crystal data collection.....	117
3.4	Results and discussion.....	118
3.4.1	Structure and weak interactions in oligo(phenyleneethynelene)s.....	118
3.4.2	Solution phase and solid state fluorescence properties of 1,4-bis (phenylethynyl) - 2,5-bis(alkoxy)benzenes.....	137
3.4.3	Dependence fluorescence emission property on cooling rate of melt formed by 1,4-bis(phenylethynyl)-2,5-bis(methoxy)benzene, C1.....	147

Conclusions.....	157
References.....	159
4. EXPERIMENTAL CHARGE DENSITY IN DESCRIBING CONJUGATION IN 1,2-PHENYLACETYLENE AND 1,4- DIPHENYLBUTADIYNE	163
Summary.....	163
4.1 Introduction.....	164
4.2 Scope of the present investigation.....	165
4.3 Experimental Section.....	166
4.4 Results and Discussion.....	167
4.4.1 Analysis of structure and weak interactions.....	167
4.4.2 Analysis of Experimental Charge Density.....	171
4.4.3 Cambridge Crystallography Data (CSD) Analysis.....	175
4.4.4 Theoretical Analysis.....	178
4.5 Conclusions.....	180
Reference.....	182
5. CHARGE DENSITY ANALYSIS OF PROTON TRANSFER COMPLEXES: UNDERSTANDING HYDROGEN BONDING AND DETERMINATION OF IN-CRYSTAL DIPOLE MOMENTS.....	187
Summary.....	187
5.1 Introduction.....	188
5.2 Scope of Present Investigation.....	189
5.3 Experimental Section.....	189
5.4 Results and Discussions.....	191
5.5 Conclusions.....	201

References.....	203
6. EXPERIMENTAL CHARGE DENSITY DISTRIBUTION IN CARBAMAZEPINE AND OXCARBAZEPINE: POTENTIAL ANTIEPILEPTIC DRUGS.....	206
Summary.....	206
6.1 Introduction.....	207
6.2 Scope of the Present Investigation.....	208
6.3 Experimental Section.....	208
6.4 Results and Discussion	210
6.5 Conclusions.....	217
References.....	219

Appendix

List of Publications

List of acronyms and formulae

D	Donor
A	Acceptor
2D	Two-dimensional
3D	Three-dimensional
CSD	Cambridge Structural Database
CCDC	Cambridge Crystallographic Data Centre
AIM	Atoms in Molecules
BCP	Bond critical point
BP	Bond path
CP	Critical point
CCP	Cage critical point
RCP	Ring critical point
LP	Lone-pair
ρ	electron density in $\text{e}\text{\AA}^{-3}$
$\nabla^2\rho$	Laplacian of the electron density in $\text{e}\text{\AA}^{-5}$
λ_1 and λ_2	negative curvatures of the electron density in $\text{e}\text{\AA}^{-5}$
λ_3	positive curvature of the electron density in $\text{e}\text{\AA}^{-5}$
ε	ellipticity ($= \lambda_1/\lambda_2 - 1$)

Residuals

Statistical factors are defined as

$$R_{\text{int}} = \frac{\sum (I - \langle I \rangle)}{\sum I} \quad R_{\text{merge}} = \left[\frac{\sum |F_o|^2 - |F_o(\text{mean})|^2}{\sum |F_o|^2} \right]$$

$$R_1 = \frac{\sum K^{-1}|F_o| - |F_c|}{\sum K^{-1}|F_o|} \quad wR_2 = \left[\frac{\sum w(K^{-1}|F_o| - |F_c|)^2}{\sum wK^{-2}|F_o|^2} \right]^{1/2}$$

$$\text{GOF} = \left[\frac{\sum w(K^{-1}|F_o| - |F_c|)^2}{n - p} \right]^{1/2}$$

I is the Bragg intensity, $|F_o|$ and $|F_c|$ are the moduli of the observed and the calculated structure factors, respectively, K is the scale factor, w is the statistical weight, p is the number of refined parameters, and n is the number of used data.

ORGANIC SUPRAMOLECULAR ASSEMBLIES, SOLID STATE PROPERTIES AND EXPERIMENTAL CHARGE DENSITY: AN OVERVIEW

The structure and property of a molecule depends on its physical state and the environment. In the gaseous state, the molecule exhibits single molecular property while in the liquid state, the property and structure of the molecule may show concentration dependence. In the solid state, the interaction between the molecules becomes much stronger where the geometrical structure may itself undergo changes with respect to that in gaseous state.¹ This is because in the solid state, the molecules have to close pack satisfying the steric requirements. In addition to packing, the intermolecular interactions influence and determine the properties in the solid state.² These are typically nonbonding interactions including various types of hydrogen bonds and weak van der Waals interactions. These interactions give rise to molecular assemblies with interesting architectures and physical properties which are different from single molecular properties. The analysis of electron density distribution of molecules in crystals opens up a scope for understanding the intermolecular interactions, structure and the in-crystal properties often in a quantitative manner.³ This chapter provides an overview on the above aspects.

1.1 Hydrogen Bonded Supramolecular Architectures

Supramolecular assembly or ‘supermolecule’ is a well-defined complex of molecules held together by non-covalent interactions.⁴ The best example for such an assembly can be procured from nature, where self-assembly plays a major role in the functioning of most of the biological systems. The self assembly of molecules can be demonstrated with the help of a double stranded DNA, where a molecular assembly is formed with minimum number of molecules.⁵ In a double stranded DNA, two single strands form a helical structure through non-covalent bonds to give a self assembly as

shown in Figure 1.1. However the word supramolecular assembly is more often used to denote larger complexes of molecules that form 1D (linear chains), 2D (sheets) and various 3-dimensional architectures by infinite number of molecules.⁶

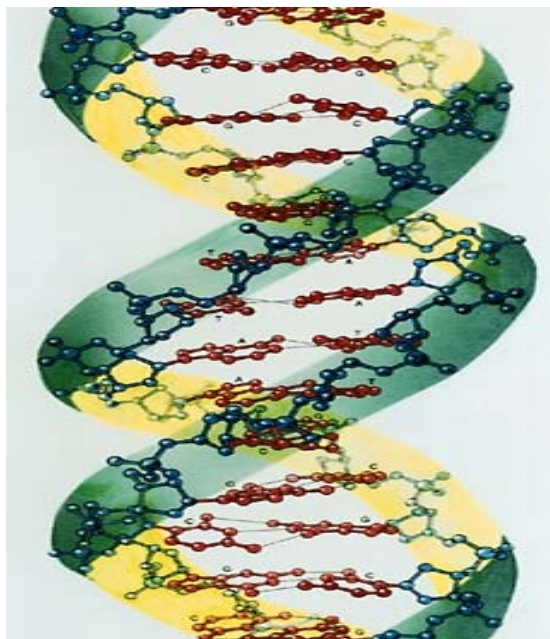
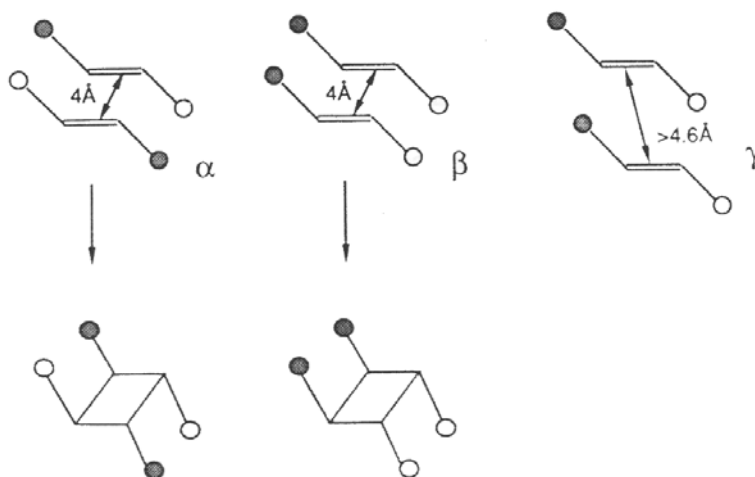


Figure 1.1: DNA double helix formed by noncovalent interactions.⁵

It is a well known fact that the property of organic molecules, organometallic compounds or coordination complexes in a supramolecular assembly depends on the molecular structure as well as the three dimensional architecture adopted in the crystalline form. In a crystalline environment, all these molecules undergo a modification



Scheme 1.1: Photoactive (α and β) and photostable (γ) forms of trans-cinnamic acids.⁷

of its single molecular properties and give rise to new materials and properties. The interest in these materials stems from the potential to manipulate the solid state properties by systematically varying the structure of the molecular sub-units. The pioneering work by Schmidt,⁷ on *trans*-cinnamic acid has shown the link between the structures of molecular assembly and the solid state reactivity. This study demonstrated different packing arrangements (ie, polymorphs α , β and γ forms) of *trans*-cinnamic acid and led to distinctly different photodimerization behaviors (Scheme 1.1). In conjunction with his interesting discovery, Schmidt suggested the term ‘crystal engineering’, which has since been used to describe the design and synthetic strategies of molecules of functional materials.⁸

1.1.1 Intermolecular interactions

The intermolecular interactions are the gluing factors of supramolecular assembly; hence crystal engineering is a study of balance and interaction.⁴ The chemistry of covalent bond is not much concerned with subtle equilibria because the energy barriers between the reactants and the products are many orders of magnitude larger than those of the individual, for instance, formation of hydrogen-bonded pairs from free acids. In order to understand and predict the structures of molecular solids, it is necessary to have a good knowledge on the relative strength of various intermolecular interactions. Noncovalent (or non-bonding) interactions are responsible for the bulk of the information that passes through living systems. These forces are the fundamental cause for the crystallization and dissolution of organic molecules as well. The various interactions present in the solid state are destroyed on dissolution; hence the detailed understanding of these interactions in the solid state becomes important. Crystallization of a pure substance is accompanied by a reduction in the translational freedom, which leads to a decrease in entropy and a gain in the enthalpy.⁹ The balance in these thermodynamic factors arises from the balance between the interacting forces such as attraction and repulsion in the crystalline state. Dispersion interactions are attractive, but weak and non-directional. Electrostatic interactions have a markedly directional character, notable among these are hydrogen bonding and charge transfer interactions. There are long-range forces that are effective within the distances of 10 nm ~ 0.2 nm. There are the weak van der Waals forces (< 8 kJ

mol⁻¹) which are non-directional, although they are responsible for bringing nonpolar molecules together and aligning them.

The basis of the crystal engineering lies in the molecular recognition, in which the molecules identify the fragments to build an interaction to reach in a balance between the attractive and repulsive forces and there by the optimizing the thermodynamic factors. The distance and direction dependence of non-bonding interactions discussed above give rise to an overall stabilizing arrangement, hence leading to close-packing of molecules in a molecular crystal. Kitaigorodskii¹⁰ described this concept as the close-packing model. Thus, it has been shown that for molecules of arbitrary shapes, close packing is possible only in a limited number of space groups: a prediction that proved to be in agreement with the analysis based on the data from the Cambridge Structural Database (CSD).

1.1.2 Hydrogen bond

Hydrogen bonding is considered to be the strongest and directional interaction of all the non-covalent and weak intermolecular interactions.^{11,12} Since the discovery of hydrogen bond till the day, study of hydrogen bonding is a realm of active research. The long lasting interest in this area is attributed to the importance of hydrogen bonding in the structure, function and dynamics of a large number molecular systems of chemical and biological relevance.¹³ Traditionally, it has been thought that hydrogen bonding is essentially an electrostatic interaction between a proton and a highly electronegative acceptor atom such as oxygen or nitrogen, the latter usually possessing a lone pair of electrons. It is now well established that the high electron density regions in ethylenic and acetylenic bonds¹⁴ as well as the π -face of aromatic or heteroaromatic rings¹⁵ can virtually act as acceptors. The other known hydrogen bond acceptors include sulfur¹⁶ and halogen atoms.¹⁷ The O-H, N-H and F-H groups are some examples of hydrogen bond donors. Less electronegative groups such as C-H and S-H also act as proton donors.¹⁸ The basic geometrical criteria for a hydrogen bond, D-H \cdots A-X (D:donor, A:acceptor) require that the hydrogen bonding distance ($d_{H\cdots A}$) should be less than the sum of the van der Waals radii of the H and A atoms with a donor- hydrogen- acceptor angle (θ) close to 180° as well as a nearly planar DHAX system (Figure 1.2a). The actual ranges of these parameters vary depending on the donor and acceptor groups. Hydrogen bonds cover a

wide energy spectrum (Figure 1.2b), ranging from a covalent-type of bond to a weak dipolar attraction.

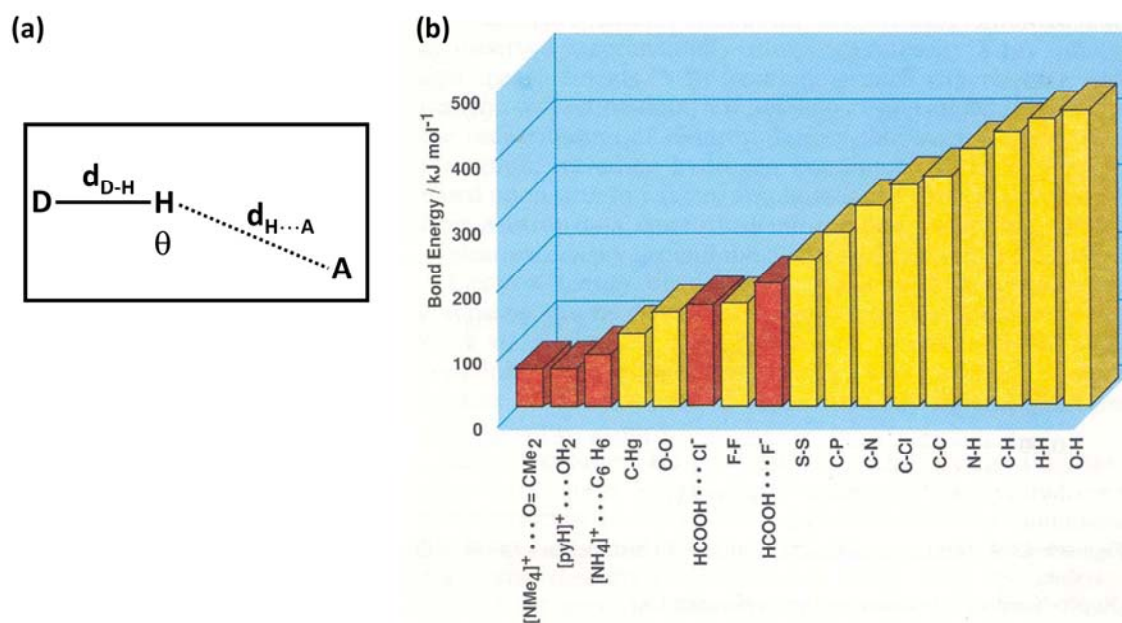
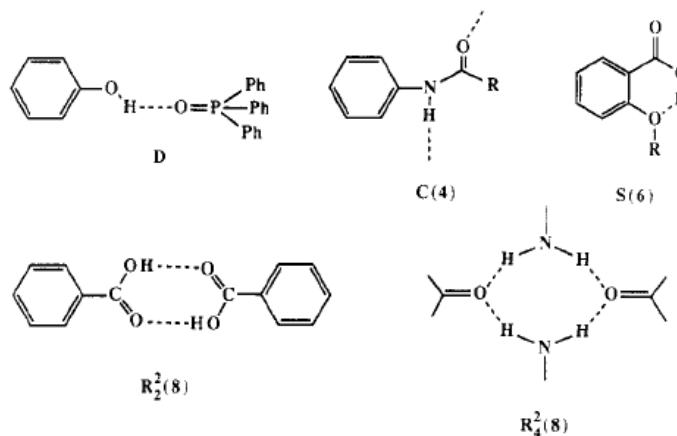


Figure 1.2: (a) Geometrical attributes of a hydrogen bond, (b) Bond energies for a range of common σ -bonds compared with a number of strong hydrogen bonds.¹⁸

The various possible hydrogen bonds are broadly classified into strong, moderate and weak interactions. To estimate the strength of the interactions, in addition to the purely geometric criteria based on structural crystallographic techniques,¹⁹ various spectroscopic techniques such as Infra red,²⁰ NMR,²¹ potential functions¹¹ and isotope effects²² have been widely used. The studies by Jeffrey²³ put forward some of the basic criteria for these classifications (see Table 1.1). In last two decades, the statistical survey of the hydrogen bond geometries using Cambridge Crystallographic Data²⁴ have resulted in a number of publications.²⁵ The hydrogen bond plays a vital role in determining the shapes and biological properties of macromolecules such as proteins and the nucleic acids.^{12,26} and they aid in molecular recognition in forming large assemblies. Etter²⁷ carried out extensive studies on hydrogen bonds and proposed a set of guidelines based on graph theory, for encoding hydrogen bond patterns in organic solids. The four basic hydrogen bond motifs (**D**: dimer, **C**: chain, **S**: intramolecular bond, **R**: ring) are illustrated through some examples in Scheme 1.2.

Table 1.1 Strong, moderate, and weak hydrogen bonds following the classification of Jeffrey.²³

	Strong	Moderate	Weak
Interaction type	Strongly covalent	Mostly electrostatic	Electrostat./dispers.
Bond lengths [Å] H...A	1.2 - 1.5	1.5 - 2.2	>2.2
Lengthening of D-H [Å]	0.08 - 0.25	0.02 - 0.08	<0.02
D-H versus H...A	X-H ≈ H...A	X-H < H...A	X-H << H...A
Directionality	Strong	Moderate	Weak
Bond angles	170 - 180	>170	>90
Bond energy [kcal mol ⁻¹]	15 - 40	4 - 15	<4
Relat. IR shift Δν _{XH} [cm ⁻¹]	25%	25% - 10%	10%
¹ H downfield shift	14 - 22	<14	

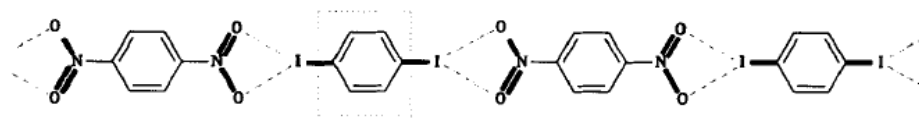
**Scheme 1.2:** Graph set notations for some hydrogen-bonded motifs.²⁷

Recent development in theoretical and computational facilities provided a better understanding of nature and properties of various hydrogen bonds in detail. The very first study towards the understanding of hydrogen bonds started by Pauling who used electrostatic model²⁸ to show the trends in the observed hydrogen bond energies.²⁹ Another study by Tsubomura and Coulson³⁰ using perturbation theory had given an insight into the contribution of various components of hydrogen bond energy. Bader rationalized the observed shifts in the D-H force constants using an electrostatic model.³¹ Such early theoretical studies on hydrogen bond, especially using molecular orbital or

semi-empirical calculations have been reviewed by many authors.³² Morokuma et al.³³ developed an energy partitioning method based on Hartree-Fock SCF formalism to study the nature of hydrogen bonding. Rao et al.³⁴ have reviewed results of semi-empirical and ab-initio studies of hydrogen-bonded complexes.

1.1.3 Supramolecular synthon and designer crystals

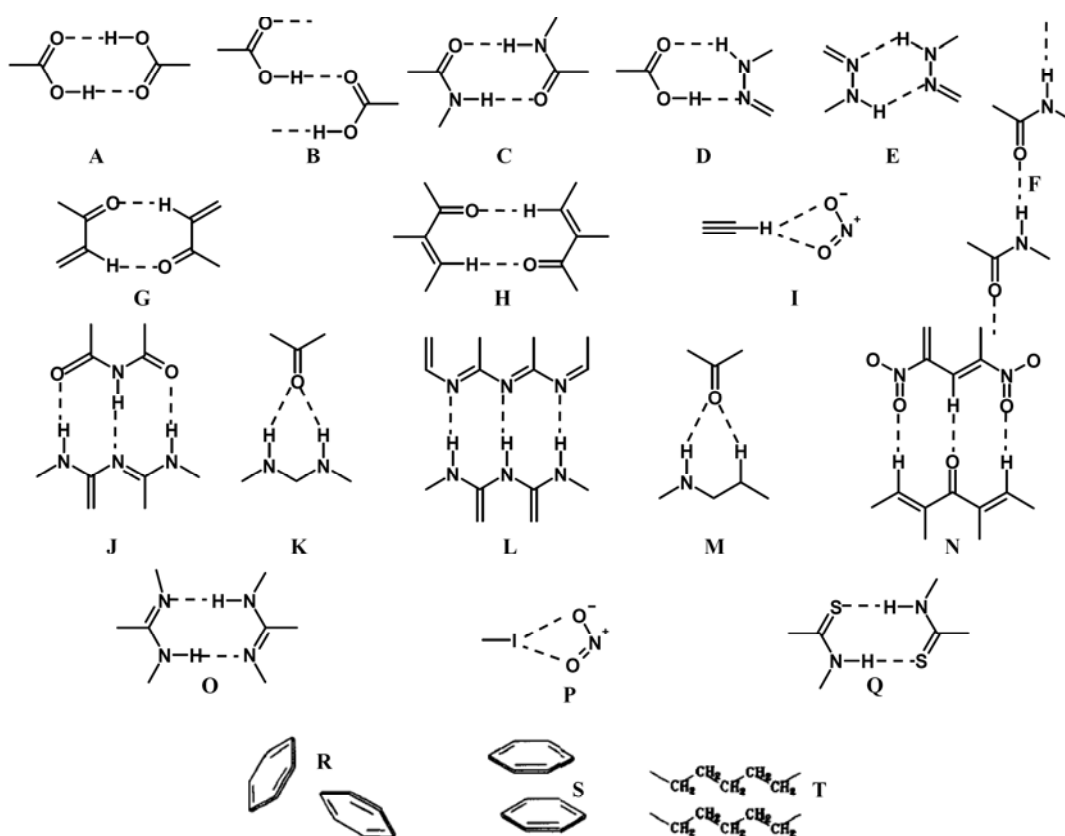
In analogy with the synthesis of molecules with covalent bonding (1-100 Å length scales), Lehn^{4,35} and Whitesides³⁶ describe the synthesis of molecular assemblies (with much larger length scales of 10-1000 Å) employing noncovalent interactions as noncovalent synthesis. This new methodology has indeed started to bridge the gap between molecular and macromolecular structures³⁷ and gave birth to a new highly interdisciplinary field called supramolecular chemistry. Lehn describes supramolecular chemistry as follows³⁵ “Just as there is a field of *molecular chemistry* based on the covalent bond, there is a field of *supramolecular chemistry*, the chemistry of molecular assemblies and of the intermolecular bond.” Following Lehn’s analogy,³⁸ if molecules formed by covalent bonds are the targets in organic synthesis, crystals assembled via intermolecular interactions may be considered as targets in supramolecular synthesis. Among the various intermolecular interactions known, the hydrogen bondings such as O-H...O, N-H...O and C-H...O have been generally used for the noncovalent synthesis of supramolecular architectures. This is because the nature, strength and directionality of these bonds are well understood both experimentally and theoretically. In addition to hydrogen bonding, there are reports on design and synthesis of supramolecular assemblies using non hydrogen bonding interactions. The non hydrogen bonding interactions include various interactions involving halogen atoms such as Cl...O, Br...O, I...O, I...I, O...I, N...Cl etc. and are also known to play important role in the design and synthesis of supramolecular architectures. The 1:1 supramolecular assembly between



Scheme 1.3: Supramolecular assembly between 1,4-dinitrobenzene and 1,4-diiodobenzene³⁹

1,4-dinitrobenzene and 1,4-diiodobenzene³⁹ is one of the examples of non hydrogen bonding interactions (scheme 1.3).

The word ‘synthon’ is very popular in synthetic organic chemistry and was introduced by E. J. Corey who defined it as ‘structural units within molecules which can be formed and/or assembled by known or conceivable synthetic operations.’⁴⁰ The word synthon has been traditionally used to represent key structural features in target molecule in organic synthesis. The use of this term has been extended by Desiraju to define supramolecular structural subunits. According to him ‘supramolecular synthons’^{13b} are



Scheme 1.4: Representative supramolecular synthons.^{13b}

structural subunits within supramolecules which can be formed and/or assembled by known or conceivable synthetic operations involving intermolecular interactions’. So supramolecular synthons are spatial arrangements of intermolecular interactions and play the directing role in formation of supramolecular assembly which is similar to that in conventional synthon approach in organic synthesis. Some of the important synthons that

are generally used for the design of various supramolecular architectures with varying dimensionality are shown in scheme 1.4.

1.1.4 Engineering strategies based on strong hydrogen bonds

The strongest and most directional hydrogen bonds are those formed between hydrogen atoms and highly electronegative acceptors such as F, O and N. The strength and directionality of these bonds have been reviewed by various authors.⁴¹⁻⁴⁶ This section discusses the utilization of various strong hydrogen bonds such as O-H...O, N-H...O, O-H...N and N-H...N bonds to design and synthesize various multidimensional supramolecular architectures.

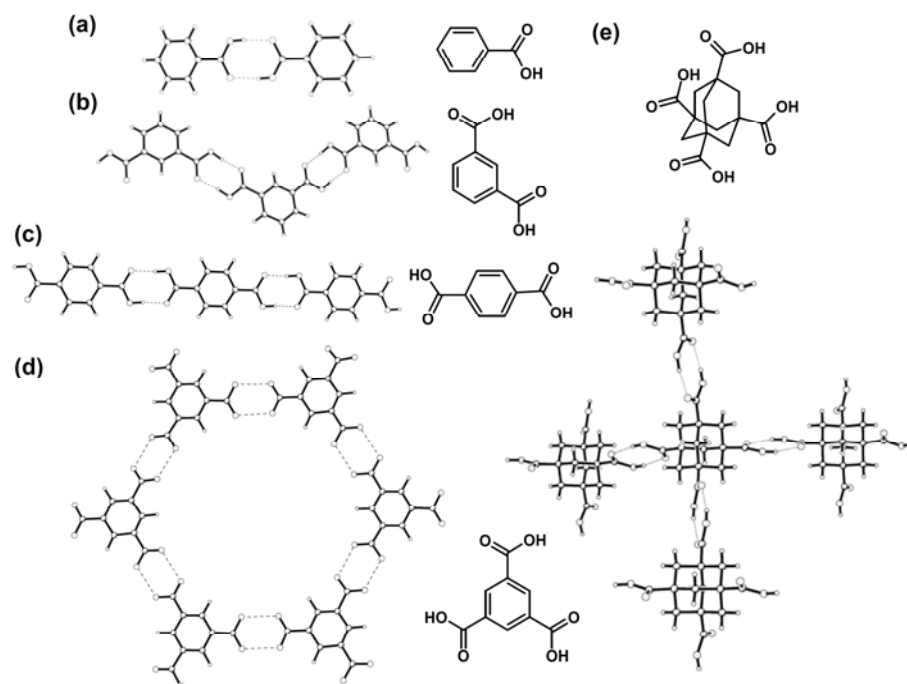


Figure 1.3: The carboxylic acid dimer coupling utilized in (a) benzoic acid,⁴⁷ (b) terephthalic acid,⁴⁸ (c) isophthalic acid,⁴⁹ (d) trimesic acid,⁵⁰ (e) adamantane-1,3,5,7-tetracarboxylic acid,⁵¹

Carboxylic acid is one of the well-utilized functionality to build various supramolecular architectures and is well known for its strong and directional nature. In most of the cases, carboxylic acid groups form strong dimeric O-H...O interactions and extent to various directions with the organization of carboxylic acid functionality in the basic molecular framework. The carboxylic acid dimer synthon (A in Scheme 1.4) is

utilized in the arrangement of aromatic carboxylic acids like benzoic,⁴⁷ terephthalic,⁴⁸ isophthalic,⁴⁹ trimesic⁵⁰ and adamantane-1,3,5,7-tetracarboxylic acid⁵¹ to produce zero-dimensional dimers, one-dimensional linear tapes, two-dimensional sheets and three-dimensional diamondoid structures, respectively as shown in Figure 1.3. There are extensive and pioneering studies on hydrogen-bonded structures formed by the carboxylic acid synthon by Leiserowitz and Etter.^{27,52}

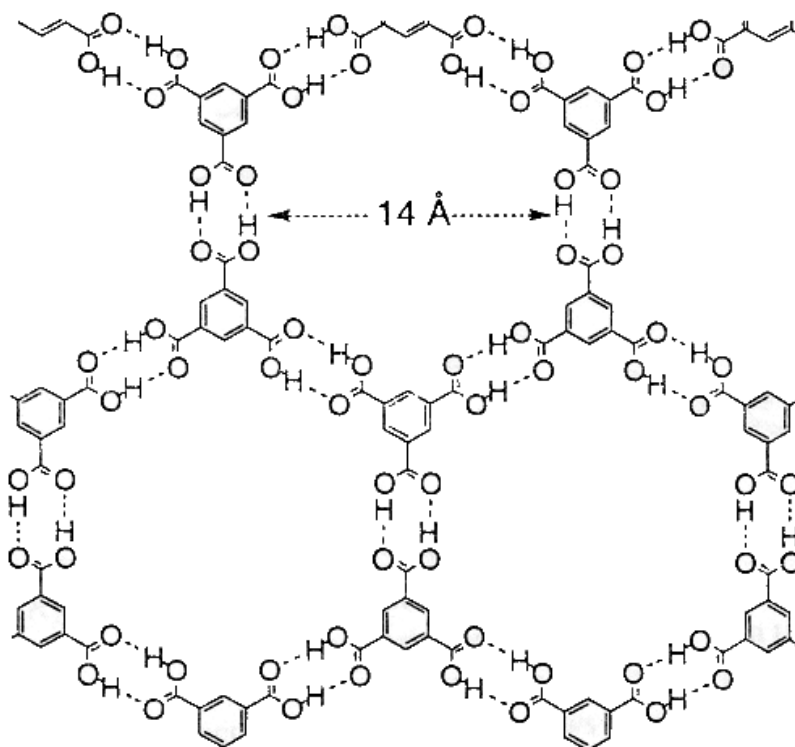


Figure 1.4: The chicken-wire network of trimesic acid where all the donors and acceptors are utilized in the formation of O-H \cdots O hydrogen bonds. The holes are filled by extensive interpenetration of independent networks.⁵⁴

As explained earlier, trimesic acid contains an infinite O-H \cdots O bonded chicken-wire motif formed by the dimerization of the COOH groups. The two-dimensional sheets interlace one another filling the voids. Herbststein et al.⁵³ have reported the first non-interlaced trimesic acid structures (again containing O-H \cdots O dimers) containing disordered alkane guests. Later, Kolotuchin et al.⁵⁴ synthesized a series of trimesic acid inclusion complexes with pyrene and ethanol molecules residing as guests in the cavities. One of such cavities formed by trimesic acid is depicted in Figure 1.4.

An X-ray structural study of the high-energy cyclic form of water hexamer trapped in an organic supramolecular complex with bimesityl dicarboxylic acid, through O-H...O bonds has been carried out⁵⁵ (see Figure 1.5). The formation of catemeric

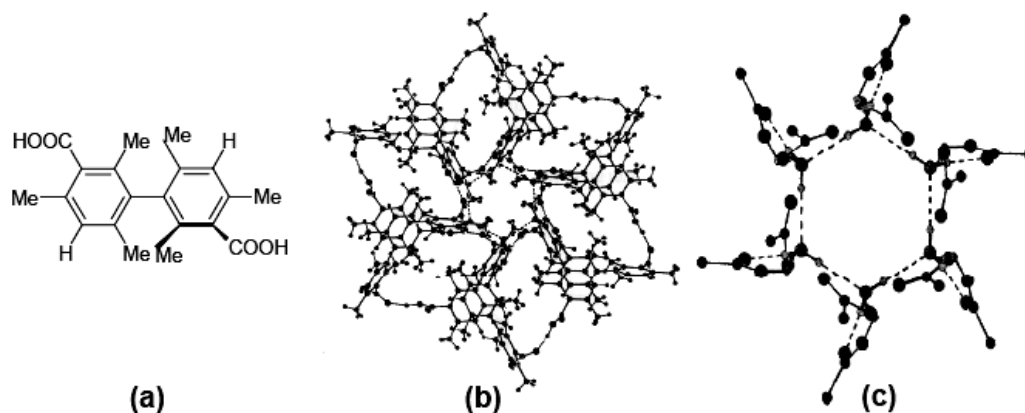


Figure 1.5: (a) bimesityl dicarboxylic acid, (b) The crystal packing of bimesityl dicarboxylic acid. \cdot H₂O, (c) The water hexamer with the acid molecules (only –COOH are shown for clarity).⁵⁵

(single) O-H...O hydrogen-bonded motifs in this complex is contrary to the ubiquitous centrosymmetric dimer motifs. A recent CSD analysis has shown that the dimer motif is found in 90% of the crystal structures reported for acids, while the catemer is found only in 4%. Very short O-H...O bonds occur in monobasic salts of diacids.⁵⁶ These bonds are usually formed between an acid and its conjugate base (O-H...O⁻) or in the hydrates of strong acids (O⁺-H...O). They have a quasi-covalent character with H...O distances in the range 1.2 to 1.5 Å (O...O, 2.2 – 2.5 Å) and θ in the range of 170° to 180°, with energy of ~ 63 to 170 kJ mol⁻¹ in contrast to strong hydrogen bonds (H...O, 1.5 - 2.2 Å, O...O, 2.5 – 3.2 Å, E = 17 - 63 kJ mol⁻¹). The O-H...O bonds formed by resonance assistance through π bonds (RAHB) are unusually short.⁵⁷ A cooperative network of O-H...O and O-H...N hydrogen-bonded synthons appear in the crystal structure of 2,3,5,7-pyrazinetetracarboxylic acid.⁵⁸

Another motif which can form highly directional and predictable hydrogen bond, compared to the COOH functionality is the amide unit (CONH₂). The crystal structure of benzamide contains centrosymmetric N-H...O dimers linked into α networks⁵⁹ (Figure

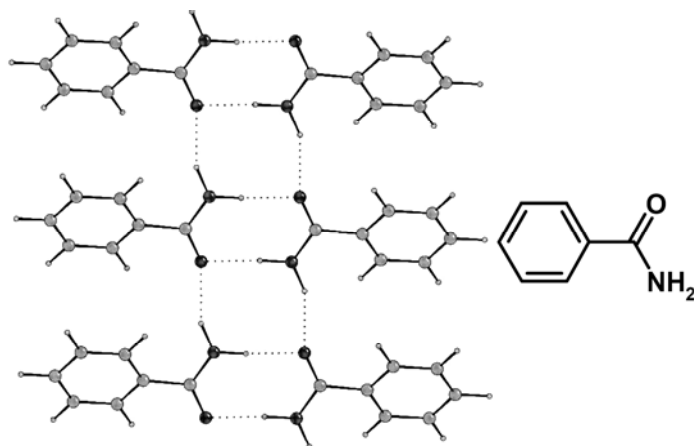


Figure 1.6: Centrosymmetric $N-H\cdots O$ dimers in benzamide - α -network.⁵⁹

1.6). Combination of such α networks can be used to generate β networks, one such example being the β network formed by 3,3'-ureylenedipropionic acid, where there is a co-existence of $O-H\cdots O$ and $N-H\cdots O$ bonds. Another interesting example where the α networks are linked into β networks by $O-H\cdots N$ hydrogen bonds is in the co-crystal of an oxalamide derivative with 1,2-(bis-4,4'-bipyridyl) ethylene.⁶⁰

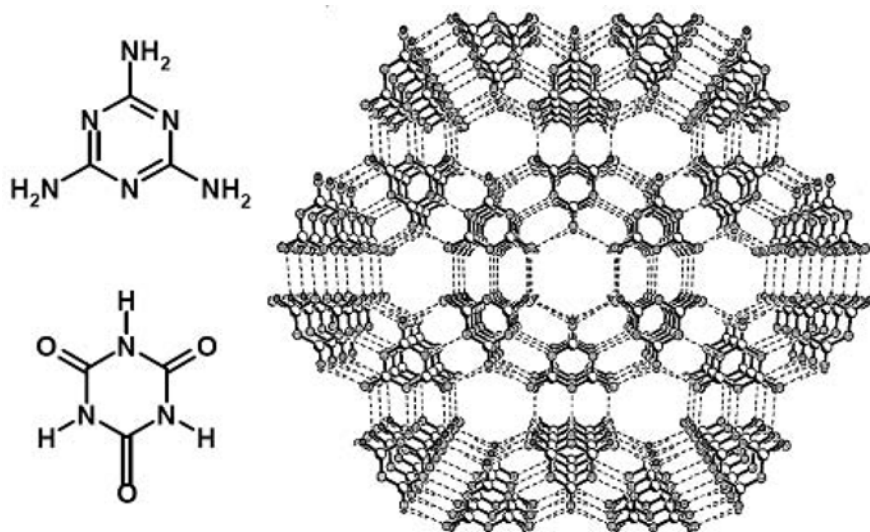


Figure 1.7: Three-dimensional arrangement of the sheets of 1:1 adduct formed by melamine and cyanuric acid giving rise to rosette and channel structures.⁶²

Whitesides and co-workers⁶¹ have studied the complexes formed between substituted melamine and substituted cyanuric acid. Three antiparallel $N-H\cdots O$ and $N-H\cdots N$ bonds stabilize the structure forming linear and crinkled tapes. They also proposed

the possibility of the formation of melamine and cyanuric acid complex. Rao and co-workers⁶² have synthesized the melamine cyanuric acid (1:1) complex (see Figure 1.7) forming similar antiparallel combination of hydrogen bonds to give rise a rosette and channel structures. This is one of the best examples for the designed synthesis of supramolecular architectures utilizing strong hydrogen bonds and their directional properties.

1.1.5 Engineering strategies based on weak hydrogen bonds

The weak hydrogen bonds are intermolecular interactions in which the hydrogen atom is bound to less electronegative atom, and are weaker compared to the strength of the previously discussed classical hydrogen bonds. The weak interactions include various C-H...O, N-H...N and interactions involving sulfur as the acceptor. Many of the studies have shown that C-H...O interactions share various characteristics of strong hydrogen bonds such as N-H...O and O-H...O hydrogen bonds.^{18,63} Generally non-classical hydrogen bonds in which the C-H act as the donor and the π -face of the aromatic ring, acetylene or ethylene act as acceptor are referred as soft hydrogen bonds. The statistical studies using crystallographic data have cleared the mist around the existence and nature of such type of weak interactions. There are a lot of ambiguities regarding the electrostatic and directional nature of these interactions in comparison to strong interactions.⁶⁴ The statistical study of the crystallographic data by Taylor and Kennard⁶⁵

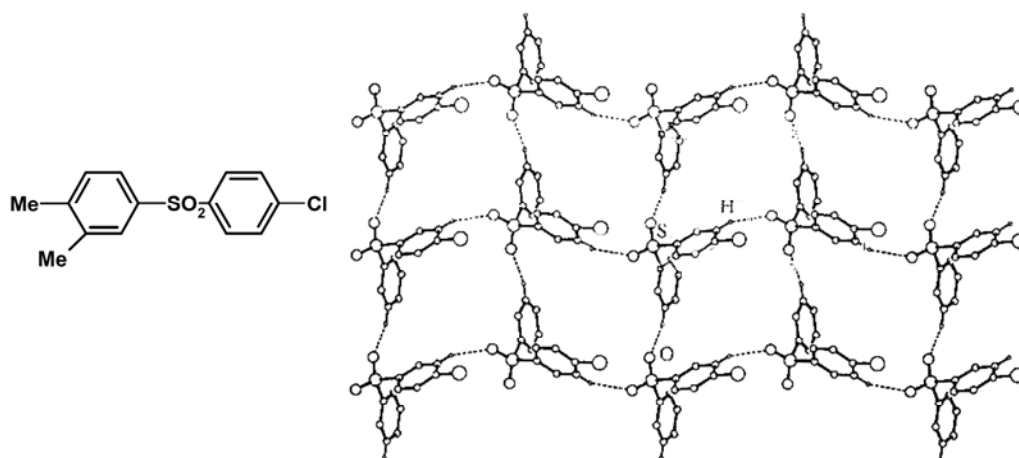


Figure 1.8: Part of the crystal structure of diarylsulfone showing a (4,4) net of R₄(24) rings.⁶⁷

and Thalladi⁶⁶ et al. have shown the directional nature of C-H...N, C-H...Cl and C-H...F hydrogen bonds. Glidewell et al.⁶⁷ has demonstrated the supramolecular structure formation in various diarylsulfones solely by C-H...O hydrogen bonds. In these supramolecular aggregates the aromatic C-H act as the hydrogen bond donor and the oxygen atoms of the SO₂ act as the hydrogen bond acceptor. The C-H...O interactions present in these systems lead to the formation of the multi dimensional assembly. Figure 1.8 depicts a two dimensional assembly formed by diarylsulfone with a (4,4) net of R₄⁴(2,4) ring.

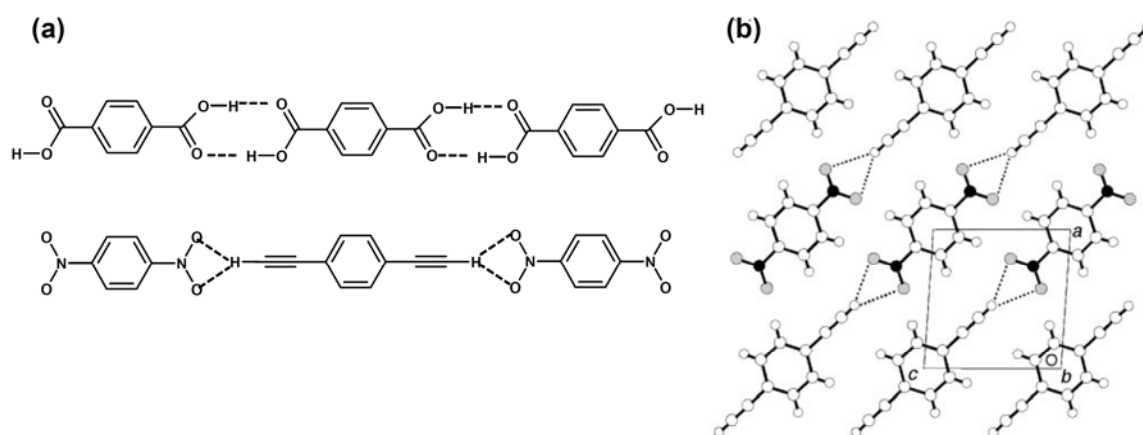


Figure 1.9: (a) Bifurcated C-H...O coupling in 1,4-diethynylbenzene with 1,2-dinitrobenzene, which is structurally analogous to the dimer coupling in carboxylic acid. (b) The co-crystal of 1,4-diethynylbenzene with 1,2-dinitrobenzene viewed along the *b* direction.⁶⁸

Among the weak hydrogen bonds, interactions formed by the terminal alkynes with oxygen acceptors deserve a special mention. Robison et al.⁶⁸ used the terminal hydrogen of the alkynes such as those in 1,4-diethynylbenzene to form a linear molecular tape like structures (see Figure 1.9). In this study the authors present the interaction of 1,4-diethynylbenzene with 1,2-dinitrobenzene where the terminal hydrogen of the alkyne form a bifurcated interaction with the nitro group of the 1,2-dinitrobenzene. The dimeric interaction (synthon **A**) in the terephthalic acid is replaced with the bifurcated hydrogen formed between the terminal alkyne and the nitro group.

Similar to C-H...O hydrogen bonds, design and synthesis of supramolecular architectures utilizing C-H...N hydrogen bonds also deserves equal importance. The

solid proof for the directional nature and applicability of these interactions for the formation of interesting hydrogen bonded net work has been demonstrated by Reddy et al.⁶⁹ using the structure formed by 1,3,5-tricyanobenzene in its 1:1 cocrystal with hexamethylbenzene. The 1,3,5-tricyanobenzene forms a hexagonal network using linear

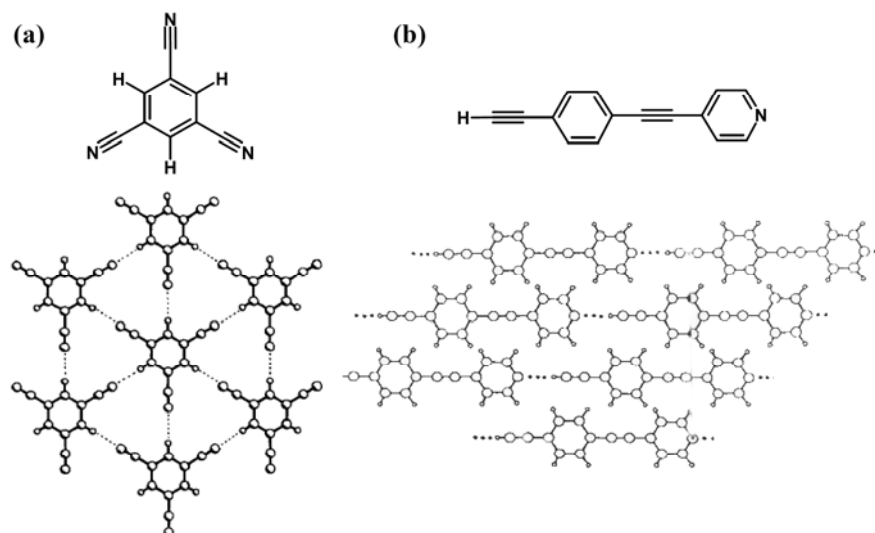


Figure 1.10: The C-H...N network of 1,3,5-tricyanobenzene molecules in the crystal structure of the 1:1 complex formed with hexamethylbenzene.⁶⁹ (b) Packing arrangement of 4-(4-Ethynyl phenyl)ethynylpyridine in the crystal. C(sp)-H...N bonds shown by dotted lines.⁷⁰

C-H...N hydrogen bond as shown in Figure 1.10a. Similar to C-H...O hydrogen bonding observed in the case of 1:1 complex of 1,4-diethynylbenzene and 1,4-dinitrobenzene,⁶⁸ a linear C-H...N interaction is formed in the crystal structure of the 4-(4-Ethynyl phenyl)ethynyl pyridine. 4-(4-Ethynyl phenyl)ethynyl pyridine crystallizes in the form of polar crystals in which the molecules are directed in straight hydrogen-bonded tapes through C(sp)-H...N hydrogen bonds (see Figure 1.10b).⁷⁰

Among the non-conventional weak interactions the C-H... π bond⁷¹ plays a crucial role in controlling the crystal packing of many organic compounds. A recent article by Nishio highlights the nature and characteristics of these interactions in comparison with other weak interactions. One of the best examples which demonstrate the importance of such weak interactions is reported by Thalladi et al.⁷¹ on the octupolar

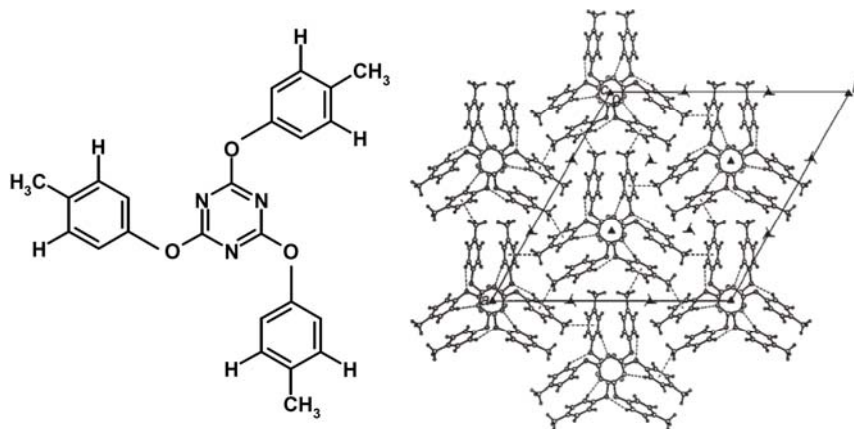


Figure 1.11: Octupolar trigonal network structure in 2,4,6-tris-(4-methoxyphenoxy)-1,3,5-triazine. The 3-fold, 3_1 - and 3_2 -axes are depicted.⁷²

trigonal network formed by 2,4,6-tris-(4-methoxyphenoxy)-1,3,5-triazine (see Figure 1.11). The C-H $\cdots\pi$ interactions have been used to achieve third dimensional control of the crystal structure and have led to octupolar NLO activity. Other than C-H $\cdots\pi$ interactions, the interactions that are of special relevance in conjunction with the biological systems are N-H $\cdots\pi$ type. The various conformationally rigid substrates complexed with the receptor have shown that amide-aromatic hydrogen bonds can have a vital effect on the recognition properties of host-guest complexes in a non-polar medium.⁷³

1.1.6 Co-existence of strong and weak hydrogen bonds

Most of the crystals structures in literature are formed by both strong and weak interactions, where the balance between these interactions results in stable structures. In many of the cases, either strong or weak hydrogen bond acts as the structure directing interaction. In order to design a stable supramolecular assembly with preconceived geometry the understanding of both the weak and strong interactions and their suitable manipulation is necessary. There are some examples of weak hydrogen bonds functioning as the organizing forces in spite of the possibility for strong hydrogen bonds.

The study by Ranganathan et al.⁷⁴ on cocrystals formed by adipic acid with 2,4,6-triaminopyrimidine depicts an example where the weak N-H \cdots O interactions dominate over the strong carboxylic acid dimer synthon interactions. The molecules of 2,4,6-triaminopyrimidine penetrate in to assembly of the adipic acid and form a two

dimensional planar architecture, where the possibility of formation of dimeric O-H...O interaction is annihilated (see Figure 1.12).

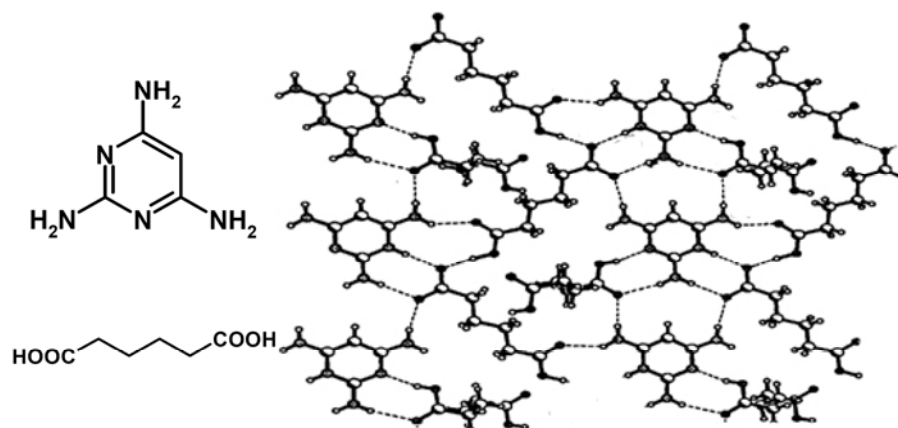


Figure 1.12: Arrangement of molecules of adipic acid and 2,4,6-triaminopyrimidine in a two-dimensional planar sheet of the complex.⁷⁴

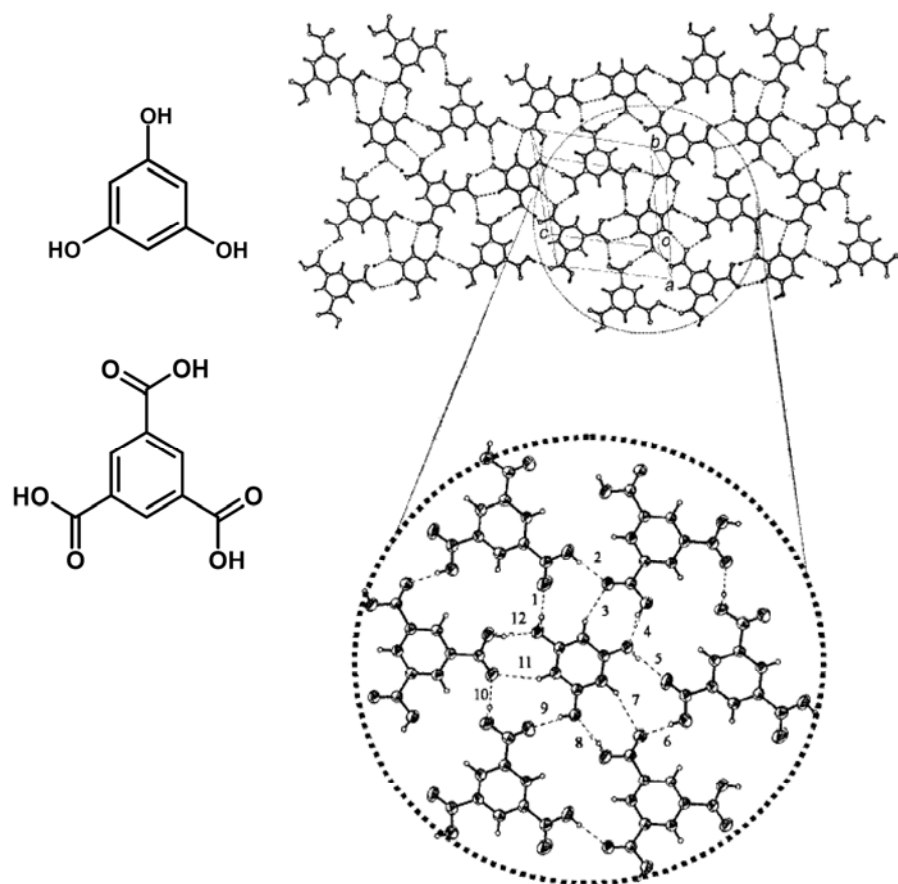


Figure 1.13: Structure of the adduct trimesic acid with phloroglucinol. One planar lamella (top right) and an enlarged rosette (bottom right) are depicted: Note the utilization of all the O-H donor and acceptor groups on phloroglucinol.⁷⁵

The coexistence of both weak and strong interactions with equal importance is demonstrated in the example of 1,3,5-trihydroxybenzene, (phloroglucinol) with trimesic acid complex.⁷⁵ In this adduct, both the O-H...O and C-H...O interactions play equal role in directing the crystal structure. The interactions shown in Figure 1.13 illustrate the rosette shaped repeating structures with fully hydrogen bonded donor and acceptors in phloroglucinol.

1.1.7 Other types of intermolecular interactions

The previous sections discussed various crystal engineering strategies using hydrogen bonding interactions. Despite of the large number of reports on hydrogen bonded supramolecular architecture; there are some interesting reports on other weak interactions, which play a structure-directing role. These interactions include halogen-halogen, halogen-nitro, nitro-nitro, aromatic (π - π) and even gold (I)-gold (I) interactions. Halogen-halogen contacts have been known and are used for design and synthesis of supramolecular architectures by Schmidt as early as the 1970s.⁸ The report on 1:1 adduct of 1,4-dinitrobenzene and 4-iodobenzoic acid (see Figure 1.14) exemplify the structure directing role of I...O contacts in spite of the possibility of strong dimeric O-H...O hydrogen bond formation within the carboxylic acid groups.⁷⁶

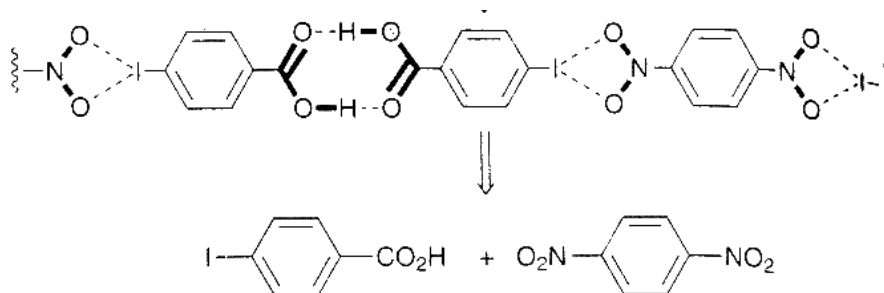


Figure 1.14: Retro-synthetic analysis for the linear ribbon patterns.⁷⁶

Bachman et al.⁷⁷ have analyzed the weak aurophilic interaction which are capable of controlling the supramolecular structure formation in the complexes of *n*-alkylisonitrile with AuCl. Aurophilicity or aurophilic bonding are attractive interactions that exists between closed-shell gold (I) centres. This interaction has been estimated to have strength similar to hydrogen bonding (29 - 46 kJmol⁻¹).⁷⁸ It is also distinctly directional like hydrogen bonding.⁷⁹

1.2 Effect of Weak Interactions and Molecular Packing on Solid State Properties of Organic Supramolecular Assemblies

The weak intermolecular interactions not only give rise to interesting supramolecular architectures but also affect the existing molecular properties and bring about new properties. Most of these newly generated properties are the aftereffects of the arrangement of molecules in the solid state. There are numerous reports in literature on interesting properties generated by the three dimensional arrangement of molecules in the crystal lattice. Some of these properties include molecular selectivity in porous structures,⁸⁰ electronic and photo physical properties,⁸¹ magnetism etc.⁸² As these properties in the solid state are due to molecular packing and weak intermolecular interactions, it is appropriate to look into the molecular assembling and solid state properties in some representative systems.

1.2.1 Organic Porous Solids

The natural and synthetic inorganic zeolites⁸³ with pore sizes of 10 to 20 Å are the classic examples of microporous materials with widespread industrial uses. Analogous microporous solids based on organic building blocks have the potential for a precise rational design, through the control of the shape and size of the pores.⁸⁴⁻⁸⁶ Host frameworks with an organic core offer some advantages: (1) The target network can be controlled by suitable manipulation of the functional groups and supramolecular synthons. (2) The nature, size and shape of pores and cavities in organic three-dimensional host frameworks can be altered with hydrogen bonding and hydrophobic interactions; (3) Inclusion and release of guest species is much more facile in organic hosts than in inorganic zeolites.

Yaghi et al.^{84,86,87} have designed many metal-organic frameworks that selectively bind aromatic guest molecules. Most often, Yaghi's group has employed hydrothermal method as one of the synthetic routes. Moore and co-workers⁸⁸ have made porous materials from ring-shaped units that stack themselves by hydrogen bonding. Each ring is made up of six rigid rod-like units and six corner pieces to form a regular hexagon. Acetylenic groups, however, gave rods; the corner pieces with benzene rings carry hydroxy groups to provide connections needed to make hexagons. The benzenes in neighboring sheets interact in a way that encourages the rings to stack on top of one

another, creating parallel channels about 9 Å in diameter. A slightly different approach has been developed by Wuest and co-workers.⁸⁹ They used building blocks that create channels as they assemble themselves into a network. Wuest, in fact introduced the concept of *tectons* into supramolecular chemistry. Tectons are molecules with sticky ends that can participate in intermolecular interactions that are strong, specific and directional. The geometry of the tectons in turn determines the geometry of the network into which they assemble. A diamondoid network can be synthesized from tectons with four sticky hydrogen bonding sites in a tetrahedral orientation. Such self-assembly often results in the formation of channel structures, which are being filled by solvent molecules.

Recent studies by Ranganathan et al.⁹⁰ to incorporate solvent molecules such as benzene, toluene and xylenes in the porous channels formed by the adduct of trithiocyanuric acid and 4,4'-bipyridyl demonstrate the ability of the organic porous material to accommodate the incoming guest molecules. This work also shows the flexibility of organic porous materials to change the structure and interactions with respect to the structure of the incoming guest molecules. Figure 1.15 depict one of the representative examples of the host-guest channel formed by trithiocyanuric acid and 4,4'-bipyridyl where benzene molecules are accommodated in the channel.

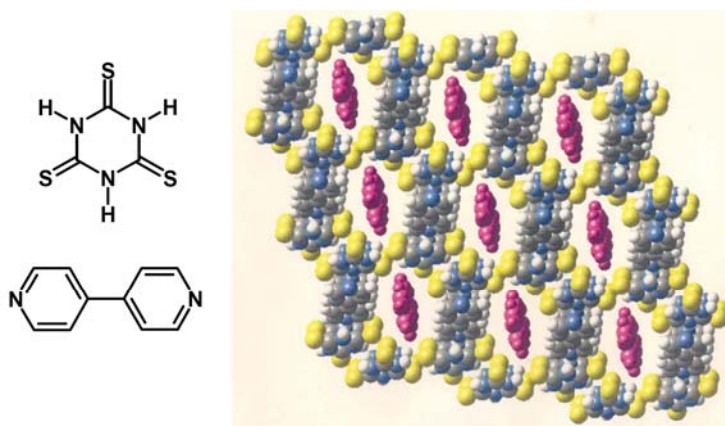


Figure 1.15: Three-dimensional structure of the 2:1 trithiocyanuric acid-4,4'-bipyridyl adduct, containing benzene in the channels.⁹⁰

1.2.2 Electronic properties of supramolecular assemblies

Recent literature covers a number of studies on electronic properties of organic molecules while they assemble to form super structures.⁹¹⁻⁹⁴ These studies have demonstrated the possibility of incorporating molecular crystal based light emitting

diodes (LED) and organic field effect transistors (OFET) into display devices and electronic circuitry. The electronic properties shown by these crystalline solids are highly dependent on the molecular packing and weak intermolecular interactions involved in the formation of the supramolecular assemblies.⁹⁵ Some of the representative systems which show rectification and field effect transistor behavior are polynuclear aromatic compounds^{96,97} (pentacene, rubrene etc.) and well known electron donor and acceptor systems like TTF and TCNQ and their derivatives.^{98,99} In addition to these systems, there are reports on organic field effect transistors based on conjugated thiophene based molecular crystals and other polymer based self-assembled films.^{100,101} It is interesting to note that the electronic property of the single crystalline FETs varies with respect to the crystallographic orientation of the crystals, hence the molecular packing. Various studies have shown that in order to obtain better electronic properties, it is preferable to have the mixing of π -density of two neighboring molecules.¹⁰² It is clear from the crystal structure of various organic electronic systems that the prevalent and preferred interactions in these systems are π - π stacking. A comparison made by Reese et al.¹⁰³ on various mobility data obtained from literature on rubrene crystals have shown that the mobility varies with crystallographic orientation.^{92b,95, 104-106} Figure 1.16 depicts the conclusion made by them where the mobility clearly depends on the crystallographic orientation and in turn the

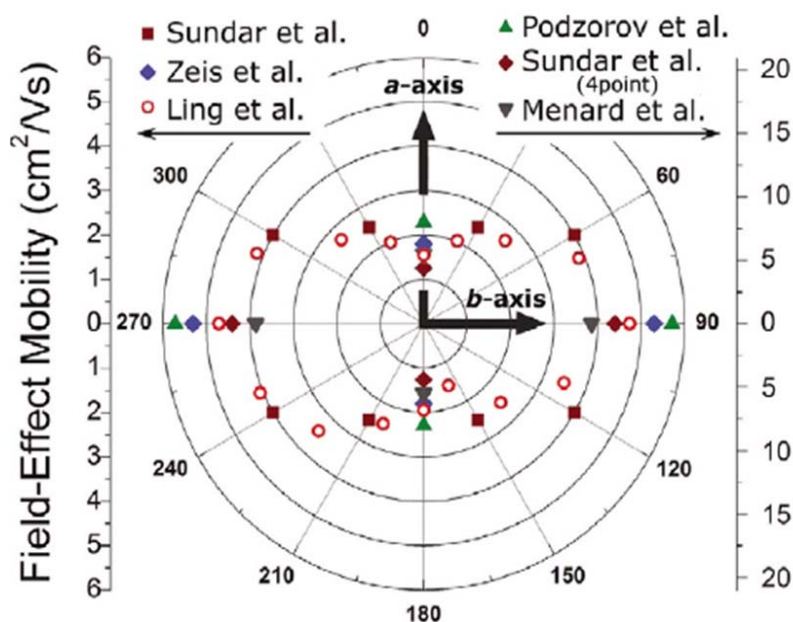


Figure 1.16: Field effect mobility in rubrene crystals with respect to crystallographic orientation of the molecules.^{92b,95, 104-106}

molecular packing and weak interactions. Recent studies by Naraso et al.⁹⁸ have shown that the various halogen substituted tetrathiafulvalne derivatives show interesting change in their electronic properties when brought into single crystal FETs. The halogen substitution not only brings about change in electronic structure of the molecules but also affects in molecular packing and weak intermolecular interactions. This study shows that these tetrathiafulvalene derivatives based FETs can be modified from p-channel to n-channel semiconductor by suitable halogen substitution.

1.2.3 Photophysical and optical properties of organic supramolecular assemblies

It is well known that when the molecules get into an assembly, the electronic states of the molecules undergo reorganization and give rise to new electronic states due to the formation of new molecular aggregates. The formation of new energy states solely depends on the arrangements of molecules in the solid state and the weak interactions holding the aggregates.^{1,107} The molecular arrangements in solid state and the various non-bonding interactions give rise to new photophysical properties such as absorption and emission,¹⁰⁸⁻¹¹⁰ that are quite different from the single molecular properties. In addition to these properties, there exist quite a number of reports on nonlinear optical properties such as second harmonic generation (SHG),¹¹¹⁻¹¹³ and higher order optical activities¹¹⁴ arising from the molecular packing and the non-bonding interactions involved in the solid state.

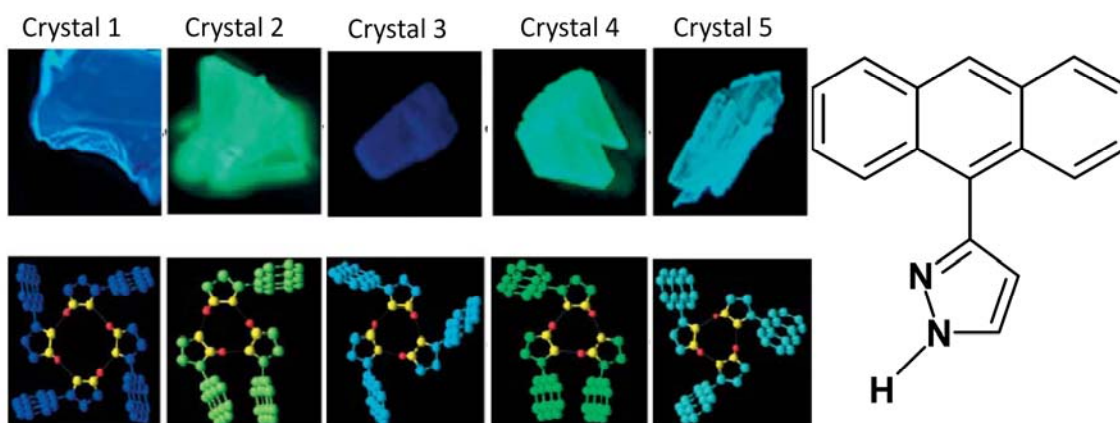


Figure 1.17: Molecular packing with N-H...N hydrogen bonding and emission from the crystals of 3(5)-(9-anthryl)pyrazole on excitation under UV light ($\lambda=365\text{nm}$)¹¹⁸

There are many studies on the tuning of absorption and emission properties of molecular systems by introducing suitable substitutions.^{115,116} However the absorption and emission properties of molecules in solid state are highly dependent on the molecular packing and weak intermolecular interactions like hydrogen bonding, C-H $\cdots\pi$ interactions and π - π stacking.^{81b} By suitably changing the molecular orientation and the intermolecular interactions, one can tune photophysical properties in the solid state.¹¹⁷ A recent study by Mutai et al,¹⁰⁹ have shown the switching of fluorescence by controlling the molecular packing in solid state using the two crystalline forms of 2,2':6',2''-terpyridine. Zhang et al.¹¹⁸ have shown the effect of changes in molecular packing and weak interactions on the emission properties of 3(5)-(9-anthryl)pyrazole. Figure 1.17 shows the weak interactions and emission from the polymorphic crystal forms. It is clear from the figure that the N-H \cdots N hydrogen bonding in these forms show drastic changes and thereby molecular packing.

Another highly active research area related to supramolecular chemistry is organic optical materials, in particular nonlinear optical (NLO) materials. Organic supramolecular assemblies and crystal engineering based on various non-bonding interactions offer a better possibility of obtaining desirable optical properties.¹¹⁹ Recent literature covers a number of reports on the second harmonic generation (SHG) activity of various organic supramolecular assemblies.¹²⁰⁻¹²¹ The uniqueness of organic based SHG active materials over traditional inorganic materials such as potassium dihydrogen tartrate (KDP) stems from the unlimited molecular engineering capability and their high

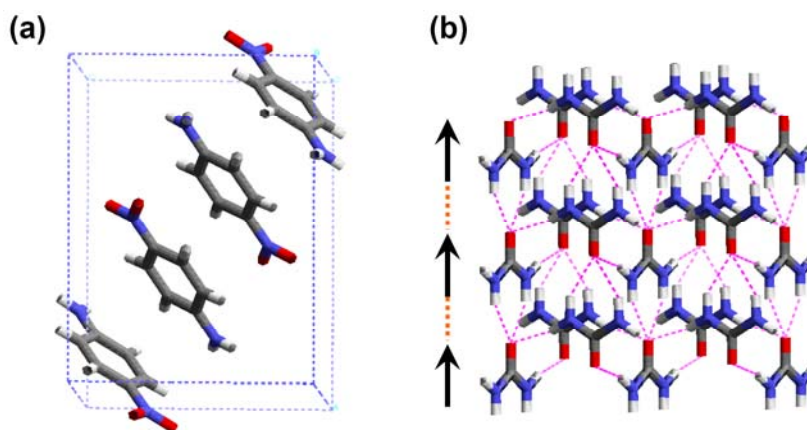


Figure 1.18: (a) Anti parallel molecular packing in *p*-nitroaniline crystal. (b) Hydrogen bonding in urea crystals along with dipole direction.¹²³⁻¹²⁴

laser threshold.¹²² A very stringent requirement for a material to exhibit non-zero SHG activity is that the crystal has to be in a non-centrosymmetric point group. In fact, most molecules (like paranitroaniline) which show very large polarizations at molecular level due to a large charge transfer from the donor to the acceptor (NH_2 to NO_2) crystallize in a centrosymmetric fashion arising from predominating anti-parallel π -stacking between the aromatic rings (Figure 1.18 a).¹²³ Hence, it is clear that the molecular packing in the crystals determine the non-zero SHG activity of a molecular system. There are some examples like urea where the dipolar interactions are overtaken by hydrogen bonding and exhibit large SHG activity.¹²⁴ In urea small molecular dipoles orient through N-H \cdots O hydrogen bonding and align as shown in Figure 1.18b giving rise to higher SHG activity. There are number of systems in literature which show hydrogen bond mediated proton transfer and higher SHG activity.¹²⁵ It has been shown that in these systems various hydrogen bonding interaction play a major role in charge redistribution and charge transfer. A dipolar system need not be highly SHG active in solid state since the non-centrosymmetry determines the SHG activity. The supramolecular chemistry provides a scope to obtain non-centrosymmetric crystals by forming complexes with chiral molecular species.¹²⁶

The studies by Thalladi et al.¹²⁷ have demonstrated the role of crystal engineering to obtain supramolecular architectures with properties such as octupolar nonlinear optical activity. Their studies on tribenzyl isocyanurate have shown the role of weak C-H \cdots O hydrogen bonding in directing the molecule to arrange in a herringbone packing with trigonal symmetry hence the octupolar activity (Figure 1.19). In another report, Zyss

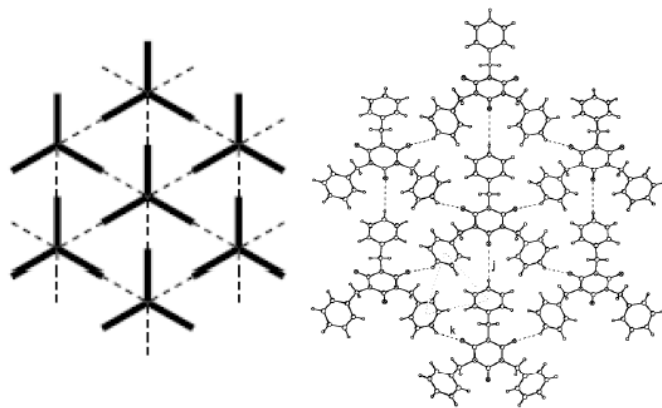


Figure 1.19: Crystal structure of tribenzyl isocyanurate down $[010]$ to show the trigonal network structure.¹²⁷

et al.¹²⁸ have shown a crystal engineering approach towards the generation of quadratic nonlinear optical activity from an acentric cocrystalline template made of two different bi-dimensional octupolar molecules: trinitrobenzene (TNB) and triphenylene (TP). The crystal structure analysis has evidenced parallel stacks with alternating vertically overlapping TNB and TP units, leading to a significant intermolecular charge transfer mediated by π - π interaction.

1.2.4 Organic ferroelectric and magnetic materials

Ferroelectricity is one of the prominent phenomena constituting an important research field in condensed matter science alongside with conductivity, superconductivity and magnetism.¹²⁹ In addition to academic interests, ferroelectrics find greater attention in technological applications from electronics to optics.^{129b} Ferroelectrics are polar crystals that exhibit spontaneous electric polarization, mostly belonging to the inorganic or hybrid organic-inorganic systems. Historically, the first organic based ferroelectric compound is ‘Rochelle salt’ [NaOOCCH(OH)CH(OH)COOK].¹³⁰ The very first initiative towards generating low molecular weight organic based ferroelectrics was based on charge transfer complexes composed of electron donor (D) and acceptor (A) molecules such as tetrathiadulvalene (TTF) and *p*-chloranil (qCl4).¹³¹ In TTF-qCl4 based systems, the π - π stacking between the donor and acceptor molecules has been exploited in gaining electric dipole along the π -molecular stack where strong electron-lattice interactions bring about the displacement of molecules with donor-acceptor dimerization. Recent literature covers a number of examples on proton transfer based ferroelectric materials where the hydrogen bonding and proton transfer play crucial role.^{130,131} Recent studies by Horiuchi et al.¹³² have demonstrated the use of crystal engineering towards the formation of displacive-type ferroelectrics using neutral co-crystals. In this study, they used the cocrystal formed from phenazine as base (acceptor) and 2,5-dihalo-3,6-dihydroxy-*p*-benzoquinones as acid (donor). The hydrogen bonded complex crystallizes in non-polar space group $P2_1/n$ and undergo a phase transition at low temperature to a polar space group $P2_1$ with the loss of *n*-glide plane.

Similar to ferroelectric properties, organic molecules based magnets also take up greater importance in the recent research scenario.^{132,133} There are quite a number of reports on organic radical based magnetic systems and these materials provide excellent

examples for the quasi one dimensional (1D) magnets because of the 1D stacking of the anisotropic π -orbitals in their crystals.¹³³ Recent report by Mandal et al.¹³⁴ have demonstrated the effect of molecular packing and weak intermolecular interactions on properties of aminophenalenyl-based neutral radical molecular conductors. A recent report by Maspoeh et al.¹³⁵ has shown the modulation of magnetic properties of organic porous structures formed by tricarboxylic substituted triphenylmethane radicals by selective inclusion of solvent molecules. On inclusion, the ferromagnetic behavior of α -phase of the tricaboxylic substituted triphenylmethane radical change to antiferromagnetic nature due to the changes in molecular packing and hydrogen bonding. It is interesting that the magnetic properties are reversible with the removal of the solvents from the crystal lattice.

1.3 Experimental Charge Density Understanding of Bonding and Non-bonding Interactions and Properties

Previous sections covered the role of various non-bonding interactions in forming supramolecular architectures and determining their solid-state properties. All the studies enumerated here had given a qualitative idea about the structure, bonding and weak interactions. The strength of various chemical bonds and weak interactions have been generally expressed in terms of bond lengths and bond angles using crystallographic methods¹³⁶ or by spectroscopic techniques such as infra red, Raman¹³⁷ or NMR.¹³⁸ The recent developments in the theoretical and experimental facilities have provided a new way of understanding the chemical bonding, weak interactions and various properties of molecular systems from the perspective of topology of charge density.^{139,140} One can obtain charge density distribution in a molecule experimentally^{140a} or theoretically. A high resolution X-ray diffraction on good quality crystals can give the charge density distribution in a molecular system experimentally¹⁴¹ while it can be obtained theoretically from high level *ab initio* calculation.¹⁴²

Since the first X-ray diffraction experiments on crystals in 1912 by von Laue,¹⁴³ X-ray crystallography has been widely applied with the purpose of determining the positions of atoms in the crystals and hence the geometrical structures of crystals and molecules. All these studies are aimed at structural information and pay little attention, if

any, to the details of the electron distribution. But both are inseparably linked in practice. The description of charge distribution in crystalline lattices has come a long way since the first quantum model of the atom. It was known from early days that a quantitative account of the chemical bonds in molecules and crystals would require the calculation of the probability density of the electron cloud between atoms. The possibility of measuring the charge density in a crystal from its X-ray diffraction pattern was envisioned many years ago when Debye and Scherrer discussed the possibility that the halos on a powder photograph were images of the electron orbits around the atoms.¹⁴⁴ This is evident from Debye's statement in 1915.

“It seems to me that experimental study of scattered radiation, in particular from light atoms, should get more attention, since along this way it should be possible to determine the arrangement of electrons in the atoms.”

Convinced that X-rays were scattered by electrons, Debye joined by Scherrer, turned his attention to chemical bonding and thereby initiated the field of X-ray charge density studies. Debye and Scherrer wondered how the valency dashes, used by chemists to describe the bond between atoms, could be replaced by an electron model that was consistent with their results from newly discovered powder diffraction method and also Bragg's ionization counter measurements.

Present day techniques for studying charge density distributions by diffraction methods originated in the 1960s with the interests of theoretical chemists' in calculating charge distributions to reproduce observed diffraction intensities for certain covalent crystals such as those of diamond and silicon. For these crystals, so-called space group-forbidden reflections are observed. Dawson¹⁴⁵ studied structure of diamond (see Figure 1.20) in 1967 using X-ray diffraction. The space group of diamond is $Fd\bar{3}m$. Carbon atoms are linked tetrahedrally to four equivalent neighbors, each having point symmetry $4\bar{3}m$ (T_d), lacking a centre of symmetry. The space group allowed reflections are $h+k+l = 4n$. However, the (222) reflection is observed for which $h+k+l = 4n+2$. In the conventional representation of X-ray structure factors, atoms are taken to be spherically symmetrical. Dawson generalized the treatment to recognize non-centrosymmetry in the

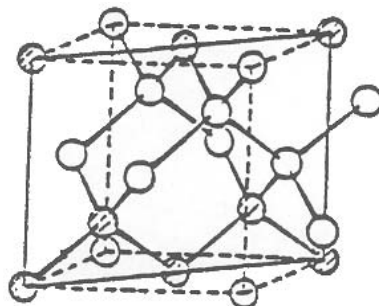


Figure 1.20: *The diamond structure*

electron charge distribution about each nuclear position. Dawson's "generalized structure factor formulation" reproduces the observed diffraction intensities, in particular for the space group-forbidden (222) reflections. The formalism showed for the first time, that it was possible to measure experimentally the aspherical features in covalent charge distributions arising from chemical bond formation.

1.3.1 The electron density

Electron or charge density in an N-electron system is the probability density of finding any of the N electrons in an infinitesimally small volume of space, the phase space, $d\tau$.

$$\rho(\mathbf{r}) = N \int |\psi|^2 d\tau \quad \dots(1)$$

where ψ is the stationary state function; τ denotes the spin coordinates of all the electrons and the cartesian coordinates of all electrons but one. It is expressed in $e\text{\AA}^{-3}$ or atomic units, au ($1 \text{ au} = 6.7483 e\text{\AA}^{-3}$). The description of electronic structure of a molecule in real space therefore relates to the charge density distribution around the constituent atoms.

1.3.2 Charge density from theoretical calculations

Charge density distribution in a molecule or a crystal may be obtained by *ab initio* Hartree-Fock calculations.¹⁴² In this method, electrons are assumed to move in a symmetric field generated by nuclei and the other electrons. Since the wave function and the potential are correlated, one obtains the wave function using an iterative procedure till the change in the potential does not produce any significant change in the wave function. Once the wave function is obtained, the electron density distribution can be readily

determined. Commercial programs such as Gaussian¹⁴⁶ and Gamess¹⁴⁷ are used regularly for this purpose. Calculations for crystals can be performed using the periodic Hartree-Fock method employing the density functional theory. Both of these options have been incorporated in the CRYSTAL program of Dovesi and co-workers.¹⁴⁸ The Kohn-Sham Density Functional approach has also been used for crystals. Within the density functional formalism, calculations can be done either at local density approximation (LDA) or using Generalized Gradient Approximation (GGA). Either of the methods is known to yield good results. R. F. W. Bader has initiated and made significant contributions in the last four decades to the understanding of the topology of charge density distribution in molecular crystals. In his book ‘Quantum Theory of Atoms in Molecules’ (AIM),³ information well beyond classical atomic connectivity has been obtained from analysis of the charge distribution. By the AIM approach, Bader has defined bond properties in terms of various topological entities. The theory of Atoms in Molecules is an interpretative theory that uses the electron density ρ as the information source. Transferability of the topological properties derived from an electron density distribution between molecules containing different functional groups is one of the important features of AIM. Bader has also defined the reactivity and stability of bonds in terms of the charge distribution.

1.3.3 Charge density from experiments

Experimental determination of charge density mostly relies on X-ray diffraction. Owing to the periodical nature of the atomic distribution in crystals and the interaction of the X-ray radiation with the electrons in it, it is possible to deduce the distribution of electron density in crystals from the intensities of the diffracted beams. What we actually measure in a crystallographic experiment are the structure factors $F(\mathbf{H})$ where \mathbf{H} are indices denoting a particular scattering direction corresponding to a crystal plane. The fundamental equations are:

$$I(\mathbf{H}) \propto |F(\mathbf{H})|^2$$

$$\propto \left| \sum_i f_i(\mathbf{H}) \exp(2\pi i \mathbf{H} \cdot \mathbf{r}_i) \right|^2 \quad \dots(2)$$

$$F(\mathbf{H}) = \int_V \rho(\mathbf{r}) \exp(2\pi i \mathbf{H} \cdot \mathbf{r}) d\mathbf{r} \quad \dots(3)$$

where \mathbf{r} is a position vector in direct space, \mathbf{H} is a reciprocal lattice vector, I the intensity of the diffracted beam, F the structure factor, $f_i(\mathbf{H})$ is the atomic scattering factor of the i^{th} atom in the unit cell, $\rho(\mathbf{r})$ is the electron density and V is the unit cell volume. The electron density is obtained from these structure factors via the following equation,

$$\rho(\mathbf{r}) = \frac{1}{V} \sum_{\mathbf{H}} F(\mathbf{H}) \exp(-2\pi i \mathbf{H} \cdot \mathbf{r}) \quad \dots(4)$$

In the final stage of data processing, non-linear least-square refinements are used to fit a model electron density to the measured one. This is equivalent to minimizing the difference density $\Delta\rho$, which is defined as $\rho_{\text{observed}} - \rho_{\text{calculated}}$. In routine molecular geometry determinations, $\rho_{\text{calculated}}$ is just a superposition of spherically symmetrical atomic densities. The density in a molecule can be conveniently modeled by partitioning it into core, spherical valence and deformation valence around each atom (the deformation being caused by the interatomic bonding).¹⁴⁹

$$\rho_{\text{atom}}(\mathbf{r}) = \rho_{\text{core}}(\mathbf{r}) + \rho_{\text{valence}}(\mathbf{r}) + \rho_{\text{deformation}}(\mathbf{r}, \theta, \phi) \quad \dots(5)$$

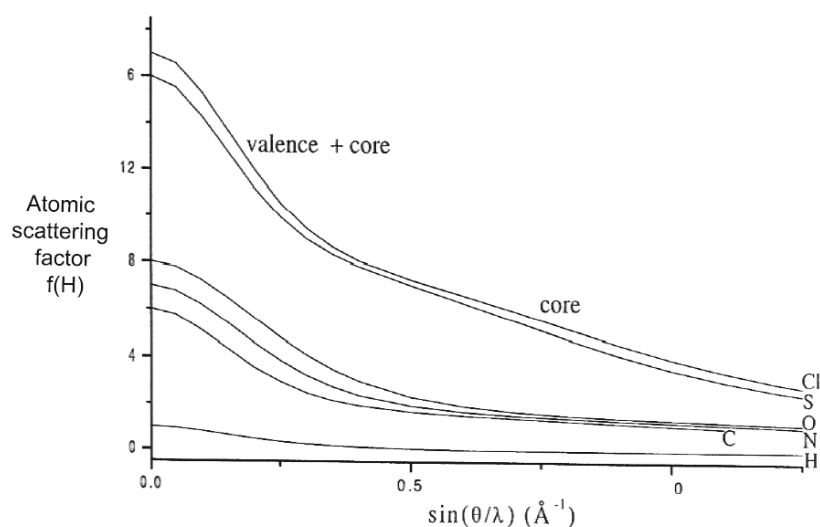


Figure 1.21: Variations of the scattering factor with $\sin\theta/\lambda$ for different atoms. Above 0.5 \AA^{-1} , the scattering due to valence electrons decreases gradually and the atom-core becomes visible. The scattering factors were obtained from the International Tables for Crystallography, Vol. IV, page 71 (1974).

For a complete description of bonding, accurate modeling of $f_i(\mathbf{H})$ becomes necessary. In parallel to $\rho(\mathbf{r})$ (see equation 5),

$$f(\mathbf{H}) = f_{\text{core}}(\mathbf{H}) + f_{\text{valence}}(\mathbf{H}) + f_{\text{deformation}}(\mathbf{H}) \quad \dots(6)$$

Such a partitioning of $f(\mathbf{H})$ is justifiable in X-ray diffraction since one can select regions of reciprocal space where core scattering is predominant. In Figure 1.21, a variation of $f(\mathbf{H})$ with scattering angle θ for various elements are shown. Each curve is composed of two regions. At low angles, the Bragg vector ($\mathbf{H}=2\sin\theta/\lambda$), $f(\mathbf{H})$ decreases sharply and above $\sim 0.5\text{\AA}^{-1}$, the fall is gradual. The first part has contributions from both the atom-core and the valence density, while the second arises mainly due to the core.

One major requirement for an experimental charge density data is to have a resolution better than 0.5\AA . For small unit cells with dimensions $\sim 30\text{\AA}$, data collection up to moderately high resolution (1.25\AA^{-1}) can be achieved using short wavelength radiation such as MoK_{α} (0.7107\AA). Moreover, data collection strategy typically depends on the type of the diffractometer. Fortunately, an increasing number of affordable and high-quality diffraction apparatus are now available, such as a low temperature rotating anode or even a dedicated synchrotron facility with state-of-the-art area detector. These powerful devices yield an experimental electron density (ρ_{observed}) which contains much more information than required merely to find atomic coordinates. In 1998, it was reported that a very high resolution picture of an amino acid could be obtained within one day,¹⁵⁰ whereas in the past this could be a matter of several months. The Atoms in Molecules (AIM) analysis is equally valid for ρ retrieved from an X-ray diffraction experiment.

1.3.4 Representation of the charge density and deformation densities

The charge density can be represented either as a two-dimensional contour map, a three-dimensional contour map or as a relief map. Figure 1.22a shows the 2D contour map of ρ evaluated in the symmetry plane of formaldehyde. The outer contour line (corresponding to $\rho = 0.001\text{ au}$ or $0.0067\text{ e}\text{\AA}^{-3}$) can be taken as the boundary of the molecule. Inside this contour line, lies a set of non-intersecting contour lines of higher electron density, each completely enclosing the next one (of higher ρ value). Figure 1.22b is termed a relief map, which utilizes the third dimension to depict the value of ρ . From these figures, it looks as if ρ is quite featureless except for indicating the positions of the nuclei. The relief map also show the density centered around the atoms with huge

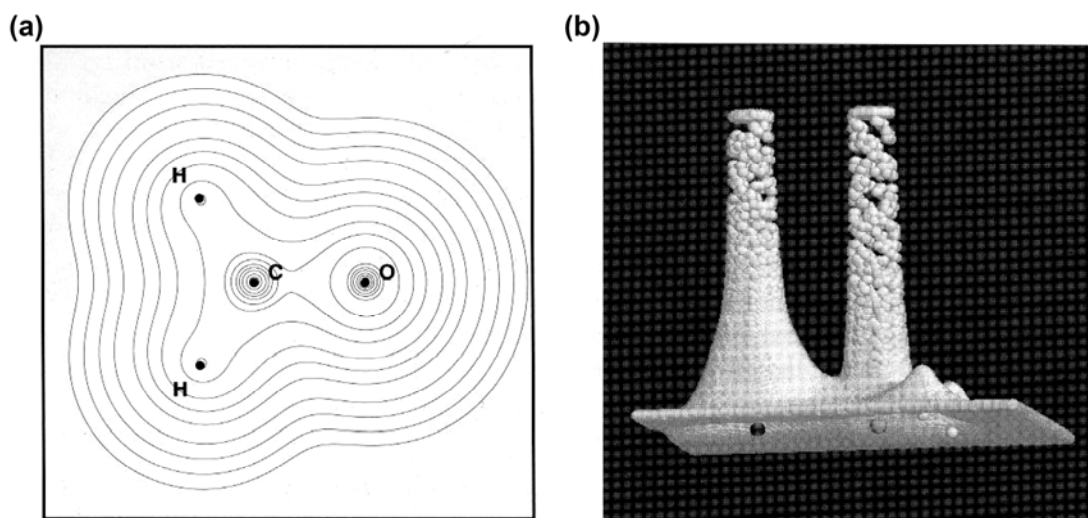


Figure 1.22: (a) A contour plot of the electron density in the symmetry plane of formaldehyde. The outer contour line corresponds to $0.0067 \text{ e}\text{\AA}^{-3}$, and the electron density increases exponentially toward the innermost contour. (b) A relief map of the electron density in the symmetry plane of formaldehyde. The nuclei are marked under the relief map, oxygen (left), carbon (middle) and hydrogen atoms (right).¹⁵¹

peaks which is overall featureless. In order to obtain the chemistry behind the charge density a new concept of deformation density has been introduced which give the eliminated density over the contributions from the nucleus. The experimental deformation density is the remainder of the subtracted promolecular density from the total density. The promolecule is a superposition of spherical atoms centered at the nuclear positions. The role of deformation density in a charge density analysis can be made clearer from the example of oxalic acid given in the Figure 1.23. The deformation density shown in the figure depicts the features of the bonding and lone-pair regions. From the figure it is clear that one can extract out the bonding density and non-bonding density like lone-pair density from the total density which include contribution from the nucleus.

$$\rho_{\text{deformation}} = \rho_{\text{total}} - \rho_{\text{promolecule}} \quad \dots(7)$$

The $\rho_{\text{deformation}}$ reveals the asphericity of the valence electron density due to chemical bonding and intra/intermolecular interactions in the crystal. Experimental charge density can be analyzed in two ways. In the first method, both the atomic positions and deformation density were obtained from the X-ray diffraction whereas in the second

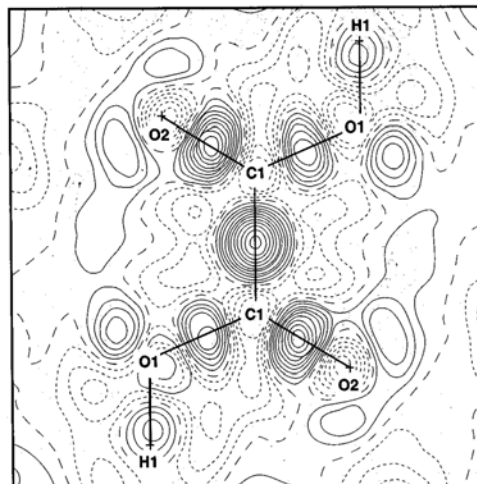


Figure 1.23: A standard deformation density in the molecular plane of the oxalic acid molecule at 15 K. Zero and negative lines are dashed. ¹⁵⁹

method the atomic positions are determined by a neutron diffraction data and the deformation density is obtained by X-ray diffraction data. The latter method is rather costly and laborious besides it requires a big crystal. In recent years the extraction of experimental charge density from the data, which is completely obtained from X-ray diffraction, is more popular and the work presented in this thesis is also based on this methods.

1.3.5 The multipole model and computer codes

The general analytical description of atomic density by R. F. Stewart¹⁵² was the stepping-stone for the present day models, which is used for experimental charge density. The further improvements by Hansen and Coppens^{149, 153} implemented a core contribution, a valence contribution, and a deformation term representing the deviation of the valence density from spherical symmetry:

$$\rho_{\text{atom}}(\mathbf{r}) = \rho_{\text{core}}(\mathbf{r}) + P_V \kappa^3 \rho_{\text{valence}}(\kappa \mathbf{r}) + \sum_l \kappa'^3 R_l(\kappa' \zeta \mathbf{r}) \sum_{m=-l}^l P_{\text{Imp}} Y_{\text{Imp}}(\theta, \varphi) \dots (8)$$

The Figure 1.24 depicts a spherical polar coordinate system of an atom. The deformation is expressed in terms of a radial function $R_l(\mathbf{r})$ modulated by angular functions $Y_{lm}(\theta, \phi)$, defined on local axes centered on the atoms. The angular functions are the same spherical harmonic functions, which are used to describe atomic orbitals,

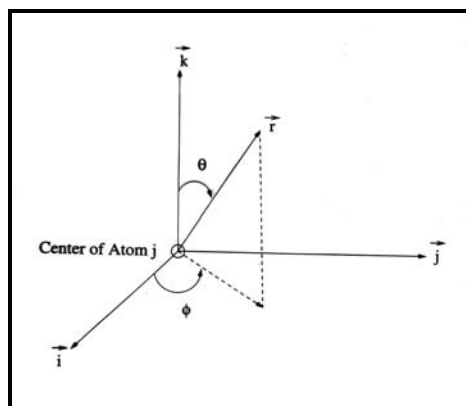


Figure 1.24: Local coordination system.

but normalized for charge density rather than for wavefunctions. The functions with $l = 1$ are called dipoles, $l = 2$ quadrupoles, $l = 3$ octopoles and $l = 4$ hexadecapoles. The population parameters P_v , P_{lm} and expansion-contraction coefficients κ and κ' are refinable parameters, together with the coordinates and temperature factors. The multipoles on the first row atoms are generally refined up to octapole moments, while for the heavier ones, moments up to hexadecapole are used. Hydrogen atoms are restricted to dipole. Kappa values greater than unity indicate contraction while lesser than unity indicate expansion. As the core is not affected by chemical bonding, there is no kappa on core, while on the valence shell, various types of kappa's namely, spherical, deformation, monopole, dipole, quadrupole, octopole and hexadecapoles are applied. As hydrogen has only one electron, the kappa value for hydrogen is quite high (close to being 1.2) compared to other atoms, which are close to 1. The above formalism is well adopted in the recently developed user-friendly program package – XD.¹⁵³ Older codes such as MOLLY, VALRAY, LSEXP, POP are also still in use. The quality of a refined model can be monitored based on the residuals and the goodness-of-fit parameter, besides closely inspecting the deformation density maps.

$$R_1 = \Sigma (|F_o| - |F_c|) / \Sigma |F_o| \quad \dots(9)$$

$$wR_2 = [\Sigma w(F_o^2 - F_c^2)^2] / \Sigma w(F_o^2)^2]^{1/2} \quad \dots(10)$$

$$S = ([\Sigma w(F_o^2 - F_c^2)^2] / (n-p))^{1/2} \quad \dots(11)$$

where n refers to the number of reflections and p is the total number of parameters refined.

1.3.6 Criteria for the use of the multipole model

The aim of electron density distribution is to analyze the finer details of charge distribution by comparing the chemically related molecules. A rigidity test of the molecule is important since anisotropic displacement parameters are known to compensate both for systematic errors in the data and also for inadequacies of the model. The rigid body libration analysis proposed by Hirshfeld¹⁵⁴ has reasoned out that the relative vibrational motion of a pair of bonded atoms has an effectively vanishing component in the direction of the bond. If $z_{A,B}^2$ denotes the mean square displacement amplitude of atom A in the direction of atom B, then for every covalently bonded pair of atoms A and B,

$$\Delta_{A,B} = z_{A,B}^2 - z_{B,A}^2 = 0 \quad \dots(12)$$

The deviation of any bond in a molecule from this postulate indicate insufficient structural model. Hirshfeld estimated that for atoms at least as heavy as carbon, $\Delta_{A,B}$ should normally be smaller than 0.001 \AA^2 . Verification of the model and the anisotropic displacement parameters by this test strengthens confidence in the experimentally determined electron density distribution. In addition, for a precise multipolar modeling of the fitted data, very accurate intensity measurements, chemical suitability and crystal suitability (ordered structure, appropriate size and a well-characterized morphology) are essential.

1.3.7 Topology of the charge density

The topology of charge distribution has many valuable features like maxima, minima, saddles and nodes. They help to characterize the fundamental elements of the structure such as atoms, bonds and lone-pair electrons etc. These are analyzed in terms of critical points, the points where the electron density exhibit a maximum or minimum. As an example, the charge density distribution in water molecule³ is depicted in Figure 1.25 in the form of contours as well as relief map. The density is maximum at the oxygen core position and it decreases sharply toward the region in between oxygen and hydrogen reaching the minimum value at the critical point (CP at which $\nabla\rho = 0$). This point carries maximum densities from the other two perpendicular directions. For example, the density in the xy-plane (normal to O-H bond) appears as a local maximum

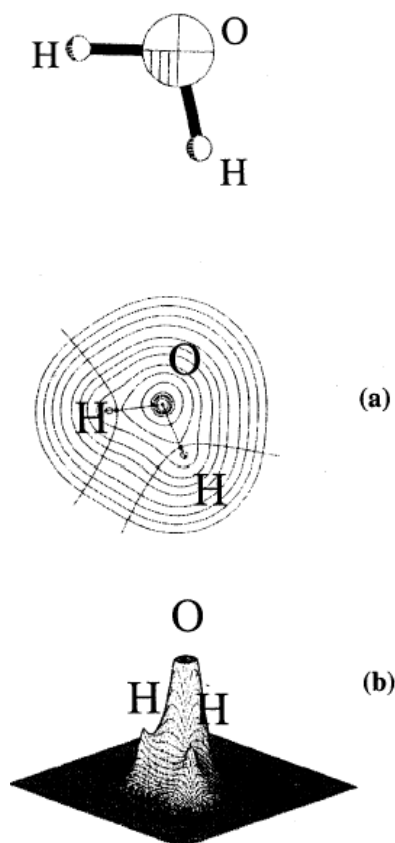


Figure 1.25: Water: charge density in the molecular plane, (a) the contour map. The outermost contour has the value $0.0067 \text{ e}\text{\AA}^{-3}$. The density increases almost exponentially for inner contours. The bond paths, the interatomic surfaces and the bond critical points are also indicated. (b) The relief map: atom-cores are seen as peaks.³

at the critical point lying between the oxygen and hydrogen nuclei, while in the other dimension, it appears as saddle. In other words moving x or y axes towards the critical point (CP) we reach maximum in $\rho(r)$ [$\partial^2\rho(r_c)/\partial x^2 < 0$ and $\partial^2\rho(r_c)/\partial y^2 < 0$]. But if we move along the z -axis towards CP, then a minimum in $\rho(r)$ is reached [$\partial^2\rho(r_c)/\partial z^2 > 0$]. A quantitative description of charge density thus turns out to be the careful examination of the number and the nature of such critical point in and around the molecule.

A critical point (CP) is characterized not only by its density but also by curvatures and associated signs.³ These vital parameters are used to ascertain the nature of bonds in molecules. For an arbitrary choice of coordinate axes, one encounters nine second derivatives of the form $\partial^2\rho/\partial x\partial y$ in the determination of the curvatures of ρ at a point in space. Their ordered 3×3 array is called the Hessian matrix of the charge density. Thus,

$$\text{Hessian, H} = \begin{pmatrix} \partial^2 \rho / \partial x^2 & \partial^2 \rho / \partial x \partial y & \partial^2 \rho / \partial x \partial z \\ \partial^2 \rho / \partial y \partial x & \partial^2 \rho / \partial y^2 & \partial^2 \rho / \partial y \partial z \\ \partial^2 \rho / \partial z \partial x & \partial^2 \rho / \partial z \partial y & \partial^2 \rho / \partial z^2 \end{pmatrix}$$

is a real, symmetric matrix and can be diagonalized. The new axes about which the Hessian is diagonalized is called the principal axes of curvature, so termed because the magnitude of the three second derivatives of ρ calculated with respect to these axes are extremized.

$$\begin{pmatrix} \partial^2 \rho / \partial x^2 & \partial^2 \rho / \partial x \partial y & \partial^2 \rho / \partial x \partial z \\ \partial^2 \rho / \partial y \partial x & \partial^2 \rho / \partial y^2 & \partial^2 \rho / \partial y \partial z \\ \partial^2 \rho / \partial z \partial x & \partial^2 \rho / \partial z \partial y & \partial^2 \rho / \partial z^2 \end{pmatrix} \longrightarrow \begin{pmatrix} \lambda_1 & 0 & 0 \\ 0 & \lambda_2 & 0 \\ 0 & 0 & \lambda_3 \end{pmatrix}$$

The trace of the Hessian matrix, that is, the sum of the diagonal elements, is invariant to the rotation of the coordinate system. Thus, the curvature of charge density $\nabla^2 \rho$, called the Laplacian, obtained as the sum of eigenvalues - $\lambda_1, \lambda_2, \lambda_3$ of the Hessian matrix, is invariant to the choice of the coordinate system.

$$\text{Trace} = \lambda_1 + \lambda_2 + \lambda_3 = \text{Laplacian of the charge density}$$

The rank and the signature of Hessian matrix uniquely define the nature of critical points. The rank (r) of the critical points refers to the number of non-zero eigenvalues of the Hessian matrix, while the signature (s) refers to the sum of their signs as given in Table 1.2 and 1.3. The critical point can be characterized in a quantitative way by

Table 1.2 Various critical points and meaning.

Critical	Meaning
(3, -3)	All curvatures are negative and ρ is a local maximum at r_c .
(3, -1)	Two curvatures are negative and ρ is a maximum at r_c in the plane defined by their corresponding axes. ρ is a minimum at r_c along the third axis, perpendicular to this plane.
(3, +1)	Two curvatures are positive and ρ is a minimum at r_c in the plane defined by their corresponding axes. ρ is a maximum at r_c along the third axis, perpendicular to this plane.
(3, +3)	All curvatures are positive and ρ is a local minimum at r_c .

evaluating properties at them. Covalent bonds are usually associated with high charge densities (1.5 to $3 \text{ e } \text{\AA}^{-3}$) and negative Laplacians, while lower densities characterize ionic bonds and positive Laplacians.¹⁵⁵ Compared to these two bonds, hydrogen bonds are associated with even lower densities and Laplacians.

Table 1.3 Chemical entity defined in terms of critical points.

Chemical entity	Property	Critical point	Acronym
Atom-cores (or nuclear attractors)	ρ (local maximum)	(3, -3)	NA
Bonds	ρ (first order saddle)	(3, -1)	BCP
Rings	ρ (second order)	(3, +1)	RCP
Cages	ρ (local minimum)	(3, +3)	CCP
Lone-pair	$\nabla^2\rho$	(3, +3)	LP

1.3.8 Other topological parameters

Bond path

The vector that points in the direction of greatest increase in the electron density is called the gradient vector and the trajectory of tiny segments of gradient vectors is known as gradient path. The pairs of gradient paths which originate at each (3,-1) critical point and terminate at the nuclei define a line through the charge distribution linking the neighboring nuclei. This line (atomic interaction line) is called a bond path (BP).³ Along BP $\rho(r)$ is maximum with respect any other neighboring line. The critical point on the bond path (BCP) is the topological definition of a chemical bond, formalizing the

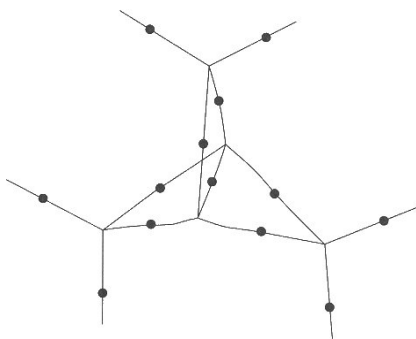


Figure 1. 26: Planar projection of the molecular graph of [1.1.1] propellane generated from a theoretical electron density. The small black dots denote the bond critical points.¹⁵⁶

theoretically predicted and experimentally observed (from deformation maps) accumulation of charge between bonded nuclei.¹⁵⁶ Figure 1.26 shows the collection of bond paths in [1.1.1] propellane.¹⁵⁶ It is clear from the figure that the bond paths are not always straight lines. These curved bond paths are consistent with the bond strain. The deviation of bond paths from straight line can be quantified by measuring the bond path length R_b , the distance between two nuclei measured along the bond path. The bond path is always greater than or equal to the bond length R_e , which is simply the distance between the bonded nuclei measured along a straight line.

Bond order

The value of electron density at the bond critical point, ρ (BCP), is a measure of the extent of charge accumulation along the bond path and can be related to the bond order. Creamer and Kraka obtained an exponential relationship between the bond order¹⁵⁵ and the electron density, ρ (BCP). The exponential relationship is given by,

$$n(A,B) = \exp \{a. [\rho (BCP)-b]\} \quad \dots(13)$$

where $n (A,B)$ is the bond order, A and B are the atoms forming the bond, ρ_{BCP} is the electron density at the BCP and a and b are the constants for the bond order relation.

Bond ellipticity

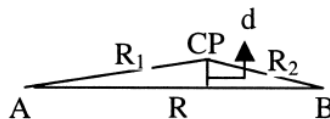
The charge density along the bond path reaches a minimum value at the BCP and the associated curvature of ρ is therefore positive. But the density along the plane normal to the bond path has maximum value at the BCP with a negative curvature. If the bond is not cylindrically symmetric (as for a bond with π -character) then charge is preferentially accumulated in a particular plane along the bond path. Thus, the bond ellipticity gives a quantitative measure of the bond ellipticity (ϵ). Values of ϵ provide a measure of the extent to which the charge density is asymmetrically concentrated at the plane perpendicular to the bond path.

$$\epsilon = \lambda_1 \backslash \lambda_2 - 1 \quad \dots (14)$$

where λ_1 and λ_2 are the negative Hessian eigenvalues, λ_2 being the curvature of smaller magnitude. The corresponding eigenvector is the major axis of curvature, defining the orientation of the plane in which the charge is smeared.

Bond polarization

An estimate of bond polarization¹⁵⁵ can be obtained from the location of the bond CP with respect to the internuclear vector,



$$\Delta_{\text{BCP}} \% = 100 \times (R_m - R_1)/R_m \quad \dots(15)$$

Where $R_m = (R_1 + R_2)/2$. The Δ value used to describe relative electronegativities of atoms forming the bond. The strain involved in the bond can be estimated¹⁵⁶ in terms of the vertical displacement, d_{cp} of the bond path from the internuclear vector

$$d_{\text{cp}} = 2 \times [s \times (s - R_1) \times (s - R_2) \times (s - R)^{1/2}] R \quad \dots(16)$$

where $s = (R_1 + R_2 + R)/2$

The above topological and charge density properties in combination with pseudoatomic charges describe a bond quantitatively.

The other quantity of interest is the kinetic energy density at the critical point, G_{cp} ¹⁵⁷ which is obtained by

$$G_{\text{cp}} = (3/10) (3\pi^2)^{2/3} \rho_{\text{cp}}^{5/3} + \nabla^2 \rho_{\text{cp}}/6 \quad \dots(17)$$

It has been used in some cases for the calculation of hydrogen bond energies¹⁵⁸ and their classification.¹⁵⁹

Ring properties

When nuclei are topologically connected to form a ring structure such as in benzene, a ring critical point (RCP) arises, which lies somewhere close to the geometric centroid of the ring. In the case of benzene, the ring consists of a set of six C-C bond paths. The spectrum of curvatures (λ_1 , λ_2 and λ_3) give rise to a (3, +1) critical point. This is because, along the ring surface, in two dimensions, the electron density is a minimum at the RCP and the associated curvatures are positive (λ_2 and λ_3). And perpendicular to the ring surface, the electron density is a maximum at the RCP with the associated curvature (λ_1) being negative. Therefore, at the RCP, the Hessian possesses two positive

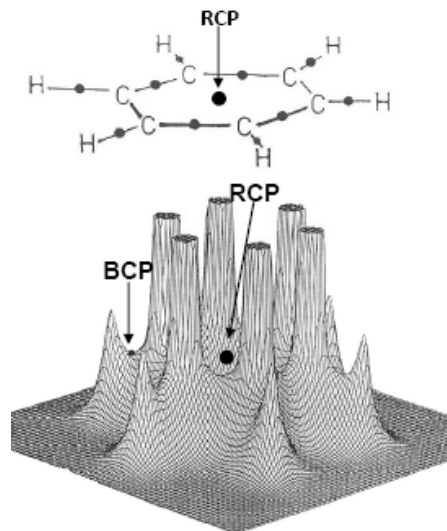


Figure 1.27: The upper half of the figure illustrates the molecular graph of benzene with BPs and BCPs. The lower half is a perspective diagram of the calculated electron density of benzene with respect to the plane containing the 12 nuclei. The position of the bond (BCP) and the ring critical point (RCP) are marked by black circles and arrows.¹⁶⁰

and one negative eigenvalues and the signature equals $(+1) + (+1) + (-1) = +1$. Figure 1.27 shows the position of the RCP in the charge density distribution of benzene.¹⁶⁰

1.3.9 Understanding of molecular properties

Dipole moment

As mentioned earlier, many chemical properties can be obtained from an analysis charge density. It is customary to evaluate molecular dipole moments from charge density using the multipole populations or using the direct integration method.¹⁶¹ In the multipolar method, the population coefficients P^i can be used to estimate the pseudo atomic charges on different atoms according to the equation,

$$q_i = n_i - P^i \quad \dots(18)$$

where, n_i is the total number of electrons of atom i . The molecular dipole moment is given by,

$$P_i = \sum_i z_i R_i + \int_V r \rho_i(r_i) dr \quad \dots(19)$$

Where R_i refers to the nuclear position vector and $r_i = r - R_i$. In the direct integration method, the corresponding equation is,

$$\mu = \int r \rho(r) dr \quad \dots(20)$$

Molecular dipole moment obtained from experimental charge density can be conveniently compared with that obtained using semi-empirical and *ab-initio* methods.¹⁶²

The dipole moment obtained can be used to evaluate many molecular properties such as interactions with various molecules and non-linear optical properties such as SHG activity.¹⁶³ The studies on dipole moment derived from charge density analysis have shown that the in-crystal dipole moment has been shown an increment in its values due to the weak interactions and the crystalline environment.¹⁶¹

Electrostatic potential

One of the important applications of charge density analysis is to obtain the electrostatic potential caused or generated by the charge distribution in the molecular species. The electrostatic potential (esp) generated by a molecule containing nuclear charge z_i , placed at R_i , with a charge distribution $\rho(r)$, is given by¹⁶⁴

$$V(r) = \sum_i \frac{z_i}{|r - R_i|} - \int \frac{\rho(r')}{|r' - r|} d^3r' \quad \dots(21)$$

As the electrostatic forces are relatively long range forces, they determine the path along which an approaching reactant will travel towards a molecule. A nucleophilic reagent will be first attracted to the regions where the potential is positive while an electrophile will approach the negative regions of the molecules.¹⁶⁵ Hence, the multipole derived electrostatic potential provides an exact idea about the intermolecular interactions such as hydrogen bonding and the possible interaction sites in various reactions in addition to the properties of the reactants.¹⁶⁶ An accurate experimental charge density derived from a X-ray diffraction experiment can provide a very good and reliable estimate of the electrostatic potential in the molecules.¹⁶⁷ Recently various groups have been using the electrostatic potential to understand the molecular properties and binding regions especially in drug receptor interactions.¹⁶⁸ Recent studies by Koritszansky et al.¹⁶⁹ on

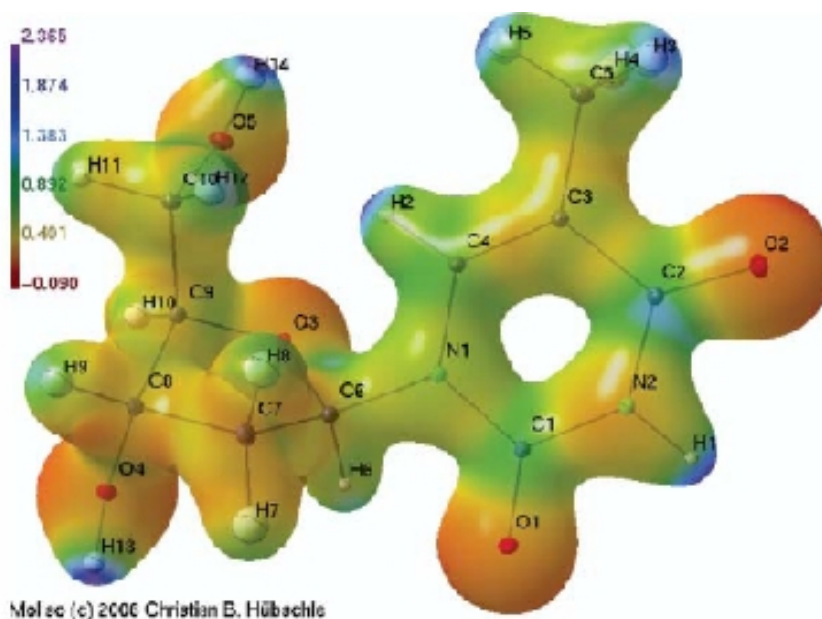


Figure 1.28: Molecular electrostatic potential of thymidine mapped on the charge density iso-surface at $0.5 \text{ e}\text{\AA}^{-3}$. The colour legend refers to units of $\text{e}\text{\AA}^{-1}$. MolIso representations are used.¹⁷⁰

penicillin derivatives have shown that the electrostatic potential can be used as a better tool for the understanding of various binding regions in a molecule. Recent development in the computer graphics provided the three dimensional visualization of the electrostatic potential using various colour codes. Figure 1.28 shows a three dimensional representation of electrostatic potential by Hübschle et al.¹⁷⁰ in thymidine molecules, which depict the positive (blue) and negative (red) regions over neutral (green) regions using an isosurface. The most relevant application such isosurfaces are the 3D QSAR models which generally used in drug designing for the drug-receptor interactions.¹⁷¹

Aromaticity

The concept of conjugation and aromaticity in various molecular systems has been widely studied employing a multitude of experimental and theoretical methods. Experimental methods include spectroscopic techniques such as NMR,¹⁷² X-ray crystallography and magnetic measurements,¹⁷³ while theoretical approaches mainly pertain to resonance energy calculations¹⁷⁴ and graph-topological evaluations.¹⁷⁵ Recently literature on charge density covers some studies on various aromatic molecules including poly nuclear hydrocarbons and other linear molecules. Various studies in these regard

include electron delocalization in citrinin¹⁷⁶ and in an annulene derivative¹⁷⁷ has been analyzed in terms of the critical point parameters. There has been an effort to obtain information on the extent of conjugation in N-containing compounds such as imidazole,¹⁷⁸ triazole,¹⁷⁹ and pyrimidine derivatives,¹⁷⁸ based on the bond properties. Though the electron densities at the bond critical points were found to be intermediate to those of single and double bonds akin to aromatic rings, the Laplacian and the ellipticity values hardly showed any systematic trend. Howard and Krygowski,¹⁸⁰ in their theoretical study of benzenoid hydrocarbons, emphasized the importance of the charge density parameters evaluated at the ring critical point (RCP) in describing the aromatic character of a molecule. The recent studies by Ranganathan et al.¹⁸¹ on squarate and croconate anion have shown that the ring critical point density can be used as a measure of the aromaticity.

1.3.10 Intermolecular regions - hydrogen bonds

The characterization of hydrogen bonds on the basis of the topological analysis of the electron density at the hydrogen bond critical point has been received considerable attention over the past decade.¹⁸² Koch and Popelier proposed a set of criteria,¹⁸³ based on the AIM [Atoms in Molecules] theory, recognizing the H...A interactions as hydrogen bond. The criteria are, [1] A well defined topology {bond critical point BCP and bond path BP} for each hydrogen bond. [2] A low value of $\rho\{\mathbf{r}_{\text{BCP}}\}$ which correlates with bond energy, [3] Positive |Laplacian of density $\nabla^2\rho\{\mathbf{r}_{\text{BCP}}\}$ [4] Mutual penetration of the donor and acceptor atoms, measured by the difference between the non-bonded and bonded atomic radii of the participating atoms, [5] loss of charge at hydrogen atoms, [6] decrease of dipolar polarization of hydrogen atom, and [7] decrease of the volume of the atomic basin associated with hydrogen atom. Early topological analysis of theoretically obtained electron densities¹⁸⁴ for a hydrogen bonded complexes between nitrile and halides have shown a linear correlation between the bond energy and density at the hydrogen bond critical point, $\rho\{\mathbf{r}_{\text{BCP}}\}$ of the H...N bonds for internuclear separation greater than 2 Å.

The atoms in molecules, AIM theory is the ideal tool for the detection and classification of hydrogen bonds. Lecomte and co-workers¹⁸⁵ related structural parameters and the topological properties at the bond critical points such as the electron density, $\rho\{\mathbf{r}_{\text{BCP}}\}$, the Laplacian of the electron density, $\nabla^2\rho\{\mathbf{r}_{\text{BCP}}\}$, and the positive

curvature of the ρ_{BCP} , along the internuclear axis, λ_3 . These researchers have shown a better correlation between hydrogen bond distances to positive curvature of the electron density $\{\lambda_3\}$. Furthermore, a study by Espinosa et al.¹⁸⁶ have shown that for closed shell interactions, the kinetic energy, $G_{\{\text{rcp}\}}$ and the potential energy density, $V_{\{\text{rcp}\}}$, at the critical point depend exponentially on the H \cdots O distance. These workers have also described relationship between the kinetic and potential energy densities and the curvatures of the electron density at the critical point $\{\text{CP}\}$.¹⁸⁷ Woźniak et al.¹⁸⁸ have analyzed the charge density distribution in the N-H \cdots O and C-H \cdots O bonds of dipicryl amine and have shown that the linear relationship between the charge density at the CPs and the N \cdots O contact distance. A recent study by Rangnathan et al.¹⁸⁹ have employed experimental charge density method to provide a detailed description of the hydrogen bond in terms of the location of the bond critical point and the geometry of the lone pair of electron. On the basis of the of a study of 7 different O-H \cdots O hydrogen bonded systems with 19 hydrogen bonds covering a wide range of hydrogen bond distances and angles, and arrived at a generalization of topological descriptors. This study provided a useful classification of hydrogen bonds in terms of new descriptors such as interaction line and nearness parameter. Besides enabling a complete charge density description of the hydrogen bond, this study provides new insights with respect to the location of the critical point and its relationship to the lone pairs involved in the formation of the hydrogen bond.

In addition to the experimental analysis of charge density at the hydrogen bond region there are also theoretical efforts to relate distances and the electron density parameters at the bond critical point. An example to illustrate the calculated electron density distribution in hydrogen bonds: Vorobyov et al.¹⁹⁰ have carried out *ab initio* calculations on the complexes of water with ethane, propene and allyl alcohol. The authors have analyzed the energetics and electron density redistribution associated with hydrogen bonding interactions in these clusters. Topological analysis of the electron density performed using Bader's AIM theory confirmed the closed shell, hydrogen-bonding nature of O-H \cdots O ($\rho \sim 0.13 \text{ e}\text{\AA}^{-3}$, $\nabla^2\rho \sim 2.30 \text{ e}\text{\AA}^{-5}$) and O-H $\cdots\pi$ interactions ($\rho \sim 0.13 \text{ e}\text{\AA}^{-3}$, $\nabla^2\rho \sim 0.92 \text{ e}\text{\AA}^{-5}$). High ellipticity values (~ 0.6) at the H $\cdots\pi$ BCPs of these complexes indicate their additional floppiness compared to the classical type of hydrogen bonds. Properties of H $\cdots\pi$ BCPs place O- H $\cdots\pi$ interactions with in the spectrum of

values proposed by Koch and Popelier for hydrogen bonds. The Laplacian maps are depicted in the Figure 1.29.

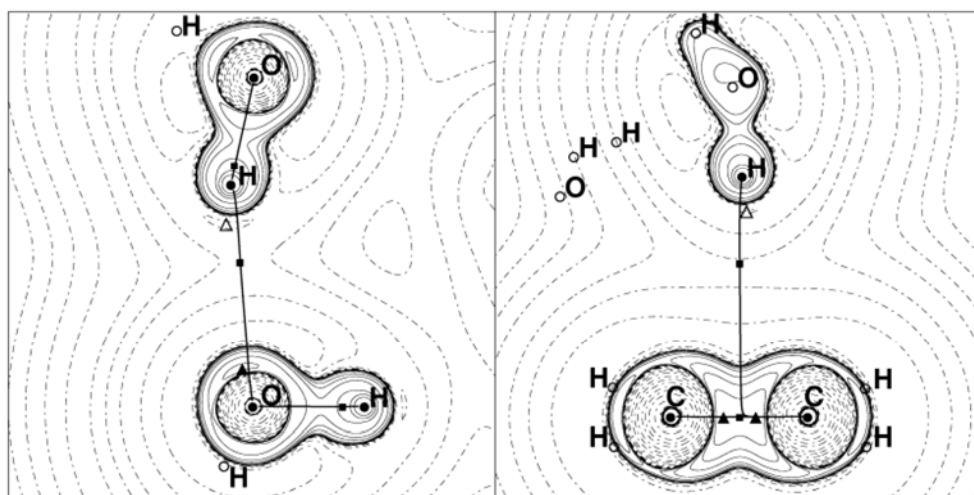


Figure 1.29: Contour plots of the negative of the Laplacian ($-\nabla^2\rho$) for the complex of ethene with the water dimer in the plane of (a) $O-H\cdots O$ and (b) $O-H\cdots\pi$ bonded atoms. Solid contours denote positive values of $-\nabla^2\rho$, regions of charge concentration, and dashed contours denote $-\nabla^2\rho < 0$, regions of charge depletion. BCPs are shown as solid squares. Bond paths: solid lines connecting nuclei. Maxima and minima in $-\nabla^2\rho$ are denoted by solid and open triangles, respectively.¹⁹⁰

Alkorta and co-workers¹⁹¹ studied various types of hydrogen bonds including dihydrogen bonds, bifurcated hydrogen bonds, $H\cdots\pi$ interactions, inverse hydrogen bonds involving carbene and silylenes as acceptors. Charge density studies on some systems that exhibit dihydrogen bonds ($H\cdots H$) have also been studied. Zhang et al.¹⁹² carried out theoretical studies on hydrogen bonded complexes, with strained organic systems like tetrahedrane acting as pseudo π -acceptors. Recent studies on charge density analysis cover interesting reports on various other interactions such as hydrogen bonds with halogen atoms¹⁹³ and halogen-halogen interactions,¹⁹⁴ such as $C-H\cdots F$ and $F\cdots F$ contacts.

1.4 Experimental and Related Aspects

1.4.1 Synthesis and crystallization of the compounds

The crystallizations of all the compounds studied in this thesis are carried out using slow evaporation or solvothermal techniques. A detailed description of synthetic methods and crystallization are provided under the experimental section of respective chapters.

1.4.2 Single crystal X-ray diffraction

Single crystal data sets were collected using a SIEMENS 3-circle X-ray diffractometer or Bruker-Nonious Kappa diffractometer. In SIEMENS 3-circle X-ray diffractometer χ -axis fixed at 54.74° in which the positive and the negative limits for 2θ and $(\omega-2\theta)$ axes are 30° and -85° ; 26° and -208° , respectively. The ϕ -axis on the other hand could be moved in the whole range of 0 to 360° . A photograph of the X-ray diffractometer is shown in Figure 1.30. The MoK_α radiation generated from a sealed X-ray tube (50 kV, 40



Figure 1.30: Single crystal X-ray diffractometer

mA) is monochromatised using a graphite monochromator held at 6° . The beam is then passed through a 0.5 mm collimator before falling on the crystal. The direct beam from

the collimator is stopped using a beam-stop, which is placed beyond the crystal. A charge coupled device (CCD) serves as the detector. It has a 1024×1024 pixelated phosphor screen protected by a beryllium window. At each pixel point on the screen, the X-ray photons are converted to optical photons, which are then carried to the CCD chip. The

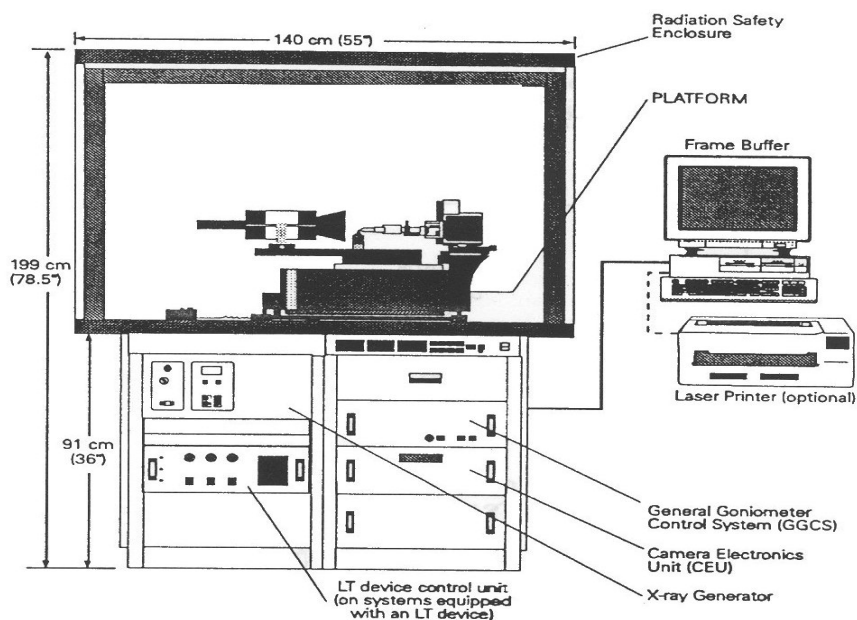


Figure 1.31: Components of the Siemens SMART/CCD system.

charge build-up is a measure of the diffracted intensity. Before data collection, dark current measurement is done without opening the shutter in order to estimate the background. The dark frames (16 frames) are collected for the same exposure time as the data and are averaged to obtain the background. The components of the SMART system are indicated in Figure 1.31.

Data collection for structural analysis

A polarizing microscope, LEICA MZ8 was used to examine the crystals. Crystals with dimensions in the range of ~ 0.1 to 0.4 mm were chosen for investigations. The crystal was mounted on a glass fiber attached to a copper pip. The copper pip with a crystal on top is mounted on the goniometer-head and the sleds on the goniometer head are adjusted to centre the crystal with respect to the cross-hairs of the optical microscope attached to the diffractometer. The data collection/reduction was done on a Pentium-DOS machine connected to the diffractometer using the SMART software.¹⁹⁵ Initially, the

orientation of the crystal with respect to the diffractometer was determined by collecting over a range of $\sim 7^\circ$ in ω in ~ 45 frames, each frame being read for about 10 seconds. The width of each frame was 0.3° . By this method, the cell parameters and the orientation of the crystal could be obtained. For extended data, a separate SGI workstation connected to the Pentium PC over the Local Area Network (100 Mbps) was used. A room temperature hemisphere data was usually recorded to check the quality of the data at various resolution levels. Depending upon the intensity of diffraction, the data is collected for 20 to 40 seconds per frame. The data reduction was carried out using the SAINT software in the SGI workstation. This computer also houses SHELXTL¹⁹⁶ for structure solution and other programs like PLATON.¹⁹⁷ The values of 2θ , ϕ and ω used for the hemisphere data are listed below in Table 1.4. For a routine structural determination, a hemisphere of data, collected at low-angle is sufficient.

Table 1.4 Optimal 2θ , ω and ϕ for hemispherical data at low resolution.

Run No.	2θ	ω	ϕ	Width	No. of frames
0	-28	-26	0	-0.3	606
1	-28	-21	88	-0.3	435
2	-28	-23	180	-0.3	230

The structure can be solved with a partial data set while the data collection is going on. This arrangement provided means of monitoring the data, so that any problems encountered during the experiment could be identified and corrected immediately. The total data and the refined matrix were used as input in the program, XPREP. The centric or the noncentric nature of the crystal was determined based on the normalized structure factor, E ; Mean $|E^2 - 1|$ being 0.968 (for centric) and 0.736 for non-centric crystal structures.¹⁹⁸ The exact space group was determined from the systematic absences. The graphic routine XP was used for the visualization purposes. All the structures were solved using direct methods of the XS routine of SHELXTL.¹⁹⁶ The XL routine of SHELXTL was used for the structure refinement over F^2 . All the non-hydrogen atoms were refined anisotropically. The fractional atomic coordinates of the various molecular crystals investigated are given in Appendix A1. Intermolecular bonds were calculated using the program PLATON.¹⁹⁷

Data collection for experimental charge density analysis

For low temperature charge density studies, the cold nitrogen gas from the dewar was made to shower on the crystal. The temperature of the stream could be recorded using a Chromel-Alumel (K-type) thermocouple. The temperature of the crystal could be

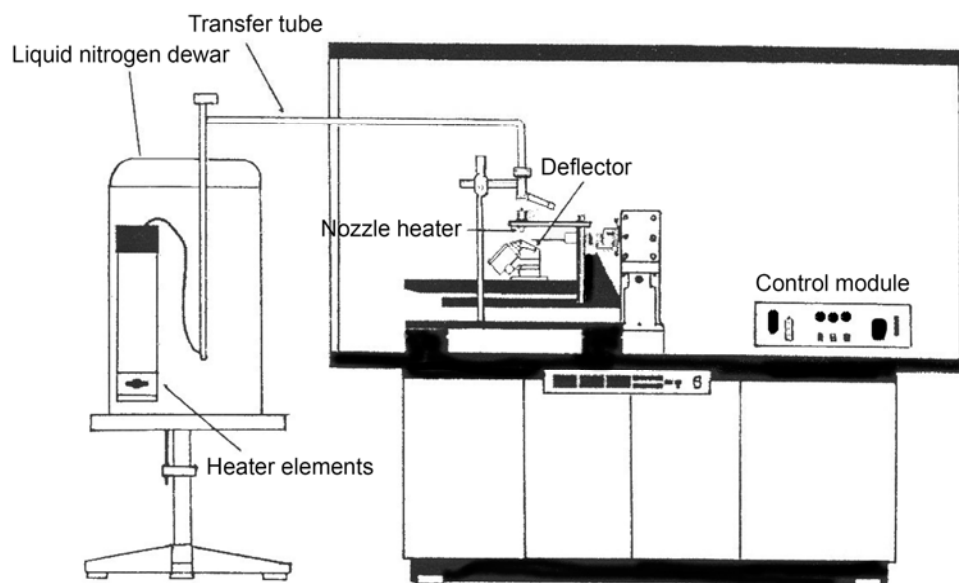


Figure 1.32: *Diagram of the low temperature setup on the SMART 3-circle goniometer.*

maintained within $\pm 1^\circ$ using the thermocontroller. The temperature was chosen such that the consumption of liquid nitrogen was optimal (~ 5 L/h). In order to circumvent ice formation on the crystal, copper pips specially designed for this purpose were used. A thin glass fiber at the end of the pip carried the crystal under measurement. With this kind of an arrangement, the data collection could be carried out without any interruption for a period of two to three days. All the charge density experiments presented in this thesis were carried out at 130 K. A diagram of the low temperature setup, on the SMART 3-circle goniometer is shown in Figure 1.32.

1.4.3 Data collection strategy

All the low temperature data sets presented in this thesis were collected on SIEMENS 3-circle X-ray diffractometer at 130 K. A hemisphere (for centric crystals) or a full sphere (for non-centric or triclinic crystals) data was collected, both at

low and high resolution ($2\theta = 28^\circ, 75^\circ$), the maximum resolution achievable being ~ 0.45 Å. The values of 2θ , ϕ and ω used for the hemisphere and the full sphere data are listed in Table 1.5 and Table 1.6, respectively. During the data reduction, the original orientation matrix along with the lattice parameters was refined every 40 frames and the orientation matrix and lattice parameters obtained using the total data is used for structure refinement and charge density.

Table 1.5 Optimal 2θ , ω and ϕ for hemispherical data at low and high resolutions^a

Run No.	2θ	ω	ϕ	Width	No. of frames
0	-28	-26	0	-0.3	606
1	-28	-21	88	-0.3	435
2	-28	-23	180	-0.3	230
3	-75	-75	0	-0.3	606
4	-75	-75	88	-0.3	435
5	-75	-75	180	-0.3	230

^aNote that two complete hemisphere of data are collected, in comparison to only a low order data for a routine structure determination

Table 1.6 Optimal 2θ , ω and ϕ for full-spherical data at low and high resolutions

Run #	2θ	ω	ϕ	Width	No. of frames
0	-28	-26	0	-0.3	636
1	-28	-21	88	-0.3	465
2	-28	-23	180	-0.3	636
3	-75	-75	270	-0.3	465
4	-75	-75	0	-0.3	636
5	-75	-75	88	-0.3	465
6	-75	-75	180	-0.3	636
7	-75	-75	270	-0.3	465

Data collection on Bruker-Nonius Kappa-CCD-diffractometer.

The Bruker-Nonius diffractometer attached with an APEX-II-CCD area detector which has been used for the data collection of the crystal structures presented in chapter 4 and 6 is a 4-circle diffractometer. This goniometer configuration is called kappa geometry where this uses a horizontally oriented kappa goniometer with 2θ , ω ,

kappa and phi drives and motorized DX track for setting the detector distance. With the kappa angle, the crystal can be oriented at chi from -92° to 92° . Kappa can be positioned so that the phi drive, which has unlimited rotation, can be swung under the incident beam collimator, allowing the free rotation in omega. In this system both the ω scan and ϕ scans are possible for extracting more data with 100% completeness and high redundancy. In this diffractometer the cell determination is carried out similar to that mentioned in the case of Siemens-SMART diffractometer. The data collection strategy for this system is prepared by using program COSMO by maximizing the completeness and redundancy to a given resolution and exposure time for a particular crystal system in a given data collection period (This procedure is similar for both room temperature and low temperature data collection). Figure 1.33 show a Bruker-Nonious diffractometer attached with an APEX-II-CCD area detector.

Bruker-Nonious diffractometer is equipped with additional accessories of low temperature device where the temperature varies by $\pm 0.05^\circ$. The air compressor and air drier mounted on this system ensure the supply of moisture free liquid nitrogen throughout the experiment. In this system the liquid nitrogen supply controller and heating elements are out inside the diffractometer and is interfaced to a Windows-XP based server computer on which the data collection is carried out. Unlike the data sets

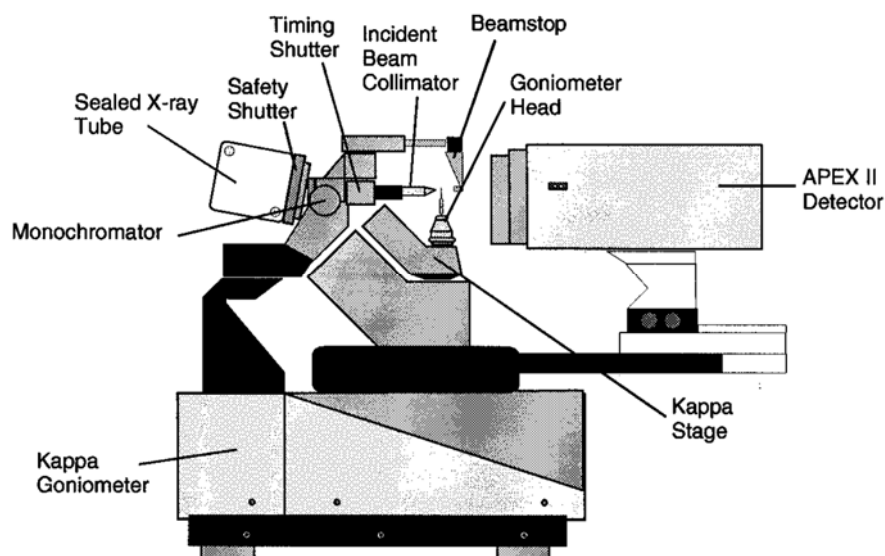


Figure 1.33: Bruker-Nonious diffractometer attached with an APEX-II-CCD area detector.

with SIEMENS 3-circle X-ray diffractometer all the low temperature high resolution data sets collected on Bruker-Nonious diffractometer were at 100 K. Data reduction and structure solution was carried out on a client computer (Windows-XP) which is similar to that described for Siemens-SMART-3 circle diffractometer.

1.4.4 Structure and multipole refinement

The crystal structure determination was carried out by routine structure solution and refinement. In all the cases, the non-hydrogen atoms were first located and refined anisotropically. The hydrogen atoms were located using the difference Fourier technique and refined isotropically. In some instances, extinction corrections were needed. The weights w_1 and w_2 were adjusted in order to obtain the goodness-of-fit close to unity. A high order refinement was performed on the structure so obtained, using the high-resolution reflections, $\sin\theta/\lambda > 0.6 \text{ \AA}^{-1}$. During this refinement, the hydrogens were moved to average neutron diffraction distances (C(ar)-H, 1.085; C(sp^3)-H, 1.06; C(sp^2)-H, 1.075; O-H, 0.96; N-H, 1.01 Å).¹⁹⁹ The positional and thermal parameters of hydrogen atoms were kept fixed thereafter. The resultant file of the high order refinement served as the initial input to the charge density analysis.

The multipole refinement is done using a full-matrix least squares refinement routine, XDLSM of XD.²⁰⁰ The details of the multipole refinement are listed below.

1. Coordinates and thermal parameters from high angle refinement ($\sin\theta/\lambda > 0.6 \text{ \AA}^{-1}$) is taken as the input to charge density analysis.
2. Scaling refinement.
3. P_{00} refined.
4. P_{lm} ($l, m > 0$) refined.
5. Spherical kappa (κ) refined on all atoms.
6. P_{00} refined.
7. P_{lm} ($l, m > 0$).
8. Deformation kappa (κ') refined on all non-hydrogen atoms.
9. P_{00} refined.
10. P_{lm} ($l, m > 0$).
11. Atom positions of non-hydrogen atoms refined.

12. P_{00} refined.
13. P_{lm} ($l, m > 0$) refined.
14. P_{00} and P_{lm} refined.

Each step is repeated till the shift/esd values become small. The quality of the refinement was constantly monitored through goodness-of-fit (S), R_1 and wR_2 . For a reliable electron density calculation, caution was exercised to maintain N_{ref}/N_V greater than ten.

The electronic properties like dipole, electron density, Laplacian etc are calculated using XDPROP. The experimental deformation map is obtained using the calculated multipole phases with the observed structure factors F_o .

$$\delta\rho^{\text{exp}}(\mathbf{r}) = \frac{1}{V} \sum_H \left[|F_o(H)| e^{i\phi_{mul}} - |F_{sph}(H)| e^{i\phi_{sph}} \right] e^{-2\pi i H \cdot \mathbf{r}} \quad \dots(18)$$

$F_{sph}(H)$ is computed with atomic positions and thermal parameters obtained from the multipole refinement. The dynamic model map is obtained from the calculated multipole factors, that is, the Fourier coefficients are the difference of the two values of F_c .

$$\delta\rho^{\text{dyn}}(\mathbf{r}) = \frac{1}{V} \sum_H \left[|F_{mul}(H)| e^{i\phi_{mul}} - |F_{sph}(H)| e^{i\phi_{sph}} \right] e^{-2\pi i H \cdot \mathbf{r}} \quad \dots(19)$$

The use of multipole phases makes the maps slightly model dependent. To check that all the significant density features of the experimental data are included in the model, one computes the residual density. This is defined as the difference between the total electron density and that obtained by the multipole model.

$$\delta\rho^{\text{res}}(\mathbf{r}) = \frac{1}{V} \sum_H \left[|F_o(H)| - |F_{mul}(H)| \right] e^{i\phi_{mul}} e^{-2\pi i H \cdot \mathbf{r}} \quad \dots(20)$$

This is obtained using the XDFOUR routine and plotted using XDGRAPH. A featureless, flat residual density means a good modeling of the electron density by the multipole model.

References

1. B. Pullman, (ed): *Environmental Effects on Molecular Structure and Properties*, Proceedings of the Eighth Jerusalem Symposium on Quantum Chemistry and Biochemistry held in Jerusalem, Israel, Springer Publishers, New York, USA, (1975)
2. A. Domenicano, I. Hargittai, (eds): *Strength from Weakness: Structural Consequences of Weak Interactions in Molecules, Supermolecules, and Crystals*, Springer Publishers, New York, USA, (2001)
3. R. F. W. Bader, *Atoms in Molecules - A Quantum Theory*, Clarendon press, Oxford, (1990).
4. J. -M. Lehn *Supramolecular Chemistry – Concepts and Perspectives*, Wiley VCH, Weinheim (1995).
5. L. Stryer, *Biochemistry*-4th edition, W. H. Freeman, New York, (1995)
6. W. Jones, C. N. R. Rao, (eds): *Supramolecular Organization and Material Design*, Cambridge University Press, Cambridge, (2002).
7. M. D. Cohen, G. M. J. Schmidt, *J. Chem. Soc.*, (1964), and the three succeeding papers.
8. G. M. J. Schmidt, *Pure Appl. Chem.*, (1971), **27**, 647.
9. W. A. Tiller, *The Science of Crystallization*, Cambridge University Press, (1989).
10. (a) A. I. Kitaigorodskii, *Molecular Crystals and Molecules*, Academic Press, New York, (1973); (b) A. I. Kitaigorodskii, *Organic Chemical Crystallography*, (1961), Consultants Bureau.
11. (a) W. M. Latimer, W. H. Rodebush, *J. Am. Chem. Soc.*, (1920), **42**, 1419; (b) G. C. Pimentel, A. L. McClellan, *The Hydrogen Bond*, W. H. Freeman, San Francisco, Calif., (1960); (c) W. C. Hamilton; J. A. Ibers, *Hydrogen Bonding In Solids*, W. A. Benjamin, Inc. N.Y., (1968).
12. (a) P. Schuster, G. Zundel, C. Sandorfy, *The Hydrogen Bond, Recent Developments in Theory and Experiments*, North-Holland, New York, (1976); (b) G. A. Jeffrey, W. Saenger, *Hydrogen Bonding in Biological Structures*, Springer, Berlin, (1991); (c) T. Steiner, *Angew. Chem. Int. Ed. Engl.*, (2002), **41**, 48.

13. (a) T. Steiner, *Angew. Chem. Int. Ed.*, (2002), **41**, 48; (b) G. R. Desiraju, *Angew. Chem. Int. Ed.*, (1995), **34**, 2311.
14. F. H. Allen, J. A. K. Howard, V. J. Hoy, G. R. Desiraju, D. S. Reddy, C. C. Wilson, *J. Am. Chem. Soc.*, (1996), **118**, 4081.
15. N. N. Laxmi Madhavi, A. K. Katz, H. L. Carrell, A. Nangia, G. R. Desiraju, *Chem. Commun.*, (1997), 1953.
16. O. A. Mikhno, Z. I. Ezhkova, G. S. Zhdanov, *Krist.*, (1973), **18**, 99; (b) S. C. Nyburg, C. H. Faerman, *Acta Cryst.*, (1985), **B41**, 274.
17. (a) H. Adams, K. D. M. Harris, G. A. Hembury, C. A. Hunter, D. Ivingstone, J. F. McCabe, *Chem. Commun.*, (1996), 2531; (b) H. Adams, F. J. Carver, C. A. Hunter, N. J. Osborne, *Chem. Commun.*, (1996), 2529; (c) U. Samanta, P. Chakrabarti, J. Chandrasekhar, *J. Phys. Chem. A.*, (1998), **102**, 8964.
18. G. R. Desiraju, T. Steiner, *The Weak Hydrogen bond*, Oxford University Press: Oxford, (1999).
19. (a) T. Steiner, E. B. Starikov, A. M. Amado, J. J. C. Teixeira-Dias, *J. Chem. Soc. Perkin Trans.*, (1995), **2**, 1321. (b) T. Steiner, *J. Phys. Chem. A*, (1998), **102**, 7041.
20. (a) D. Hadzi, *Pure Appl. Chem.*, (1965), **11**, 435. (b) S. J. Barlow, G. V. Bondarenko, Y. E. Gorbaty, T. Yamaguchi, M. Poliakoff, *J. Phys. Chem. A*, (2002), **106**, 10452.
21. D. F. Brougham, R. Caciuffo, A. J. Horsewill, *Nature*, (1999), **397**, 241.
22. J. M. Robertson, A. R. Ubbelohde, *Proc. Roy. Soc. London*, (1939), **A170**, 222.
23. G. A. Jeffrey, *An Introduction to Hydrogen Bonding*, Oxford University Press, Oxford, (1997).
24. F. H. Allen, *Acta Cryst.*, (2002), **B58**, 380.
25. For a survey, see: F. H. Allen, W. D. S. Motherwell, *Acta Cryst.*, (2002), **B58**, 407.
26. (a) D. Ranganathan, C. Lakshmi, I. L. Karle, *J. Am. Chem. Soc.*, (1999), **121**, 6103; (b) N. Patel, D. K. Jones, E. L. Raven, *Eur. J. Biochem.*, (2000), **267**, 2581; (c) G. Gemmecker, *Angew. Chem. Int. Ed.*, (2000), **39**, 1224; (d) E. T. Kool, J. C. Morales, J. C. K. M. Guckian, *Angew. Chem. Int. Ed.*, (2000), **39**, 991.
27. M. C. Etter, *Acc. Chem. Res.*, (1990), **23**, 120.

28. (a) L. Pauling, *Proc. Nat. Acad. Sci.*, (1928), **14**, 359; (b) S. Bratoz, *Advan. Quantum. Chem.*, (1967), **3**, 209; (c) J. Lennard-Jones, J. A. Pople, *Proc. Roy. Soc., Ser. A*, (1951), **205**, 155; (d) J. A. Pople, *Proc. Roy. Soc., Ser. A*, (1951), **205**, 163.
29. L. Pauling, *The Nature of the Chemical Bond*, Cornell University Press, (1944).
30. (a) H. Tsubomura, *Bull. Chem. Soc.*, (1954), **27**, 445; (b) C. A. Coulson, *Research (London)*, (1957), **10**, 149.
31. R. F. W. Bader, *Can. J. Chem.*, (1964), **42**, 1822.
32. (a) A. S. N. Murthy, C. N. R. Rao, *J. Mol. Struct.*, (1970), **6**, 253; (b) C. N. R. Rao, In *Water*, Ed: F. Franks, Plenum Press, New York, (1972), **1**, 93; (c) P. A. Kollman L. C. Allen, *Chem. Rev.*, (1972), **72**, 283.
33. H. Umeyama, K. Morokuma, *J. Am. Chem. Soc.*, (1977), **99**, 1316.
34. C. N. R. Rao, B. S. Sudhindra, H. Ratajczak, W. J. Orville-Thomas, *Molecular Interactions*, (1980), ch.3, 67.
35. (a) J. -M. Lehn, *Angew. Chem. Int. Ed.*, (1988), **27**, 89. (b) J. M. Lehn, *Pure Appl. Chem.*, (1978), **50**, 871.
36. G. M. Whitesides, E. E. Simanek, J. P. Mathias, C. T. Seto, D. N. Chin, M. M. Mammen, D. M. Gordon., *Acc. Chem. Res.*, (1995), **28**, 37.
37. G. R. Desiraju in *Comprehensive Supramolecular Chemistry* Vol. 6. Eds: D. D. MacNicol, F. Toda, R. Bishop), Pergamon, Oxford, (1996).
38. (a) J. D. Dunitz, *Pure Appl. Chem.*, (1991), **63**, 177
39. F. H. Allen, B. S. Goud, V. J. Hoy, J. A. K. Howard, G. R. Desiraju., *J. Chem. Soc. Chem. Commun.*, (1994), 2729.
40. (a) E. J. Corey, *Pure Appl. Chem.* (1967), **14**, 19; (b) E. J. Corey, *Chem. Soc. Rev.*, (1988), **17**, 111.
41. J. Bernstein, M. C. Etter, L. Leiserowitz, in *The Role of Hydrogen Bonding in Molecular Assemblies*, Eds. H. -B. Burgi, J. D. Dunitz, VCH, Weinheim (1994).
42. M. C. T. Fyfe, J. F. Stoddart, *Synthetic Supramolecular Chemistry*, (1997), **30**, 393.
43. C. B. Aakeröy, K. R. Seddon, *Chem. Soc. Rev.*, (1993), **22**, 397.
44. C. B. Aakeröy, *Acta Cryst.*, (1997), **B53**, 569.
45. A. Nangia, G. R. Desiraju, *Acta Cryst.*, (1998), **A54**, 934.

46. R. Taylor, O. Kennard, *Acc. Chem. Res.*, (1984), **17**, 320.
47. G. A. Sim, J. M. Robertson, T. H. Goodwin, *Acta Cryst.*, (1955), **8**, 157.
48. M. Bailey, C. J. Brown, *Acta Cryst.*, (1967), **22**, 387.
49. R. Alcala, S. M. Carrera, *Acta Cryst.*, (1972), **B28**, 1671.
50. D. J. Duchamp, R. E. Marsh, *Acta Cryst.*, (1969), **B25**, 5.
51. O. Ermer, *J. Am. Chem. Soc.*, (1988), **110**, 3747.
52. L. Leiserowitz, *Acta Cryst.*, (1976), **B32**, 775.
53. F. H. Herbstein, M. Kapon, *Acta Cryst.*, (1978), **B34**, 1608.
54. S. V. Kolotuchin, E. E. Fenlon, R. W. Wilson, C. J. Loweth, S. C. Zimmerman, *Angew. Chem. Int. Ed.*, (1995), **34**, , 2654.
55. J. Narasimha Moorthy, R. Natarajan, P. Venugopalan, *Angew. Chem. Int. Ed.*, (2002), **41**, 3417.
56. M. Currie, J. C. Speakman, *J. Chem. Soc. A.*, (1970), 1923.
57. P. Gilli, V. Bertolasi, V. Ferretti, G. Gilli, *J. Am. Chem. Soc.*, (1994), **116**, 909.
58. P. Vishweshwar, A. Nangia, V. M. Lynch, *Chem. Commun.*, (2001), 179.
59. B. R. Penfold, J. C. B. White, *Acta Cryst.*, (1959), **12**, 130.
60. T. L. Nguyen, A. Scott, B. Dinkelmeyer, F. W. Fowler, J. W. Lauher, *New. J. Chem.*, (1998), **22**, 129.
61. (a) J. A. Zerkowski, C. T. Seto, G. M. Whitesides, *J. Am. Chem. Soc.*, (1992), **114**, 5473; (b) J. A. Zerkowski, J. C. MacDonald, C. T. Seto, D. A. Wierda, G. M. Whitesides, *J. Am. Chem. Soc.*, (1994), **116**, 2382.
62. A. Ranganathan, V. R. Pedireddi, C. N. R. Rao, *J. Am. Chem. Soc.*, (1999), **121**, 1752.
63. (a) J. Donohue, in *Selected Topics in Hydrogen Bonding*, Eds. A. Rich, N. Davidson, Freeman, San Francisco, (1968). (b) F. A. Cotton, L. M. Daniels, G. T. Jordan, C. A. Murillo, *J. Chem. Soc. Chem. Commun.*, (1997), 1673.
64. T. Steiner, G. R. Desiraju, *Chem. Commun.*, (1998), 891.
65. R. Taylor, O. Kennard, *J. Am. Chem. Soc.*, (1982), **104**, 5063.
66. V. R. Thalladi, H. C. Weiss, D. Blaser, R. Boese, A. Nangia, G. R. Desiraju, *J. Am. Chem. Soc.*, (1998), **120**, 8702.
67. C. Glidewell, W. T. A. Harrison, J. N. Low, J. G. Sime, J. L. Wardell, *Acta Cryst.*, (2001), **B57**, 190.

68. J. M. A. Robinson, D. Philip, B. M. Kariuki, K. D. M. Harris, *Chem. Commun.*, (1999), 329.
69. D. S. Reddy, B. S. Gaud, K. Panneerselvam, G. R. Desiraju. *J. Chem Soc. Chem. Commun.*, (1993), 663.
70. M. Ohkita, T. Suzuki, K. Nakatani, T. Tsuji, *Chem. Commun.*, (2001), 1454.
71. M. Nishio, M. Hirota, Y. Umezawa, *The CH/ π Interaction. Evidence, Nature, and Consequences*. Wiley-VCH, New York, (1998).
72. V. R. Thalladi, R. Boese, S. Brasselet, I. Ledoux, J. Zyss, R. K. R. Jetti, G. R. Desiraju, *Chem. Commun.*, (1999), 1639.
73. H. Adams, F. J. Carver, C. A. Hunter, N. J. Osborne, *Chem. Commun.*, (1996), 2529.
74. V. R. Pedireddi, S. Chatterjee, A. Ranganathan, C. N. R. Rao, *Tetrahedron*, (1998), **54**, 9457.
75. R. Liu, K. -F. Mok, S. Valiyaveetil, *New J. Chem.*, (2001), **25**, 890.
76. V. R. Thalladi, B. S. Goud, V. J. Hoy, F. H. Allen, J. A. K. Howard, G. R. Desiraju, *Chem. Commun.*, (1996), 401.
77. R. E. Bachman, M. S. Fioritto, S. K. Fetcs, T. M. Cocker, *J. Am. Chem. Soc.*, (2001), **123**, 5376.
78. (a) H. Schmidbaur, W. Graf, G. Müller, *Angew. Chem. Int.*, (1988), **27**, 417; (b) J. Zank, A. Schier, H. Schmidbaur, *J. Chem. Soc. Dalton Trans.*, (1998), 323; (c) C. B. Aakeroy, D. S. Leinen in *Crystal Engineering: From Molecules and Crystals to Materials*. Eds. D. Braga, F. Grepioni, A. G. Orpen, Kluwer, Academic, Dordrecht, The Netherlands, (1999), pp 89 - 106.
79. S. S. Pathaneni, G. R. Desiraju, *J. Chem. Soc. Dalton Trans.*, (1993), 319.
80. H. v. Bekkum, J. Cejka, A. Corma, F. Schueth, *Introduction to Zeolite Molecular Sieves*, Elsevier Science, London, (2007).
81. (a) G. Lanzani, *Photophysics of Molecular Materials: From Single Molecules to Single Crystals*, Wiley-VCH, Weinheim, (2006); (b) J. R. Reynolds, S. P. Ermer, J. W. Perry, K-Y. Alex, *Electrical, Optical, and Magnetic Properties of Organic Solid-state Materials IV*, Materials Research Society, Michigan, USA, (1998)
82. E. Coronado, *Molecular Magnetism: From Molecular Assemblies to the Devices*, Springer, (1996)

83. (a) J. C. Scaiano, H. Garcíá, *Acc. Chem. Res.*, (1999), **32**, 783; (b) G. A. Ozin, A. Kuperman, A. Stein, *Angew. Chem. Int. Ed.*, (1989), **28**, 359; (c) D. R. Robinson, *Chem. Rev.*, (1990), **90**, 867.
84. O. M. Yaghi, G. Li, *Angew. Chem. Int. Ed.*, (1995), **90**, 867.
85. G. B. Gardner, D. Venkataraman, J. S. Moore, S. Lee, *Nature*, (1995), **374**, 792.
86. L. R. MacGillivray, S. Subramanian, M. J. Zaworotko, *J. Chem. Soc. Chem. Commun.*, (1994), 1325.
87. O. M. Yaghi and H. Li, *J. Am. Chem. Soc.*, (1996), **118**, 295.
88. D. Venkataraman, S. Lee, J. Zhang, J. S. Moore, *Nature*, (1994), **371**, 591.
89. X. Wang, M. Simard, J. D. Wuest, *J. Am. Chem. Soc.*, (1994), **371**, 591.
90. A. Ranganathan, V. R. Pedireddi, S. Chatterjee, C. N. R. Rao, *J. Mater. Chem.*, (1999), **9**, 2407.
91. C. D. Dimitrakopoulos, P. R. L. Malenfant, *Adv. Mater.*, (2002), **14**, 99.
92. (a) V. Podzorov, S. E. Sysoev, E. Loginova, V. M. Pudalov, M. E. Gershenson, *Appl. Phys. Lett.*, (2003), **83**, 3504; (b) V. C. Sundar, J. Zaumseil, V. Podzorov, E. Menard, Willett, R. L.; Someya, T.; Gershenson, M.E.; Rogers, J. A. *Science*, (2004), **303**, 1644.
93. H. E. Katz, A. Dodabalapur, Z. Bao, *Oligo- and Polythiophene-Based Field-Effect Transistors*, Wiley-WCH, Weinheim, (1998).
94. H. Klauk, *Organic Electronics: Materials, Manufacturing and Applications*, Wiley-VCH, Weinheim, (2006)
95. R. Zeis, C. Besnard, T. Siegrist, C. Schlockermann, X. Chi, C. Kloc, *Chem. Mater.*, (2006), **18**, 244.
96. M. Bendikov, F. Wudl, D. F. Perepichka, *Chem. Rev.*, (2004) **104**, 4891.
97. R. W. I. de Boer, M. E. Gershenson, A. F. Morpurgo, V. Podzorov, *Phys. Stat. solidi*, (2004), **201**, 1302.
98. Naraso, J.-i. Nishida, S. Ando, J. Yamaguchi, K. Itaka, H. Koinuma, H. Tada, S. Tokito, Y. Yamashita, *J. Am. Chem. Soc.*, (2005), **127**, 10142.
99. I. Shokaryev, A. J. C. Buurma, O. D. Jurchescu, M. A. Uijtewaal, G. A. de Wijs, T. T. M. Palstra, R. A. de Groot, *J. Phys. Chem. A.*, (2008), **112**, 2497.
100. (a) N. Kiriy, A. Kiriy, V. Bocharova, M. Stamm, S. Richter, M. Plotner, W.-J. Fischer, F. C. Krebs, I. Senkowska, H.-J. Adler, *Chem. Mater.*, (2004), **16**,

- 4757; (b) A. Facchetti, M. Mushrush, M.-H. Yoon, G. R. Hutchison, M. A. Ratner, T. J. Marks, *J. Am. Chem. Soc.*, (2004), **126**, 13859.
101. A. Babel, S. A. Jenekhe, *Macromolecules*, (2003), **36**, 7759.
102. C. Reese, M. Roberts, M. Ling, Z. Bao, *Materials Today*, (2004), **7**, 20.
103. C. Reese, Z. Bao, *Materials Today*, (2007), **10**, 20.
104. V. Podzorov, E. Menard, A. Borissov, V. Kiryukhin, J. A. Rogers, M. E. Gershenson, *Phys. Rev. Lett.*, (2004), **93**, 086602.
105. E. Menard, V. Podzorov, S. -H. Hur, A. Gaur, M. E. Gershenson, J. A. Rogers, *Adv. Mater.*, (2004), **16**, 2097.
106. J. Locklin, M. M. Ling, A. Sung, M. E. Roberts, Z. Bao, *Adv. Mater.*, (2006), **18**, 2989.
107. M. Brinkmann, G. Gadret, M. Muccini, C. Taliani, N. Masciocchi, Angelo Sironi, *J. Am. Chem. Soc.*, (2000), **122**, 5147
108. M. Cölle, W. Brütting, *phys. stat. soli. (a)*, (2004), **201**, 1095.
109. T. Mutai, H. Satou, K. Araki, *Nature Mater.*, (2005), **4**, 685.
110. K. Horie, T. Yamashit, *Photosensitive Polyimides*, CRC Press, London, UK, (1995)
111. M. Sahara, H. Ichioka, S. Yano, F. Fujimoto, M. Ehara, K. Wakita, N. Sonoda, *Jpn. J. Appl. Phys.*, (1994) **33**, 169.
112. P. J. A. Kenis, O. F. J. Noordman, H. Schönherr, E. G. Kerver, B. H. M. Snellink-Ruël, G. J. van Hummel, S. Harkema, C. P. J. M. van der Vorst, J. Hare, S. J. Picken, J. F. J. Engbersen, N. F. van Hulst, G. J. Vancso, D. N. Reinhoudt, *Chem. Eur. J.*, (2000), **4**, 1225.
113. (a) Z. Yang, M. Jazbinsek, B. Ruiz, S. Aravazhi, V. Gramlich, P. Günter, *Chem. Mater.*, (2007), **19**, 3512; (b) M.-Y. Jeong, H. M. Kim, S.-J. Jeon, S. Brasselet, B. R. Cho, *Adv. Mater.*, (2007), **19**, 2107
114. B. Ruiz, B. J. Coe, R. Gianotti, V. Gramlich, M. Jazbinsek, P. Günter, *CrystEngComm*, (2007), **9**, 772.
115. L. Li, D. M. Collard, *Macromolecules*, (2005), **38**, 372.
116. F. C. Krebs, H. Spanggaard, *J. Org. Chem.*, (2002), **67**, (21), 7185.
117. T. -Q. Nguyen, V. Doan, B. J. Schwartz, *J. Chem. Phys.*, (1999), **110**, 4068.

118. H. Y. Zhang, Z. L. Zhang, K. Q. Ye, J. Y. Zhang, Y. Wang, *Adv. Mater.*, (2006), **18**, 2369.
119. D. F. Eaton, *Science*, (1991) **253**, 281
120. A. Datta, S. K. Pati, *Chem. Soc. Rev.*, (2006), **35**, 1305.
121. T. P. Radhakrishnan, *Acc. Chem. Res.*, (2008), **41**, 367.
122. M. Arivanandhan, K. Sankaranarayanan, P. Ramasamy, *Mater. Lett.*, (2007), **61**, 4836
123. H. -Y. Qian, Z. -G. Yin, J. Jia, N. Zhou, L. -Q Feng, *Acta. Cryst. B*, (2006), **62**, 5048.
124. D. Mullen, *Acta. Cryst. B*, (1980), **36**, 1610.
125. (a) S. R. Marder, J. W. Perry, W. P. Schaefer, *Science*, (1989), **245**, 4918; (b) F. Pan, M. S. Wong, C. Bosshard, P. Günter, V. Gramlich, *Adv. Mater. Opt. Elec.*, (1998), **6**, 261.
126. (a) P. Srinivasan, T. Kanagasekaran, R. Gopalakrishnan, G. Bhagavannarayana, P. Ramasamy, *Cryst. Growth Des.*, (2006), **6**, 1663. (b) P. Srinivasan, Y. Vidyalakshmi, R. Gopalakrishnan, *Cryst. Growth Des.*, (2008), **8**, 2329.
127. V. R. Thalladi, S. Brasselet, D. Blaser, R. Boese, J. Zyss, A. Nangia, G. R. Desiraju, *J. Chem. Soc. Chem. Commun.*, (1997) 1841.
128. J. Zyss, I. Ledoux-Rak, H. -C. Weiss, D. Blaser, R. Boese, P. K. Thallapally, V. R. Thalladi, G. R. Desiraju, *Chem. Mater.*, (2003), **15**, 3063.
129. (a) M. E. Lines, A. M. Glass, *Principles and Applications of Ferroelectrics and Related Materials*, Oxford University Press, New York, (1977); (b) K. Uchino, *Ferroelectric Devices*, Marcel Dekker, New York, (2000).
130. J. Valasek, *Phys. Rev.*, (1921), **17**, 475
131. (a) S. Horiuchi, R. Kumai, Y. Tokura, *Chem. Commun.*, (2007), 2321; (b) S. Horiuchi, Y. Okimoto, R. Kumai, Y. Tokura, *Science*, (2003), **299**, 229.
132. (a) S. Horiuchi, F. Ishii, R. Kumai, Y. Okimoto, H. Tachibana, N. Nagaosa and Y. Tokura, *Nat. Mater.*, (2005), **4**, 163; (b) S. Horiuchi, R. Kumai and Y. Tokura, *J. Am. Chem. Soc.*, (2005), **127**, 5010.

133. (a) J. S. Miller, M. Drillon, (eds) *Magnetism: Molecules to Materials II*, Wiley-VCH, Weinheim, (2001) (b) K. Itoh, M. Kinoshita (eds) *Molecular Magnetism*, Kodansha, Gordon and Breach Science, Tokyo, (2000).
134. S. K. Mandal, M. E. Itkis, X. Chi, S. Samanta, D. Lidsky, R. W. Reed, R. T. Oakley, F.S. Tham, R. C. Haddon, *J. Am. Chem. Soc.*, (2005), **127**, 8185.
135. D. MasPOCH, N. Domingo, N. Roques, K. Wurst, J. Tejada, C. Rovira, D. R. Molina, J. Veciana, *Chem. Eur. J.*, (2007), **13**, 8153.
136. W. Clegg, *Crystal Structure Analysis: Principles and Practice*, Oxford University Press, Oxford, (2001)
137. M. D. Fayer, *Ultrafast Infrared and Raman Spectroscopy*, CRC Press, (2001).
138. G. S. Kapur, E. J. Cabrita, S. Berger, *Tet. Lett.*, (2000), **41**, 7181.
139. (a) *Electron Distributions and the Chemical Bond* Eds: P. Coppens, M. B. Hall, Plenum Press, New York, (1982). (b) P. Coppens, *J. Chem. Edu.* (1984), **61**, 761. (c) K. Angermund, K. H. Claus, R. Goddard, C. Krüger, *Angew. Chem. Int. Ed.*, (1985), **24**, 237.
140. (a) P. Coppens, *J. Phys. Chem.*, (1989), **93**, 7979. (b) P. Coppens, *Ann. Rev. Phys. Chem.*, (1992), **43**, 663. (c) *X-Ray Charge Densities and Chemical Bonding*, P. Coppens, Oxford University Press, IUCr Texts on Crystallography No. 4 (1997). (d) G. U. Kulkarni, R. S. Gopalan, C. N. R. Rao, *J. Mol. Struct. (Theochem)*, (2000), **500**, 339.
141. T. Koritzansky and P. Coppens, *Chem. Rev.*, (2001), **101**, 1583.
142. W. J. Hehre, L. Radom, P. v. R. Schleyer, J. A. Pople, *Ab initio Molecular Orbital Theory*, Wiley, New York (1986).
143. W. Friedrich, P. Knipping, M. von Laue, *Interferenz-Erscheinungen bei Röntgenstrahlen*. Sitzungsberichte der Mathematisch-Physikalischen Classe der Königlich-Bayerischen Akademie der Wissenschaften zu München (1912)
144. (a) P. Debye, P. Scherrer, *Phys. Z.*, (1918), **19**, 474; (b) P. Debye, Dispersion of Roentgen rays, *Ann. Phys.*, (1915), **46**, 809.
145. B. Dawson, *Proc. Roy. Soc.*, (1967), **A298**, 264.
146. M. J. Frisch, G. W. Trucks, H. B. Schlegel, P. M. W. Wong, J. B. Foresman, M. A. Robb, M. Head-Gordon, E. S. Replogle, R. Gomperts, J. L.

- Andres, K. Raghavachari, J. S. Binkley, C. Gonzales, R. L. Martin, D. J. Fox, D. J. Defrees, J. Baker, J. J. P. Stewart, J. A. Pople, GAUSSIAN 98/DFT, Rev. A.1.
147. GAMESS, M. W. Schmidt, K. K. Baldridge, J. A. Boatz, S. T. Elbert, M. S. Gordon, J. H. Jensen, S. Koseki, N. Matsunaga, K. A. Nguyen, S. J. Su, T. L. Windus, M. Dupuis, J. A. Montgomery, *J. Comput. Chem.*, (1993), **14**, 1347.
148. R. Dovesi, V. R. Saunders, C. Roetti, M. Causa, N. M. Harrison, R. Orlando, R. Apra, CRYSTAL 95 User's Manual, University of Torino, Torino, Italy (1996).
149. N. K. Hansen, P. Coppens, *Acta Cryst.*, (1978), **A34**, 909.
150. T. Koritsanszky, R. Flaig, D. Zobel, H. -G. Krane, W. Morgenroth, P. Luger, *Science*, (1998), **279**, 356.
151. R. F. Stewart, *J. Chem. Phys.*, (1973), **58**, 1668.
152. P. Coppens, T. N. Guru Row, P. Leung, E. D. Stevens, P. J. Becker and Y. W. Yang, *Acta Cryst.*, (1979), **A35**, 63.
153. T. Koritsanszky, S. T. Howard, T. Richter, P. R. Mallinson, Z. Su, N. K. Hansen, XD, *A computer program package for multipole refinement and analysis of charge densities from diffraction data*, Cardiff, Glasgow, Buffalo, Nancy, Berlin, (1995).
154. F. L. Hirshfeld, *Acta Cryst.*, (1976) **A32**, 239.
155. Cremer, E. Kraka, *Croat. Chem. Acta.*, (1984), **57**, 1259.
156. R. F. W. Bader, T. Nguyen-Dang, Y. Tal, *Rep. Prog. Phys.*, (1981), **44**, 893.
157. Y. Abramov, *Acta Cryst.*, (1997), **A53**, 264.
158. P. Coppens, Y. Abramov, M. Carducci, B. Korjov, I. Novozhilova, C. Alhambra, M. R. Pressprich, *J. Am. Chem. Soc.*, (1999), **121**, 2585.
159. E. Espinosa, E. Mollins, C. Lecomte, *Chem. Phys. Lett.*, (1998), **285**, 170.
160. E. Kraka, D. Cremer, *J. Mol. Struct. (Theochem)*, (1992), **255**, 189.
161. M. A. Spackman, P. Munshi, B. Dittrich, *Chemphyschem*, (2007), **8**, 2053
162. M. A. Spackman, *Chem. Rev.*, (1992), **92**, 1769.
163. R. S. Gopalan, G. U. Kulkarni, C. N. R. Rao, *Chemphyschem*, (2000), **1**, 127.

164. Z. W. Su, P. Coppens, *Acta Cryst.*, (1992), **A48**, 188.
165. F. S. Dukhovich, M. B. Darkhovskii, *J. Mol. Recognit.*, (2003), **16**, 191.
166. P. Politzer, P. R. Laurence, K. Jayasuriya, *Envir. Health Perspect.*, (1985), **61**, 191.
167. T. Koritsanszky, R. Flaig, D. Zobel, H.-G. Krane, W. Morgenroth, P. Luger, *Science*, (1998), **279**, 356
168. R. Destro, R. Soave, M. Barzaghi, L. L. Presti, *Chem. Eur. J.*, (2005), **11**, 4621.
169. A. Wagner, R. Flaig, B. Dittrich, H. Schmidt, T. Koritsánszky, P. Luger, , *Chem. Eur. J.*, (2004), **10**, 2977.
170. C. B. Hubschle and P. Luger, *J. Appl. Crystallogr.*, 2006, **39**, 901.
171. P. Gund, J. D. Andose, J. B. Rhodes, G. M. Smith, *Science*, (1980), **208**,1425.
172. J. A. N. F. Gomes, R. B. Mallion, *Chem. Rev.*, (2001), **101**, 1349.
173. Mitchell R H *Chem. Rev.*, 2001, **101**, 1301
174. A. Julg, P. H. Francois, *Theor. Chem. Acta.*, (1967), **7**, 249.
175. D. J. Klein *Pure Appl. Chem.*, (1989) **61**, 2107.
176. P. Roversi, M. Barzaghi, F. Merati, R. Destro, *Can. J. Chem.*, (1996), **74**, 1145.
177. R. Destro, F. Merati, *Acta Cryst.*, (1995), **B51**, 559.
178. R. F. Stewart, in *Applications of Charge Density Research to Chemistry and Drug Design*; G. A. Jeffrey, J. F. Piniella, Eds; Plenum: New York, (1991).
179. P. Fuhrmann, T. Koritsanszky, P. Luger, *Z. Krist.*, (1997), **212**, 213.
180. S. T. Howard, T. M. Krygowski, *Can. J. Chem.*, (1997), **75**, 1174.
181. A. Ranganathan, G. U. Kulkarni, *J. Phys. Chem. A*, (2002), **106**, 7813.
182. (a) A. Ranganathan, G. U. Kulkarni, C. N. R. Rao, *J. Mol. Struct.*, (2003), **656**, 249; (b) D. Madsen, C. Flensburg, S. Larsen, *J. Phys. Chem. A*, (1998), **102**, 2177; (c) K. Hermansson, R. Tellgren, *Acta Cryst.*,(1989), **B45**, 252; (d) J. Overgaard, B. Schiott, F. K. Larsen, B. B. Iversen, *Chem. Eur. J.*, (2001), **7**, 3756; (e) E. D. Stevens, J. Rys, P. Coppens, *J. Am. Chem. Soc.*, (1978), **100**, 2324; (f) C. Gatti, E. May, R. Destro, F. Cargnoni, *J. Phys. Chem. A*, (2002), **106**, 2707; (g) P. Macchi, A. J. Schultz, F. K. Larsen, B. B. Iversen, *J. Phys. Chem. A*, (2001), **105**,

- 9231; (h) P. K. Bakshi, T. S. Cameron, O. Knop, *Can. J. Chem.*, (1996), **74**, 201;
(i) R. Bianchi, C. Gatti, V. Adovasio, M. Nardelli, *Acta Crystallogr.*, (1996), **B52**, 471.
183. U. Koch and P. L. A. Popelier, *J. Chem. Phys.*, (1995), **99**, 9747.
184. R. J. Boyd, S. C. Choi, *Chem. Phys. Lett.*, (1986), **129**, 62.
185. E. Espinosa, C. Lecomte, E. Molins, S. Veintennillas, A. Cousson, W. Paulus, *Acta Cryst.*, (1996), **B52**, 519.
186. E. Espinosa, E. Molins, C. Lecomte, *Chem. Phys. Lett.* (1998), **285**, 170.
187. E. Espinosa, M. Souhassou, H. Lachekar, C. Lecomte, *Acta Cryst.*, (1999), **B55**, 563.
188. P. R. Mallinson, C. C. Wilson, E. Hovestreydt, E. Grech, *J. Phys. Chem. A*, (2002), **106**, 6897.
189. A. Ranganathan, G. U. Kulkarni, C. N. R. Rao, *J. Phys. Chem. A*, (2003), **107**, 6073.
190. I. Vorobyov, M. C. Yappert, D. B. DuPré, *J. Phys. Chem. A*, (2002), **106**, 10691.
191. I. Alkorta, J. Elguero, O. Mó, M. Yáñez, J. E. Del Bene, *J. Phys. Chem. A*, (2002), **106**, 3325.
192. Y. H. Zhang, J. -K. Hao, X. Wang, W. Zhou, T. -H. Tang, *J. Mol. Struct. (Theochem)*, (1998), **455**, 85.
193. A. Bach, D. Lentz, P. Luger, *J. Phys. Chem. A*, (2001), **105**, 7405.
194. (a) D. Chopra, T. S. Cameron, J. D. Ferrara, T. N. Guru Row, *J. Phys. Chem. A*, (2006), **110**, 10465; (b) R. Bianchi, A. Forni, T. Pilati, *Chem. Eur. J.*, (2003), **9**, 1631.
195. Siemens Analytical X-ray Instruments Inc., Madison, Wisconsin, USA (1995).
196. SHELXTL (SGI version) Siemens Analytical X-ray Instruments Inc., Madison, Wisconsin, USA (1995).
197. A. L. Spek, *Acta Cryst.*, (1990), **A46**, C34
198. G. H. Stout and L. H. Jensen, *X-ray Structure Determination – A practical guide*, John Wiley & sons, NY, (1989).

199. Allen, F. H.; Kennard, O.; Watson, D. G.; Brammer, L.; Orpen, A.G.; Taylor, R. *J. Chem. Soc., Perkin Trans. II*, (1987), S1-S19.
200. T. S. Koritsanszky; S. Howard; P. Macchi; C. Gatti; L. J. Farrugia; P. R. Mallinson, A. Volkov; Z. Su; T. Richter and N. K. Hansen, *XD-Manual, version 4.10*, A Computer Program Package for Multipole Refinement and Analysis of Electron Densities from Diffraction Data, Free University of Berlin: Berlin; University of Wales: Cardiff, U. K.; Universita` di Milano: Milano, Italy; University of Glasgow: Glasgow, U. K.; State University of New York: Buffalo, NY; University of Nancy: Nancy, France, (2003) and related references of each sections.

A STUDY OF THE SUPRAMOLECULAR ASSEMBLIES INVOLVING PYRIMIDINE BASES AND 5-NITROURACIL*

Summary

This chapter discusses the hydrogen bonding interactions and patterns found in cocrystals and solvates of pyrimidine bases, cytosine and uracil with various hydrogen bond donor-acceptor compounds. Another related compound 5-nitrouracil forms supramolecular assemblies with variety of compounds including solvents. A molecular complex of uracil with melamine, (1:1), protons-transfer complexes (1:1) of cytosine with trimesic and pyromellitic acids as well as the solvates of 5-nitrouracil with solvent molecules, dioxane, pyridine, DMSO, formamide, ethanol and cocrystals with piperazine, N, N'-dimethylpiperazine, 3-aminopyridine and diazabicyclo [2.2.2] octane have been examined by X-ray crystallography. The crystal structures of a 1:1 complex of uracil and melamine involves hydrogen bonded layers with apertures stacked along the *a* and *b* directions giving rise to channels. The complexes of cytosine with trimesic and pyromellitic acids exhibit layered structures, each layer containing a plethora of N-H...O and O-H...O hydrogen bonds between the proton-transfer duplets. The cytosine-trimesic acid complex exhibits a bilayered structure (2.87 Å) in contrast to the layered structure seen in the cytosine-pyromellitic acid complex (3.98 Å). The hydrogen bonded complexes of 5-nitrouracil with various partner molecules show interesting hydrogen bonding patterns. The tape structure found in the parent centric form of nitrouracil is retained with some modifications in the cocrystals with dioxane, piperazine, diazabicyclo [2.2.2] octane, N,N'-dimethylpiperazine, pyridine and DMSO, with the guest molecules forming alternate tapes. In cocrystals involving formamide, ethanol and 3-aminopyridine,

* Papers based on above studies have appeared in Beil. J. Org. Chem. (2005), Beil. J. Org. Chem. (2007), J. Mol. Struct. (2008)

the molecular tapes exhibit mixed compositions. The observed bonding patterns have been classified into six types. In the cocrystal containing diazabicyclo [2.2.2] octane and water, a dodecameric ring structure have been found within in the network formed by water molecules where the tetrahedral pentamers of water serve as the corners.

2.1 Introduction

Molecular recognition and templating are key components of the supramolecular chemistry, while the basis of molecular recognition is the presence of information in the interacting components.¹ Molecular recognition thus implies the storage and read out of the molecular informations.² In supramolecular assemblies, information expressed depends on the potential of a component to enter non-covalent bonding relationships with its partners by satisfying the steric requirements. For the designed synthesis of supramolecular architectures, large number of variables have to be addressed, that is, the magnitude and direction of non-covalent interactions involved, makes this a non-trivial task in multicomponent systems.³ Last several decades, considerable effort has been made to understand the relationship between molecular recognition process and formation of supramolecular assemblies, in terms of the prevalent hydrogen bonding patterns.⁴⁻⁹ There exist numerous examples of organic molecules functionalized with hydrogen bond donor-acceptor groups, which upon recognition of complementary functional moieties give rise to supramolecular architectures, often exotic.¹⁰ Hydrogen bonds like O-H...O, N-H...O, O-H...N, N-H...N (the classical hydrogen bonds) are being extensively used in the analysis and design of novel supramolecular assemblies which has opened up a new realm in the synthesis of advanced functional material with tailor made properties.¹¹ Some of the applications of these supramolecular assemblies include catalysis, separation science, optical activity, sensors, electronic materials, conducting and magnetic materials, polymorphism, crystal growth, supramolecular devices, surfactants.

In addition to the fascinating properties shown by the supramolecular assemblies, the study of molecular recognition and non-covalent interactions are of greater importance in an academic point of view to understand the chemical binding processes involved in chemical and biological reactions. There exists large number of reports in the literature towards the understanding of weak interactions and also on modification of

functionalities for the designing of biological mimics.¹² The peptide nanotube is example for such a biological mimic where the interactions, functionality and structure of the interacting molecules play a major role.¹³ The designing and fabrication of molecular level machines and motors¹⁴ (rotaxanes and catenanes) also call for a sound knowledge of structure, interaction possibilities of various molecules and functional groups.

Besides the interesting physical properties, a study on various non-bonding interactions and molecular recognition processes shown by various supra molecular assemblies provides insight into the drug designing and their binding with proteins and other such functional moieties.¹⁵ The reports on peptide nucleic acids show the relevance of these studies for the synthesis and design of molecules of biological importance.¹⁶

2.2 Scope of the Present Investigation

The biological systems such as DNA and RNA depict wonderful example for the formation supramolecular assembles where the purine and pyrimidine bases interact each other to give a beautiful organization.¹⁷ However, it is rather surprising that utilization of the native nucleobases in molecular recognition studies for the creation of adducts or assemblies is rare, except for a few studies reported by Sasada and co-workers¹⁸ conducted as part of their study on the interactions of nucleic acids with amino acids. A recent report by Perumalla et al,¹⁹ on supramolecular assembles of nucleobases with mono and dicarboxylic acids, where this study point out that in spite of the cocrystallization partner molecules the nucleobases form dimeric interactions among themselves. In this perspective, it is found interesting to look on to the details of molecular recognition process and hydrogen bond formation in the molecular complexes of nucleobase with other molecules and solvents. (see Table 2.1).

2.2.1 A hydrogen-bonded channel structure formed by a complex of uracil and melamine

Of the many interesting hydrogen bonded supramolecular architectures, those formed by cyanuric acid and melamine²⁰ are specially interesting as it involves a rosette type structure wherein each molecule of cyanuric acid and melamine forms three hydrogen bonds on either side. Such a structure of the 1:1 molecular complex between cyanuric acid and melamine first proposed by Whitesides,²¹ was synthesized under

hydrothermal conditions.²⁰ Cyanuric acid also forms hydrogen bonded adducts with melamine,²⁰ 4,4'-bipyridyl²² and 4,4'-bipyridylethene.²³ Although hydrogen bonding aspects of cyanuric acid have been studied in detail, similar structures formed by uracil possessing two imide groups has not been studied adequately, except for its hydrogen bonding with adenine in RNA.²⁴ In view of the above, it was the interest of present study to understand the hydrogen bonding and structure in the cocrystal formed by uracil and melamine.

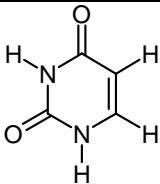
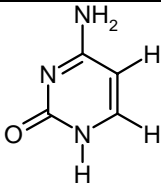
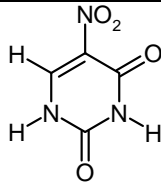

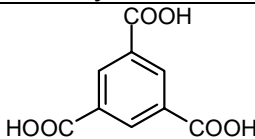
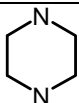
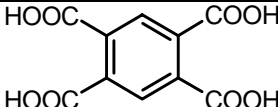
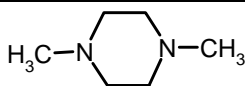
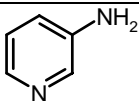
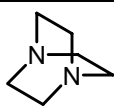
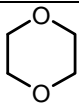
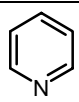
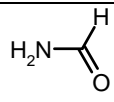
2.2.2 Hydrogen bonding in proton-transfer complexes of cytosine with trimesic and pyromellitic acids

Carboxylic acids are one of the most utilized functionality in the formation of the various supramolecular assemblies due to its ability to form robust hydrogen bonding interactions with various donor and acceptor functional groups also for its property of proton transfer.²⁵ Proton transfer in various molecular complexes leads to strong and directional interactions²⁶ sometimes giving rise to interesting properties such as non-linear optical behavior.²⁷ Moreover, proton transfer is considered relevant in chemical and biological processes involving reaction intermediates. In this context a study aimed to understand structure and self-assembling nature of higher aromatic carboxylic acids such as 1,3,5-benzene tricarboxylic acid (trimesic acid) and 1,2,4,5-benzene tetracarboxylic acid (pyromellitic acid) with nucleobase cytosine involving proton transfer and various strong hydrogen bonding interactions have been carried out.

2.2.3 Hydrogen bonding patterns in the cocrystals of 5-nitrouracil with hydrogen bond donor and acceptor molecules

5-nitrouracil, **5NU**, is an interesting molecule which can be crystallized in centric and non-centric structures.^{28, 29} The previous study have shown that the two polymorphic forms of this molecule show distinctly different interaction and property such as dipole-moments in the solid state. The centro-symmetric structure of **5NU** obtained by crystallizing **5NU** from water, exhibits tapes of nitrouracil molecules, each of which forms on either side, linear N-H...O hydrogen bonds in cyclic $R_2^2(8)$ arrangement³⁰ (H...O distance, 1.81-1.86 Å). It also forms C-H...O linear bonds with neighbouring tape engaging oxygen of the nitro group. Present study on this molecule investigates how the

Table 2.1 Molecules used for various co-crystallization experiments.

Nucleo bases (pyrimidines) and derivatives	 <p>Uracil</p>	 <p>Cytosine</p>	 <p>5-nitouracil, 5NU</p>
Crystallization partner molecules	 <p>Melamine</p>	 <p>1,3,5, benzenetricarboxylic acid, Trimesic acid, TMA</p>	 <p>Piperazine</p>
		 <p>1,2,4,5, benzenetetracarboxylic acid, Pyromellitic acid, PMA</p>	 <p>N, N'-dimethylpiperazine</p>
			 <p>3-aminopyridine</p>
			 <p>Diazabicyclo [2.2.2] octane, DABCO</p>
Solvates		 <p>Dioxane</p>	
		 <p>Pyridine</p>	
		 <p>Formamide</p>	
		<p>Ethanol +H₂O</p>	

hydrogen-bonded structure of **5NU** is affected when it is cocrystallized with different molecules and scope of the new interactions and patterns. For this purpose, solvates of

5NU with different solvents such as dioxane, pyridine, dimethylsulfoxide (DMSO), formamide and aqueous ethanol were prepared, of which the first three are clearly electron donors. In addition, crystallizations of **5NU** with other electron donor compounds such as piperazine, N,N'-dimethylpiperazine, 3-aminopyridine and diazabicyclo[2.2.2]octane have also been carried out.

2.3 Experimental Section

Table 2.1 presents a summary of various cocrystallizations carried out with molecules uracil, cytosine and 5-nitrouracil with various compounds and solvents. All the chemicals used in the present studies, were used directly as obtained from commercial sources and the solvents used for the crystallization have been distilled prior to the experiments and collected over molecular sieves.

2.3.1 Preparation of the various molecular complexes and solvates

Crystallization of uracil with melamine

Cocrystals of the 1:1 molecular complex of melamine and uracil was obtained by the slow evaporation of an equimolar solution of the two compounds in methanol at room temperature. The rod shaped crystals formed in the walls of the test tubes were separated by filtration and characterized by single crystal X-ray diffraction method (see general experimental and related aspects in Chapter 1).

Crystallization of cytosine with 1,3,5-tricarboxylic acid (trimesic acid), TMA and 1,2,4,5-tetracarboxylic acid (pyromellitic acid), PMA

Crystals of the 1:1 cytosine complexes with 1,3,5-benzene tricarboxylic acid (trimesic acid, **TMA**) and 1,2,4,5-benzene tetracarboxylic acid (pyromellitic acid, **PMA**) were synthesized by hydrothermal methods. The reactants were taken in 1:1 molar ratio and mixed thoroughly by stirring in 3 ml of water for 2 hours. The reactions were carried out in a PTFE-lined autoclave of 7 ml capacity for 24 hours at 125 and 150 °C respectively. Good quality single crystals were obtained on cooling the autoclave to room temperature. The crystals were separated from the mother liquor by filtration, washed with water and dried under ambient conditions.

Preparation of solvates and cocrystals of 5-nitrouracil

Solvates of 5-nitrouracil, **5NU** with DMSO, formamide, pyridine, dioxane and ethanol were obtained by slow evaporation of a solution of **5NU** in respective solvents. Cocrystals of **5NU** with non-solvent guests - piperazine, N,N'-dimethylpiperazine, 3-aminopyridine and diazabicyclo[2.2.2]octane (DABCO)- were made by solvothermal method. In all the cases, the compound **5NU** and the guest molecule were taken in 1:1 ratio in aqueous methanol and stirred for 1 hour at ambient temperature. The final suspension was placed inside a Teflon-lined autoclave (21 cm³, 70% filling). The reaction was carried out at 145° C under autogenous pressure for 24 hours. The autoclave was removed and left at ambient temperature for 12 h before opening. The crystals obtained were examined under an optical microscope and those suitable for single-crystal diffraction were separated out.

2.3.2 Crystal data collection

The crystals were analyzed under a polarizing microscope and good quality single crystals were separated for X-ray structure determination. The crystal data were collected on a Simens SMART diffractometer attached with CCD area detector and a graphite monochromator for the Mo K α radiation (50 kV, 40 mA) at room temperature (298 K). The data collection and structure solution were carried out using the procedure describes in the general experimental and related aspects section.

2.4 Results and Discussion

2.4.1 A hydrogen-bonded channel structure formed by a complex of uracil and melamine, 1

The crystal structure determination of the cocrystal formed by uracil with melamine gave the asymmetric unit as shown in Figure 2.1. The molecular complex crystallizes in C2/c space group with single molecules of melamine and uracil in the asymmetric unit. The crystallographic and refinement parameters are given in the Table 2.2. The aromatic C-N bond lengths in melamine molecule are in the range of 1.335(2) - 1.355(2) Å while the C-N distances of which formed with -NH₂ group is given by the range 1.319(1) - 1.349(2) Å. The C-N bond distances in uracil molecule is given by the range of 1.365(2) - 1.377(2) Å whereas the average carbonyl group bond length is given by 1.228(2) Å. The

complete list of bond lengths and bond angles for this molecular complex, **1**, is provided in Appendix Table A2.1. In this 1:1 complex, both melamine and uracil offer several

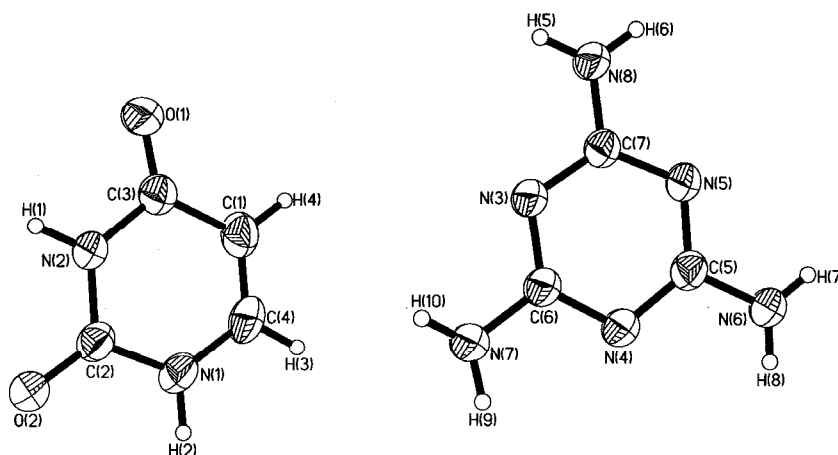


Figure 2.1: ORTEP drawing of the asymmetric unit of the 1:1 molecular complex of uracil and melamine.

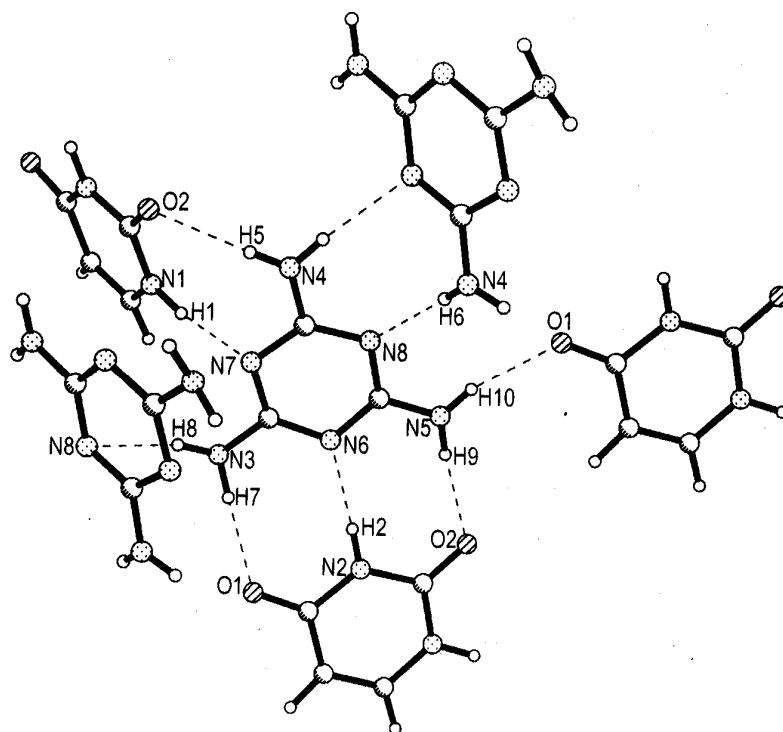


Figure 2.2: Unique hydrogen bonds present in the 1:1 molecular complex of uracil and melamine, **1**.

Table 2.2 Crystal structure data for adduct of uracil with melamine.

Empirical formula	C ₃ H ₆ N ₆ .C ₄ H ₄ N ₂ O ₂
Formula wt	238.23
Cell setting	Monoclinic
Space group	C2/c
a (Å)	14.3618(10)
b (Å)	7.5472(6)
c (Å)	18.9922(14)
α (°)	90
β (°)	91.838(4)
γ (°)	90
Cell volume (Å ³)	2057.5(3)
Z	8
F (000)	992
ρ (Mg/m ³)	1.538
λ(Å)	0.7107
Crystal size (mm)	0.27 x 0.22 x 0.15
Diffractometer	Bruker-Nonius
	- 4-circle diffractometer
Crystal detector distance(cm)	5.0
Radiation type	MoKα
Temperature (K)	298 (2)
No. of measured reflections	4727
No. of independent reflections	1861
Range for data collection θ (°)	1– 25
Range of h, k, l	-17 to 17
	-9 to 7
	-22 to 22
R ₁	0.0373
wR ₂	0.1053
S	1.043
No. of parameters refined	195
Max. eÅ ⁻³	0.160

donor-acceptor sites for hydrogen bonding and each melamine molecule engages in hydrogen bonding via N-H...O and N-H...N bonds with three uracil and two melamine molecules, as shown in Figure 2.2 (see Table 2.3). It is clear that the amino groups of the melamine molecule act as hydrogen bond donors and ring nitrogens as acceptors. Unlike with adenine, uracil forms two N-H...O bonds (H9...O2, 2.08 Å; H7...O1, 2.03 Å) on either side of the N-H...N bond (H2...N6, 1.98 Å). All the three hydrogen bonds are strong, with the hydrogen bond angles in the range of 172 - 179°. These hydrogen-

Table 2.3 List of intermolecular interactions in melamine-uracil molecular complex

H-bond	H...A (Å)	D...A(Å)	D-H...A(°)
N1-H1...N7	1.93(2)	2.833(2)	174.3(1)
N2-H2...N6	1.98(2)	2.876(2)	178.7(2)
N4-H5...O2	2.19(2)	3.004(2)	165.4(1)
N4-H6...N8	2.27(2)	3.079(2)	169.2(2)
N3-H7...O1	2.03(2)	2.941(2)	177.3(2)
N3-H8...N8	2.50(2)	3.328(2)	153.6(1)
N5-H9...O2	2.08(2)	2.937(2)	172.3(2)
N5-H10...O1	2.02(2)	2.860(2)	164.2(2)

bonded pairs are interconnected through a N-H...O hydrogen bond to form a molecular chain as shown in the Figure 2.3a. The triply bonded melamine-uracil pairs are stacked parallelly and the chains run along both *a* and *b* axes. Such an arrangement of the chains gives rise to an aperture structure as shown in Figure 2.3b.

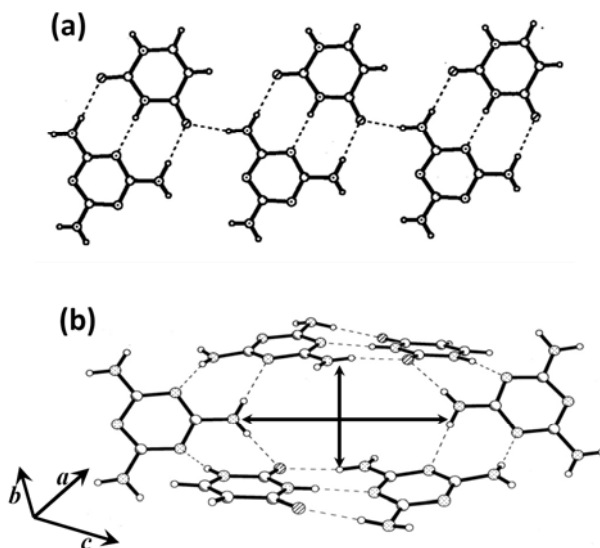


Figure 2.3: (a) Molecular chain formed by melamine and uracil molecules, (b) the aperture formed by the triply hydrogen-bonded melamine-uracil pairs.

Four melamine and two uracil molecules thus enclose the aperture. The apertures are connected through N-H...O (H10...O1, 2.02Å) bonds giving rise to infinite channels along both *a* and *b* directions. One perspective in Figure 2.4 show the channels run along the *a*-direction. It is interesting to note that melamine engages in hydrogen bonding

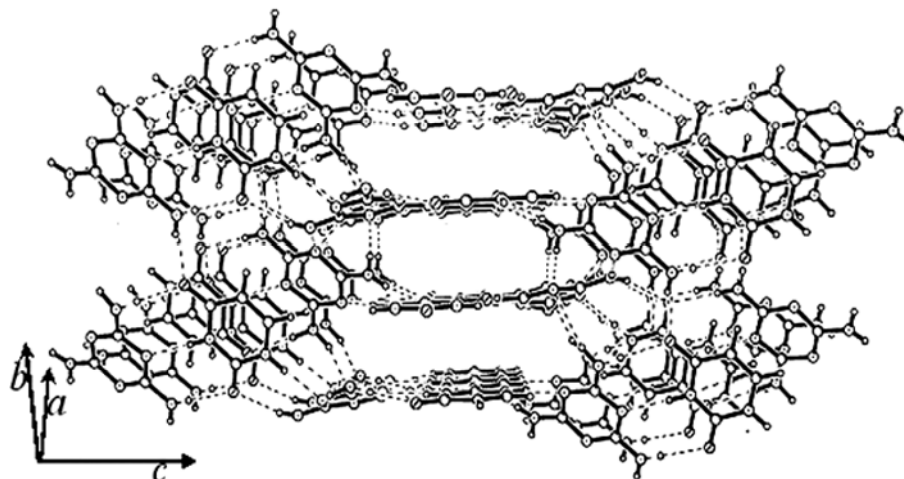


Figure 2.4: Three-dimensional packing of melamine and uracil molecules.

utilizing all the donor-acceptor sites, much the same way it does in the cyanuric acid adduct.²⁰ However, the channel structure is somewhat different, in shape and dimension. This clearly indicates the role of the uracil molecule in directing the shape of the channel structure.

2.4.2 Hydrogen bonding in proton-transfer complexes of cytosine with trimesic and pyromellitic acids

The asymmetric units of the complexes of cytosine with 1,3,5-tricarboxylic acid (trimesic acid, **TMA**) and 1,2,4,5-tetracarboxylic acid (pyromellitic acid, **PMA**) are shown in Figure 2.5. Both complexes carry water of crystallization. In the asymmetric unit of the 1:1 trimesic acid -cytosine complex (Figure 2.5a), the two molecules lie in a plane along with a water molecule. The 1:2 pyromellitic acid-cytosine molecular complex crystallizes in a non-centric space group Pc with a large asymmetric unit (Figure 2.5b) consisting of two molecules of pyromellitic acid and four molecules of cytosine along with two molecules of lattice water. Intermolecular proton transfer is observed in both the systems. The crystallographic and refinement details of the compounds are given in the Table 2.4. For trimesic acid – cytosine complex, the proton transfer (H7) occurs from a carboxylic acid group of trimesic acid (O5-C9-O6) to the ring-nitrogen of the cytosine (N2) (Figure 2.5a). In the case of pyromellitic acid -cytosine, each pyromellitic acid transfers two of the carboxylic acid protons to two cytosine molecules. As a result, neighboring carboxylic acid groups form strong intramolecular hydrogen bonds (O...H, 1.25-1.47 Å) as shown in the inset of Figure 2.5b. The C-N bond lengths in cytosine molecules in both

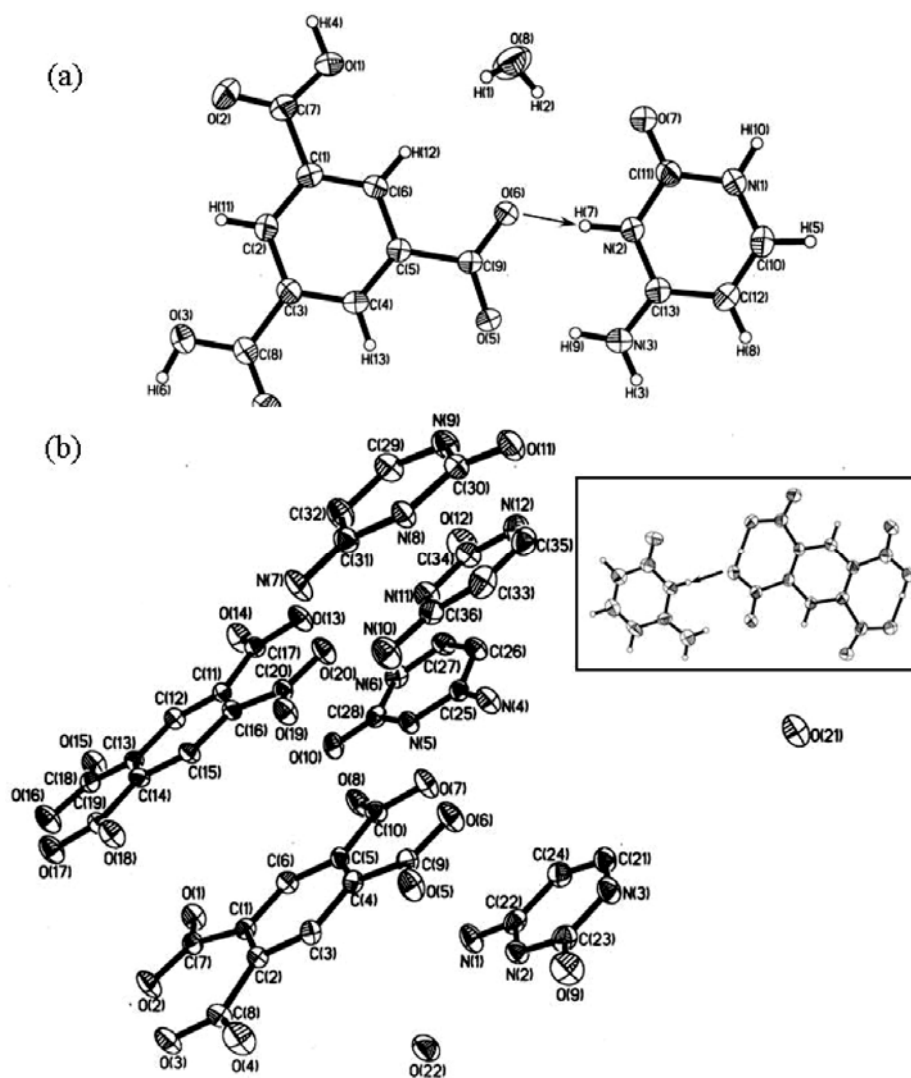


Figure 2.5: ORTEP plot (50% probability) of the molecular entities in the asymmetric unit of (a) cytosine and 1,3,5,-tricarboxylic acid (**TMA**), **2a**. (b) cytosine and 1,2,4,5-tetracarboxylic acid (**PMA**), **2b**, hydrogen atoms are removed for clarity. A proton transfer between **PMA** and cytosine is shown in the inset along with the intramolecular hydrogen bonds.

the complexes are in the range of 1.350(2) – 1.380(5) Å, whereas the bond lengths for the C-O bonds in carboxylate groups in both the complexes are ~ 1.255 Å. The detailed list of the bond lengths and bond angles are given in the Appendix Tables A2.4 and A2.6.

The trimesic acid –cytosine complex contains hydrogen bonded layers of the type shown in Figure 2.6a, wherein the trimesic acid molecules are arranged in a row forming mixed C-H...O and O-H...O hydrogen bonds (see 3 and 10 in Table 2.5) representing a $R_2^2(9)$ cyclic pattern (see Scheme 1.2 in Chapter 1 for Etter notations). Each trimesic acid

molecule is linked to cytosine molecules on either side via two $R_2^2(8)$ type interactions, one being mixed O-H...O and N-H...O (4,8) and the other, purely N-H...O, (6,7). In the

Table 2.4 Crystal structure data for molecular complexes of cytosine with 1,3,5-benzene tricarboxylic acid (trimesic acid), **2a** and 1,2,4,5-benzene tetracarboxylic acid (trimesic acid), **2b**.

Complexes	2a	2b
Empirical formula	C ₄ N ₃ O ₁ H ₆ . C ₉ O ₆ H ₅ . H ₂ O	4 C ₄ N ₃ O ₁ H ₆ . 2 C ₁₆ O ₈ H ₄ . 2H ₂ O
Formula wt	339.26	985.74
Cell setting	Triclinic	Monoclinic
Space group	P -1	P c
a (Å)	7.6722(2)	12.3975(3)
b (Å)	8.6710(2)	13.7484(3)
c (Å)	10.6740(3)	12.9425(3)
α (°)	91.060(2)	90.00
β (°)	92.263(2)	113.3230(10)
γ (°)	100.662(2)	90.00
Cell volume (Å ³)	697.05(3)	2025.74(8)
Z	2	2
F (000)	352	1018
ρ (mg/m ³)	1.616	1.616
λ(Å)	0.7107	0.7107
Crystal size (mm)	0.1x0.1x0.05	0.1x0.1x0.05
Crystal detector distance(cm)	5.0	5.0
Radiation type	Mo Kα	Mo Kα
Temperature (K)	298(2)	298(2)
No. of measured reflections	7823	14517
No. of independent reflections	2638	6607
Range for data collection θ (°)	1 – 26	1 – 26
Range of h, k, l	-9 to 9 -10 to 10 -12 to 12	-15 to 14 -16 to 16 -15 to 15
R ₁	0.0375	0.0394
wR ₂	0.0989	0.0867
S	1.033	1.071
No. of parameters refined	269	695
Max. eÅ ⁻³	0.305	0.278

Table 2.5 Unique set of hydrogen bonds in molecular complexes of cytosine with 1,3,5-benzene tricarboxylic acid, (TMA)

Sl. No	H-bond	H...A (Å)	D-A (Å)	D-H...A (°)
1	O(8)-H(1)...O(2)	1.97(1)	2.849(3)	155.7(1)
2	O(8)-H(2)...O(7)	2.30(2)	3.012(1)	145.3(2)
3	O(1)-H(4)...O(5)	1.72(2)	2.602(1)	154.8(2)
4	O(3)-H(6)...O(7)	1.90(2)	2.789(4)	178.5(2)
5	N(3)-H(3)...O(8)	2.00(1)	2.831(4)	159.0(5)
6	N(2)-H(7)...O(6)	1.67(1)	2.657(1)	174.2(1)
7	N(3)-H(9)...O(5)	1.84(2)	2.773(1)	175.1(1)
8	N(1)-H(10)...O(4)	1.80(4)	2.701(1)	170.4(1)
9	C(6)-H(12)...O(8)	2.90(4)	3.802(3)	159.1(1)
10	C(4)-H(13)...O(2)	2.85(1)	3.757(1)	172.1(2)

Cyclic patterns: $R_2^2(8)$ -{(4,8), (6,7)}, $R_2^2(9)$ -{(3,10)}, : $R_3^3(11)$ -{(2,6,9)}, $R_4^2(11)$ -{(3,5,7)}

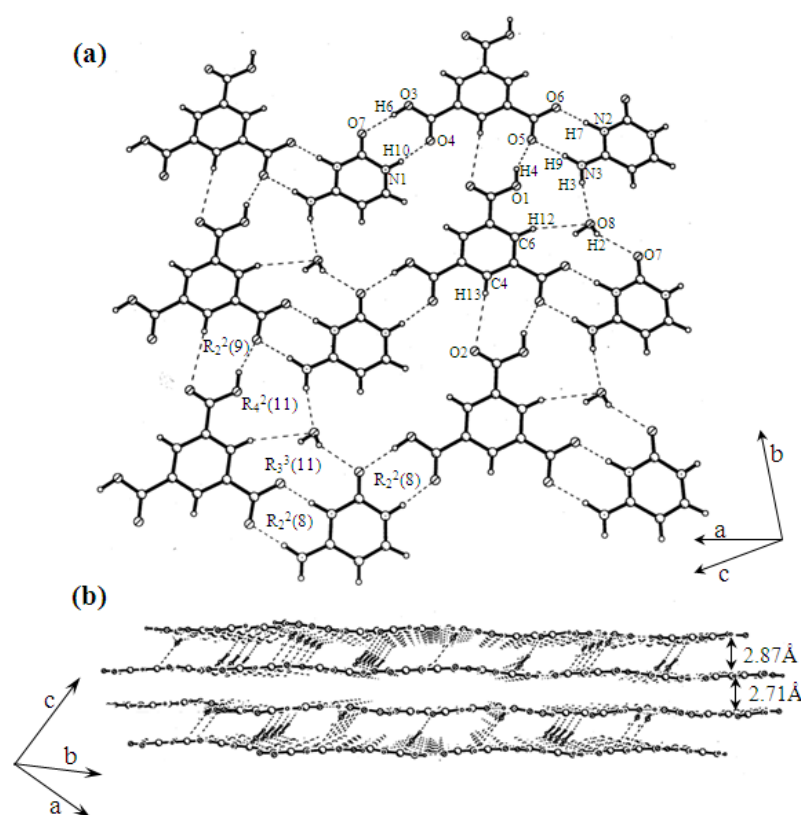


Figure 2.6: (a) Hydrogen bonded layer formed by cytosine, 1,3,5-tricarboxylic acid and water molecules. (b) Packing of molecular bilayers.

latter, both the donors originate from the cytosine molecule the amino group (N3-H9) and the ring nitrogen (N2-H7) respectively. Accordingly, N2 exists as an iminium ion, with

remarkable increment ($\sim 0.1 \text{ \AA}$) in the N-C bond lengths compared to that in cytosine^{31,32} (see Appendix Tables A2.4 and A2.6). From Figure 2.6a, we see that the cytosine molecules are arranged in rows with the intervening water molecule linking them through O-H...O (2) and N-H...O (5) interactions. There is an additional C-H...O (9) interaction involving the ring C-H group of the trimesic acid and one of the lone pairs on water. This gives rise to large hydrogen bonded cyclic systems, *viz.* $R_3^3(11)$ and $R_4^2(11)$ (see Table 2.5). Water molecules play a strategic role of packing molecular layers via O-H...O (1) interactions from the carboxylate oxygens of the neighbouring layer. As a result, water molecules assume a distorted tetrahedral geometry with internal angles of 95° , 131.8° , 95.3° and 114.9° . As shown in Figure 2.6b, there is reciprocating hydrogen bonding from

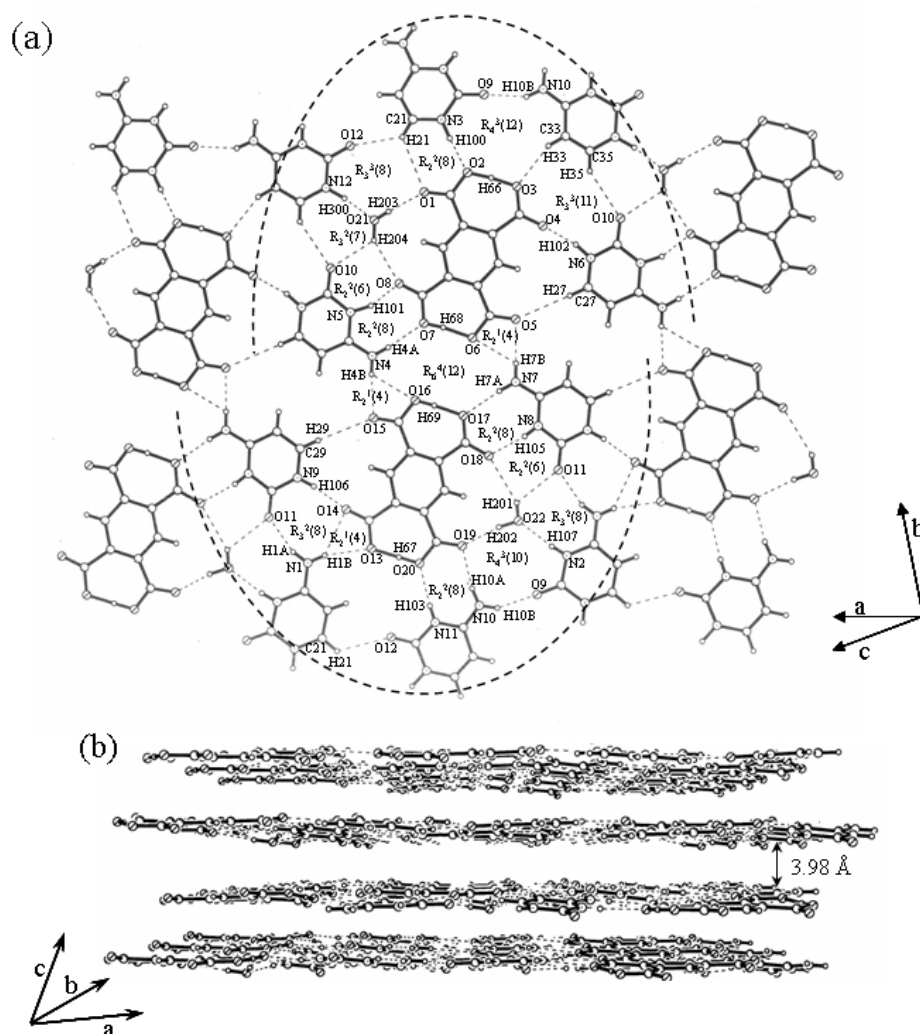


Figure 2.7: (a) Molecular layer formed by hydrogen bonded cytosine, 1,2,4,5-benzene tetracarboxylic acid and water molecules. (b) Packing molecular layers.

Table 2.6 Unique set of hydrogen bonds in molecular complexes of cytosine with 1,2,4,5-benzene tetracarboxylic acid (**PMA**)

Sl. No	H-bond	H...A (Å)	D-A (Å)	D-H...A (°)
1	N(1)-H(1A)...O(11)	1.9746	2.7990	160.24
2	N(1)-H(1B)...O(13)	2.2211	3.0575	164.15
3	N(1)-H(1B)...O(14)	2.3619	3.0620	138.83
4	N(4)-H(4A) ...O(7)	2.0645	2.9120	168.32
5	N(4)-H(4B)...O(15)	2.0521	2.9099	175.11
6	N(4)-H(4B) ...O(16)	2.4217	2.9210	117.57
7	N(7)-H(7A)...O(17)	2.0511	2.8993	168.72
8	N(7)-H(7B)...O(5)	2.0416	2.9012	178.05
9	N(7)-H(7B)...O(6)	2.3591	2.8750	118.90
10	N(10)-H(10A)...O(19)	2.0125	2.8630	169.80
11	N(10)-H(10B)...O(9)	1.9923	2.7893	153.67
12	N(3)-H(100)...O(2)	1.8057	2.7255	169.07
13	N(5)-H(101)...O(8)	1.6861	2.6627	158.96
14	N(6)-H(102).. O(4)	1.7826	2.6970	164.85
15	N(11)-H(103)...O(20)	2.0326	2.8415	174.32
16	N(8)-H(105)...O(18)	1.9037	2.6805	166.97
17	N(9)-H(106).. O(14)	1.8778	2.7416	172.23
18	N(2)- H(107).. O(22)	1.9422	2.7731	168.90
19	N(12)-H(300)...O(21)	1.7302	2.7269	168.70
20	O(22)-H(201).. O(18)	2.5247	3.2947	153.90
21	O(22)-H(201)...O(11)	2.4575	2.9933	122.83
22	O(22)-H(202)...O(19)	2.0426	2.9491	160.27
23	O(21)-H(203)...O(1)	1.9796	2.8249	174.14
24	O(21)-H(204)...O(8)	2.4048	3.2601	148.16
25	O(21)-H(204)...O(10)	2.4260	3.0708	124.26
26	O(2)-H(66)...O(3)	1.2536	2.372	174.00
27	O(20)-H(67)...O(13)	1.3660	2.3810	178.97
28	O(7)-H(68)...O(6)	1.4601	2.3908	173.14
29	O(16)-H(69)...O(17)	1.4720	2.3908	174.85
30	C(21)-H(21)...O(12)	2.6525	3.2886	126.21
31	C(21)-H(21)...O(1)	2.7303	3.3701	126.75
32	C(27)-H(27)...O(5)	2.7954	3.7202	172.91
33	C(29)-H(29)...O(15)	2.8232	3.7343	166.69
34	C(35)-H(35)...O(10)	2.5910	2.3967	145.25
35	C(33)-H(33)...O(3)	2.3552	3.2312	156.89

Cyclic patterns: $R_2^1(4)$ - (2,3), (5,6), (8,9); $R_2^2(6)$ - (16,20,21), (13,24,25); $R_2^2(8)$ - (10,15), (7,16), (4,13), (12,31); $R_3^2(7)$ - (19,25,34); $R_3^2(8)$ - (1,3,17), (1,18,21); $R_3^3(8)$ - (19,23,30,31), $R_3^3(11)$ - (14,34,35); $R_4^3(10)$ - (10,11,18,22); $R_4^3(12)$ - (11,12,26,35); $R_6^4(12)$ - (4,6,7,9,28,29)

the neighboring layer, giving rise to a hydrogen-bonded bilayer. The interlayer distance is found to be 2.87 Å. Such bilayers are stacked parallelly and the distance between the neighbouring bilayers is surprisingly somewhat less, 2.71 Å (see Figure 2.6b).

The molecular stacking diagram of **PMA**-cytosine complex shown in Figure 2.7 reveals how the molecules are arranged in hydrogen-bonded layers. The interlayer distance is 3.98 Å (Figure 2.7b). This system is rich in hydrogen bonding interactions as shown in Figure 2.7a and listed in Table 2.6. It can be clearly seen that rows of molecules roughly along the b-direction, where for every four consecutive cytosine molecules there exist two **PMA** molecules (not shown). As a result, every **PMA** molecule is surrounded by five cytosine molecules from the neighboring rows (see dashed lines in Figure 2.7a), producing a number of cyclic patterns of hydrogen bonding interactions. The molecular arrangement enclosed by the dashed lines carry an apparent inversion symmetry in the middle of the $R_6^4(12)$ (4,6,7,9,28,29 of Table 2.6) cyclic pattern, which is covered by two $R_2^1(4)$ and two $R_2^2(8)$ interactions. The $R_2^1(4)$ pattern comprises of bifurcated N-H...O interactions involving carboxylate oxygens of **PMA** and an amino hydrogen of cytosine. The two patterns (5,6) and (8,9) exhibit only small differences in the hydrogen bond parameters and are similar to another $R_2^1(4)$ pattern seen at the bottom, labeled (2,3). Likewise, the $R_2^2(8)$ interactions are formed by a pair of N-H...O hydrogen bonds, (4,13) and (16,17). A $R_2^2(8)$ is also seen at the bottom of the figure involving the (10,15) set. In addition, the presence of a $R_2^2(8)$ pattern at the top, but in this case the interactions are N-H...O(12) and C-H...O(31) in nature. The $R_2^2(6)$ pattern in the two segments carry similar hydrogen bonds, one N-H...O and two O-H...O, (16,20,21) and (13,24,25) respectively. In the bottom arrangement, there are two $R_3^2(8)$ interactions, one comprising N-H...O interactions (1,3,17) and the other pattern is formed by two N-H...O (1,18) and one O-H...O (21) hydrogen bonds. Along the bottom line, there exists a $R_4^3(10)$ interaction formed by three N-H...O (10,11,18) and one O-H...O (22) interactions involving two cytosine molecules, one water and one **PMA** molecule. Other important interactions present in the upper line are $R_3^2(7)$ pattern formed by C-H...O (34), O-H...O (25) and N-H...O (19) hydrogen bonding, where the carbonyl oxygen participates in bifurcated interaction using its both the lone pairs. In addition, there is $R_3^3(8)$ interaction involving a pair of bifurcated C-H...O (30,31), N-H...O (19) and O-

H...O (23) hydrogen bonds. There is a $R_3^3(11)$ interaction formed by two C-H...O (34,35) and one N-H...O (14) hydrogen bonds and this is the only pattern where cytosine uses both of the C-H hydrogens. The biggest cyclic pattern $R_4^3(12)-(11,12,26,35)$, along the upper ring involves an intramolecular O-H...O (26) hydrogen bond. The arrangement of the cytosine and water molecules around the **PMA** molecule as discussed above, is shown vividly in Figure 2.8 with a space-filling model. It is noteworthy that the cytosine and water molecules form a half-ring structure. Two such ring structures come face-to-face, where the interactions are purely hydrophobic in nature and the resulting cavities are filled by the **PMA** molecules (Figure 2.8). The presence of such cavities is clear from Figure 2.8b, where the **PMA** molecules have been removed.

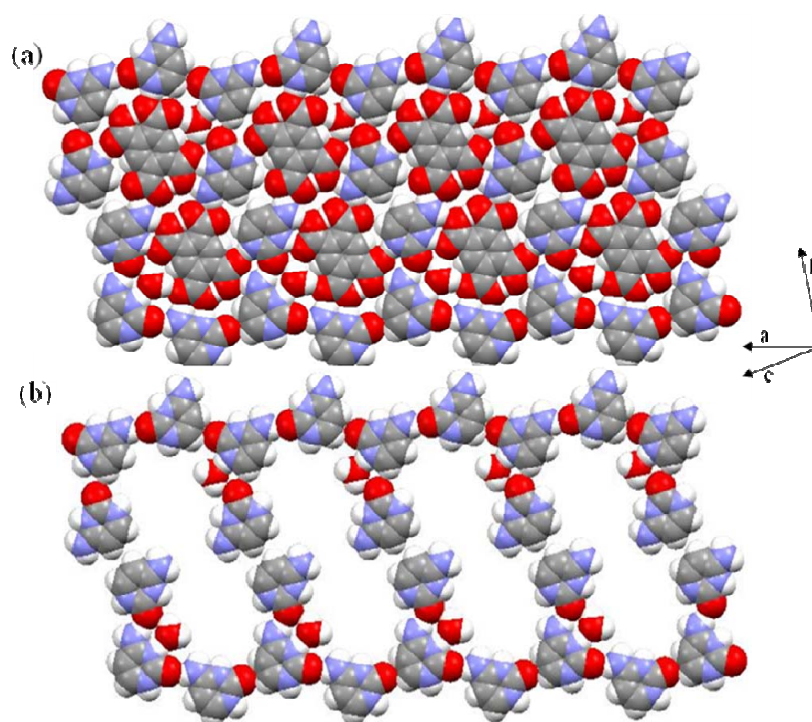


Figure 2.8: Space filling model of the molecular packing in a single layer of 1,2,4,5-benzene tetracarboxylic acid-cytosine molecular complex, **2b** (a) The ring structures formed by cytosine and water filled by two 1,2,4,5-tetracarboxylic acid molecules. (b) Ring structures on removal of **PMA** molecules.

2.4.3 Hydrogen bonding patterns in the cocrystals and solvates of 5-nitouracil

In order to understand hydrogen bonded patterns in the cocrystals of 5-nitouracil, **5NU**, it would be instructive to examine interactions that **5NU** itself can have in such

cocrystals. Molecule **5NU** is nearly symmetric and has several hydrogen bond donor and acceptor sites, which provide a number of possibilities for hydrogen bonding (see Figure 2.9). While the two-ring carbonyl oxygens and nitro-oxygens act as acceptors, the two N-H groups along with the C-H groups are donors. Figure 2.10 present six hydrogen

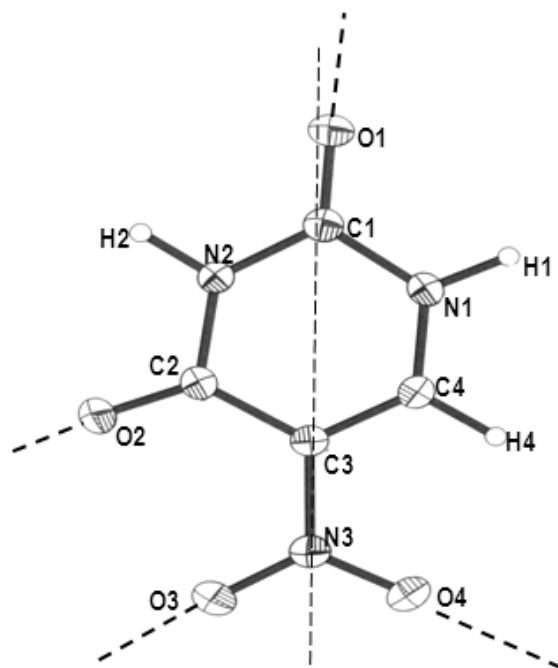


Figure 2.9: 5-nitrouracil, **5NU** with the acceptor sites in the molecules are marked.

bonding possibilities in the all the cocrystals and solvates presented in study. Figure 2.10a, where **5NU** involves two N-H...O cyclic bonds ($R_2^2(8)$) on either side, is similar to that found in centric nitrouracil structure.^{33,34} Here it is designate the two dimeric bonds as D_1 and D_2 based on the participating carbonyl oxygens. Thus, D_1 and D_2 are seen alternating along the molecular tape. Neighboring tapes interact through C-H...O interactions from the nitro-oxygens. A slight variation to this type is one where only one cyclic dimer, either D_1 or D_2 is present (Figure 2.10b and c, respectively), alternating with cyclic C-H...O bonds (D_3). The other structure in the figure contains bifurcated hydrogen bonds involving NH and CO groups of neighboring molecules forming a zig-zag arrangement (Figure 2.10d). Another case is one where C-H...O and N-H...O interactions form a cyclic arrangement, $R_3^2(9)$, involving the acceptor sites of the solvent molecules present in the cocrystal (Figures 2.10e and f). The two patterns differ slightly in that e is linear while f appears staggered.

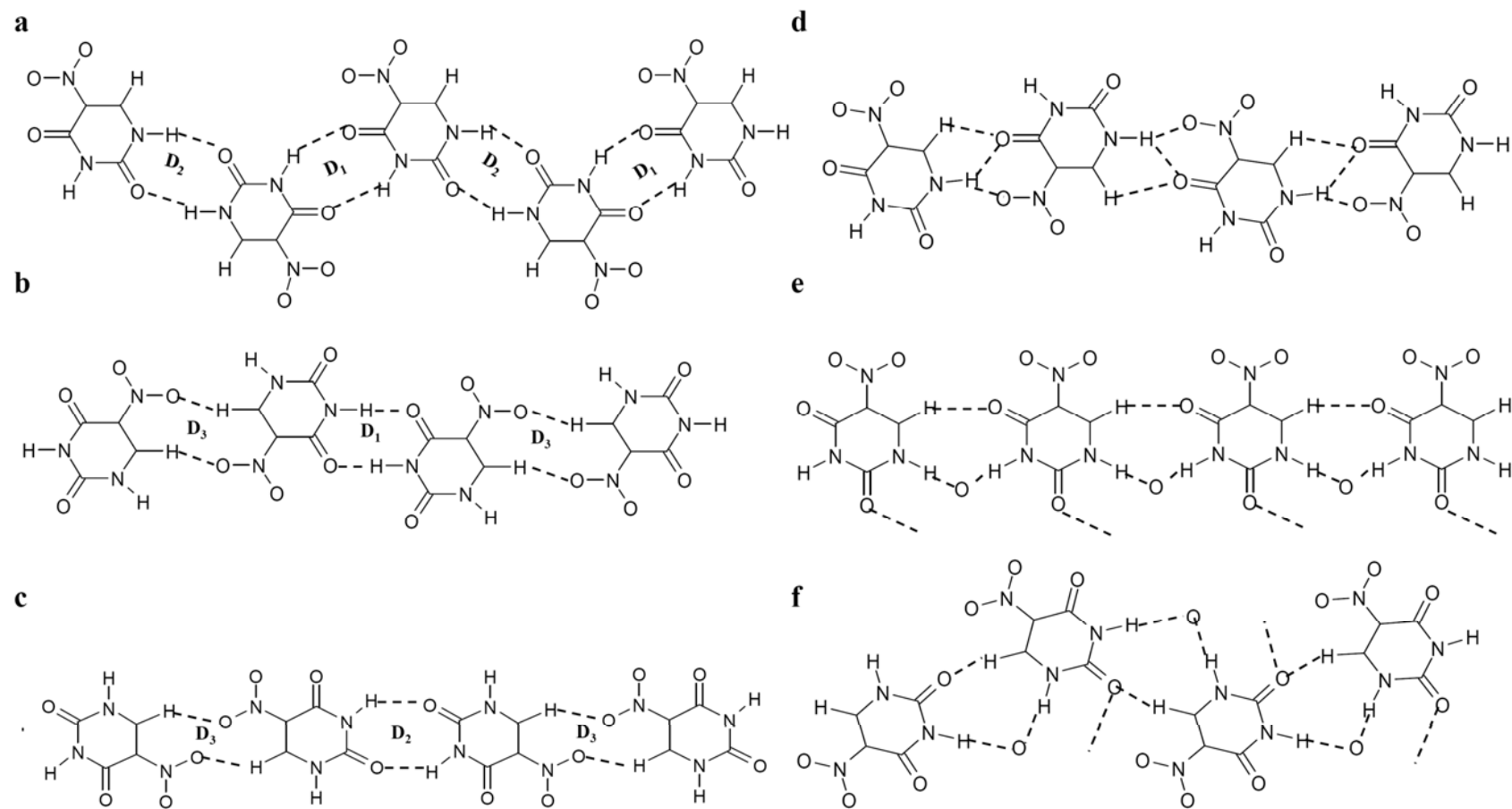


Figure 2.10: Hydrogen bonding patterns of 5-nitrouracil, 5NU, commonly found in its cocrystals with other molecules. Cyclic N-H...O (D_1 and D_2) and C-H...O (D_3) dimeric bonds are marked.

Table 2.7 Crystal data for the cocrystals and solvates of 5-nitrouracil

Complexes	3a	3b	3c	3d	3e	3f	3g	3h
Empirical formula	C ₄ H ₃ N ₃ O ₄ · C ₂ H ₄ O ₁	C ₄ H ₃ N ₃ O ₄ · 2C ₂ H ₅ N ₁	C ₄ H ₃ N ₃ O ₄ · C ₃ H ₇ N ₁	C ₄ H ₃ N ₃ O ₄ · C ₅ H ₅ N ₁	2 C ₄ H ₃ N ₃ O ₄ · 4 C ₁ H ₃ N ₁ O ₁	2 C ₄ H ₃ N ₃ O ₄ · 2C ₂ H ₆ O ₁ ·H ₂ O	C ₄ H ₃ N ₃ O ₄ · C ₅ H ₇ N ₂	2 C ₄ H ₃ N ₃ O ₄ · 2 C ₆ H ₁₂ N ₂ ·5H ₂ O
Formula wt	201.15	243.23	214.19	236.19	494.36	424.34	252.22	628.62
Cell setting	Monoclinic	Triclinic	Triclinic	Monoclinic	Monoclinic	Monoclinic	Monoclinic	Monoclinic
Space group	P 2(1)/n	P -1	P -1	P 2(1)/c	P 2(1)/c	P 2(1)/c	P 2(1)/c	P 2(1)/c
a (Å)	8.3535 (1)	4.3579 (1 [°])	7.1052 (1)	7.5173 (1)	14.1865 (1)	11.8264 (1)	8.2825 (1)	9.2323 (1)
b (Å)	6.4277 (1)	9.8014 (1)	7.6010 (2)	12.7817 (1)	11.5840 (7)	11.8738 (1)	4.9546 (1)	9.6598 (1)
c (Å)	15.7030 (2)	12.7310 (2)	10.150 (2)	10.8938 (1)	12.7907 (1)	12.6511 (1)	25.6080 (2)	32.2899 (1)
α (°)	90	94.7120 (2)	93.023 (1)	90	90	90	90	90
β (°)	101.810 (3)	99.4520 (2)	106.631 (1)	97.780 (5)	94.775 (1)	98.696 (1)	98.293 (1)	90.801 (1)
γ (°)	90	97.603 (1)	117.689 (1)	90	90	90	90	90
Cell volume (Å ³)	825.3 (1)	528.7 (1)	453.8(2)	1037.1 (1)	2094.7 (2)	1756.1 (2)	1039.9 (2)	2879.4 (1)
Z	4	2	2	4	4	4	4	4
F (000)	416	256	224	488	1024	888	524	1024
ρ (g/cm ³)	1.619	1.528	1.567	1.513	1.568	1.605	1.611	1.45
Crystal size (mm)	0.45x0.25x0.25	0.35x0.3x0.2	0.35x0.32x0.10	0.35x0.20x0.20	0.50x0.40x0.15	0.35x0.30x0.20	0.50x0.50x0.45	0.50x0.35x0.25
Temperature (K)	298(2)	298 (2)	298 (2)	298 (2)	298 (2)	298 (2)	298 (2)	298 (2)
No. of measured reflections	3318	2242	1537	4241	8395	7210	3311	11716
No. of independent reflections	1190	1495	1274	1485	2998	2004	1502	4148
Range for data	3-23	2 to 24	2 - 23	2 - 24	2 - 24	2-24	2 - 24	1 - 24
Range of <i>h, k, l</i>	-9 to 7	-4 to 4	-7 to 7	-7 to 8	-15 to 14	-13 to 8	-9 to 9	-10 to 10
	-7 to 7	-9 to 10	-4 to 8	-14 to 10	-9 to 12	-13 to 12	-5 to 5	-10 to 9
	-17 to 17	-13 to 14	-11 to 11	-10 to 12	-14 to 14	-14 to 14	-28 to 18	-29 to 35
R ₁	0.0688	0.0636	0.7107	0.0474	0.0439	0.0754	0.1235	0.0584
wR ₂	0.1561	0.1674	0.3522	0.1315	0.1244	0.2280	0.3196	0.1680
S	1.170	1.152	1.054	1.123	1.205	1.103	0.974	1.049
No. of parameters	155	155	137	155	380	2524	163	428
Max. eÅ ⁻³	0.238	0.535	0.914	0.201	0.165	0.725	0.695	0.475

Solvate of 5-nitrouracil with dioxane, **3a**

The asymmetric unit of a 2:1 solvate, **3a**, of 5-nitrouracil, with dioxane is shown in Figure 2.11. The asymmetric unit comprises of a full molecule of 5-nitrouracil along with a half molecule of dioxane. This solvate crystallizes in a monoclinic space group

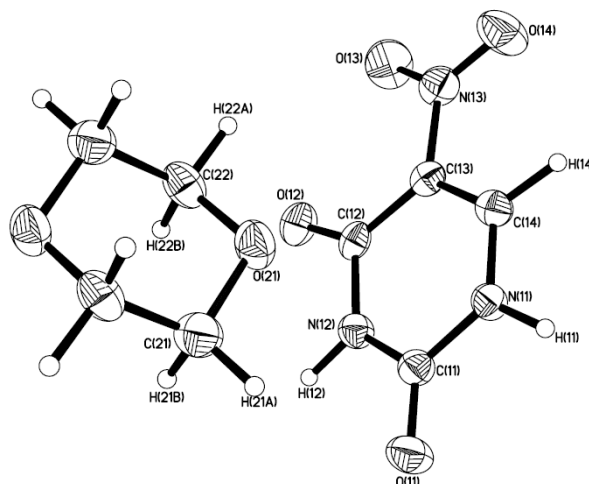


Figure 2.11: ORTEP plot of 5-nitrouracil-dioxane **3a**. Thermal ellipsoids are given at 50% probability.

$P2_1/n$. The crystallographic data and experimental details are given in Table 2.7. The C-O distance in dioxane molecule is given by 1.425(6) and 1.436(6) Å whereas the C-C bond length is 1.505(7) Å. The $-C=O$ bond length in 5-nitrouracil is given by 1.219(5) Å while the average C-N bond lengths are in the range of 1.348(5)- 1.391(6) Å. A complete list of bond lengths and bond angles are provided in Table A2.7 (see Appendix A2) and the atomic coordinates and isotropic displacement parameters are provided in Table A2.8.

In this adduct, dioxane molecule serve as both hydrogen bond donor and acceptor through its C-H bond and oxygen atoms (see table 2.8). In the solvate **3a**, the hydrogen-bonded tapes of **5NU** are retained (Figure 2.12) as in the parent structure^{33,34}. Cyclic N-

Table 2.8 Unique set of hydrogen bonds in solvate of 5-nitrouracil, **5NU** with dioxane.

H-bond	H...A (Å)	D-A (Å)	D-H...A (°)
N(12) -- H(12) .. O(12)	1.84(4)	2.836(5)	171.0(4)
C(14) -- H(14) .. O(21)	2.18(4)	3.200(6)	156.0(4)
C(22) -- H(22A).. O(11)	2.38(3)	3.301(6)	145.0(3)
N(11) -- H(11) .. O(11)	1.79(3)	2.788(5)	170.0(3)

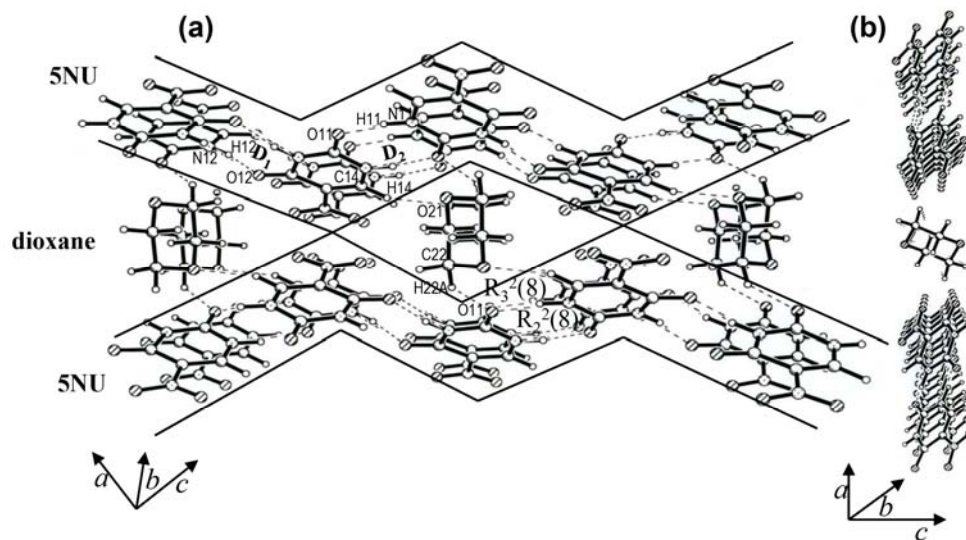


Figure 2.12: Dioxane molecules held between the zig-zag rows of 5-nitrouracil, **5NU**, viewed (a) perpendicular and (b) parallel to the molecular layer. Cyclic arrangements of bonds are marked using Etter's notation.³⁰

H...O dimers of both types, D₁ and D₂ are present with H...O distances of 1.79 and 1.84 Å respectively. This structure belongs to Figure 2.10a. The dioxane molecule is accommodated between the tapes of **5NU** giving rise to new C-H...O interactions (see Table 2.8) in a R₃²(8) arrangement (see Figure 2.10a). It is as though the neighboring rows of 5-nitrouracil molecules slide against each other by approximately the size of a molecule thereby creating a cavity for the guest molecule. The molecular layers appear as a set of parallel planes as shown in Figure 2.12b.

Hydrogen-bonded cocrystal of 5-nitrouracil with piperazine, 3b

The (1:1) molecular complex (**3b**) of 5-nitrouracil, **5NU** with piperazine crystallize in triclinic space group P(-1) with two half molecules of piperazine and a full molecule of **5NU** in the asymmetric unit. (see Figure 2.13) Crystallographic and refinement details are given in Table 2.7. The average C-C and C-N bond lengths in piperazine are given by 1.510(5) Å and 1.476(5) Å respectively. A detailed list of bond lengths and bond angles are given in Appendix Table A2.9. Atom coordinates and isotropic displacement parameters are given in the Table A2.10 (see Appendix A2).

Unlike the case of dioxane solvate, cocrystallization of **5NU** with piperazine, destroys the hydrogen-bonded tape structure involving D₁ and D₂, and instead giving rise

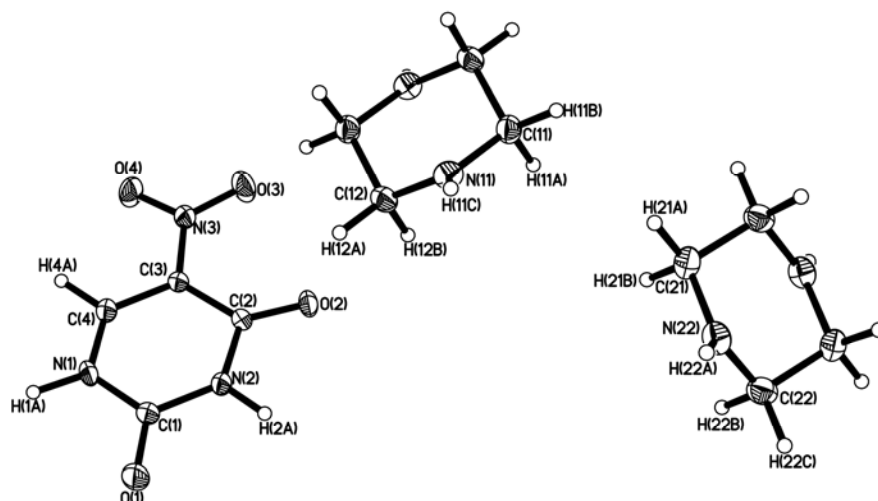


Figure 2.13: ORTEP plot of (1:1) molecular complex of 5-nitrouracil, 5NU–piperazine (**3b**). Thermal ellipsoids are given at 50% probability.

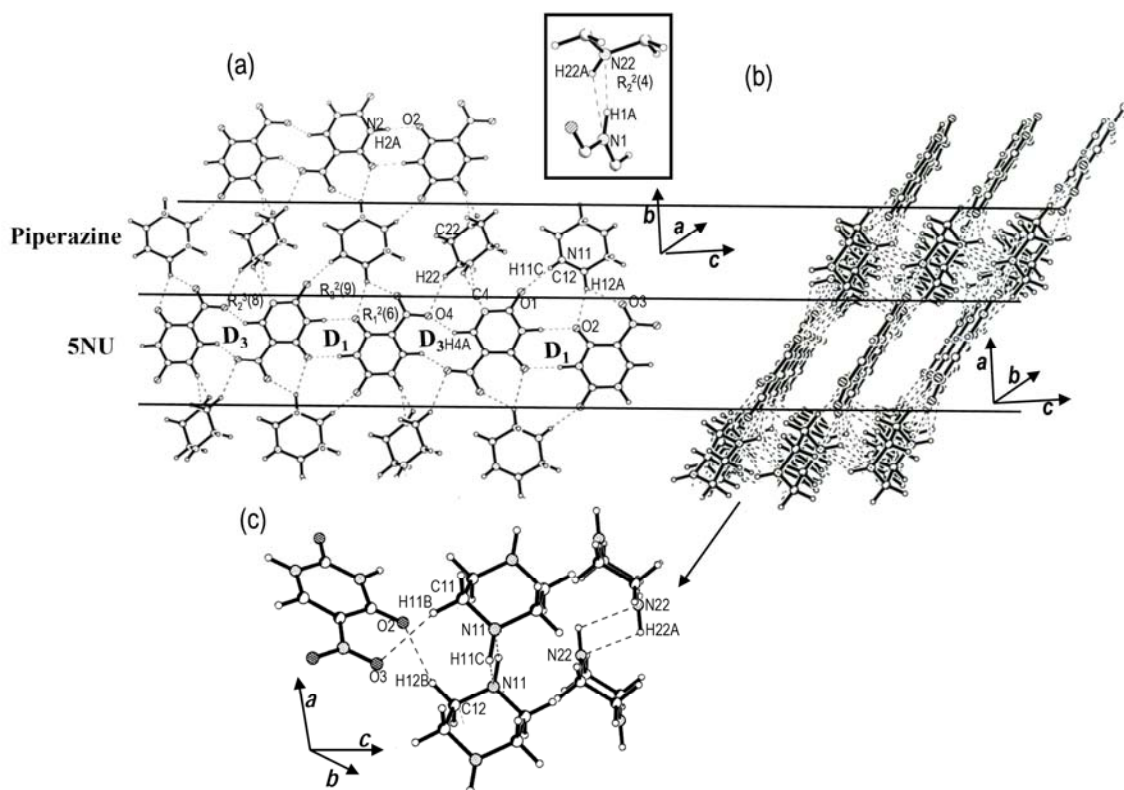


Figure 2.14: Cocystal of 5-nitrouracil and piperazine, **3b**: (a) A molecular layer showing alternating tapes of 5NU and piperazine. Inset shows a cyclic N-H...O dimer formed between adjacent tapes. (b) A packing view of layers formed by 5NU-piperazine. (c) hydrogen bonding between the layers.

Table 2.9 Unique set of hydrogen bonds in molecular complexes of 5-nitrouracil, **5NU** with piperazine.

H-bond	H...A (Å)	D-A (Å)	D-H...A (°)
N(1) -- H(1A) .. N(22)	2.046(4)	3.008(4)	158.6(3)
N(2) -- H(2A) .. O(2)	1.942(4)	2.945(4)	172.5(3)
N(11) -- H(11C).. O(1)	2.338(4)	2.828(4)	108.7(3)
N(11) -- H(11C).. N(11)	2.304(4)	2.771(4)	106.9(3)
N(22) -- H(22A).. N(1)	2.487(4)	3.008(4)	111.6(3)
N(22) -- H(22A).. N(22)	2.359(5)	2.808(5)	105.9(3)
C(4) -- H(4A) .. O(4)	2.384(5)	3.267(5)	138.3(4)
C(11) -- H(11B).. O(3)	2.536(5)	3.569(5)	164.7(4)
C(12) -- H(12A).. O(2)	2.453(5)	3.472(5)	160.9(4)
C(12) -- H(12A).. O(3)	2.446(5)	3.198(5)	127.0(3)
C(12) -- H(12B).. O(2)	2.594(5)	3.172(5)	113.7(3)
C(22) -- H(22C).. O(4)	2.540(5)	3.495(5)	149.4(4)

to a new structure with alternating rows of **5NU** and piperazine (Figure 2.14). Within the tape formed by **5NU**, only D₁ type of N- H...O dimeric bonds are seen in addition to C-H...O type of interactions (H...O, 2.38 Å) involving the nitro groups. This situation is similar to the one shown in Figure 2.10b where D₁ and D₃ dimeric bonds alternate along the molecular tape. The tapes of **5NU** are held in place by the hydrogen bonds from the neighboring tape of piperazine molecules, which do not interact among themselves (Figure 2.14a). There are two sets of C-H...O (H...O, 2.54 Å) and dimeric N-H...N (H...N, 2.05 and 2.49 Å) bonds (see inset of Figure 2.14a) originating from the piperazine molecules that appear rotated in the given perspective. Alternating molecules make linear N-H...O contacts (H...O, 1.94 Å) in addition to bifurcated C-H...O contacts (H...O, 2.45 Å) involving acceptor oxygens from **5NU** (see Table 2.9). The 5-nitrouracil-piperazine layers are connected by dimeric N-H...N bonds as well as by C-H...O bonds, which are considerably weak due to unfavorable bond angles (~ 108°, see Figure 2.14c).

Hydrogen-bonded cocrystal of 5-nitrouracil with N,N'-dimethylpiperazine, 3c

The cocrystal formed between 5-nitrouracil, **5NU** and N,N'-dimethylpiperazine (**3c**), show 2:1 composition comprising a full molecule of **5NU** and a half molecule of where the latter carry the centre of inversion at its geometric centre. Similar to the

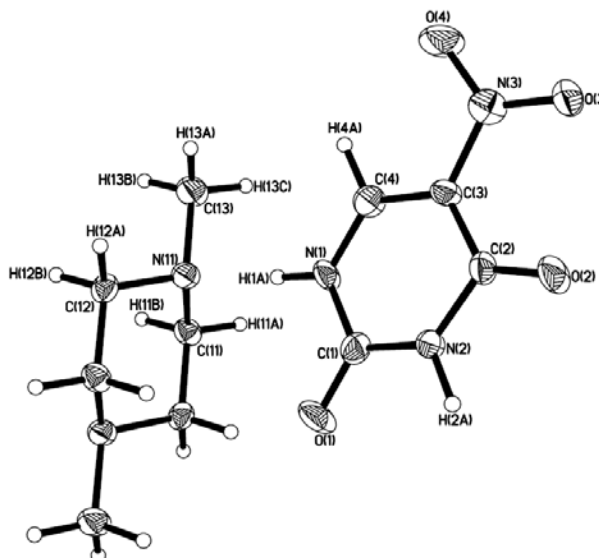


Figure 2.15: ORTEP plot of 5-nitrouracil, 5NU-*N,N'*-dimethylpiperazine, **3c**. Thermal ellipsoids are given at 50% probability.

complex **3b** the complex **3c** also crystallize in triclinic P (-1) space group. The asymmetric unit with numbering scheme is shown in Figure 2.15 and the crystallographic and refinement details are given in the Table 2.7. The C-N single bond lengths in piperazine is given by 1.499(12) Å. A complete list of bond lengths and bond angles (Table A2.11) along with the atomic coordinates and isotropic displacement parameters (Table A2.12) are provided in the Appendix A2.

The cocrystal of 5NU with *N,N'*-dimethylpiperazine (2:1), contains alternating rows of 5NU and dimethylpiperazine (Figure 2.16), an architecture similar to that in the

Table 2.10 Unique set of hydrogen bonds in molecular complexes of 5-nitrouracil, 5NU with *N,N'*-dimethylpiperazine.

H-bond	H...A (Å)	D-A (Å)	D-H...A (°)
N(1) -- H(1A) .. N(11)	1.754(11)	2.754(11)	169.7(11)
N(2) -- H(2A) .. O(1)	1.885(11)	2.857(10)	160.4(12)
C(4) -- H(4A) .. O(4)	2.340(14)	3.290(13)	145.3(12)
C(11) -- H(11A).. O(2)	2.332(13)	3.368(14)	165.2(10)
C(11) -- H(11B).. O(3)	2.504(15)	2.999(14)	107.5(10)
C(12) -- H(12A).. O(2)	2.333(13)	3.355(14)	161.7(10)
C(12) -- H(12B).. O(3)	2.500(16)	2.958(15)	105.0(10)
C(12) -- H(12B).. O(1)	2.504(13)	3.465(12)	150.3(11)
C(13) -- H(13B).. O(2)	2.393(12)	3.409(12)	160.1(9)

cocrystal of **5NU** with piperazine (see Figure 2.14). The main difference is that in the present case, the hydrogen-bonded tape of **5NU** is formed by D2 type of N-H...O dimers (H(2A)...O(1), 1.885(11) Å), alternating with the C-H...O dimers (D3). This bonding pattern may be referred to Figure 2.10c. The central region of the molecule *N,N'*-dimethylpiperazine makes mixed dimeric N-H...N, (H(1A)...N(11), 1.754(11) Å) and C-H...O (H(12B)...O(1), 2.504(13) Å) bonds with **5NU** on either side. In addition, there exists C-H...O interactions from the methyl groups (see Table 2.10). The **5NU**-*N,N'*-dimethylpiperazine layers are held by N-H...N and C-H...O bonds similar to the case in Figure 2.14b.

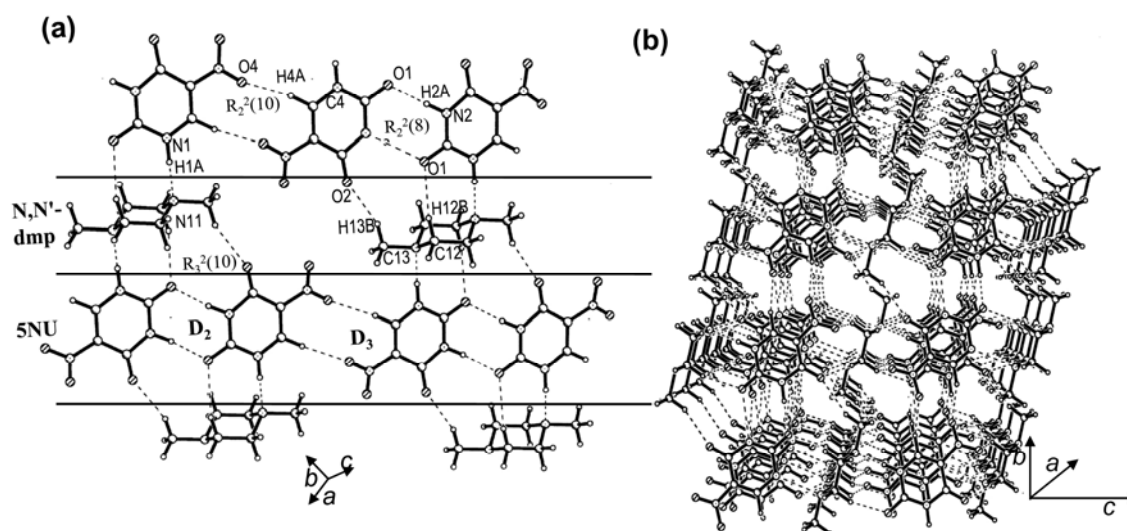


Figure 2.16: Cocrystal of 5-nitrouracil and *N,N'*-dimethylpiperazine, **3c**: (a) A molecular layer showing alternating tapes of **5NU** and *N,N'*-dimethylpiperazine, (b) A packing of alternating **5NU** and *N,N'*-dimethylpiperazine layers in the crystal.

Solvate of 5-nitrouracil with pyridine, **3d**

The crystallization of 5-nitrouracil, **5NU** with pyridine had given a 1:1 solvate, **3d** containing a full molecules of both the molecules as shown in the Figure 2.17. The molecules crystallize in monoclinic P2(1)/c space group. Crystallographic and refinement details of the solvate are given in the Table 2.7. The C-C bond lengths in the molecule pyridine are in the range of 1.358(5) - 1.390(5) Å with the average bond angles $\sim 118.6^\circ$ whereas the average C-N bond lengths are given by 1.325Å where the C-N-C bond angles is 117.6° . Other important bond lengths and bond angles in the molecules are given in the appendix A2 (Table A2.13) and the atom coordinates and isotropic displacement parameters are given in Table A2.14.

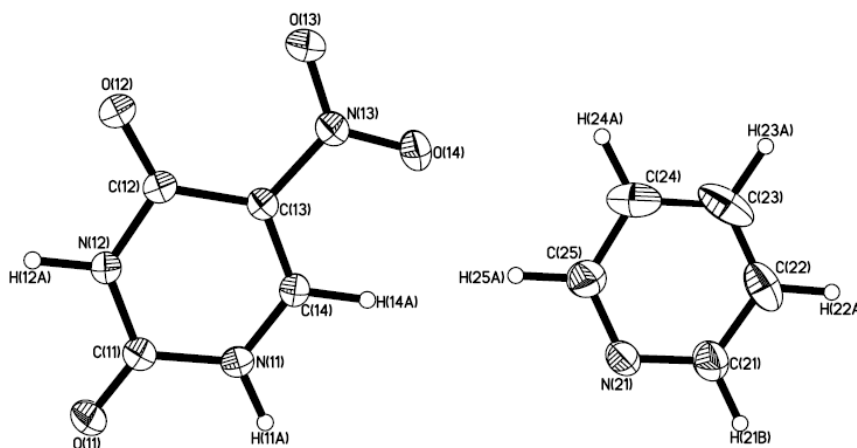


Figure 2.17: ORTEP plot of 5-nitrouracil, 5NU-pyridine solvate, **3d**, Thermal ellipsoids are given at 50% probability.

In the cocrystal of **5NU** with pyridine, there are no cyclic dimeric bonds although the alternating tape structure is retained (Figure 2.18). Thus, the tapes of **5NU** are stabilized by bifurcated N-H...O and C-H...O bonds as shown in Figure 2.10d. The corresponding H...O distances are 2.05 and 2.19 Å for N-H...O and 2.4 Å for C-H...O bonds. The pyridine molecules in the adjacent tape make linear N-H...N (H...N, 1.81 Å) (see Table 2.11) and C-H...O (H...O, 2.22 Å) bonds with the 5-nitrouracil molecules. Pyridine being a strong electron donor, it is not surprising that the characteristic hydrogen-bonded dimeric structure present in the parent crystal (centric form of **5NU**, Ref. 33,34) is destroyed in this cocrystal. Such hydrogen bond breaking ability of good electron donors becomes more evident when we examine the structure of the molecular tapes in the solvate of **5NU** with DMSO²⁸ (also see CCDC - 267379). In this case, the

Table 2.11 Unique set of hydrogen bonds in molecular complexes of 5-nitrouracil with pyridine.

H-bond	H...A (Å)	D-A (Å)	D-H...A (°)
N(11) -- H(11A).. O(12)	2.048(3)	2.786(3)	128.0(2)
N(11) -- H(11A).. O(13)	2.188(3)	3.107(3)	150.4(2)
N(12) -- H(12A).. N(21)	1.810(3)	2.812(3)	171.0(2)
C(14) -- H(14A).. O(12)	2.400(3)	2.956(3)	111.3(2)
C(23) -- H(23A).. O(11)	2.216(4)	3.251(4)	164.9(3)

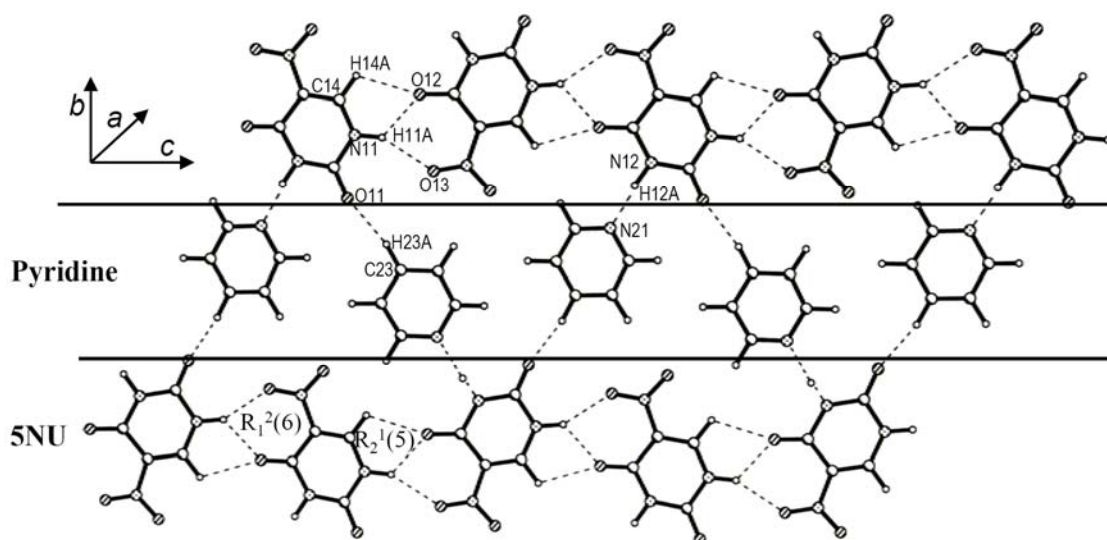


Figure 2.18: Solvate of 5NU with pyridine, **3d**: A molecular layer showing alternating tapes of 5NU and pyridine.

rows of **5NU** are stabilized by C-H...O contacts (H...O, 2.49 Å) along the tape and bifurcated N-H...O bonds originating from the sulfoxide oxygens of DMSO giving rise to a cyclic arrangement, $R_3^2(9)$, similar to Figure 2.10e. The other signature of this bonding pattern is a C-H...O interaction (parallel to N-H...O), involving one of the carbonyl oxygens and a methyl hydrogen. In addition, the sulfur atom of the DMSO seems to interact through a N-H...S contact (H...S, 2.66 Å). The 5-nitrouracil-DMSO layers arrange in a zig-zag manner with the methyl groups of DMSO sticking out in the interlayer region.

Solvate of 5-nitrouracil with formamide, 3e

Figure 2.19 depicts the asymmetric unit of 1:2 solvate, **3e** of 5-nitrouracil, **5NU** with formamide. Crystallographic and refinement details of the solvate are given in the Table 2.7 and a complete list of bond lengths and bond angles present in this adduct is given in the Appendix A2 (Table A2.15). The average C-N and C=O bond lengths in the formamide molecule is given by 1.298(3) Å and 1.227(3) Å. This solvate **3e**, crystallize in monoclinic $P2(1)/c$ space group. Atomic coordinates along with isotropic displacement parameters for the solvate are given in the Appendix A2 (Table A2.16).

All the cocrystals discussed so far, have essentially a layered structure with alternating tapes of **5NU**, the guest molecule being stabilized by different modes of

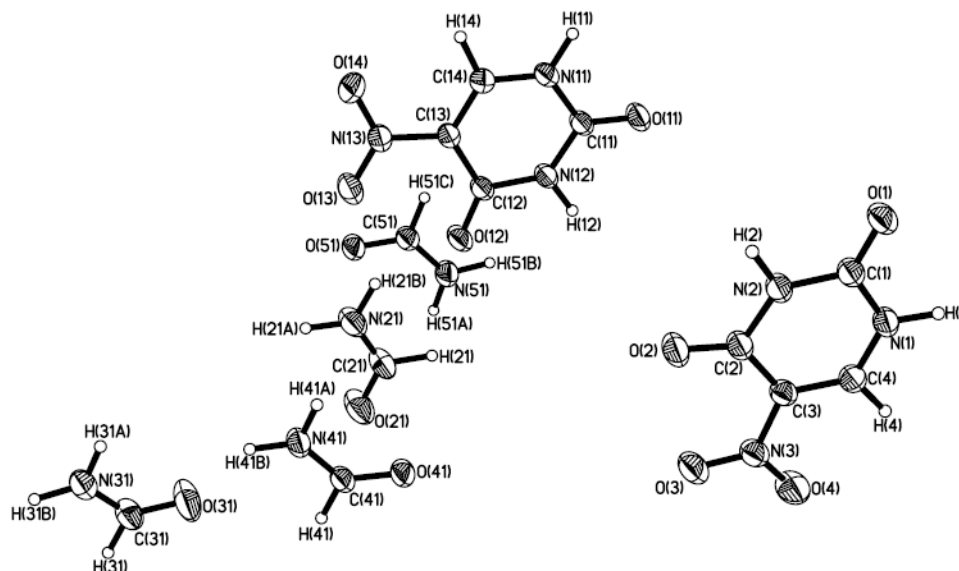


Figure 2.19: ORTEP plot of formamide solvate of 5-nitrouracil, 5NU, 3e, Thermal ellipsoids are given at 50% probability.

hydrogen bonding (Figures 2.10a to e). In the solvate **3e**, the layered structure is retained but the tapes have a mixed composition, comprising both **5NU** and formamide molecules in alternating positions enclosed on either side by rows of formamide molecules (Figure 2.20). The nitrouracil molecules in a tape are rotated with respect to their cousins by 120°

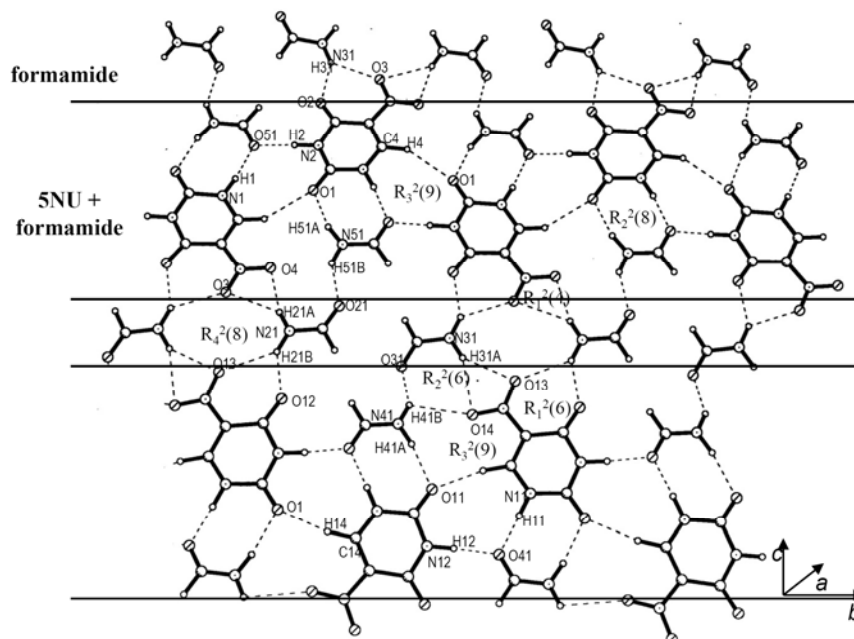


Figure 2.20: formamide solvate of 5-nitrouracil, 3, A molecular layer showing tapes of mixed composition, 5NU and formamide, alternating with formamide tapes.

Table 2.12 Unique set of hydrogen bonds in molecular complexes of 5-nitrouracil, **5NU** with formamide, **3e**.

H-bond	H...A (Å)	D-A (Å)	D-H...A (°)
N(1) -- H(1) .. O(51)	1.741(17)	2.742(2)	170.8(17)
N(2) -- H(2) .. O(51)	1.719(4)	2.728(2)	176(2)
N(11) -- H(11) .. O(41)	1.714(15)	2.724(2)	178.4(18)
N(12) -- H(12) .. O(41)	1.735(5)	2.744(2)	177(2)
N(21) -- H(21A).. O(3)	2.47(2)	3.319(3)	141.4(17)
N(21) -- H(21A).. O(4)	2.40(2)	3.387(3)	166.2(18)
N(21) -- H(21B).. O(12)	2.035(19)	2.923(2)	145.3(19)
N(21) -- H(21B).. O(13)	2.40(2)	3.228(3)	139.0(17)
N(31) -- H(31A).. O(13)	2.38(2)	3.293(3)	149.8(16)
N(31) -- H(31A).. O(14)	2.471(19)	3.429(2)	158.0(17)
N(31) -- H(31B).. O(2)	1.995(18)	2.887(2)	146.0(19)
N(31) -- H(31B).. O(3)	2.29(2)	3.085(3)	135.2(16)
N(41) -- H(41A).. O(11)	2.06(2)	3.059(2)	171.6(19)
N(41) -- H(41B).. O(31)	1.891(19)	2.783(3)	145.4(19)
N(41) -- H(41B).. O(14)	2.49(2)	2.976(3)	108.7(14)
N(51) -- H(51A).. O(1)	2.12(2)	3.082(3)	159(2)
N(51) -- H(51B).. O(21)	1.888(17)	2.771(3)	144.3(19)
C(4) -- H(4) .. O(1)	2.334(13)	3.333(3)	152.2(17)
C(14) -- H(14) .. O(11)	2.222(11)	3.247(3)	156.9(16)

and do not have any direct interaction except for a C-H...O contact (H...O, 2.22 and 2.3 Å). The nitrouracil molecule is bonded to formamide through a cyclic N-H...O dimer (H...O, 1.71 and 2.06 Å), which resembles closely D₂ in Figure 2.10a. It is as though formamide mimics a portion of the nitrouracil molecule. This leads to a highly optimized hydrogen bond pattern with several possible cyclic arrangements, as marked in the figure and illustrated by Figure 2.10f. From the crystal structure, it appears that both DMSO and formamide, which exhibit high dielectric constants can significantly influence the hydrogen bonding pattern in the cocrystal with 5-nitrouracil. Tables 2.12 gives a complete listing of hydrogen bonding present in the solvate **3e**.

Solvate of 5-nitrouracil with ethanol and water, 3f

Figure 2.21 shows the asymmetric unit of the solvate formed on crystallization of 5-nitrouracil, **5NU**, from a solvent mixture of ethanol and water (**3f**). The solvate incorporates water molecule along with ethanol molecules in the crystal lattice and crystallize in monoclinic P2(1)/c space group with a 2:2:1 molecular composition. The

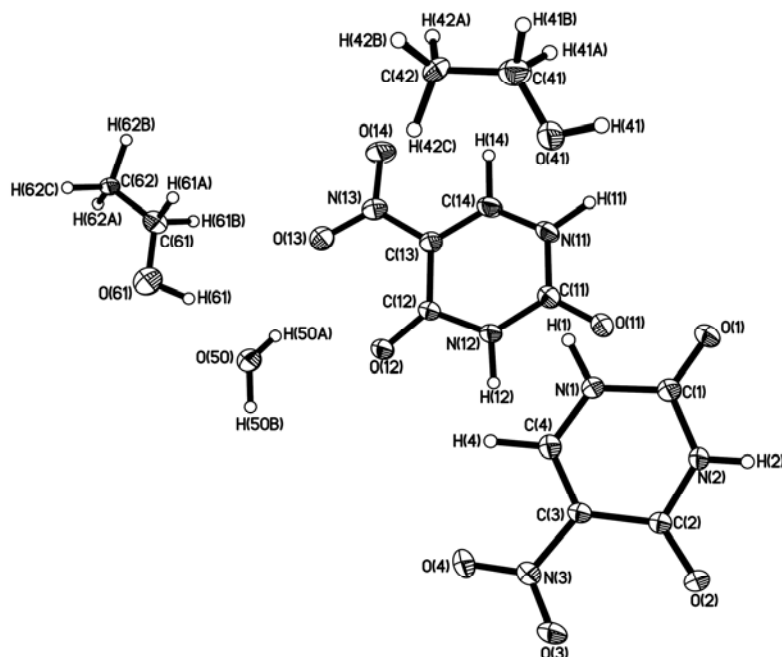


Figure 2.21: ORTEP plot of 5-nitrouracil-ethanol, **5NU** and water, **3f**, Thermal ellipsoids are given at 50% probability.

crystallographic and refinement detail for the solvate is provided in the Table 2.7. The average C-C bond lengths for the ethanol molecule in this adduct is given by 1.297(7) Å and whereas that for C-O bond is 1.269 (6) Å. The detailed list of bond lengths and bond angle is provided in Appendix A2 (Table A2.17) and atomic coordinates along with isotropic displacement parameters are given in Table A2.18.

The molecular packing in the solvate of **5NU** with ethanol and water bears some resemblance to the structures described earlier. It forms a layered structure, with each layer containing alternating molecular tapes of **5NU** -ethanol and **5NU**-ethanol-water (Figure 2.22). The molecular arrangement in the **5NU** -ethanol tape is similar to that of **5NU** - formamide in Figure 2.20 (Figure 2.10f). The bonding in the **5NU**-ethanol-water tape is, however, different. Here, pairs of nitrouracils molecules are bonded through dimeric N-H...O bonds (D_1) besides four O-H...O bonds (H...O, 1.86-2.32 Å) induced by two water molecules from strategic positions, thus forming a set of parallel-antiparallel bonding arrangement. A similar bonding pattern has been observed for a monohydrate of 5-nitrouracil.³⁴ This is also similar to quadruple hydrogen bond pattern found usually in copolymer and peptide structures.³⁵⁻³⁷ The two tape structures alternate in a layer with C- H...O bonds from the methyl group connecting them. Interlayer

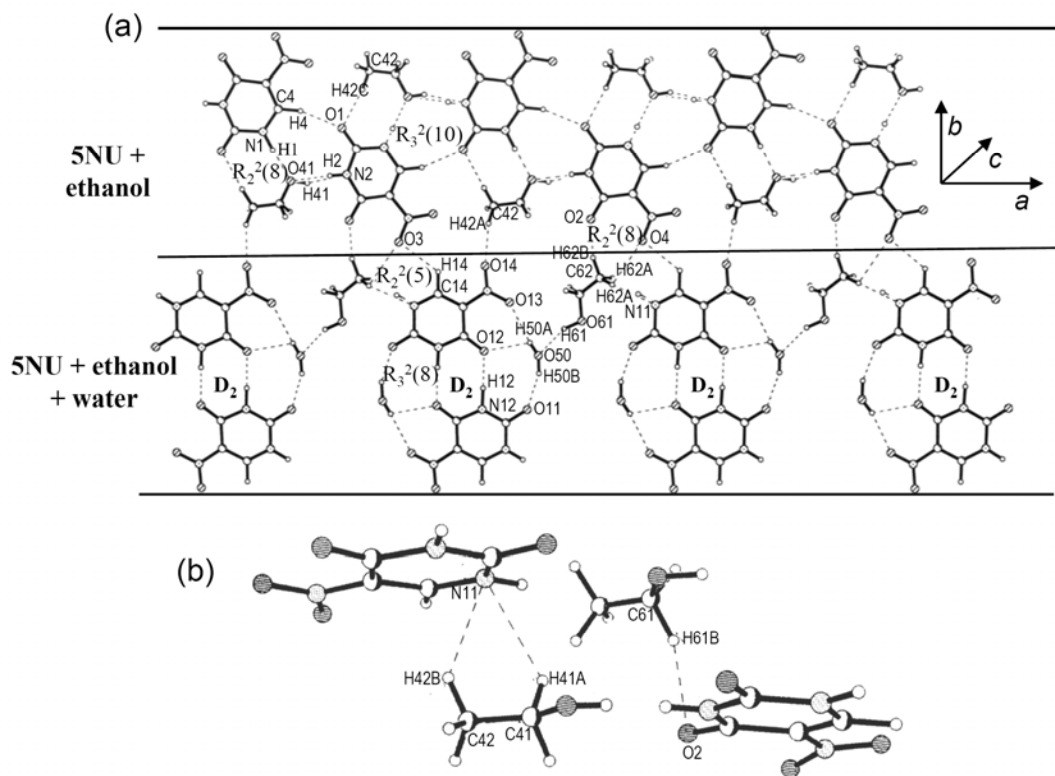


Figure 2.22: Solvate of 5NU with ethanol and water, **3f**, (a) A molecular layer showing tapes of mixed compositions- tapes containing 5NU and ethanol alternating with those containing 5NU, ethanol and water (b) Hydrogen bonding between the layers.

contacts are of the type, C-H...O and C-H...N (H...O, 2.32 Å; H...N, 2.51 and 2.61 Å). Table 2.13 provides a complete list of hydrogen bonding interactions present in this solvate of 5-nitrouracil.

Table 2.13 Unique set of hydrogen bonds in molecular complexes of 5-nitrouracil with ethanol and water.

H-bond	H...A (Å)	D-A (Å)	D-H...A (°)
N(1)-H(1)...O(41)	1.740(5)	2.748(5)	174.3(4)
N(2)-H(2)...O(41)	1.963(5)	2.821(5)	175.0(4)
N(12)-H(12)...O(12)	1.861(5)	2.871(5)	178.5(4)
O(41)-H(41)...N(2)	2.045(5)	2.821(5)	157.9(4)
O(50)-H(50A)...O(12)	2.32(11)	2.732(5)	113(8)
O(50)-H(50A)...O(13)	2.26(10)	2.962(6)	148(8)
O(50)-H(50B)...O(11)	1.92(7)	2.835(6)	160(5)
O(61)-H(61)...O(50)	1.864(6)	2.775(5)	157.6(4)
C(4)-H(4)...O(1)	2.196(6)	3.247(6)	162.2(5)
C(14)-H(14)...O(3)	2.445(6)	3.226(6)	127.8(4)
C(41)-H(41A)...N(11)	2.353(6)	3.168(6)	132.6(5)

Table 2.13 (continued)

C(41)-H(41B)...N(11)	2.614(6)	3.418(6)	132.2(4)
C(42)-H(42A)...O(14)	2.45(2)	3.037(6)	113.9(17)
C(42)-H(42B)...N(11)	2.509(7)	3.383(5)	139.1(5)
C(42)-H(42C)...O(1)	2.123(12)	3.108(6)	153.6(18)
C(61)-H(61A)...O(4)	2.317(6)	3.231(6)	143.5(5)
C(61)-H(61B)...O(2)	2.324(6)	3.215(6)	140.7(5)
C(62)-H(62A)...N(11)	2.627(17)	3.009(6)	100.6(10)
C(62)-H(62B)...O(2)	1.852(9)	2.883(5)	163.4(6)
C(62)-H(62C)...N(11)	2.492(17)	3.009(6)	109.0(13)

Hydrogen-bonded cocrystal of 5-nitrouracil with 3-aminopyridine, **3g**

Figure 2.23 shows the asymmetric unit of the 1:1 molecular complex formed by 5-nitrouracil with 3-aminopyridine. This complex crystallizes in a monoclinic $P2(1)/c$ space group with two complete molecules. In this complex the 3-aminopyridine exists in a protonated form at the ring nitrogen atom N(11). The average C-N bond lengths with aromatic ring and $-NH_2$ in 3-aminopyridine is 1.362(8) Å. The average C-C (aromatic) lengths in 3-aminopyridine is 1.368 (7) Å. All the bond lengths and bond angles present complex **3g** are provided in the Appendix Table 1.19. Atomic coordinates and isotropic displacement parameters for the cocrystal are given in Table A2.20.

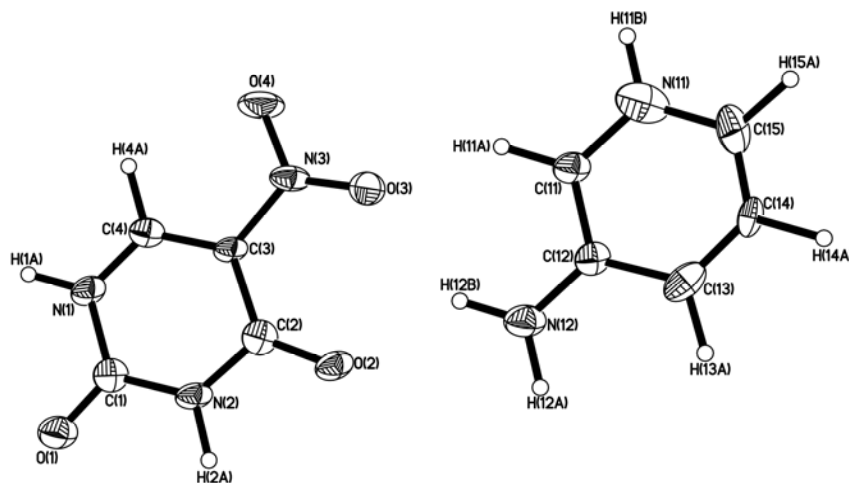


Figure 2.23: ORTEP plot of cocrystal (1:1) of 5-nitrouracil with 3-aminopyridine, **3g**, Thermal ellipsoids are given at 50% probability.

Figure 2.24 shows the packing in the cocrystal of **5NU** with 3-aminopyridine, where it can be readily identified the bonding motif of Figure 2.22, albeit with a

difference. Due to the presence of the amino group from 3-aminopyridine, the bonds belonging to the parallel-antiparallel arrangement are of N-H...O type (H...O, 1.91 and 1.92 Å), involving the D₁ motif. It can be also noticed that bifurcated N-H...O and C-H...O bonds connect adjacent 5NU and 3-aminopyridine, much like in the 5NU-pyridine solvate (Figure 2.18 and Figure 2.10d). Unlike the cocrystal structures discussed so far,

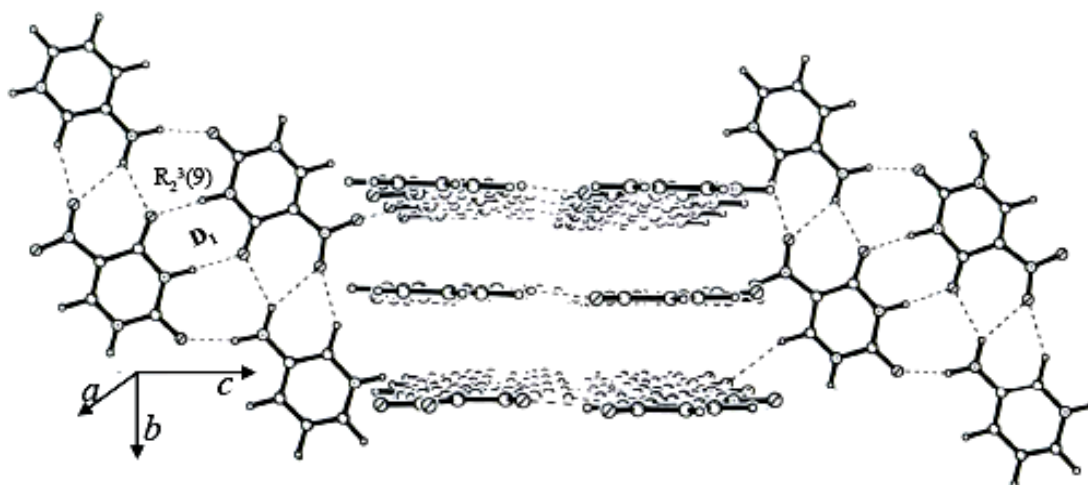


Figure 2.24: Cocrystal of 5-nitrouracil and 3-aminopyridine, **3g**: Stacks of molecular tapes arranged in alternating parallel and perpendicular orientations.

the molecular tapes in this structure do not extend sidewise into infinite layers but instead allow similar tapes to stack perpendicularly as depicted in the figure. The two systems of tapes are bonded though C-H...O interactions (H...O, 2.51 Å).

Table 2.14 Unique set of hydrogen bonds in molecular complexes of 5-nitrouracil, 5NU with 3-aminopyridine.

H-bond	H...A (Å)	D-A (Å)	D-H...A (°)
N(2) -- H(2A) ..O(2)	1.919(7)	2.922(7)	172.1(6)
N(12) -- H(12A)..O(1)	1.908(7)	2.894(7)	164.4(6)
N(12) -- H(12B).. O(2)	2.172(7)	2.979(8)	135.7(5)
N(12) -- H(12B).. O(3)	2.268(8)	3.160(8)	146.5(5)
C(4) -- H(4A) .. O(4)	2.509(8)	3.536(8)	157.4(6)
C(11) -- H(11A).. O(3)	2.182(9)	3.137(9)	145.6(5)
C(14) -- H(14A).. O(1)	2.418(9)	3.310(9)	138.6(7)
C(14) -- H(14A).. N(1)	1.774(8)	2.804(8)	156.9(7)
C(15) -- H(15A).. O(4)	2.345(9)	3.402(9)	164.4(7)

Hydrogen-bonded cocrystal of 5-nitrouracil with Diaza [2.2.2.] bicyclooctane, (DABCO), 3h

The cocrystal formed between 5-nitrouracil and Diaza [2.2.2.] bicyclooctane, DABCO and water (2:2:5) fall in different group compared to the previously cocrystals of 5-nitrouracil with other molecules and solvates. This is because of the structural difference of this cocrystal with a three dimensional architecture. Figure 2.25 depicts the asymmetric unit of the cocrystal with its components 5-nitrouracil, DABCO and water of

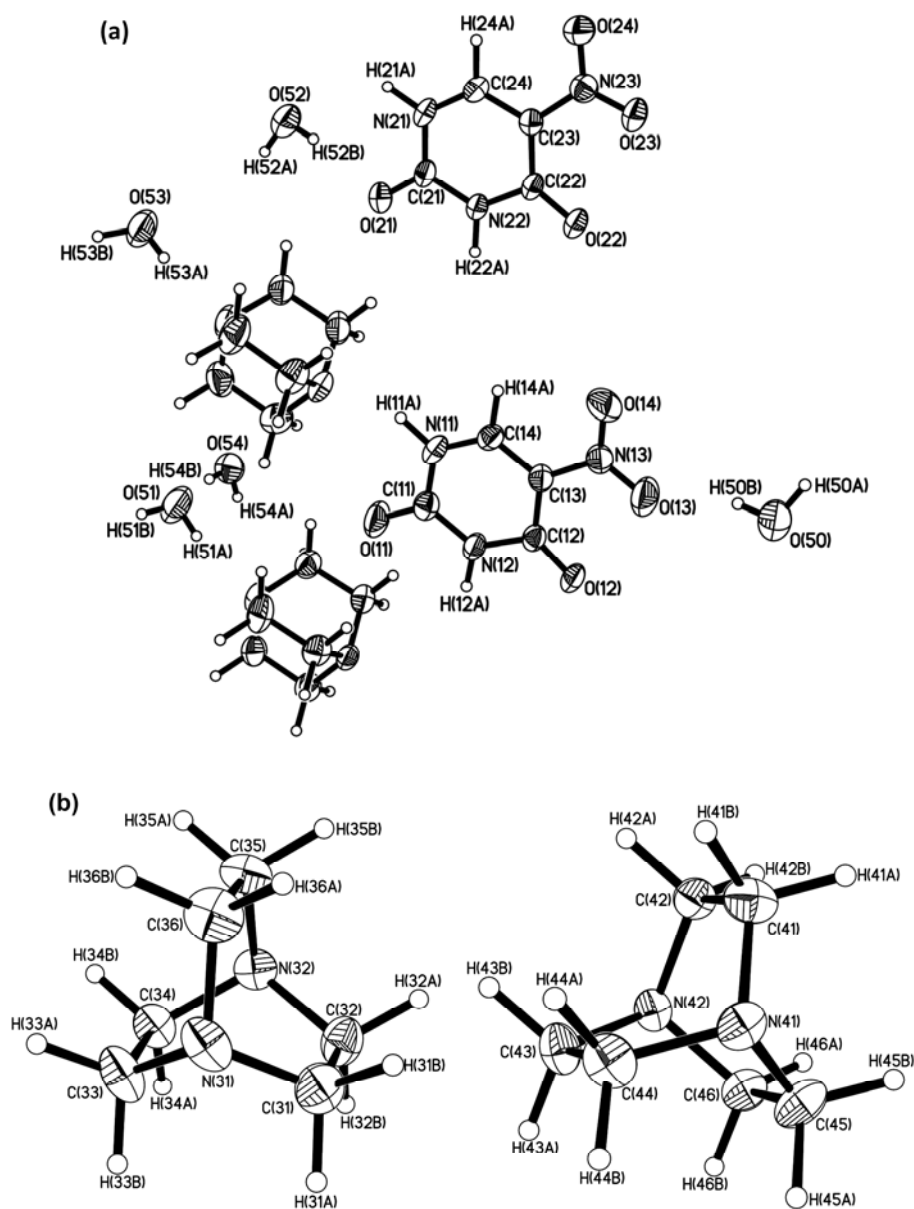


Figure 2.25: (a) ORTEP plot of 5-nitrouracil- DABCO, **3h** (b) labeling scheme for DABCO molecules. Thermal ellipsoids are given at 50% probability.

crystallization. The average bond lengths for C-N and C-C bonds in **DABCO** are 1.479(4) Å and 1.525(5) Å respectively. The average C-N-C bond angles in **DABCO** are 109.2 (3)°. The average C=O bond lengths in molecule **5NU** are given by 1.231 Å whereas that for that for the C-N bonds are 1.364 (4) Å. A detailed list of bond lengths and bond lengths are given in the Appendix (Table A2.21) along with the atomic coordinates and isotropic displacement parameters (Table A2.21).

Another example for 3D-stacking of molecules is the cocrystal of **5NU** with diazabicyclo [2.2.2] octane, **DABCO** and water (molar composition, 2:2:5), as shown in Figure 2.26. The structure contains cyclic dimers of nitrouracil (see inset of Figure 2.26) formed through N-H...O interactions (H...O, 1.88 and 2.19 Å), arranged in the form of parallel set of tapes. The nitrouracil tapes are held between sheets of the **DABCO**

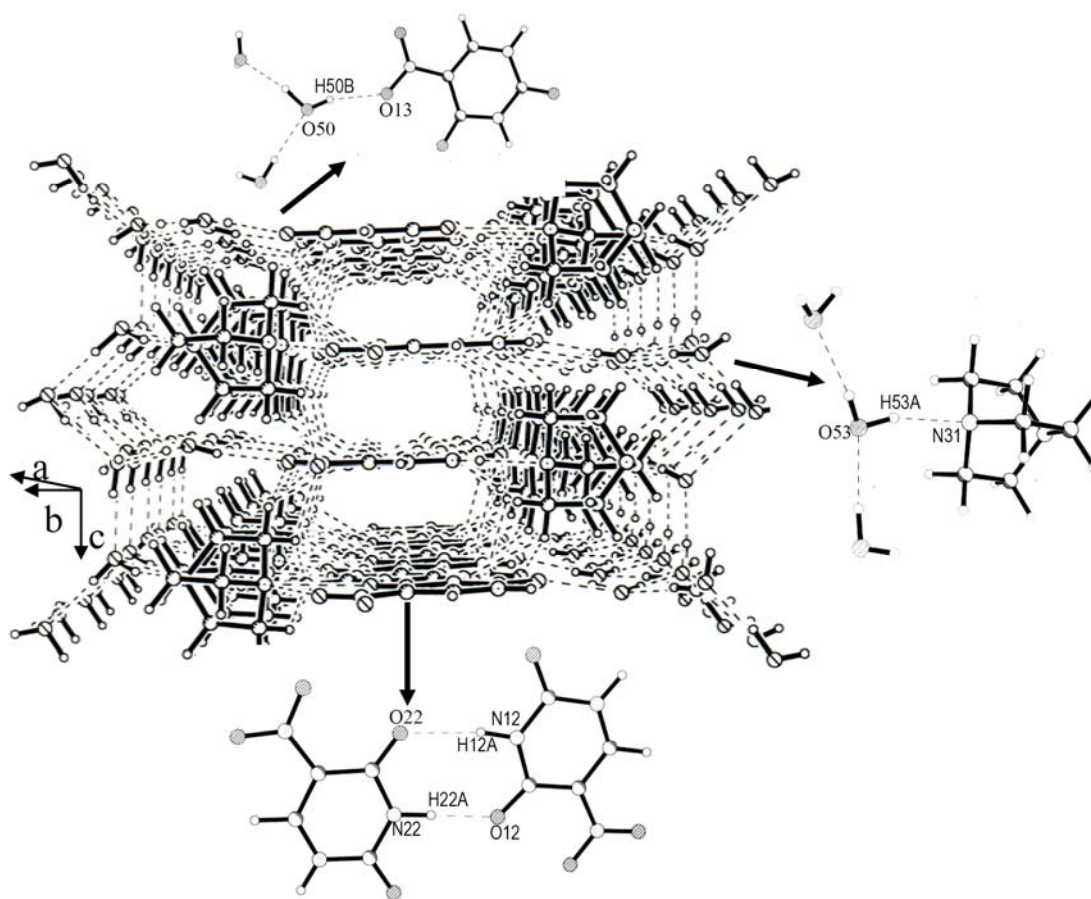


Figure 2.26: Cocrystal of **5NU** and **DABCO**, **3h**: A view along the diagonal of the *ab* plane showing the supramolecular assembly. Insets show a 5-nitrouracil dimer and hydrogen bonding between water with **DABCO** and **5NU**.

molecules, which in turn are covered by layers of water molecules. These supramolecular assemblies get rotated along the *a* axis by 90° alternately. There is extensive hydrogen bonding between DABCO and nitrouracil (N-H...N, 1.94 Å, C-H...N, 2.42 and 2.52 Å, C-H...O, 2.45 – 2.57 Å), water and DABCO (O-H...N, 1.98 Å) as well as water and nitrouracil (O-H...O, 2.06 and 2.11 Å). The donor-H-acceptor angles are generally favorable, N-H...N (153°), O-H...N (162°-163°), O-H...O (161°-178°) and C-H...N (145°). There are also some C-H...O interactions, with the angle in the 118°-152° range.

Table 2.15 Unique set of hydrogen bonds in molecular complexes of 5-nitrouracil, **SNU** with diazabicyclo [2.2.2] octane and water.

H-bond	H...A (Å)	D-A (Å)	D-H...A (°)
N(11) -- H(11A).. N(32)	1.940(4)	2.881(4)	153.9(3)
N(12) -- H(12A).. O(22)	2.189(3)	3.189(3)	170.6(2)
N(22) -- H(22A).. O(12)	1.878(3)	2.885(3)	174.6(3)
O(50) -- H(50A).. O(54)	1.81(7)	2.778(5)	170(6)
O(50) -- H(50B).. O(13)	2.06(6)	2.884(5)	161(7)
O(51) -- H(51A).. N(41)	1.98(6)	2.856(5)	162(5)
O(51) -- H(51B).. O(50)	1.98(6)	2.826(5)	171(5)
O(52) -- H(52A).. O(54)	1.97(6)	2.831(5)	164(5)
O(52) -- H(52B).. O(21)	2.11(5)	2.883(4)	172(5)
O(53) -- H(53A).. N(31)	1.98(6)	2.849(4)	163(6)
O(53) -- H(53B).. O(52)	1.85(5)	2.851(5)	178(5)
O(54) -- H(54A).. O(53)	1.94(6)	2.752(5)	172(5)
O(54) -- H(54B).. O(51)	1.86(6)	2.732(5)	170(5)
C(34) -- H(34A).. O(12)	2.511(4)	3.175(4)	118.1(3)
C(34) -- H(34A).. O(13)	2.566(5)	3.531(5)	146.9(3)
C(34) -- H(34B).. O(24)	2.535(4)	3.537(4)	121.9(3)
C(35) -- H(35B).. N(21)	2.523(5)	3.472(5)	144.6(3)
C(42) -- H(42A).. N(21)	2.427(4)	3.380(5)	145.0(3)
C(42) -- H(42B).. O(11)	2.448(5)	3.273(4)	131.3(3)
C(42) -- H(42B).. O(14)	2.495(4)	3.160(4)	118.2(3)
C(46) -- H(46A).. O(11)	2.464(5)	3.292(5)	131.6(3)
C(46) -- H(46B).. O(12)	2.495(4)	3.167(4)	118.6(3)

The significant aspect of this supramolecular system is the structure of the water layer, consisting of a well-defined, isolated network of hydrogen-bonded acyclic pentamers as shown in Figure 2.27. This is yet another example of a supramolecular assembly hosting acyclic pentamer clusters of water.³⁸⁻⁴² The tetrahedral pentameric unit corresponds exactly to that described by Walrafen,^{43, 44} involving a central H₂O molecule

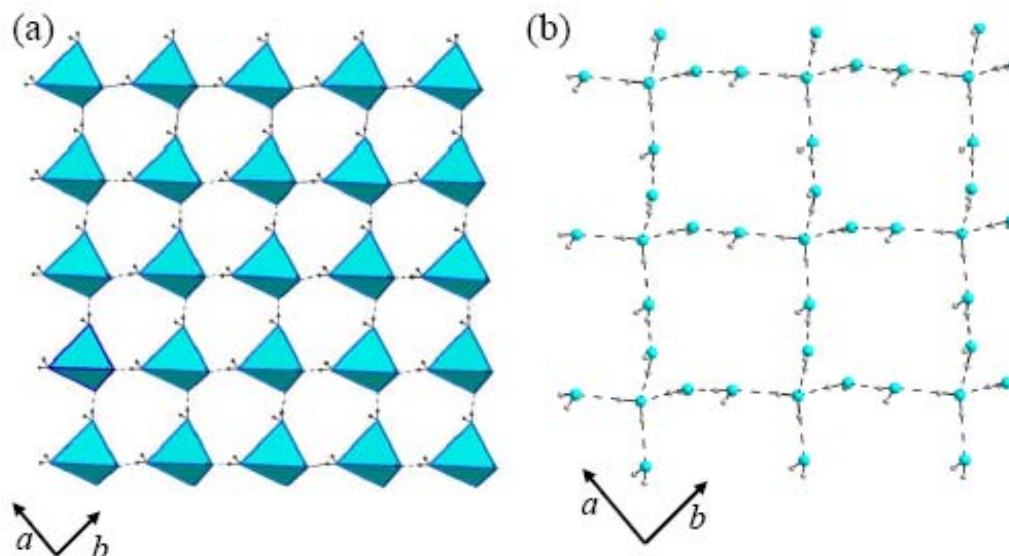


Figure 2.27: (a) Tetrahedral pentamers of water in the *ab*-plane forming a nearly square arrangement (b) Hydrogen bonded network in the water layer.

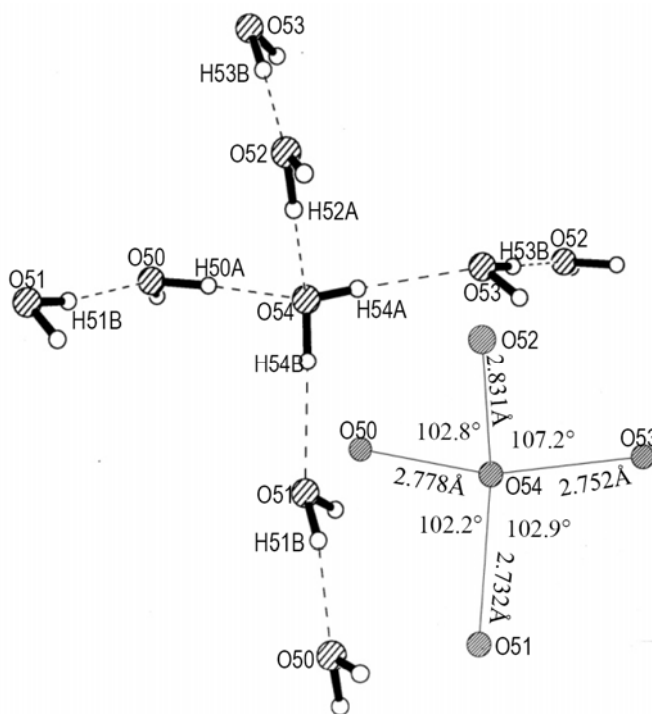


Figure 2.28: A tetrahedron pentamer of water. The O...O distances and H-OH angles are indicated in the inset.

where the two hydrogen donors of the central molecule engage two water molecules, while the two lone-pairs of the oxygen act as acceptors bringing in two more water molecules (Figure 2.28). The O...O distances are in the 2.73 – 2.83 Å range, comparable

to the values obtained by *abinitio* calculations on water oligomers.^{45, 46} Three of the H-O-H angles involving the central molecule are within 0.4° of the average value of 102.6°, while the other H-O-H angle, extended from the outer proton donors, is 107.2° due to lone-pair lone-pair repulsion. Besides the hydrogen bonds with the central molecule, the hydrogens of the molecules at the tetrahedral corners bond alternatively to DABCO and nitrouracil molecules above and below the water layer. It appears as though the tetrahedral pentamers are formed to stabilize the water molecules bonded to DABCO and 5-nitrouracil molecules. The tetrahedral pentamers in the water layer are arranged in a nearly square lattice in the *ab* plane, with basis vectors of 6.58 and 6.78 Å, rotated with respect to the parent lattice by ~45° (Figure 2.26b). The tetrahedral units are connected to one another through a O-H...O bonds with O...O distances of 2.83 and 2.85 Å in the two directions, which are slightly longer than those found inside the tetrahedra (see Figure 2.28). The array of water molecules in Figure 2.27b can be described as a network of cyclic dodecameric species sharing the four edges.

2.5 Conclusions

This study brings out the results of hydrogen bonding possibilities of molecules uracil, cytosine and 5-nitrouracil with various solvents and other compounds by deliberate inclusion. The structural analysis of the adduct formed by melamine with uracil illustrates the molecular recognition process of nucleobase uracil and also establishes the presence of channels, in the three-dimensional supramolecularly hydrogen-bonded structure. The study on 1:1 complexes of cytosine with trimesic and pyromellitic acids has clearly brought out a molecular recognition process facilitated by proton-transfer interactions. Both complexes possess layered structures with various N-H...O and O-H...O hydrogen bonding interactions, involving several cyclic patterns. The interlayer distance is uniformly 3.98 Å in cytosine-pyromellitic acid complex, while in cytosine-trimesic acid complex, there exists a bilayer structure with 2.87 Å separation.

The study of the cocrystals of 5-nitrouracil, **5NU**, brings out clearly the high propensity of the molecule in forming interesting hydrogen bond patterns. Of the several cocrystals investigated in this category, all except those involving 3-aminopyridine exhibit layered structures with layers comprising two different compositions. In the cocrystals of **5NU** with piperazine, N,N'-dimethylpiperazine, diazabicyclo[2.2.2]octane,

pyridine and DMSO, tapes of **5NU** alternating with rows of the partner molecule occur, while in other cocrystals with formamide and ethanol, the molecular tapes exhibit mixed compositions. In the cocrystal of **5NU** with dioxane, the hydrogen bonding pattern of **5NU** is somewhat modified compared to the parent centric structure, where instead of tapes, dimers of **5NU** are present. Here, cyclic N-H...O dimeric bonds (alternating D₁ and D₂) are seen on either side of the molecule (Figure 2.10a). In some cases, dimeric C-H...O bonds (D₃) are seen alternating with D₁ (**5NU** - piperazine) or D₂ (**5NU** - N,N'-dimethylpiperazine) as in Figure 2.10b and c. A new type of bonding pattern is seen in the cocrystal of **5NU** with pyridine involving zig-zag arrangement of a linear C-H...O and bifurcated N-H...O bonds (Figure 2.10d). Cocrystals with DMSO and formamide exhibit tapes of **5NU** where bonding between adjacent nitrouracil molecules involves acceptor oxygen from the partner molecule (Figure 2.10e and f). Another interesting feature of these cocrystals is the presence of a quadruple-like hydrogen bonding pattern involving either O-H...O (**5NU** -ethanol-water) or N-H...O (**5NU** -3-aminopyridine) bonds. The presence of a network of acyclic tetrahedral pentamers of water in the cocrystal of **5NU** with diazabicyclo[2.2.2]octane is also a novel finding.

References

1. J. M. Lehn, *Supramolecular Chemistry: Concepts and Perspectives*, VCH, Weinheim, (1995).
2. E. Fischer, *Ber. Dtsch. Chem. Ges.*, (1894), **27**, 2985.
3. (a) G. M. Whitesides, E. E. Simanek, J. P. Mathias, C. T. Seto, D. N. Chin, M. Mammen, D. M. Gordon, *Acc. Chem. Res.*, (1995), **28**, 37. (b) J. C. MacDonald, G. M. Whitesides, *Chem. Rev.*, (1994), **94**, 2383.
4. G. R. Desiraju, *Angew. Chem. Int. Ed.*, (1995), **34**, 2311.
5. T. Steiner, *Angew. Chem. Int. Ed.*, (2002), 4148.
6. C.S. Lai, F. Mohr, E. R. T. Tiekink, *CrystEngComm*, (2006), **8**, 909.
7. G. Cooke, V.M. Rotello, *Chem. Soc. Rev.*, (2002), **5**, 275.
8. J. M. Adams, R. G. Pritchard, J. M. Thomas, *J. Chem. Soc. Chem. Commun.*, (1976), 358.
9. D. D. MacNicol, F. Toda, R. Bishop (Eds.), *Comprehensive Supramolecular Chemistry*, Vol. 6, Pergamon, New York, 1996.
10. (a) M. Lahav, G. M. J. Schmidt, *J. Chem. Soc. B*, (1967), 239; (b) J. Hulliger, *Angew. Chem. Int. Ed.*, (1994), **33**, 143; (c) L. R. MacGillivray, J. L. Reid, J. A. Ripmeester, *J. Am. Chem. Soc.*, (2000), **122**, 7817; (d) F. Guo, K. D. M. Harris, *J. Am. Chem. Soc.*, (2005), **127**, 7314; (e) J. L. Atwood, J. E. D. Davies, D. D. MacNicol, F. Vogtle, *Comprehensive Supramolecular Chemistry*, Pergamon, Oxford, 1996. (f) J. M. Lehn, *Angew. Chem. Int. Ed.*, (1990), **29**, 1304; (g) K. Biradha, *CrystEngComm*, (2003), **5**, 374; (h) R. P. Sijbesma, E. W. Meijer, *Chem. Commun.*, (2003), 5; (i) G. R. Desiraju, *Nature*, (2001), **412**, 397; (j) M. D. Hollingsworth, *Science*, (2002), **295**, 2410; (k) C. B. Aakeroy, J. Desper, J. F. Urbina, *Chem. Commun.*, (2005) 2820; (l) L. E. Cheruzel, M. S. Mashuta, R. M. Buchanan, *Chem. Commun.*, (2005) 2223.
11. J. L. Atwood, J. W. Steed, *Encyclopedia of Supramolecular Chemistry - volume 1*, CRC Press, London, UK, (2004)
12. T. M. Fyles, C. C. Tong, *New J. Chem.*, (2007), **31**, 655.
13. (a) J. D. Hartgerink, J. R. Granja, R. A. Milligan, M. R. Ghadiri, *J. Am. Chem. Soc.*, 1996, **118**, 43; (b) K. Lu, L. Guo, A. K. Mehta, W. S. Childers, S. N.

- Dublin, S. Skanthakumar, V. P. Conticello, P. Thiyagarajan, R. P. Apkarian, D. G. Lynn, *Chem. Comm.*, 2007, 2729; (c) X. Zhao, S. Zhang, X. Zhao, S. Zhang, *Macromol. Bioscie.*, (2007), **7**, 13.
14. P.F. Barbara, *Acc. Chem. Res.*, (2001), **34**, 409 and the entire articles in the same issue.
15. C. G. Wermuth, N. Koga, Medicinal Chemistry for the 21st Century: a chemistry for the 21st century monograph, International Union of Pure and Applied Chemistry, Blackwell Scientific Publications, University of Michigan (1992)
16. S. Bauer, S. Pigisch, D. Hangel, A. Kaufmann, S. Hamm, *Immunobiology*, (2008), **213**, 315.
17. S. Sivakova, S.J. Rowan, *Chem. Soc. Rev.*, (2005), **34**, 9.
18. (a) M. Ohki, A. Takenaka, H. Shimanouchi, Y. Sasada, *Bull. Chem. Soc. Jpn.*, (1975), **48**, 848; (b) A. Takenaka, Y. Sasada, *Bull. Chem. Soc. Jpn.*, (1982), **55**, 680; (c) S. Fujitha, A. Takenaka, Y. Sasada, *Bull. Chem. Soc. Jpn.*, (1983), **56**, 2234.
19. S.R. Perumalla, E. Suresh, V. R. Pedireddi, *Angew. Chem. Int. Ed.*, (2005), **44**, 7752.
20. A. Ranganathan, V. R. Pedireddi, C. N. R. Rao, *J. Am. Chem. Soc.* (1999), **121**, 1752.
21. J. C. McDonald, G. M. Whitesides, *Chem. Rev.*, (1994), **94**, 2383.
22. A. Ranganathan, V. R. Pedireddi, G. Sanjayan, K. N. Ganesh, C. N. R. Rao, *J. Mol. Str.*, (2000), **522**, 87.
23. V. R. Pedireddi, S. Chatterjee, A. Ranganathan, C. N. R. Rao, *J. Am. Chem. Soc.*, (1997), **119**, 10867.
24. Tinaco I, Gesteland RF, Atkins JF: *The RNA World*, Cold Spring Harbour Laboratory Press, Cold Spring Harbor: 1993.
25. (a) O. Felix, M.W. Hosseini, A. D. Cian, J. Fischer, *Chem. Commun.*, (2000), 218; (b) O. Felix, M.W. Hosseini, A. D. Cian, J. Fischer, *Angew. Chem. Int. Ed.*, (1997), **36**, 102.

26. C. C. Evans, M. B. Beucher, R. Masse, J. –F. Nicoud, *Chem. Mater.*, (1998) **10**, 847.
27. P. Srinivasan, T. Kanagasekaran, R. Gopalakrishnan, G. Bhagavannarayana, P. Ramasamy, *Cryst. Growth Des.*, (2006), **6**, 1663.
28. R. Kennedy, M. O. Okoth, D. B. Sheen, J. N. Sherwood, K. M. Vrcelj, *Acta Crystallogr Sect. C* (1998), **54**, 547.
29. R. S. Gopalan, G. U. Kulkarni, C. N. R. Rao, *ChemPhysChem*, (2000), **1**, 127.
30. M.C. Etter, *Acc. Chem. Res.*, (1990), **35**, 566.
31. R. J. McClure, B. M. Craven, *Acta Cryst. Sect. B*, (1973), **29**, 1234.
32. M. Eisenstein, *Acta Cryst. Sect. B*, (1988), **44**, 412.
33. B. M. Craven, *Acta Cryst.* (1967), **26**, 376.
34. G. B. W. Ligthart, H. Ohkawa, R. P. Sijbesma, E. W. Meijer, *J. Am. Chem. Soc.*, (2005), **127**, 810.
35. B. Umadevi, P. Prabhakaran, P. T. Muthiah, *Acta Cryst. C*, (2002), **58**, 510.
36. G. Cooke, V. M. Rotello *Chem. Soc. Rev.*, (2002) **31**, 275.
37. D. E. Lynch, I. McClenaghan, *Acta Cryst. Sect. E*, (2002), **58**, 1150.
38. A. M. Galibert, O. Cortadellas, B. Soula, B. Donnadieu, P. –L. Fabre: *J. Chem. Soc. Dalton Trans.*, (2002) 3743.
39. D. Mootz, H. –G. Wussow, *J. Chem. Phys.*, (1981), **75**, 1517.
40. Y. –Q. Zheng, F. Y. –W. Sun, *Z. Kristallogr.-New Cryst. Struct.*, (2003), **218**, 221.
41. Audebrand, S. Raite, D. Louer,: *Sol. Stat. Sci.*, (2003), **5**, 783.
42. J. N. Low, S. N. Scrimgeour, C. Egglshaw, R. A. Howie, M. N. Moreno-Carretero, F. Hueso-Urena: *Acta Cryst. C*, (1994), **50**, 1329.
43. G. E. Walrafen, *J. Chem. Phys.*, (1964), **40**, 3249.
44. G. E. Walrafen, W. H. Yang, Y. C. Chu, M. S. Hokmabadi, *J. Phys. Chem.*, (1996), **100**, 1381.
45. R. Ludwig, *Angew. Chem. Int. Ed.*, (2001), **40**, 1808.
46. K. Hermansson, *J. Chem. Phys.*, (1987), **89**, 2149.

**UNDERSTANDING THE WEAK INTERACTIONS IN ALKYOXY
SUBSTITUTED OLIGO(PHENYLENE-ETHYNYLENE)S AND
THEIR EFFECT ON THE SOLID STATE FLUORESCENCE
PROPERTIES***

Summary

This chapter deals with synthesis, structure and analysis of weak supramolecular interactions in dialkyloxy substituted oligo(phenyleneethynylene)s. In addition, this study investigates the dependence of solid state fluorescence properties of these molecules with change in molecular packing in crystals and cooling rate during the formation of thin films from the melt. The intermolecular interactions present in these compounds are weak in nature and include C-H $\cdots\pi$ interactions with the aromatic rings or with the triple bonds as well as the chain-chain interactions involving the alkyl chains. These molecules show change in planarity of the phenyleneethynylene back bone depending on the alkyl chain length. The highest twist from the planarity is observed in the molecule with methoxy substitution. The deviation from planarity in the molecules improves the ability of the triple bond to participate in various C-H $\cdots\pi$ interactions by diminishing the conjugation in the molecules. In addition to the variation from the molecular planarity, these molecules exhibit in-plane lifting and out of plane bending of the phenyleneethynylene backbone which is an after effect of their involvement in C-H \cdots O interactions with the alkyloxy oxygen atom. In the solution phase, all the molecules exhibit fluorescence with maximum intensity around 400 nm. Their solid state emission properties are however varied being dependent on the length of the alkyloxy chain. In the solid state, the presence of electronic coupling between the molecules leads to a red- shifted emission, the shift being proportional to the distance between the interacting molecules (J-aggregate). All the

*Manuscripts based on these studies are under preparation

molecules show a high fluorescence quantum yield in the solid state, range from 0.3 to 0.8, with a maximum error of 3% in reproducibility. A melt cooling study in methoxy substituted oligo(phenyleneethynylene) have shown a cooling rate dependence on the solid state emission properties of this molecule. This study has established a close relation between fluorescence emission and the preferred orientation of the crystallites on the glass substrate.

3.1 Introduction

Conjugated oligomers and polymers are of great interest in current research scenario due to their interesting electronic and photophysical properties.¹ Recent literature covers numerous reports on synthesis and property studies of different types of oligomers and polymers having conjugated backbone, based on *p*-phenylenevinylenes,² *p*-phenyleneethynylenes,³ *p*-phenylenes⁴ and thiophenes⁵ etc. The electronic properties exhibited by these systems have made them important in single molecular electronics⁶ and display applications⁷ such as light emitting diode (LED) and flat panel display. In addition to the electronic applications conjugated oligomers and polymers have been tested for solar cell applications⁸ and also for nonlinear optical applications such as second and third harmonic generations (SHG and THG).⁹ The uniqueness of these systems over their inorganic counterparts is the tunability of the properties which is offered by structural and functional group modifications.¹⁰

Among the various conjugated oligomers and polymers mentioned above, *p*-phenyleneethynylenes take the central stage owing to the possibility of tuning the properties by way of substituting functional groups and introducing the changes in molecular geometry.¹¹ Last decade witnessed tremendous effort from both experimental and theoretical side towards the designing and understanding of the properties of various single molecular conductors particularly oligo(phenyleneethynylene)s. A major portion of such studies on oligo(phenyleneethynylene)s focus on the effect of the functional groups effects (donor-acceptors) on the conducting properties of the phenyleneethynylene back bone.^{11a,12} Among them, the molecule carrying nitro-amino functionality is interesting is that it showed a negative differential resistance (NDR) behavior, a prototype switch action.¹³ In addition to the substitution effects, structural attributes such as the

planarity of the phenyleneethynylene backbone also seems to have a large impact on the electronic and the photophysical properties of the *p*-phenyleneethynylenes.^{3d,14}

Towards this end a number of studies have been carried out during last decade, especially that to study how in the solid state the molecular structure and packing play a major role in deciding the photophysical properties.^{3c,15} Accordingly, the weak interactions responsible for molecular packing have come under focus in many studies.¹⁶ Reports by Bunz on phenyleneethynylene based polymers and oligomers cover the effect of the molecular geometry especially the planarization of the phenyleneethynylene backbone on various photophysical properties.¹⁷ The experimental efforts to understand the solid state structure and packing of the molecules are mainly based on scanning probe microscopic techniques and are modeled with the help of various theoretical methods.¹⁸ These studies mainly deal with the two dimensional arrangement of the conjugated chains on the surfaces and also could bring about a correlation between the property and the structure in the solid state.

3.2 Scope of the Present Investigation

Untill now there has been no systematic study on phenyleneethynylnes, relating functional group substitution, molecular geometry, crystal packing involving weak interactions and photophysical properties. The present study is an effort in this direction. It deals with dialkyloxy substituted phenyleneethynylene oligomers with varying hydrocarbon chain lengths (methoxy to dodecyloxy) as model crystal systems. These are 2,5-bis(phenylethynyl)benzene, named briefly as **C0**; 1,4-bis(phenylethynyl)-2,5-bis(methoxy)benzene, **C1**; 1,4-bis(phenylethynyl)-2,5-bis(ethoxy)benzene, **C2**; 1,4-bis(phenylethynyl)-2,5-bis(*n*-propoxy)benzene, **C3**; 1,4-bis(phenylethynyl)-2,5-bis(*n*-butyloxy)benzene, **C4**; 1,4-bis (phenylethynyl)-2,5-bis(*n*-pentyloxy)benzene, **C5**; 1,4-bis(phenylethynyl)-2,5-bis (*n*-hexyloxy)benzene, **C6** and 1,4-bis(phenylethynyl)-2,5-bis(*n*-dodecyloxy) benzene, **C12**. The main objective of the study is to see how increasing alkyl chain length influences molecular geometry and the interactions prevalent in the crystal structure. These in turn are responsible for the photophysical properties.

3.3 Experimental Section

All the compounds were synthesized following reported procedures with slight modifications.¹⁹⁻²⁰ All the chemicals for the synthesis have been purchased from Aldrich chemical company and used as obtained. All the solvents used for synthesis and spectroscopic studies were distilled and dried using general procedures.²¹

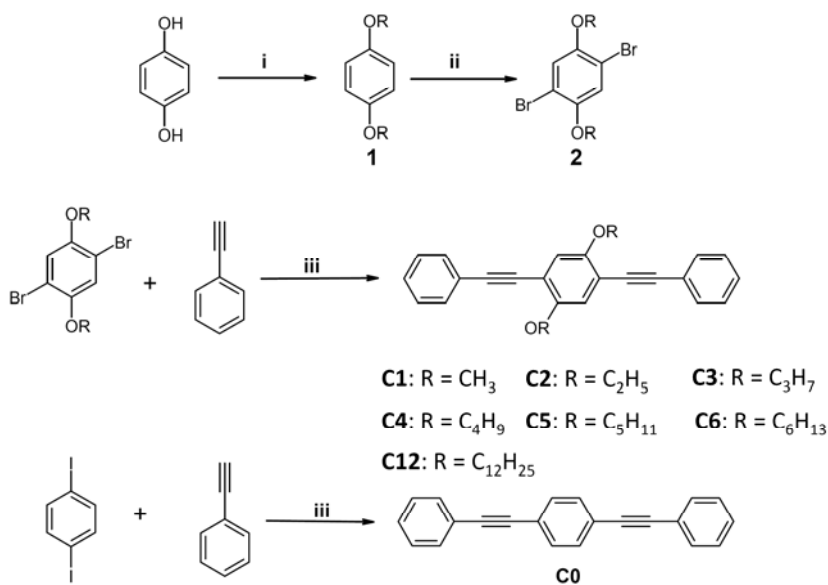
3.3.1 General method of synthesis

1,4-dialkyloxybenzene (1): A procedure analogous to that of Tour et al,²⁰ was followed (see Scheme 3.1). To a 100 mL two necked round bottom flask fitted with condenser and an addition funnel, 1,4-dihydroxybenzene (30 mmol), was dissolved in 50 mL dry ethanol. To this solution, KOH (65 mmol) was added and refluxed for 20 minutes and added respective alkyl bromide (65 mmol) in 20 minutes. The reaction mixture was refluxed for 2 hours and cooled to room temperature. Ethanol was removed on a rotavapor and the solid was dissolved in dichloromethane and washed with water (3x). The organic layer was separated and dried over Na₂SO₄. The resultant products were purified over silica gel column chromatography using hexanes. Desired products were obtained with ~ 87-93% yield. All the compounds were obtained as colorless crystals from hexanes and characterized using single crystal X-ray diffraction.

2,5-dibromo-1,4-dialkyloxybenzene (2): In a 100 mL round bottom flask, 1,4-dialkyloxybenzene (20 mmol) was dissolved in glacial acetic acid (6 mL). A solution of bromine (40 mmol) in acetic acid (3 mL) was added dropwise over 40 minutes. The resulting mixture was allowed to stir for 2 hours. The reaction mixture was poured into ice cold water. The precipitate was filtered and column chromatographed over silica gel using hexanes as the eluent. All the brominated compounds formed with a yield ranging from 75-78 %. All the compounds were yielded colorless crystals and are characterized using single crystal X-ray diffraction.

2,5-bis(phenylethynyl)-1,4-bis(alkyloxy)benzene (C1-C12): To an oven dried 100 mL two necked round bottom flask, 2,5-dibromo-1,4-dialkyloxybenzene (6 mmol) was dissolved in THF (7 mL). To the solution bis(triphenylphosphine)palladium(II)dichloride (0.12 mmol) was added and stirred for 15 minutes. To the reaction mixture triphenylphosphine (0.24mmol), diisopropylethylamine (24 mmol) and copper(I)iodide

(0.24) were added and the atmosphere replaced with argon (3x). To this reaction mixture phenylacetylene (14.2 mmol) was added



Scheme 3.1: Reagents and conditions: i) NaOH, RBr, ii) Br₂, AcOH iii) PdCl₂(PPh₃)₂, CuI, Diisopropylethylamine (DIEA), PPh₃, THF, 65 °C, 24 hours

and once again the argon atmosphere maintained and the round bottom flask was sealed. The reaction mixture was heated at 65 °C for 24 hours and filtered over celite to remove the inorganic products. The organic portion was extracted using dichloromethane and purified using flash column chromatography (silica gel and using hexanes as the eluent). The dialkyloxy substituted oligo(phenyleneethynylene)s yielded 80 to 90% and were characterized using NMR (¹H and ¹³C) spectroscopy (Appendix for chapter 3, page:A-31) in addition to the single crystal X-ray diffraction.

1,4-bis(phenylethynyl)benzene (C0): Compound **C0** was prepared by following previous procedure by replacing 2,5-dibromo-1,4-dialkyloxybenzene with 1,4-diiodobenzene (see Scheme 3.1)

3.3.2 Photophysical studies

The absorption spectra were recorded on a Shimadzu UV-3101PC UV-vis-NIR spectrophotometer and excitation and emission spectra were recorded on a SPEX

Fluorolog F112X spectrofluorimeter. All the commercially obtained spectrometric grade solvents were dried using standard procedures²¹ before preparation of the solutions for the various studies in the solution state. Fluorescence quantum yields, with an estimated reproducibility around 2%, were determined by comparison with diphenylanthracene, **DPA** ($\Phi_f = 0.9$) which was used as the fluorescence standard.

In order to study fluorescence with sample **C1** cooled at different rates, the compound was held between two glass cover slips by heating above its melting points on hot stage attached to a digital temperature controller (Linkam). The melt formed by this method have been cooled at different rates to room temperature. Measurements of solid state photoluminescence were carried out using front face emission scan mode on a SPEX Fluorolog F112X spectrofluorimeter. Solid state quantum efficiency was measured using a calibrated integrating sphere in a SPEX Fluorolog spectrofluorimeter.²² A Xe-arc lamp was used to excite the thin film sample placed in the sphere, with 360 nm excitation wavelength. The quantum yield of solid state fluorescence was determined by comparing the spectral intensities of the lamp and sample emission using a reported procedure. Using this experimental system and integrating sphere system, the solid state quantum yield of thin film of the standard green OLED material tris-8-hydroxyquinolinolato aluminium (Alq3) was determined to be 0.19, which is consistent with previously reported values.²³

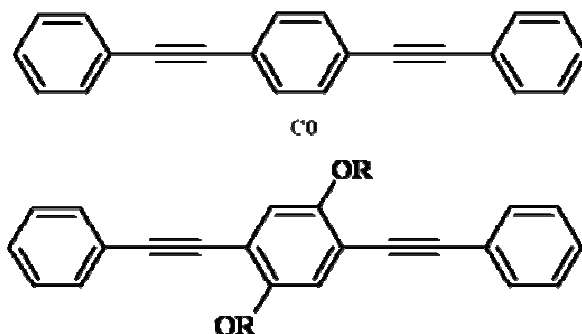
3.3.3 Crystal data collection

Crystals of the compounds **C1** to **C12** were obtained by the slow evaporation of their saturated solution in toluene and the crystals were separated from the mother liquor. However, good quality crystals of **C0** could not be obtained. The crystals were analyzed under a polarizing microscope and good quality single crystals were separated for X-ray structure determination. The crystal data were collected on a Bruker-Nonius diffractometer with Kappa geometry attached with an APEX - II-CCD area detector and a graphite monochromator for the Mo K α radiation (50 kV, 40 mA) at room temperature (298 K). The data collection and structure solution were carried out using the procedure described in the general experimental and related aspects section.

3.4 Results and Discussion

3.4.1 Structure and weak interactions in oligo(phenyleneethynylene)s

In order to understand the effect of varying chain length and the resulting weak interactions, a systematic analysis of the molecular crystallographic structure in 8 oligo(phenyleneethynylene)s systems have been carried out. Scheme 3.2 represents the molecules presented in this study.



Scheme 3.2: Molecules presented under this study **C0** : 2,5-bis(phenylethynyl)benzene;²⁴
R = **C1**: 1,4-bis(phenylethynyl)-2,5-bis(methoxy)benzene; **C2**: 1,4-bis(phenylethynyl)-2,5-bis(ethoxy) benzene; **C3**: 1,4-bis(phenylethynyl)-2,5-bis(*n*-propoxy)benzene; **C4**: 1,4-bis(phenylethynyl)-2,5-bis(*n*-butyloxy)benzene; **C5**: 1,4-bis(phenylethynyl)-2,5-bis(*n*-pentyloxy)benzene; **C6**: 1,4-bis(phenylethynyl)-2,5-bis(*n*-hexyloxy)benzene; **C12**: 1,4-bis(phenylethynyl)-2,5-bis(*n*-dodecyloxy)benzene.^{16b}

Figures 3.1 and 3.2 depict the ORTEP plots and atom numbering schemes for all the oligo(phenyleneethynylene)s presented in this study. All the dialkyloxy substituted oligo(phenyleneethynylene)s (**C1** to **C12**) crystallize in monoclinic space group with half molecule in the asymmetric unit. The crystal structures of compounds **C0**, **C6** and **C12** are previously known in the literature and the structure solution obtained in this study match closely with the reported.^{24,16b} From the literature it is also known that the molecule 2,5-bis(phenylethynyl)benzene, **C0**, crystallizes in triclinic P(-1) space group with two half molecules in the asymmetric unit. Table 3.1 provides the complete crystallographic data and refinement parameters for the molecules **C1** to **C12**. A complete list of bond lengths and bond angles for all the molecules along with the atom coordinates and isotropic displacement parameters (**C1** to **C12**) are provided in the Appendix for Chapter 3 (Appendix Tables A3.1 to A3.16). The aromatic carbon-carbon

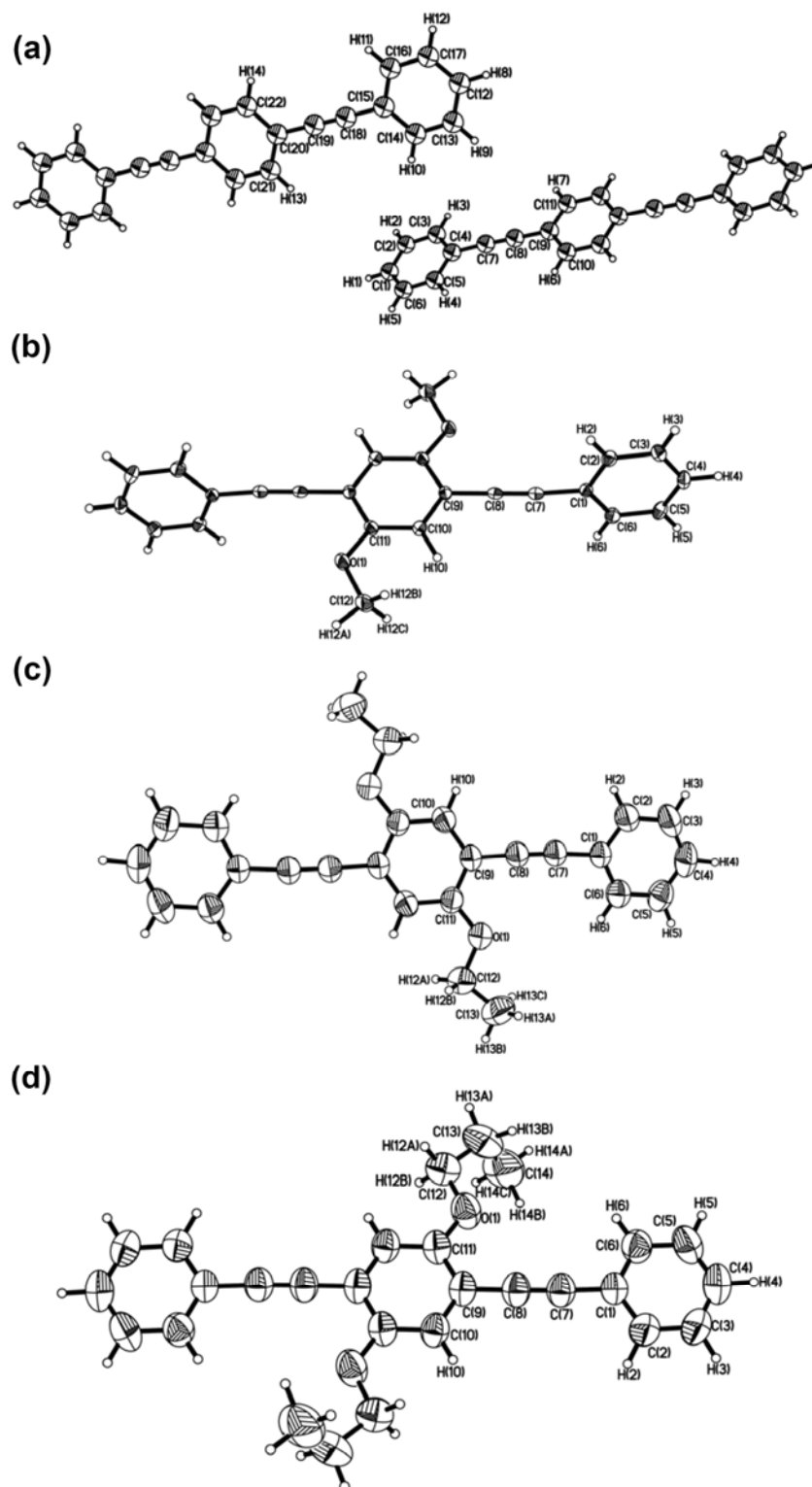


Figure 3.1: ORTEP plot of the molecules (a) 2,5-bis(phenylethynyl)benzene, **C0** (ref. # 24), (b) 1,4-bis(phenylethynyl)-2,5-bis(methoxy)benzene, **C1**, (c) 1,4-bis(phenylethynyl)-2,5-bis(ethoxy)benzene, **C2** and (d) 1,4-bis(phenylethynyl)-2,5-bis(*n*-propyloxy)benzene, **C3** where the asymmetric units are labeled.

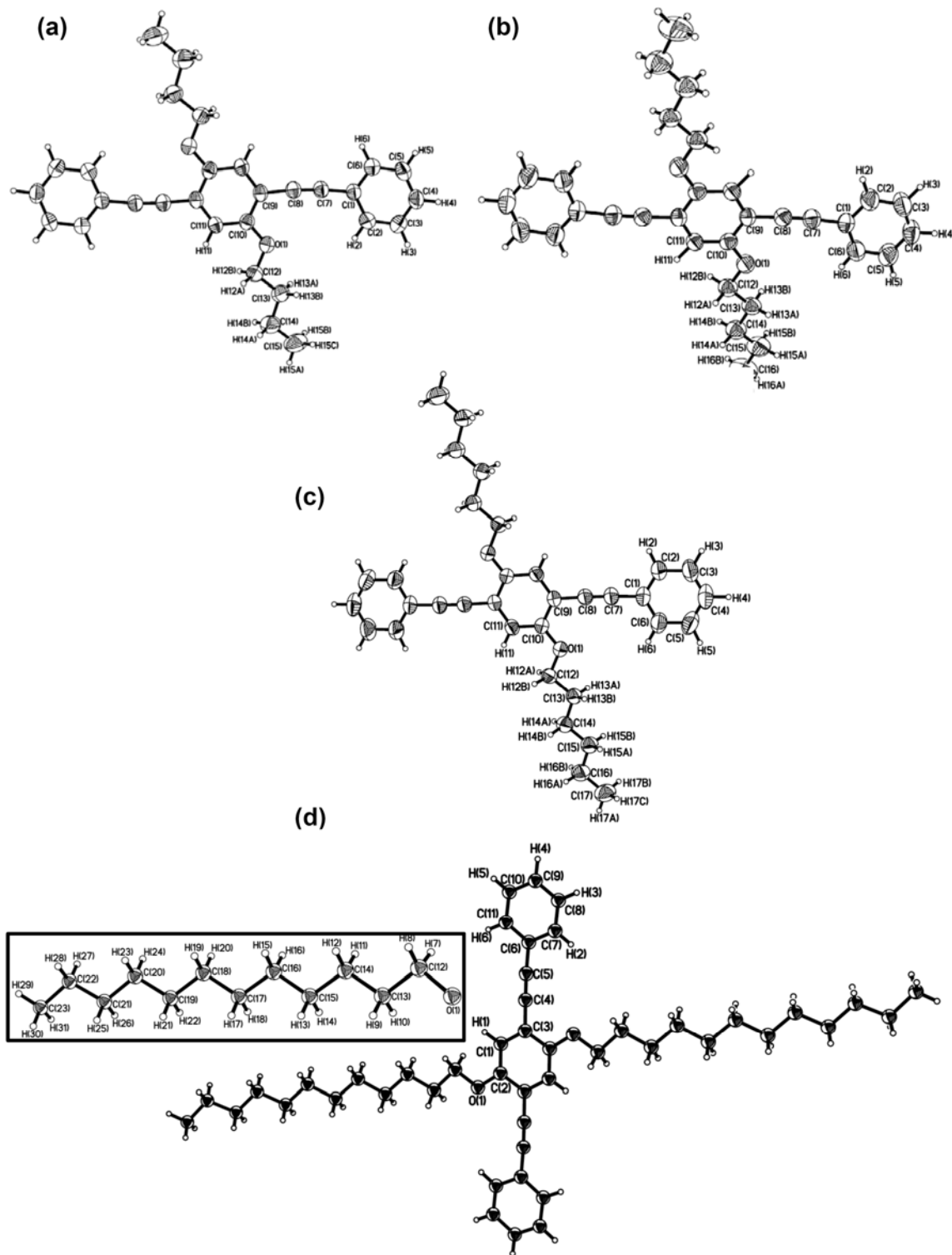


Figure 3.2: ORTEP plot of the molecules (a) 1,4-bis(phenylethynyl)-2,5-bis(*n*-butylloxy)benzene, **C4**, (b) 1,4-bis(phenylethynyl)-2,5-bis(*n*-pentylloxy)benzene, **C5**, (c) 1,4-bis(phenylethynyl)-2,5-bis(*n*-hexylloxy)benzene, **C6** and (d) 1,4-bis(phenylethynyl)-2,5-bis(*n*-dodecylloxy)benzene, **C12** (ref. # 26b) where the asymmetric units are labeled.

Table 3.1 Crystal structure data for adduct of 2,5-bis(phenylethynyl)-1,4-bis(alkyloxy)benzenes.*

Compound	C1	C2	C3	C4	C5	C6	C12
Empirical formula	C ₂₄ H ₁₈ O ₂	C ₂₆ H ₂₂ O ₂	C ₂₈ H ₂₆ O ₂	C ₃₀ H ₃₀ O ₂	C ₃₂ H ₃₄ O ₂	C ₃₄ H ₃₈ O ₂	C ₄₆ H ₆₂ O ₂
Formula wt	338.38	366.44	394.48	422.54	450.60	478.64	646.96
Cell setting	Monoclinic	Monoclinic	Monoclinic	Monoclinic	Monoclinic	Monoclinic	Monoclinic
Space group	C2/c	C2/c	P2(1)/c	P2(1)/n	P2(1)/n	P2(1)/n	P2(1)/c
a (Å)	15.4950(5)	13.0543(5)	5.78560(10)	6.2637(2)	6.2298(2)	6.2970(2)	25.7045(9)
b (Å)	11.0758(4)	11.0691(4)	14.9764(4)	21.4804(6)	22.1029(6)	22.7824(8)	5.0710(3)
c (Å)	10.6108(3)	15.2735(5)	13.3619(3)	9.2590(2)	10.0247(3)	10.6411(2)	16.4935(6)
α (°)	90	90	90	90	90	90	90
β (°)	102.3920(10)	109.434(2)	90.1120(10)	93.187(1)	99.168(2)	105.493(1)	107.729(4)
γ (°)	90	90	90	90	90	90	90
Cell volume (Å ³)	1778.59(10)	2081.27(13)	1157.77(5)	1243.84(6)	1362.73(7)	1471.11(7)	2047.8(2)
Z	4	4	2	2	2	2	2
F (000)	712	776	420	452	484	516	708
ρ (g/cm ³)	1.264	1.169	1.132	1.128	1.098	1.081	1.049
Crystal size (mm)	0.35 x 0.30 x 0.30	0.35 x 0.30 x 0.25	0.35 x 0.30 x 0.30	0.35 x 0.25 x 0.25	0.35 x 0.35 x 0.20	0.30 x 0.25 x 0.25	0.35 x 0.30 x 0.20
Crystal detector distance(cm)	5.0	5.0	5.0	5.0	5.0	5.0	0.50
No. of measured	6893	12036	15485	12331	14626	5968	31015
No. of independent reflections	1684	1965	2191	2323	2586	2087	3869
Range for data collection θ (°)	2.28 - 25.68	2.56 - 25.69	2.04 - 25.69	2.91-25.65	1.84 - 25.68	1.79 - 23.24	0.83-25.67
Range of h, k, l	-18 to 18 -12 to 13 -12 to 11	-15 to 15 -13 to 13 -18 to 16	-7 to 6 -18 to 18 -16 to 16	-7 to 6 -26 to 26 -11 to 11	-6 to 7 -26 to 26 -12 to 12	-6 to 6 -25 to 25, -6 to 11	-31 to 31 -6 to 6 -20 to 20
R ₁	0.0364	0.0432	0.0424	0.0387	0.0515	0.0448	0.0994
wR ₂	0.0914	0.1097	0.1120	0.0985	0.1532	0.1151	0.3122
S	1.103	1.026	1.016	1.026	1.113	0.952	1.078
No. of parameters refined	154	171	188	205	222	239	322
Max. eÅ ⁻³	0.256	0.120	0.105	0.122	0.254	0.167	0.417

*Crystal data for **C0** is not shown as good quality crystals could not be obtained. The residual factors being high for **C12** in the present study, the reported structure (ref. #16b) has been used in the discussion.

bond lengths are in the range of 1.353(3) - 1.404(2) Å and the single bond connectors between the aromatic ring and the triple bond are in the range of 1.428(2) - 1.451(2) Å. However, no systematic variation observed. The lengths of the triple bonds in all the molecules vary within the range 1.182(2) - 1.205(2) Å, whereas the C-O bond lengths between the aromatic ring and the oxygen atom range from 1.363 to 1.376(3) Å.

A comparative study of molecular geometries and packing of dialkyloxy substituted oligo(phenyleneethynylene)s

The possible chemical effect in alkyloxy substituted oligo(phenyleneethynylene)s are electronic effects such as +M (mesomeric) and -I (inductive) effects on the central phenyl ring from the alkyloxy group.²⁵ The possible variation in -I (inductive) effect can extend upto second carbon atom in the alkyl chain while it becomes negligible from the third carbon onwards. Since the chemical effect is more or less similar in higher alkyloxy substitutions, the possible difference in the properties of these molecules can be attributed to the geometry induced electronic effects. This is due to the fact that, phenyl rings being connected though the triple bond, posses enough freedom to rotate along the molecular axis to get rid of the steric repulsion between the end phenyl rings and the alkyloxy groups.

A detailed analysis of the molecular geometry of the dialkyloxy substituted oligo(phenyleneethynylene)s shows the presence of various kinds of distortions in their phenyleneethynylene backbone. The distortions in the molecules are classified into three types (i) Angular deviation (α) between the middle and terminal phenyl rings, (ii) In-plane lifting (**L**) of phenyl ring, (iii) out of plane bending of single-triple bond linker defined by angle (θ). Graphical representations of the above mentioned deviations in these molecules are shown in Figure 3.3. In these systems, the most important deformation is the deviation from the planarity (α) created by the rotation of the phenyl rings.

Figure 3.4 shows a paddle wheel representation of all the molecules with their asymmetric units. This figure shows the out of plane movements in each molecule keeping the middle phenyl ring in the plane. It is clear from this figure that on dialkyloxy

substitution the phenyleneethynylene backbone undergoes different types of geometric variations.

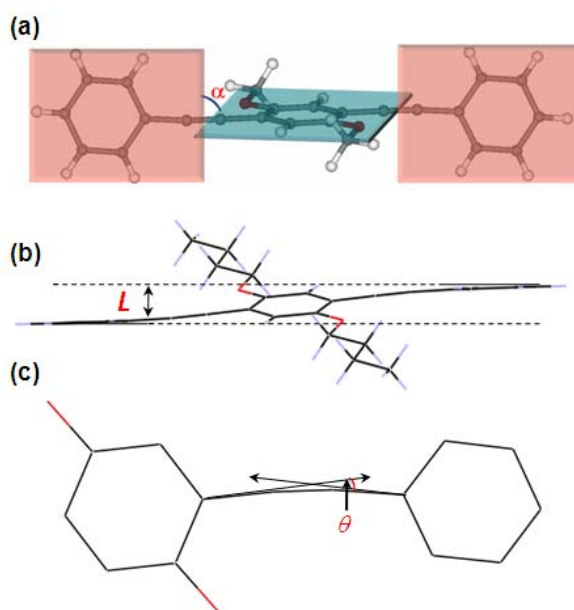


Figure 3.3: Conformational variations present in the alkyloxy substituted oligo (phenyleneethynylene)s (a) Angular deviation (α) between the middle and terminal phenyl rings (b) In-plane lifting (L) of phenyl ring (c) out of plane bending of single-triple bond linker (θ).

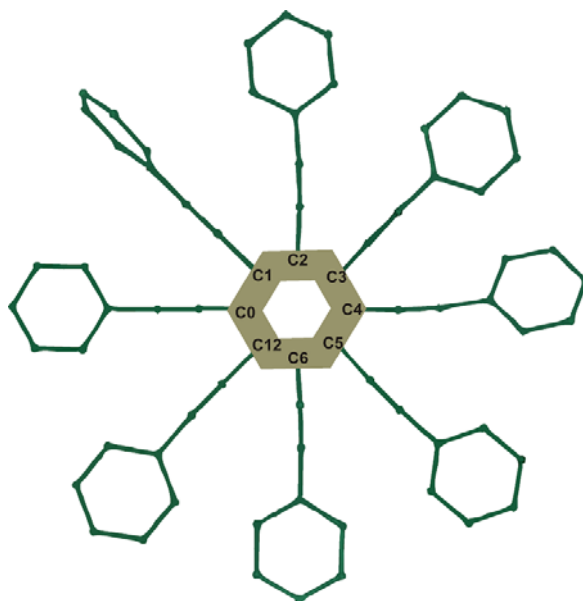


Figure 3.4: A paddle wheel representation oligo(phenyleneethynylene)s which shows various deformation from the planarity (asymmetric units where alkyloxy groups and hydrogen are removed for clarity)

In order to obtain a quantitative picture on the various distortions in dialkyloxy substituted molecules, various deformation parameters α , L and θ were plotted against the increasing chain length, n . Figure 3.5a shows a sharp increase in deviation from planarity ($\alpha = 80^\circ$) on methoxy substitution. Further increment in the alkyloxy chain length (ethoxy substitution) brings about a sharp decrease in the angle indicating the building up of a restoring force towards planarization. On increasing the side chain length further with propyloxy substitution, the value of α decreases further to 5.5° . This can be attributed to the decrease in the strain in phenyleneethynylene backbone by introducing a *gauche* conformation in the alkyloxy chain. Butyloxy substitution brings about a small increase in α by $\sim 16^\circ$ but the chain is in *trans* conformation. Further increase in alkyloxy chain length (C5 and C6) brings down the deviation from planarity. Almost complete planarization ($\alpha \sim 0.5^\circ$) of the phenyleneethynylene backbone occurs with dodecyloxy C12.

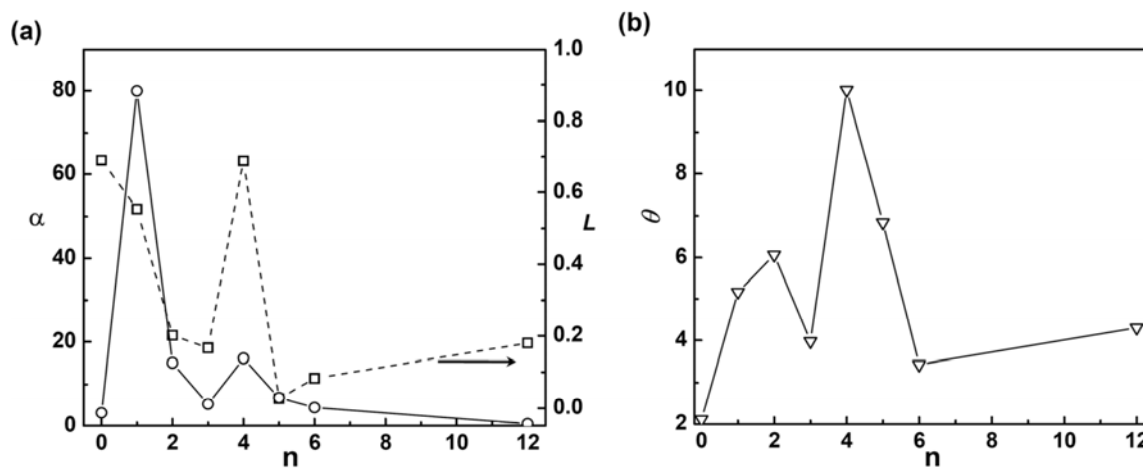


Figure 3.5: The deformations in the phenyleneethynylene backbone with respect to variations in alkyloxy chain lengths (a) Angular deviation (α) between the middle and terminal phenyl rings (solid) and in-plane lifting (L) of phenyl ring (dotted) (b) out plane bending of single-triple bond linker (θ).

In addition to the deviation from planarity, the variations in L and θ with increasing alkyloxy chain length are also analyzed. The plot of in-plane lifting of phenyleneethynylene backbone, L , versus chain length n , (see Figure 3.5a dotted lines) shows a maximum value with butyloxy substitution among various alkyloxy substitutions

with value of 0.688 Å. Similar to in-plane lifting, the backbone bending θ also shows a maximum with butyloxy substitution (see Figure 3.5b).

The molecular packing analysis of all the phenyleneethynylene systems has shown that all the molecules adopt a herringbone packing pattern along different molecular axes. Figure 3.6a shows the packing of molecule **C0**, which forms a herringbone packing along its short axis. Molecule **C1** also packs in a herringbone pattern through its long axis, where the individual layers form a herringbone layer (see Figure 3.6b) and each such layer stacks over, with a slip of half molecular length to give slipped herringbone pattern as shown in the inset of the Figure 3.6b. The molecules from **C2** to **C12** also follow herringbone packing along their molecular long axis as shown in Figure 3.7. There are variations in the interpenetration of the herringbone layers, and these interpenetration is maximum in the case of **C3** (see Figure 3.7b). The molecule **C12** also shows a somewhat different kind herringbone packing with a slip in the molecules in each molecular stack.

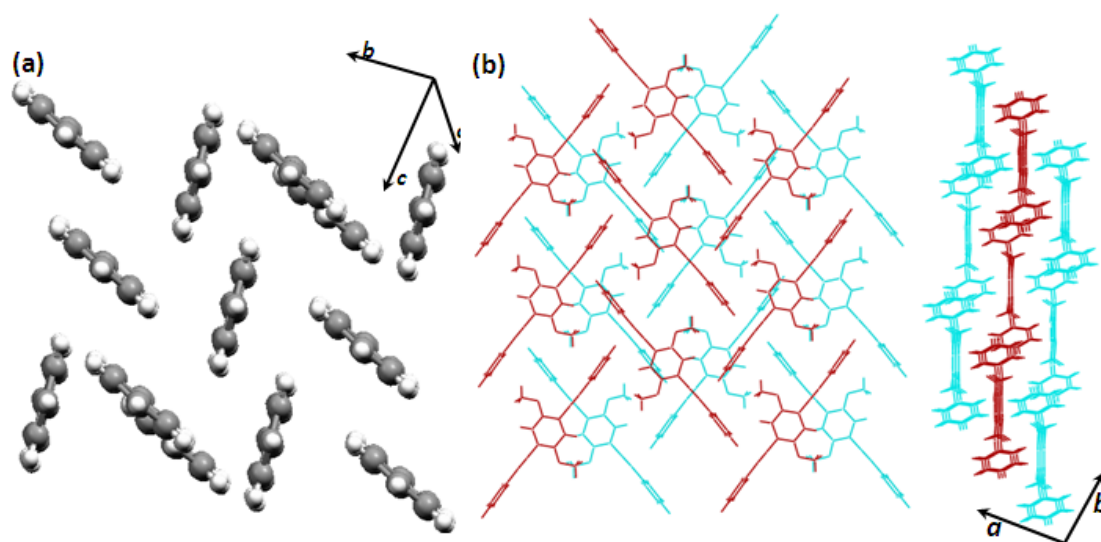


Figure 3.6: Herringbone packing of (a) 2,5-bis(phenylethynyl)benzene, **C0** and (b) 1,4-bis(phenylethynyl)-2,5-bis(methoxy)benzene, **C1**.

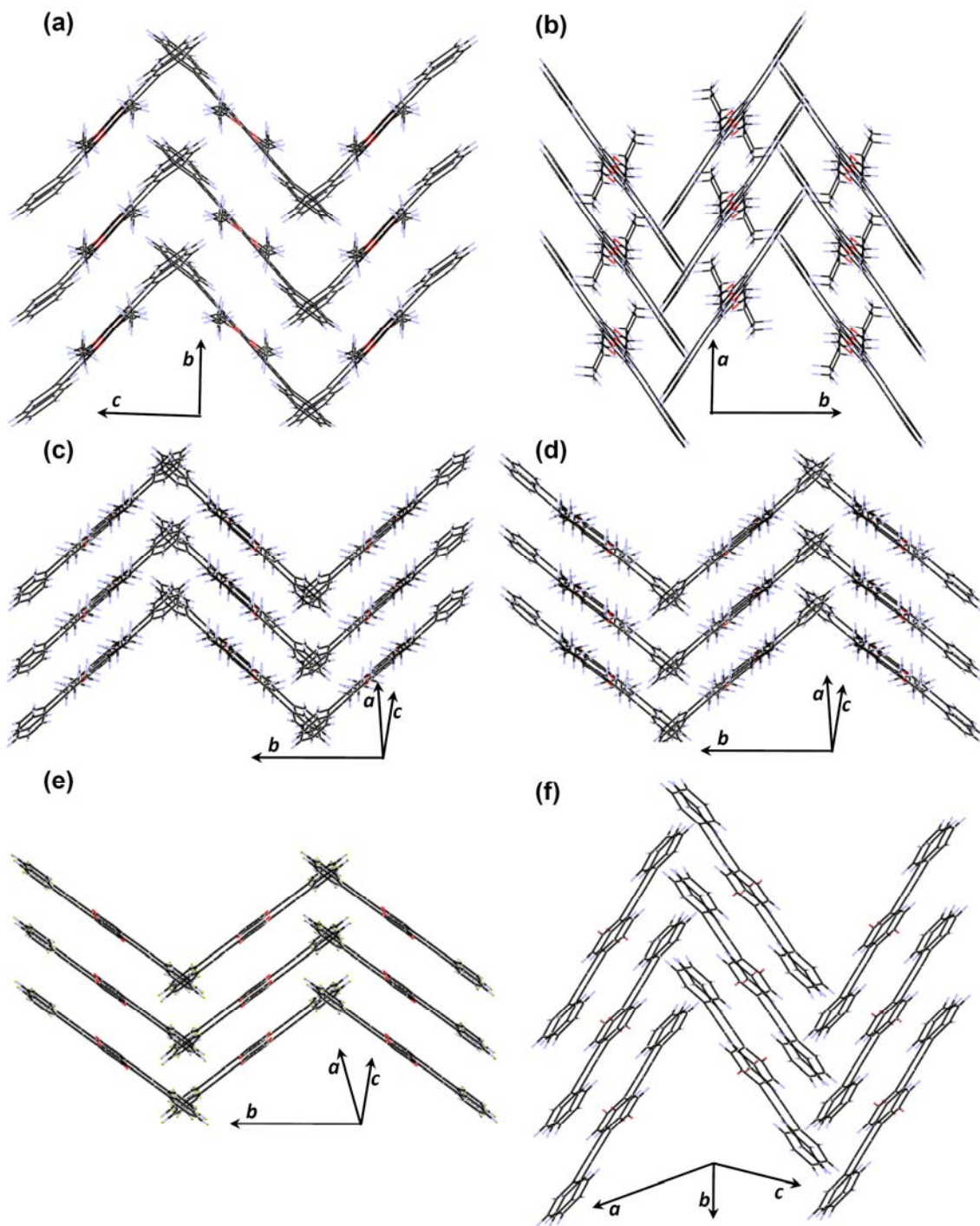


Figure 3.7: Herringbone packing of (a) 1,4-bis(phenylethynyl)-2,5-bis(ethoxy) benzene, **C2**, (b) 1,4-bis(phenylethynyl)-2,5-bis(n-propyloxy)benzene, **C3**, (c) 1,4-bis(phenylethynyl)-2,5-bis(n-butyloxy) benzene, **C4**, (d) 1,4-bis(phenylethynyl)-2,5-bis(n-pentyloxy)benzene, **C5**, (e) 1,4-bis(phenylethynyl)-2,5-bis(n-hexyloxy)benzene, **C6** and (f) 1,4-bis(phenylethynyl)-2,5-bis(n-dodecyloxy) benzene. **C12** (in molecules **C6** and **C12** alkyl chains are removed for clarity).

In order to understand the forces operating for the molecular planarization and also to account for the role played by the triple bonds in these molecules, a detailed analysis of weak interactions has been carried out. It is interesting to note that the major interactions in all these molecules are C-H... π in nature. All interactions with H... π distance $< 3.05 \text{ \AA}$ and angle $> 130^\circ$ are considered in accordance with the previous literature.²⁶ Based on the molecular structure one may speculate that there are two types of donors, aromatic ring and alkyl C-H groups and two types of acceptors namely aromatic ring and the triple bond. Figure 3.8 shows the interactions present in **C0** where the molecules pack through various C-H... π interactions which are originating from aromatic C-H groups and the acceptors being aromatic rings (see Table 3.2). Thus, in this system, the aromatic ring acts as acceptor for various C-H... π interactions.

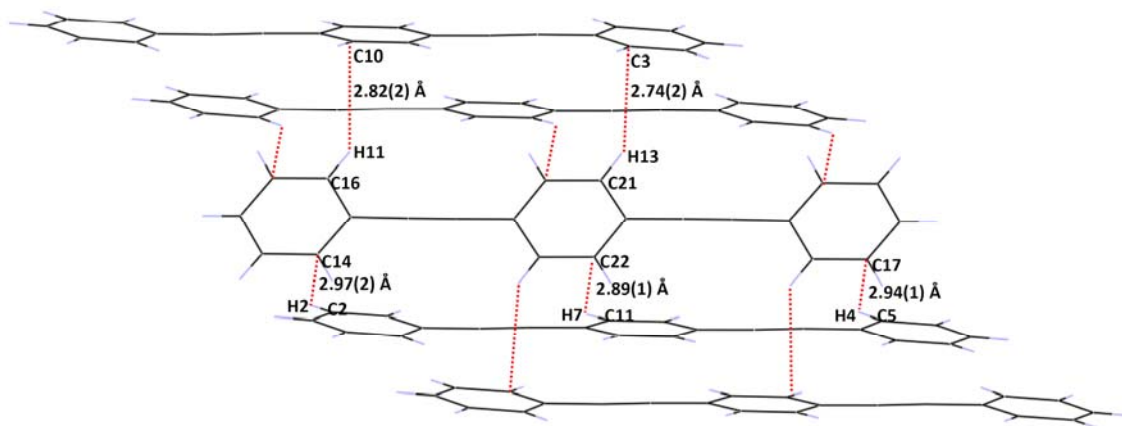


Figure 3.8: Unique hydrogen bonding interactions in molecule 2,5-bis(phenylethynyl)benzene **C0**.

Unlike molecule **C0**, molecule **C1** shows a different set of interactions, where in spite of the presence of phenyl ring acceptors, here the triple bond plays a major role as an acceptor. (see Figure 3.9a). Out of seven C-H... π interactions present in this molecule, four interactions are directed towards the triple bond π -density as indicated by Figure 3.9b. This is a clear evidence for the localization of electron density at the triple bond region due to the reduced conjugation (see Chapter 4 for detailed discussions).

Table 3.2 Unique non-bonding interactions observed in various phenyleneethynylenes presented in this study.

compound	Interactions	H...A (Å)	D-H...A (°)
C0	C(16) -H(11) ... π C(10)	2.82(2)	142.4(2)
	C(21) -H(13) ... π C(3)	2.74(2)	145.2(1)
	C(11) -H(7) ... π C(22)	2.89(1)	137.1(1)
	C(2) -H(2) ... π C(14)	2.97(2)	136.3(1)
	C(5) -H(4) ... π C(17)	2.94(1)	137.0(1)
C1	C(12) -H(12A)... π (Cg(1))	2.86(1)	143.3(3)
	C(5) -H(5) ... π C(10)	3.04(2)	130.7(2)
	C(10) -H(10)... π (C(5))	2.88(2)	154.8 (1)
	C(4) -H(4) ... π C(7)	2.82(1)	133.4(1)
	C(3) -H(3) ... π C(7)	2.95(1)	136.7(1)
	C(6) -H(6) ... π C(8)	3.00(2)	174.4(4)
	C(2) -H(2) ... π C(7)	2.78(2)	155.8(2)
C2	C(4) -H(4) ... π C(8)	2.81(1)	145.7(2)
	C(12) -H(12A)... π (Cg(1))	3.07(1)	132.7(1)
C3	C(12) -H(12A) ... π (Cyl)	2.73(2)	140.6(1)
	(12) -H(12B) ... π (Cg(1))	3.02(2)	135.0(1)
C4	C(13)-H(13B)... π Cg(2)	2.95(1)	145.0(2)
	C(12) -H(12A) ... π C(8)	2.79(1)	152.6(2)
	C(4) -H(4)...O(1)	2.70(1)	144.5(2)
C5	C(12) -H(12A) ... π C(8)	2.84(2)	156.2(2)
	C(13)-H(13A)... π Cg(2)	2.88(2)	140.6(1)
C6	C(13)-H(13B)... π Cg(2)	2.72(2)	141.6(1)
	C(12)-H(12B)... π C(9)	2.86 (1)	132.1(1)
	C(12)-H(12B)... π C(8)	2.88(1)	160.0(1)
C12	C10-H10... π C3	2.82(1)	164.5(2)
	C10-H10... π C2	2.89(2)	138.5(2)
	C12-H12B... π C5	2.87(2)	146.7(1)
	π (Cyl)... Cg(1)	3.37(2), 3.37(1)	
	π (Cyl)... π Cg(2)	3.33(2), 3.35(2)	

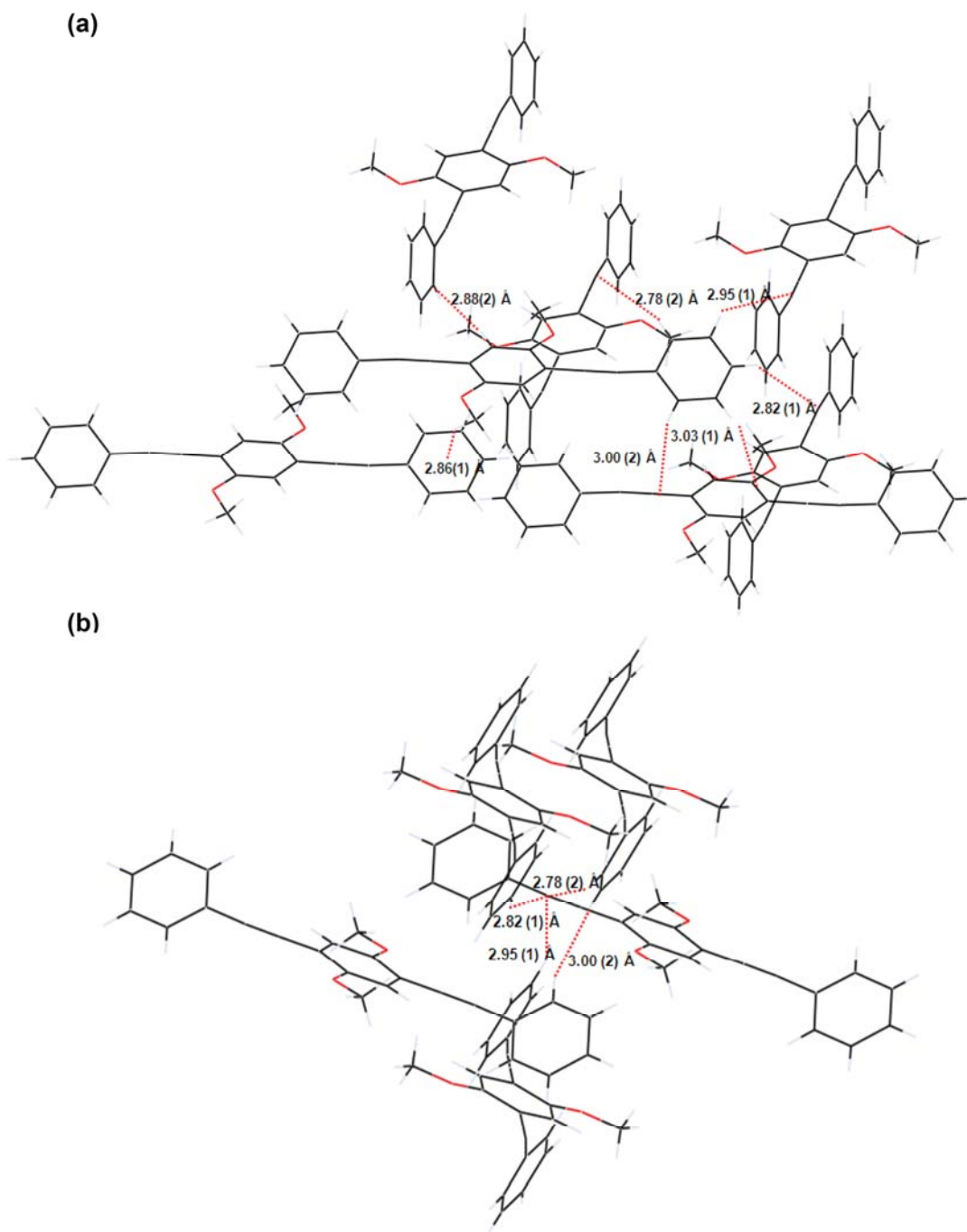
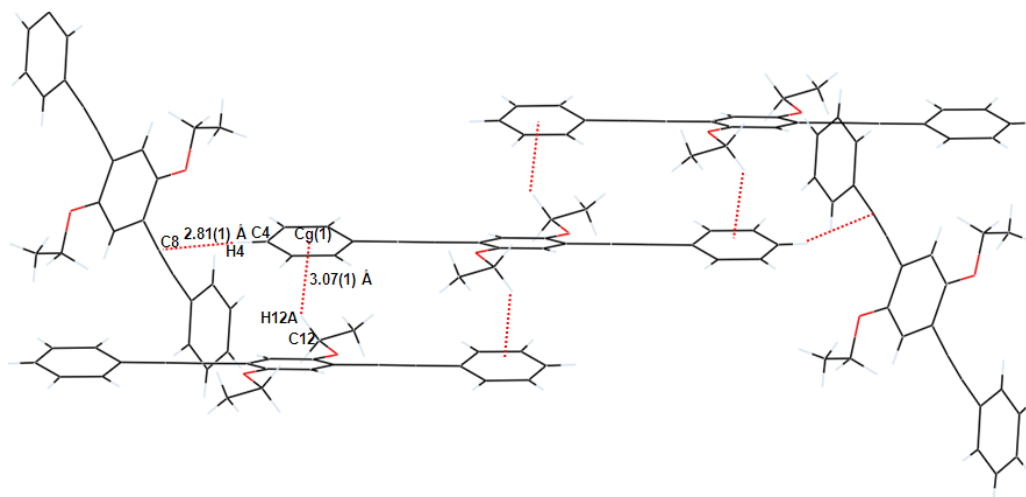


Figure 3.9: Unique hydrogen bonding interactions in molecule 1,4-bis(phenylethynyl)-2,5-bis(methoxy)benzene, **C1** (a) and (b) triple bond as acceptor.

The ethoxy (**C2**) substituted molecule shows only two interactions of C-H... π type which originate from the alkyl chain and the aromatic rings (see Figure 3.10a). In these systems, the aromatic rings as well as the triple bond participate equally as acceptors. The C-H... π interaction formed between the aromatic ring and the triple bond serves to bring together two stacks of molecules in the herringbone packing.

(a)



(b)

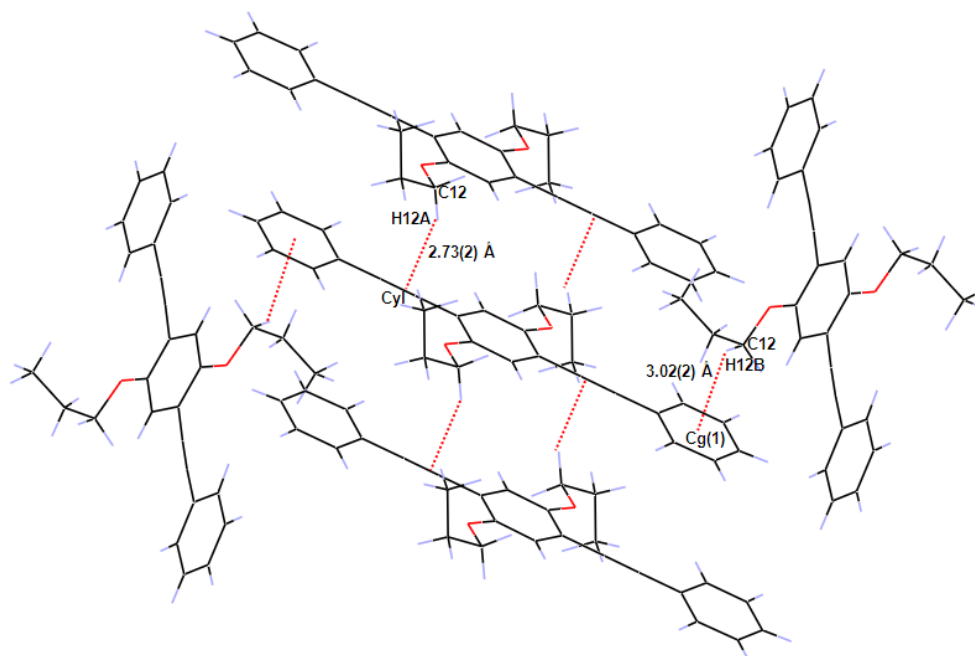


Figure 3.10: Unique C-H... π interactions in molecule (a) 1,4-bis(phenylethynyl)-2,5-bis(ethoxy)benzene, **C2** and (b) 1,4-bis(phenylethynyl)-2,5-bis(propyloxy)benzene, **C3**.

A further increment in the alkyl chain length from **C2** to **C3** results in an important structural change by forming a *gauche* conformation in the alkyl chain with a torsion angle of 66.72° (see Figure 10b). It is noteworthy that in **C3**, all the C-H... π interactions originate from alkyl group, while both triple bond and phenyl rings act as acceptors. In this system the interaction between the alkyl C-H and aromatic π -density acts as the connector between two molecular stacks.

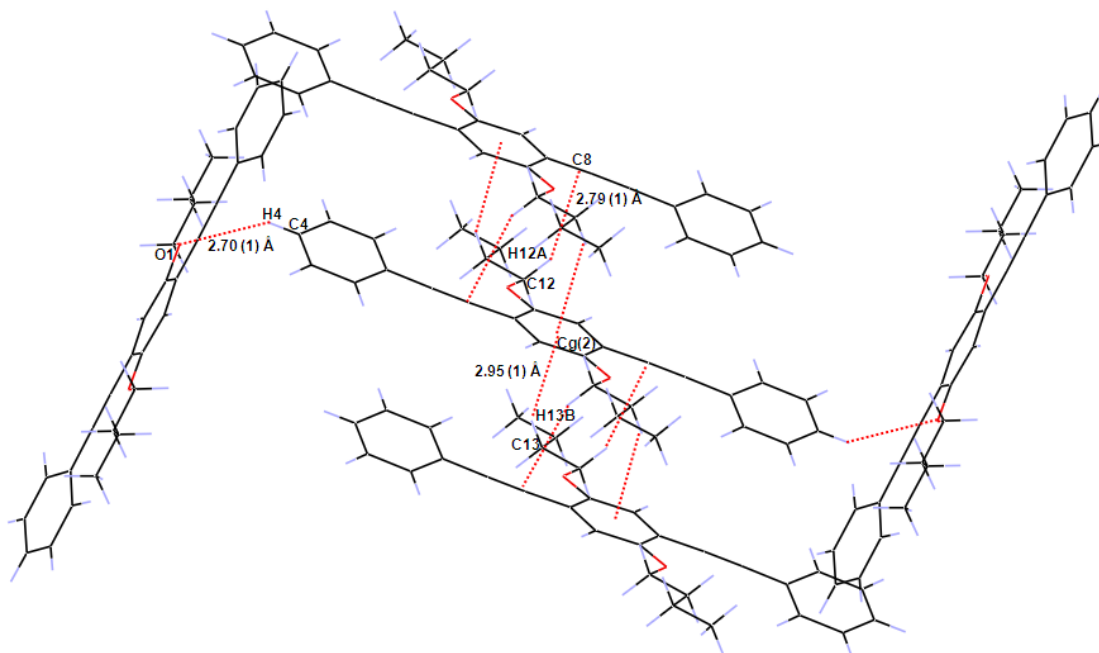


Figure 3.11: Unique hydrogen bonding interactions in molecule 1,4-bis(phenylethynyl)-2,5-bis(butyloxy)benzene, **C4**.

Similar to the C-H... π interactions observed in **C3**, in molecules **C4** to **C6** the only C-H donors are methylene hydrogens, and both the aromatic rings and the triple bond form the acceptors (see Figure 3.11). It is clear from the Figures 3.12 and 3.13 that in molecules **C4** and **C5**, contribution of triple bond and aromatic rings towards C-H... π interactions are equal. Among molecules presented in this study, the uniqueness of the molecule **C4** is due to the presence of a weak C-H...O interaction (see Table 3.2). This C-H...O interaction acts as a connector between the molecules in two different stacks. Figure 3.13 shows the weak interactions present in molecule **C6**. This is in clear contrast to the molecules **C3** to **C5**, for **C6**, the acceptor contribution is mainly from the aromatic ring.

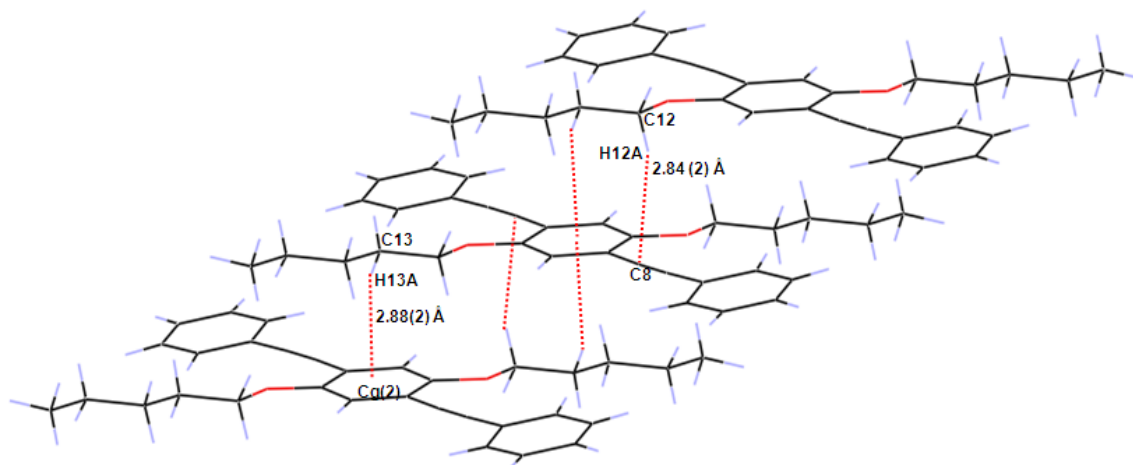


Figure 3.12: Unique hydrogen bonding interactions in molecule 1,4-bis(phenylethynyl)-2,5-bis(pentyloxy)benzene, **C5**.

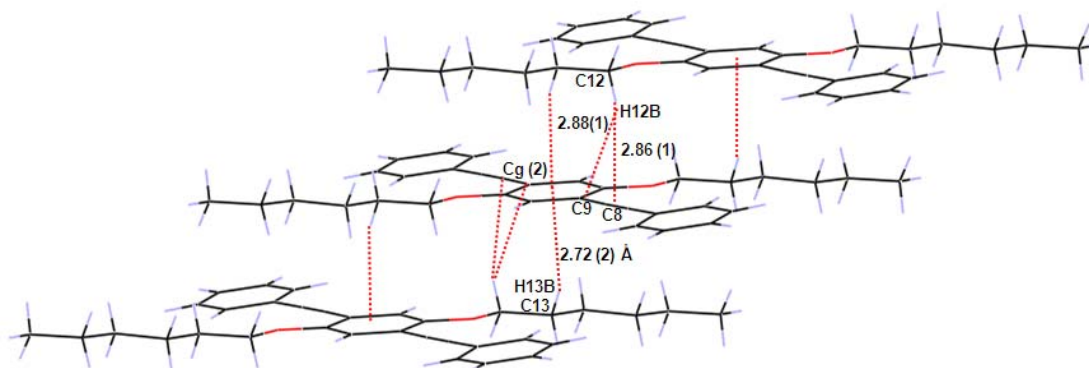


Figure 3.13: Unique hydrogen bonding interactions in molecule 1,4-bis(phenylethynyl)-2,5-bis(hexyloxy)benzene, **C6**.

The weak interactions present in the molecule **C12** are quite different from those present in other molecules. In **C12**, in addition to the C-H... π interactions (see Figure 3.14), the π - π stacking between the triple bond and the aromatic rings (see Figure 3.14b) also play a major role in the molecular packing. The π ... π stacking interactions function as linker between successive molecular layers while the C-H... π interactions link the nearest molecular stacks to give a herringbone pattern. The π ... π stacking distances are in the range of 3.33(2) - 3.37(2) Å, whereas the C-H... π interactions distances range from 2.82(1) to 2.87(2) Å. It is interesting to see that the participation of triple bond π -density in C-H... π interactions is completely absent in this molecule.

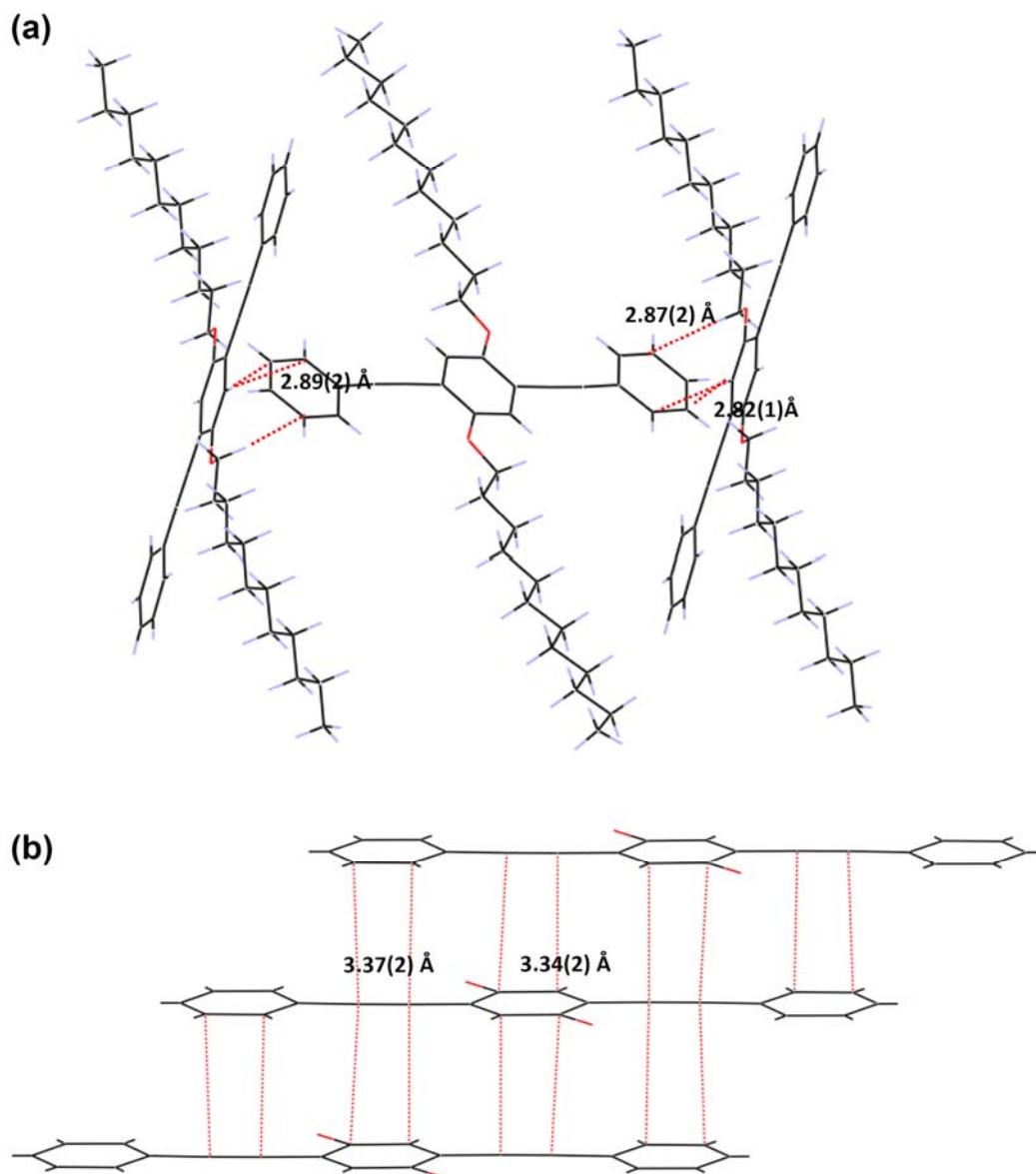


Figure 3.14: Unique interactions in molecule 1,4-bis(phenylethynyl)-2,5-bis(dodecyloxy) benzene, **C12**.

In order to correlate the weak interactions in alkyloxy substituted oligo(phenyleneethynylene)s with molecular geometry, a comparative study of weak interactions and deformation in molecular geometry has been carried out. Figure 3.15 shows the possible H...O interaction distances between the terminal hydrogen atom of the end phenyl ring and the chain length, **n**. As clearly seen from the figure a sensible H...O distance (2.7 Å) occurs only in the molecule **C4**. In this context, a comparison of the minimum H...O distance with the maximum in-plane lifting (**L**) and out of plane

bending (θ) observed in molecule **C4** conclude that the possible C-H...O contact plays a major role in determining the molecular geometry to a greater extent.

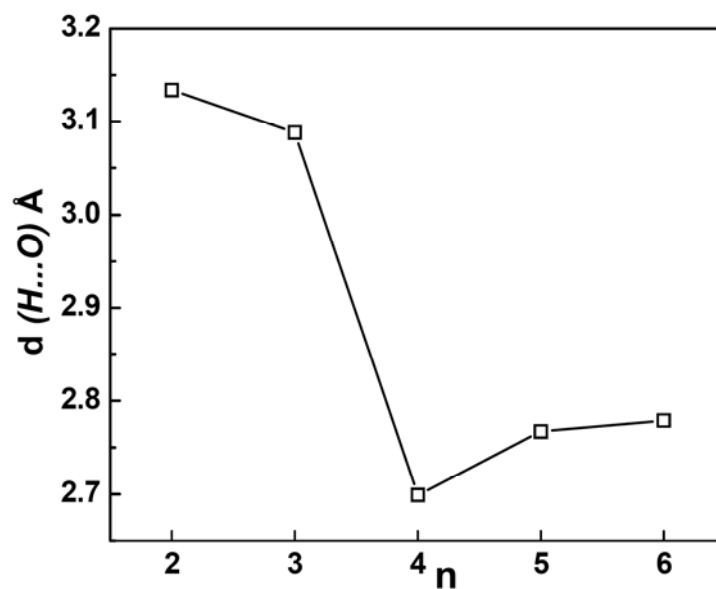


Figure 3.15: (a) A plot showing alkyloxy chain length versus C-H...O distance.

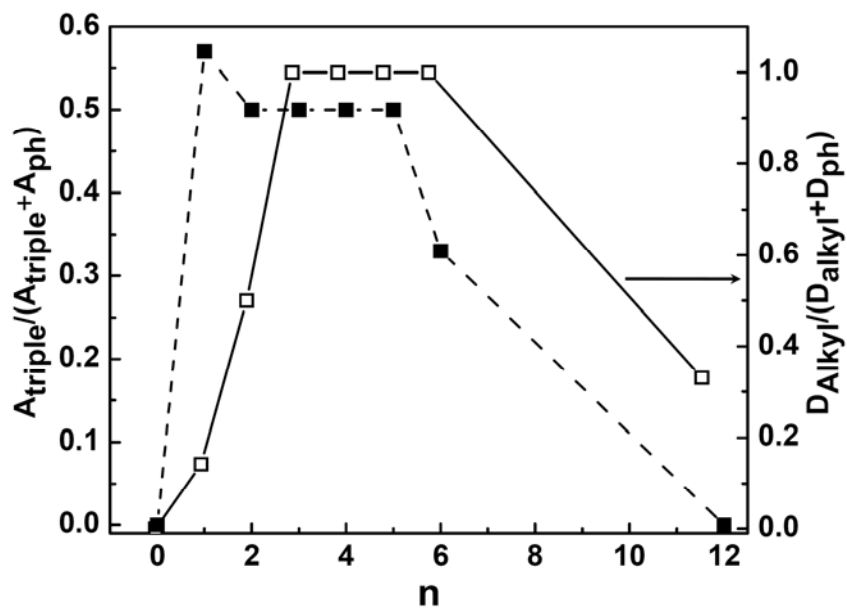


Figure 3.16: Acceptor contribution from triple bond and donor contribution from alkyl chains in alkyloxy substituted oligo(phenyleneethynylene)s.

This study also looks into the details of the participation of triple bond as well as the alkyl C-H in various C-H... π interactions with varying alkyloxy chain length. Figure 3.16 shows a plot of the variation in acceptor contribution of triple bond (i.e., acceptor

contribution of triple bond over sum of the acceptor contributions from phenyl ring and the triple bond) with respect to alkyloxy chain length. It is interesting to see that the triple bonds in highly planar molecules such as **C0** and **C12** are not at all participating in C-H... π interactions. The maximum acceptor contribution of the triple bond is observed in **C1**, while in the molecules **C2** to **C5**, the triple bond shows equal participation as that of the phenyl rings. The alkyl chain contribution (i.e., donor contribution of alkyl group hydrogens over sum of the donor contributions from phenyl ring and the alkyl group) as C-H donors towards various C-H... π interactions with varying alkyloxy chain length, **n** is shown in Figure 3.16 (open squares). As chain length increases, the contribution from the alkyl chain increases to maximum. It is clear from the plot that the methylene hydrogen participation in C-H... π interactions increases systematically from **C1** to **C3**, maintained hundred percent in molecules **C3** to **C6** and drops in molecule **C12**.

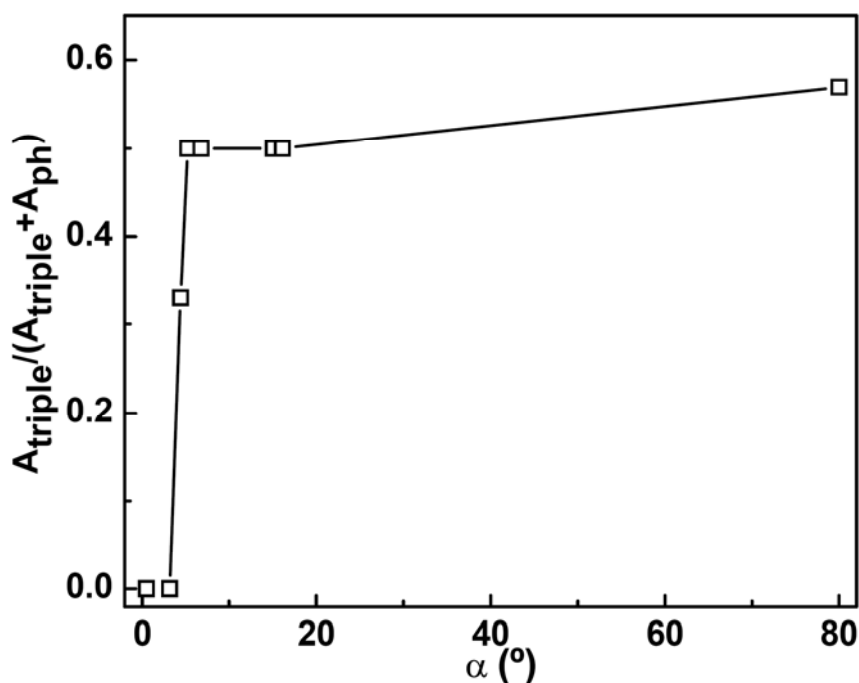


Figure 3.17: Triple bond as an acceptor in C-H... π interactions. Its participation is shown with respect to molecular planarity.

From the analysis of acceptor contribution of triple bond in C-H... π interactions with variation in alkyloxy chain length, it can be seen that the maximum contribution is in the molecule **C1** and the minimum is in **C0** and **C12**. Figure 3.17 shows a plot of acceptor contribution of the triple bond versus the deviation from planarity α . The plot

shows a clear synergy between the acceptor contribution of the triple bond and the deviation from planarity, where the triple bond has become good acceptor at higher angles of deviation. This may be attributed to localization of electron density at the triple bond region due to the reduced conjugation.

Previous studies on various conjugated oligomers and polymers have shown that the chain-chain interaction can also play a major role in determining the property of these compounds in solid state. To understand the role of such interactions, an analysis of weak chain-chain interactions in these molecules has been carried out. In order to obtain a

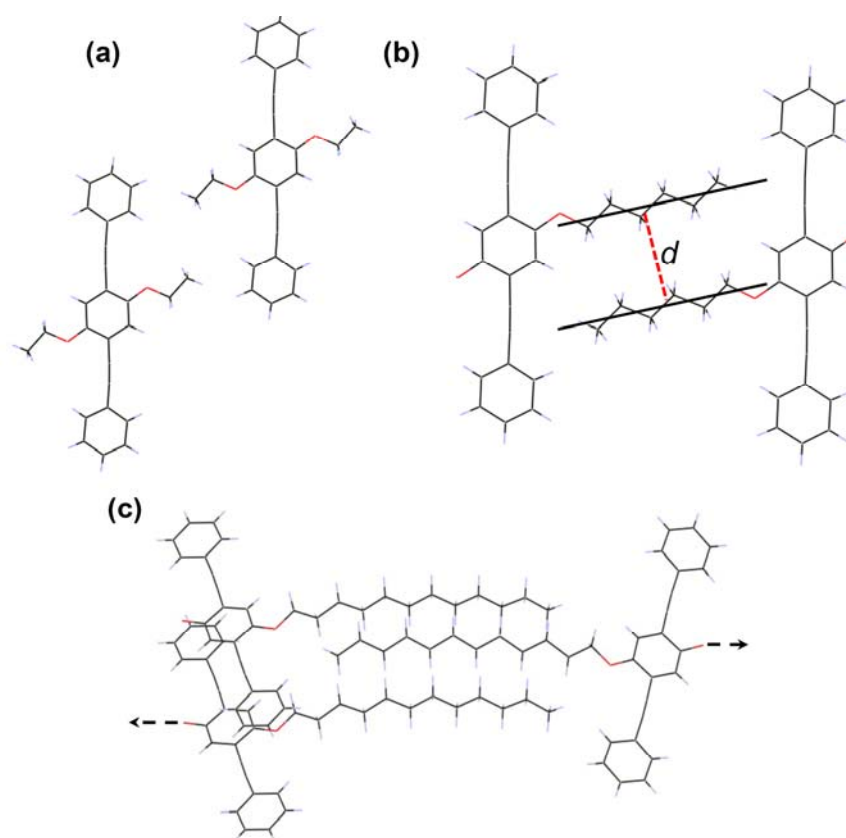


Figure 3.18: (a) Non-interacting alkyl chains (b) interaction between alkyl chains on increasing the chain length (eg. molecule **C6**). (c) Interaction of three alkyl chains in molecule **C12**.

quantitative picture of these interactions, a parameter, **d**, is defined (see Figure 3.18) which is the shortest distance between two mean lines passing through the carbon atoms of the alkyl chains. It is interesting to note that the distance, **d** varies as 4.85, 4.31 and 3.88 Å respectively for **C4**, **C5** and **C6** indicating that on increasing the chain length, an

interaction between the alkyl chain builds up. Unlike these molecules, **C12** shows a different kind of interaction with a mean distance of 4.1 Å, where crowding of three alkyl chains gives rise to a strong interaction as shown in Figure 3.18c.

3.4.2 Solution phase and solid state fluorescence properties of 1,4-bis(phenylethynyl)-2,5-bis(alkyloxy) benzenes

This section deals with the photophysical properties exhibited by dialkyloxy substituted oligo(phenyleneethynylene)s, both in solution phase and solid state. The molecule, **C0**, has been used as a reference molecule for understanding the chemical effect of the alkyloxy substitution on the phenyleneethynylene backbone. Figure 3.19 shows the photophysical properties of the molecule **C0** in toluene (15 μM). The UV-vis absorption spectrum shows maximum intensity at 325 nm with shoulders at 310 and 345 nm. The emission spectrum for the solution of **C0** shows two maxima at 355 and 375 nm with various shoulders. The excitation spectrum recorded by collecting emission at 375 nm shows similar spectral features to that of the absorption spectrum with differences in the peak intensities (see Figure 3.19). The spectral characteristics from the solution resemble the previous reports in the literature.^{18a} Figure 3.20 shows the normalized fluorescence emission spectra for the compounds **C1** to **C12** recorded from their dilute

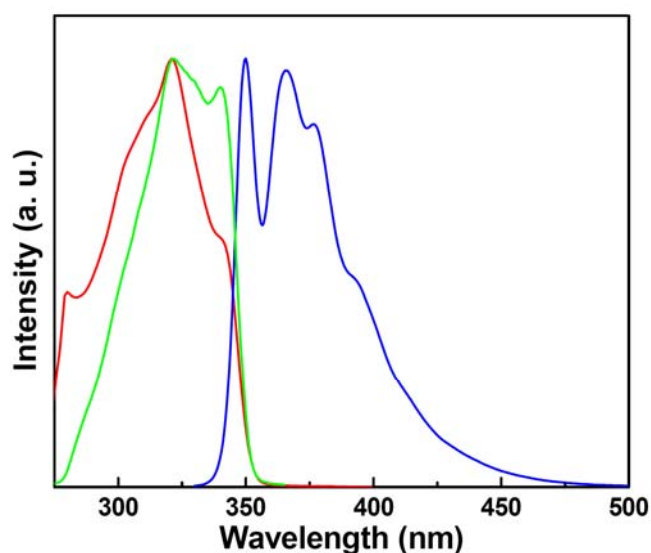


Figure 3.19: Solution state photophysical properties of compound **C0**. Absorption (red), fluorescence emission (blue) recorded by exciting with 330 nm and excitation spectra (green) recorded by collecting emission at 375 nm.

toluene solutions (15 μM). All the compounds show almost similar fluorescence spectral features with maxima centered around 401 nm along with a shoulder at 420 nm. The molecules **C1** and **C6** are blue and red shifted respectively by ~ 4 nm. In dilute solutions, the emission behavior of the different molecules is similar which indicates that alkyloxy chain length induced chemical effects have minimal role.

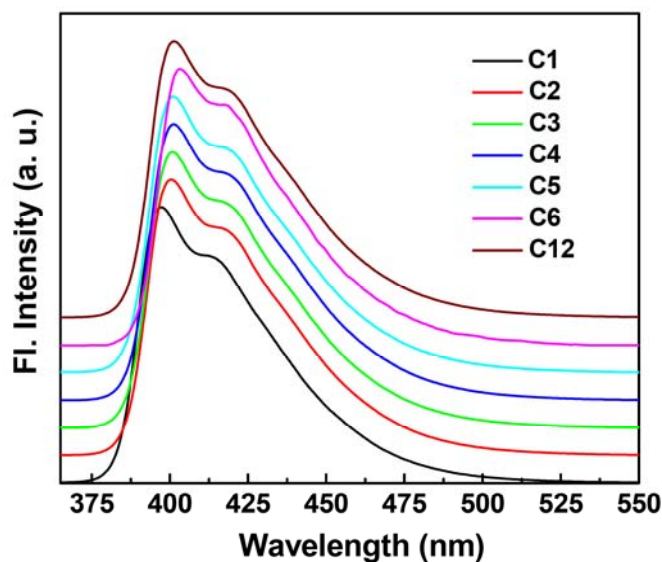


Figure 3.20: Fluorescence in dilute solutions (15 μM in toluene) of oligo(phenyleneethynylene)s recorded by exciting with 360 nm.

The solution phase absorption spectra and excitation spectra for **C1** to **C12** are shown in Figure 3.21. The absorption spectra (Figure 3.30a) shows two intensity maxima centered around 307 and 367 nm. The presence of the two absorption maxima is understandable. A theoretical study on **C6** has shown that in solution,²⁷ the molecule exists in the planar form and the alkyloxy substituent modifies the center arene ring π -orbitals through the resonance interaction with the oxygen lone pairs. This leads to the development of very similar orbital features for HOMO and HOMO-1 resulting in electronic transitions from both HOMO and HOMO-1 to LUMO. The scenario is expected to be similar in other molecules as well. The excitation spectra in Figure 3.21b also shows similar features to that of the absorption spectra with maxima at 310 and 367 nm indicating that the absorbing and the emitting species are similar.

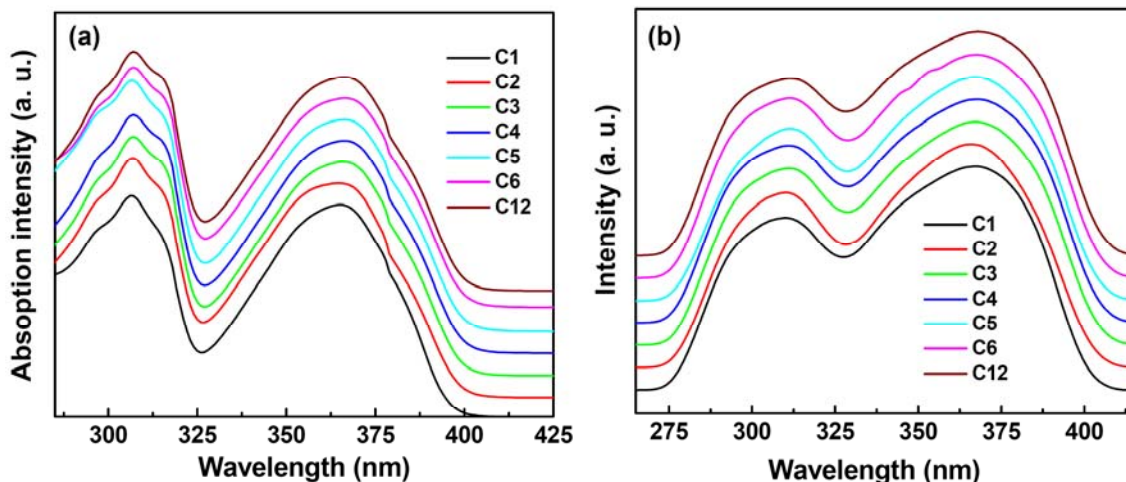


Figure 3.21: (a) Absorption in dilute solutions ($15\mu\text{M}$ in toluene) of oligo(phenyleneethynylene)s. (b) Excitation spectra (emission collected at 425 nm).

Table 3.3 Absorption and emission properties of phenyleneethynylenes in toluene ($15\mu\text{M}$)

Compound	λ_{max} (abs.)	$\epsilon, \text{M}^{-1} \text{cm}^{-1}$	λ_{max}	τ (ns)	χ^2	Q. yield
C0	321	5.288×10^4	350	0.97	1.032	0.91
C1	365	3.198×10^4	397	1.23	1.016	0.90
C2	365	2.964×10^4	401	1.32	1.013	0.92
C3	366	3.001×10^4	401	1.37	1.069	0.91
C4	366	3.209×10^4	401	1.45	1.047	0.91
C5	366	3.186×10^4	402	1.45	1.022	0.89
C6	367	3.093×10^4	403	1.35	1.099	0.91
C12	366	3.108×10^4	401	1.33	1.052	0.89

Table 3.3 lists the details of the absorption and emission characteristics of all the molecules (in solution). The fluorescence lifetimes were determined using time-correlated single photon counting (TCSPC) technique.²⁸ In all the cases, the emission decay exhibited monoexponential decay confirming the presence of a single emitting species. Molecule **C0** shows singlet excited state lifetime of 0.97 ns, in good agreement with the value previously reported in the literature.^{18a} Singlet excited state lifetimes of **C1** to **C12** lie within a narrow range of 1.23 to 1.45 ns with no systematic dependence on the chain length. The fluorescence quantum yield in toluene solutions were recorded using diphenylanthracene in cyclohexane as an internal standard ($\Phi = 0.9$). All the molecules

show high quantum yield of ~ 0.9 . Thus, it is clear that the chain length of dialkyloxy substitution does not have a significant effect on the photophysical properties of phenyleneethynylenes.

The solid state behavior of these molecules is quite different. Figure 3.22 shows the fluorescence emission spectra of **C1-C12** from crystalline samples. The crystals were obtained by slow evaporation of the solvent, toluene. The emission maxima of the crystals lie within the range, 444 to 515 nm with various shoulders. However, there is no systematic variation with respect to the chain length. It may be observed from Figures 3.20 and 3.22 that the main peak in **C1** showed a minimal red shift between the solution phase and the crystalline state, while **C2**, the maximum shift.

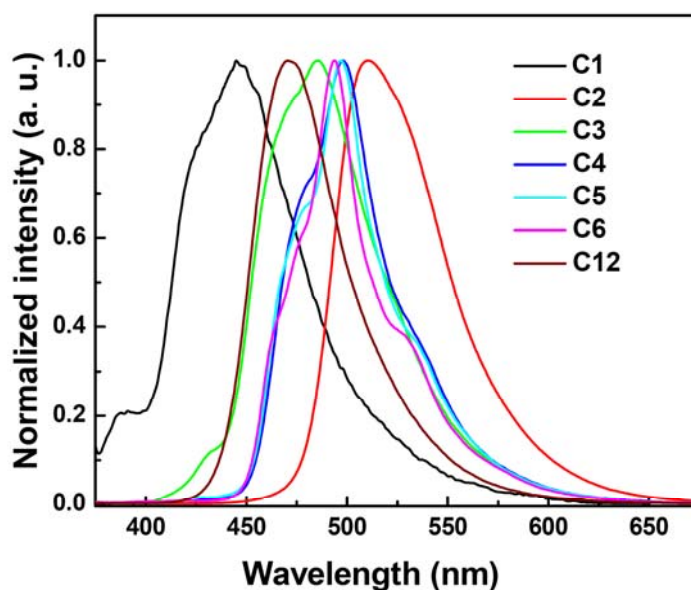


Figure 3.22: Fluorescence emission (excitation 360 nm) spectra for the crystals of oligo(phenyleneethynylene)s.

Figure 3.23 contains the excitation spectra of the crystalline samples. A number of intensity maxima are observed in each case indicating the presence of various emitting levels in the crystalline samples. The emission colors from the crystalline samples are represented with the help of chromaticity diagram CIE 1931 standard (see Figure 3.24). The **C1** system lies in the extreme blue region while **C2** is in the green region (see also Figure 3.22) and the rest of the molecules exhibit intermediate colors.

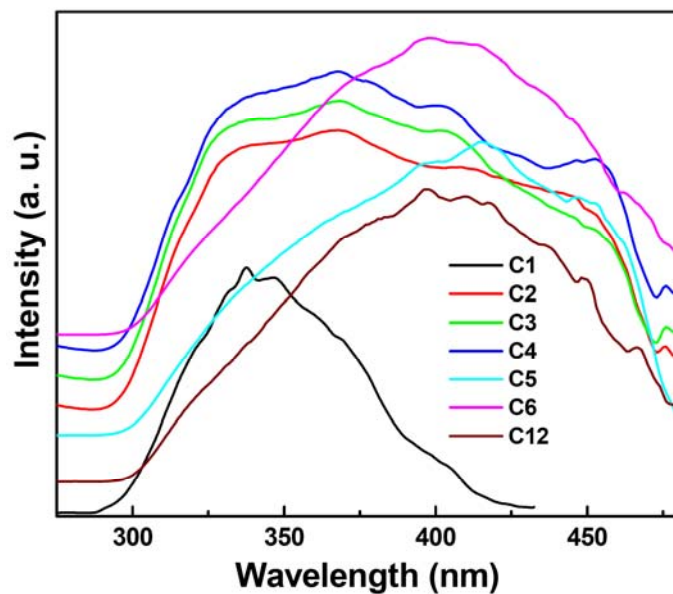


Figure 3.23: Excitation spectra (emission collected at 480 nm) for the crystals of oligo(phenyleneethynylene)s C2 to C12, Excitation spectrum for molecule C1 is recorded by collecting emission at 440 nm.

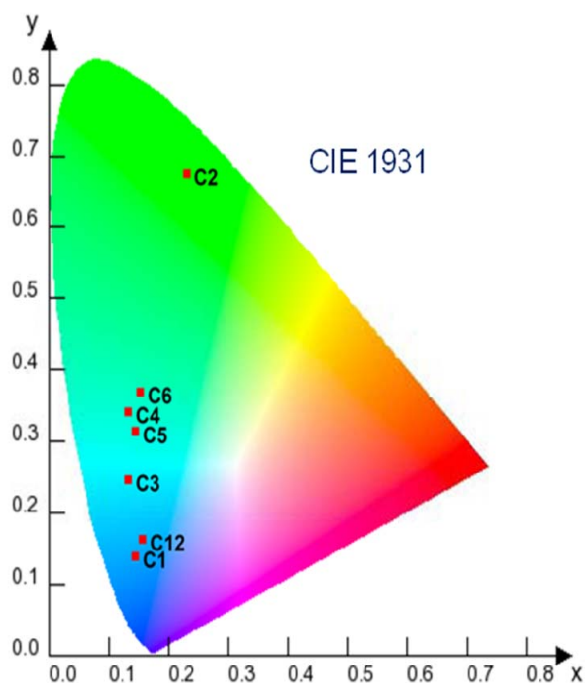


Figure 3.24: Chromaticity diagram (CIE 1931) showing the fluorescence emission colours from alkyloxy substituted oligo(phenyleneethynylene)s.

The solid state fluorescence quantum yields have been obtained using the integrating sphere.²² All the crystals exhibited quantum yields (up to 0.8) but these are

less compared to the values from the solution phase (compare Tables 3.3 and 3.4). Also, there is a spread in the values (0.28 - 0.82) in the crystalline state which is absent in solution. No systematic trend is observed with respect to the alkyl chain length.

Table 3.4 Solid state fluorescence quantum yield for various dialkyloxy substituted oligo(phenyleneethynylene)s.

Compound	$\Phi(\text{solid})$
C1	0.51(2)
C2	0.53(3)
C3	0.82(2)
C4	0.73(3)
C5	0.74(3)
C6	0.78(3)
C12	0.28(3)

In order to gain an insight into the fluorescence behavior of the various molecules (**C1** to **C12**), it is suggestive to study the underlying packing in the crystalline state. A detailed analysis of molecular packing revealed that for each molecule, there exist two neighbors. Thus, one finds two kinds of molecular pairs. Figure 3.25 shows the molecular pairs in the case of **C1**. In Figure 3.25a, the partner molecule extends an angle of 78.5° while in Figure 3.25b, they are parallel with spacing of 4.65 \AA . It is reasonable to consider

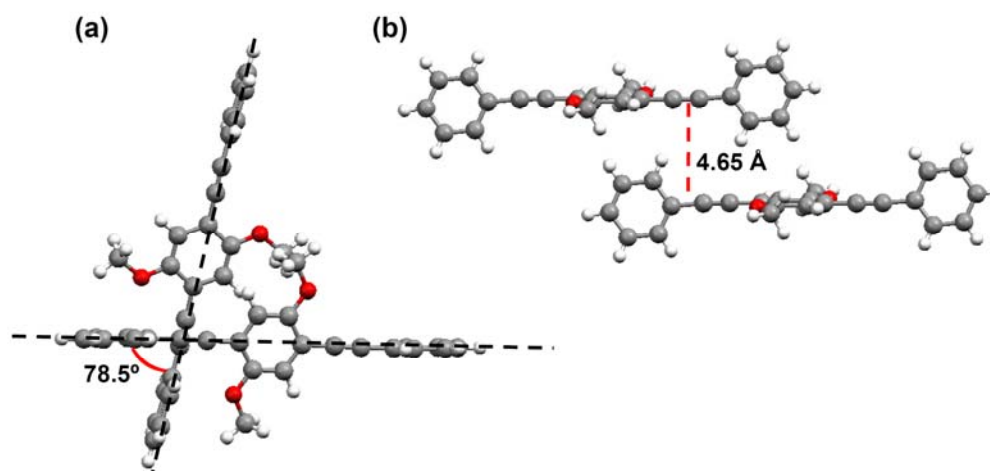


Figure 3.25: Intermolecular interaction possibility in molecule **C2** (a) a tilted pair of molecule and (b) a J-aggregate pair.

that first pair turns to be a non-interacting or weakly interacting, while the second as is an interacting pair. Such pairs are seen in Figures 3.26 and 3.27 taking **C2** and **C3** as examples. The molecular packing being similar (see Figures 3.6 and 3.7) such pairs may be expected in all the cases. The only differences will be in the values of the angle in non-interacting pairs and the molecular plane spacing in the interacting pairs. These values are listed in Table 3.5.

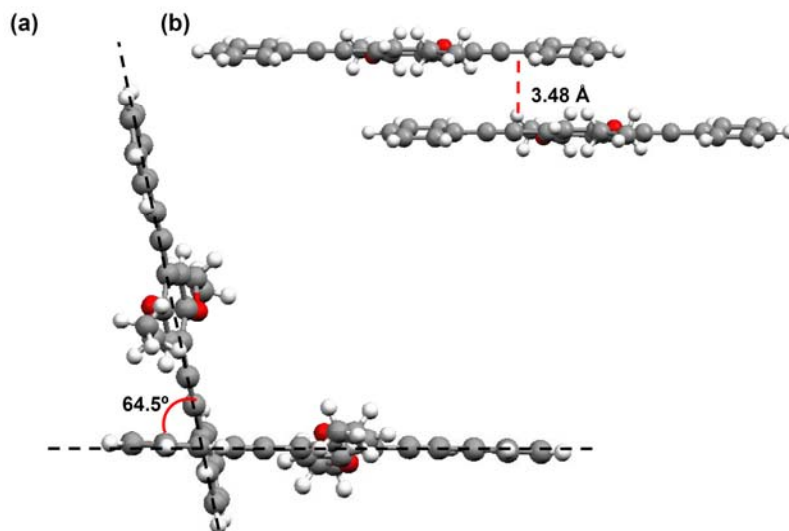


Figure 3.26: Intermolecular interaction possibility in molecule **C2** (a) a tilted pair of molecule and (b) a J-aggregate pair.

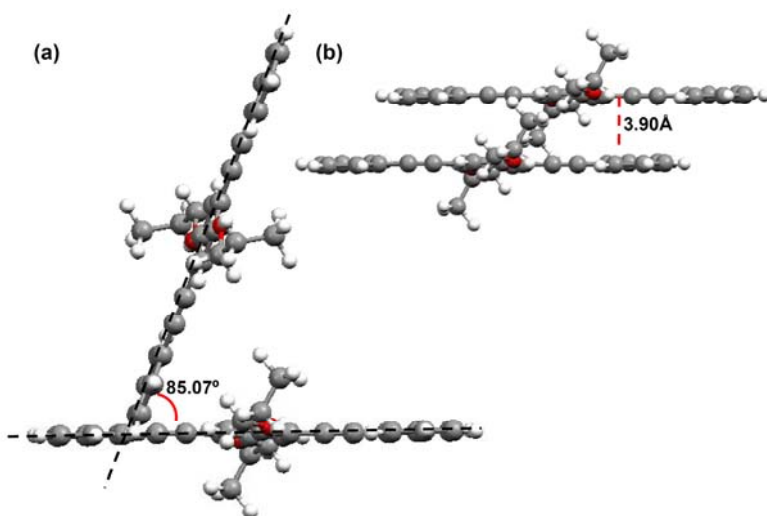


Figure 3.27: Intermolecular interaction possibility in molecule **C3** (a) a tilted pair of molecule and (b) a J-aggregate pair.

Table 3.5 The spacing between the mean molecular planes (interacting pair) and the angle (non-interacting pairs) between various dialkyloxy substituted oligo(phenyleneethynylene)s.

Compound	Molecular plane spacing (Å)	Angle between the molecules (°)
C1	4.65	78.5
C2	3.48	64.5
C3	3.90	85.1
C4	3.59	83.2
C5	3.67	79.1
C6	3.71	72.4
C12	3.47	67.2

Figure 3.28 shows a plot of spacing between the interacting molecules versus corresponding emission maxima. The observed red shift in the emission of crystalline samples shows a linear dependence with the decreasing spacing distance between the interacting pairs indicating that it plays a major role in determining the electronic coupling between the molecules. This is also a clear indication of the presence of J-aggregates in the crystalline samples. The molecule **C12** shows a deviation from planarity and this can be attributed to the slightly different molecular packing, with π - π stacking between the molecular pairs.

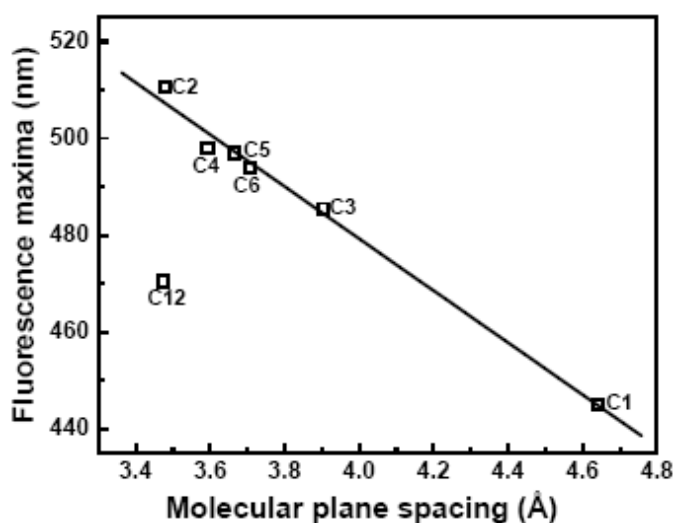


Figure 3.28: Variation of the emission maximum with the spacing between the interacting molecules in various crystals, **C1** to **C12** (excitation 360 nm)

Since the molecules in crystals exhibit interactions akin to J-aggregate where the distance between the interacting pair is different, the red shift in observed fluorescence emission in the solid state can be explained on the basis of exciton coupling theory developed by Kasha and coworkers.²⁹ According to this theory, the excited state energy levels of the monomeric compound splits in to two energy levels upon aggregation such that one level is lower in energy and the other, higher in energy than the monomer excited state. When the molecules are arranged in ‘head to tail’ fashion, it comprises a ‘J-aggregate’ where the transition moments align as shown in Figure 3.29. Hence, the allowed transition to the lowest excited state energy level gives rise to red shifted absorption and emission. On the other hand, when the molecules are arranged in a card pack type of arrangement the transition moments align parallel to form H-aggregate, where the transition to highest excited state energy level is allowed and this aggregate gives rise to a blue shifted absorption or emission.

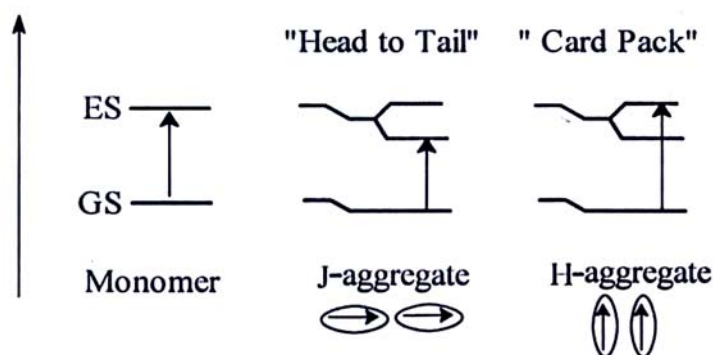


Figure 3.29: A representation of the allowed excited-state transitions for J-aggregated and H-aggregated molecules relative to that of the monomer.

In order to prove the presence of J-aggregate in the crystalline samples, KBr (potassium bromide) dilution of the crystalline samples of molecule **C6** has been carried out (see Figure 3.30). The dotted curve represents the emission spectrum from the crystalline sample of the molecule **C6**. On diluting with KBr (14.4 μM of **C6** in 100 mg of KBr), the spectrum shows a blue shift compared to that of the crystalline sample with similar spectral features, but with varying intensity which is attributed to the emission from the microcrystalline form of the compound **C6**. It is clear from the figure that on further dilution, red shifted peak disappears with the formation of a new blue shifted peak, which is comparable to the of the monomer fluorescence (see Figure 3.20) with an

isosbestic point. This clearly indicates that the red shifted emission in the crystalline samples of the dialkyloxy substituted oligo(phenyleneethynylene)s is due to the formation of the J-aggregate.

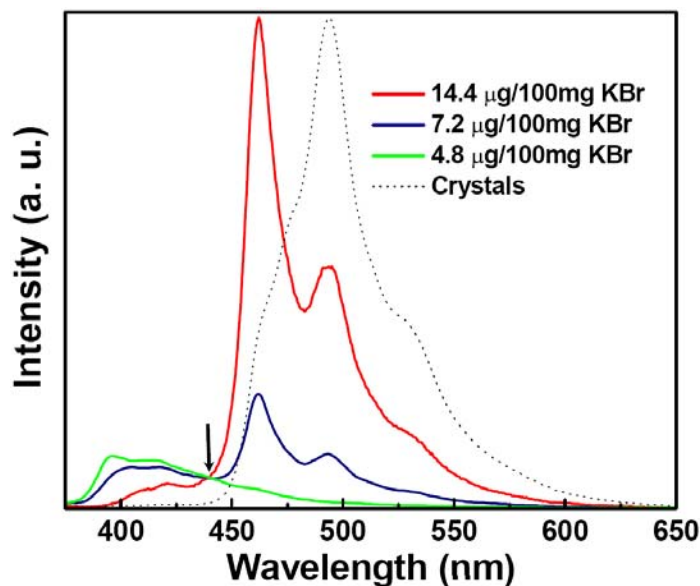


Figure 3.30: Fluorescence emission spectra (excitation 360 nm) for molecule 1,4-bis(phenylethynyl)-2,5-bis(hexyloxy)benzene, **C6**, recorded on dilution with KBr at different concentrations.

Table 3.6 Fluorescence lifetimes of dialkyloxy substituted oligo(phenyleneethynylene)s in the solid state.

Compound	Lifetime						
	τ_1 (ns)	F ₁ %	τ_2 (ns)	F ₂ %	τ_3 (ns)	F ₃ %	χ^2
C1	2.83	61	4.59	25	0.72	14	1.0
C2	3.10	55	4.68	42	0.35	3	1.01
C3	2.24	84	0.24	4	4.13	12	1.06
C4	0.22	3	2.63	97	-	-	1.07
C5	2.22	66	0.27	3	3.35	31	1.01
C6	0.20	2	2.55	95	5.29	3	1.00
C12	2.57	8	5.32	90	0.35	2	1.04

To further confirm that the red shifted emission in dialkyloxy substituted oligo(phenyleneethynylene)s is because of aggregation, a detailed fluorescence lifetime studies in the crystalline samples have been carried out. Table 3.6 shows the summary of the fluorescence lifetime measurements. All the compounds show tri-exponential decay except the molecule **C4**, which shows a bi-exponential decay with the longest lifetime species as the major one. Molecule **C2** shows two lifetimes with comparable relative abundance, whereas for molecules **C1**, **C3**, **C5** and **C6**, species with intermediate lifetime are the major components. For molecule **C12**, the major species was the one with the longest lifetime indicating the formation of the long lived excitons in the crystals.

3.4.3 Dependence of the fluorescence emission property on the cooling rate of the melt of 1,4-bis(phenylethynyl)-2,5-bis(methoxy)benzene, **C1**

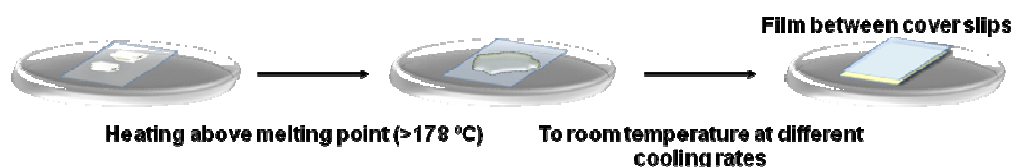


Figure 3.31: Cartoon showing the different steps cooling rate dependent experiments

Figure 3.31 shows the cartoon of the melt cooling experiments carried out on the crystalline samples of 1,4-bis(phenylethynyl)-2,5-bis(methoxy)benzene, **C1**. The melt of the compound **C1** was formed by heating the crystals of **C1** on clean glass cover slip by heating above its melting point (>178°) on a thermally isolated hot stage attached with digital temperature controller (Linkam stage). The melt was covered with a another glass cover slip and brought back to room temperature at different cooling rates varying from 1 to 13°C/min. The accuracy in temperature control was ± 0.1 °C.

Figure 3.32 shows the fluorescence emission spectra recorded for the films cooled from the melt at a cooling rate of 1 to 13 °C/min. The emission spectrum for 1°C/min cooled film shows a maxima centered around 480 nm with a slight broadening towards higher wavelengths. On increasing the cooling rate to 2 °C/min the fluorescence emission spectrum shows a quite different emission behavior i.e., a blue shift in the emission maximum. The emission from 2 °C/min cooled film consists of two maxima centered at 390 and 444 nm with a shoulder at 425 nm indicating the coexistence of various emitting species. The fluorescence maxima at 425 and 444 nm are similar to the emissions

observed in the case of single crystalline sample of the compound **C1** (see Figure 3.22). Similarly, the emission spectra were recorded for films obtained with the cooling rates of

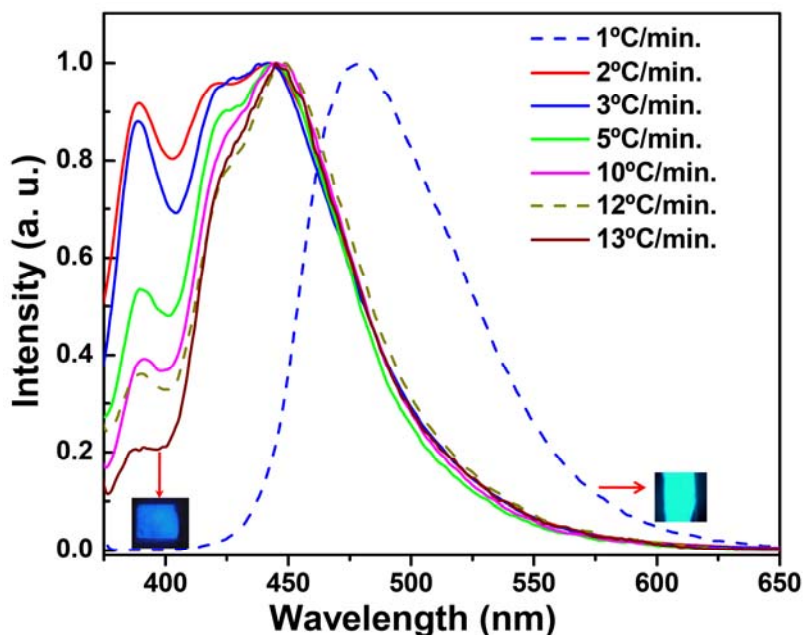


Figure 3.32: Cooling rate dependent emission behavior of molecule **C1**: cooling rate varies from 1 to 13°C/min.

3, 5, 10, 12 and 13° C/min and normalized with respect to the emission maximum at 444 nm (Figure 3.32). It is interesting to note that the peak centered at 390 nm shows a successive reduction in the intensity with increasing cooling rate and becomes a small shoulder for a cooling rate of 13 °C/min. The spectrum of the 13 °C/min cooled film resembles that of the crystals grown from solution (see Figure 3.22). The observed emission color is bluish-green 1 °C/min film which gradually shifts to blue as shown in the Figure 3.32.

Figure 3.33 shows the excitation spectra recorded for the films formed by cooling the melt at different cooling rates. Similar to that in the emission spectra, the difference in the spectral features is obvious in the excitation spectra as well. The excitation spectrum is recorded for the film formed by 1 °C/min cooling by collecting the emission at 490 nm. It shows the excitation maxima around 415 nm with a shoulder at 430 nm. In addition to this, a peak at lower wavelength region (335 nm) is also present which corresponds to the peak observed in the spectrum of the crystals grown from solution.

The excitation spectra are recorded for the films with cooling rates from 2-13 °C/min by collecting the emission at 440 nm. They show a maxima centered on the 335 nm along with two other shoulders at 365 nm and 415 nm; these shoulders show small variations in intensity with the cooling rates. The excitation spectra for the films collected at different cooling rates indicate that the nature of the emitting species are clearly different in the 1 °C/min cooled film as against other films with higher cooling rates.

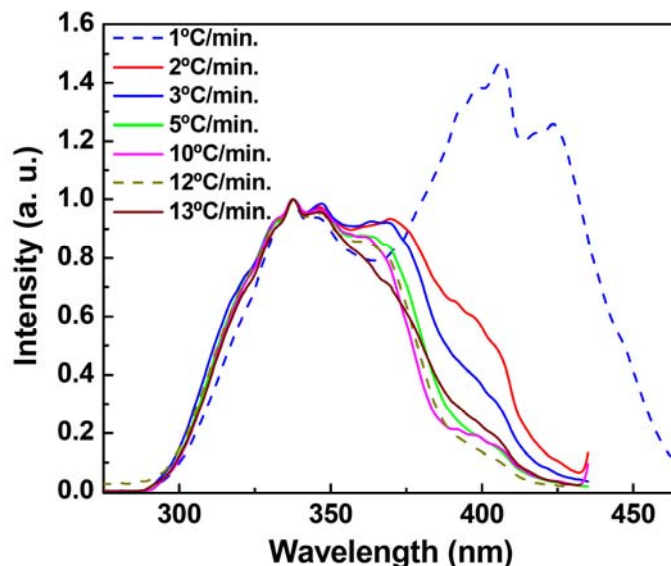


Figure 3.33: Excitation spectra recorded for the films formed with different cooling rate dependent emission behavior of molecule **C1**: cooling rate varies from 1 to 13 °C/min.

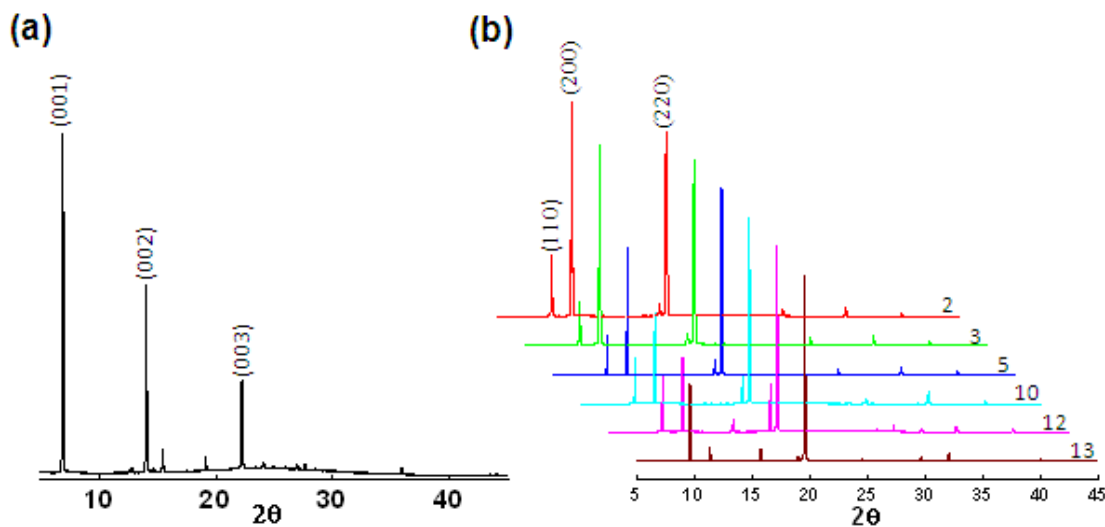


Figure 3.34: X-ray diffraction patterns for the film of molecule **C1** formed at different cooling rate from its melt (a) 1 °C/min (b) 2 to 13 °C/min. The patterns in (b) have been normalized with respect to the intensity of the (220) plane.

In order to understand the nature of the films of molecule **C1** formed at different cooling rates and also to investigate the reason for the fluorescence behavior, a detailed analysis of X-ray (XRD) diffraction patterns was carried out. Figure 3.34 shows the XRD pattern recorded for the 1 °C/min film. The pattern shows (see Figure 3.34a) three major peaks with varying d-values with ratios of 1:2:3 indicating the formation of a lamellar structure on the glass cover slip. Figure 3.34b shows the XRD patterns recorded

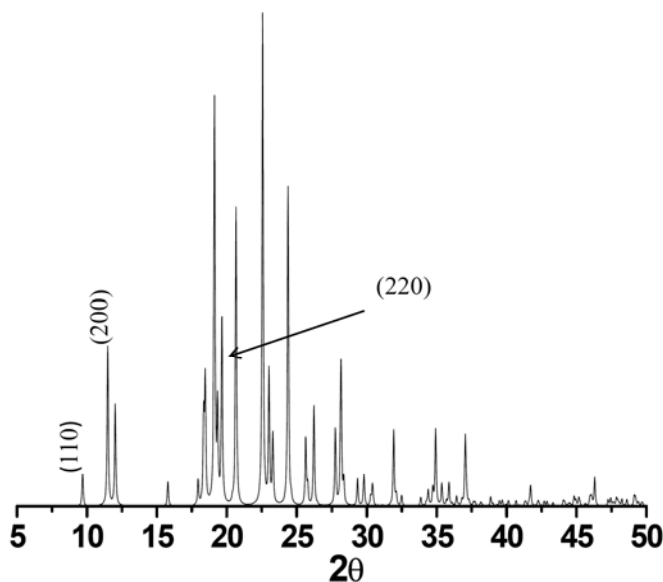


Figure 3.35: A simulated powder X-ray diffraction pattern from the single crystal data of molecule **C1**. (For details on single crystal data see section 3.4.1)

for the films with different cooling rates, 2 to 13 °C/min. These patterns are quite different from observed for the 1 °C/min film. The detailed analysis of that patterns revealed that all the peaks present could be indexed using a simulated powder pattern, obtained from the single crystal XRD data of **C1** grown from solution (see Figure 3.35). From Figure 3.34b, the peak corresponding to the (200) plane shows a decrease in intensity with increase in the cooling rate. Figure 3.36 depicts a plot of the fluorescence intensity at 390 nm as well as the XRD peak intensity (corresponding to the peak (200) plane) with respect to the cooling rate. The fluorescence intensity at the 390 nm peak is normalized with respect to the 444 nm peak whereas the XRD peak corresponding to (200) plane is normalized with respect to the intensity of the (220) plane. From the plot, it is clear that both the intensities show a systematic decrease with increase in the cooling rate. Figure 3.37 shows a plot where the fluorescence intensity at 390 nm is plotted

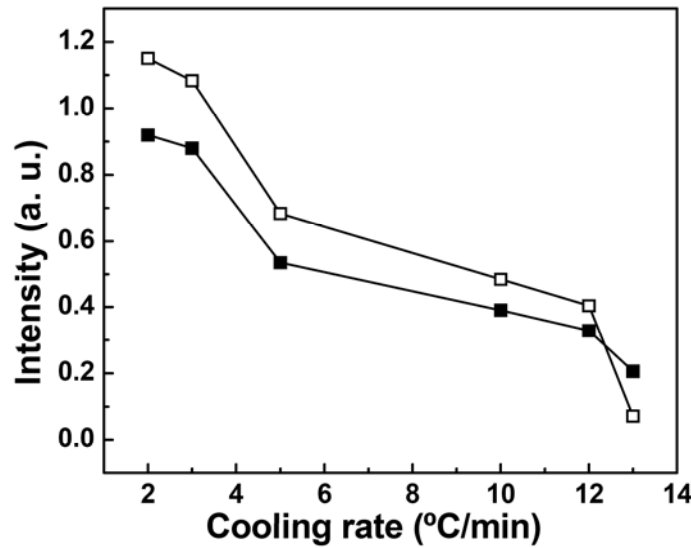


Figure 3.36: Variation in fluorescence intensity at 390 nm (filled squares) and the (200) peak intensity normalized with respect to that of (220) (open squares) for films obtained with different cooling rates.

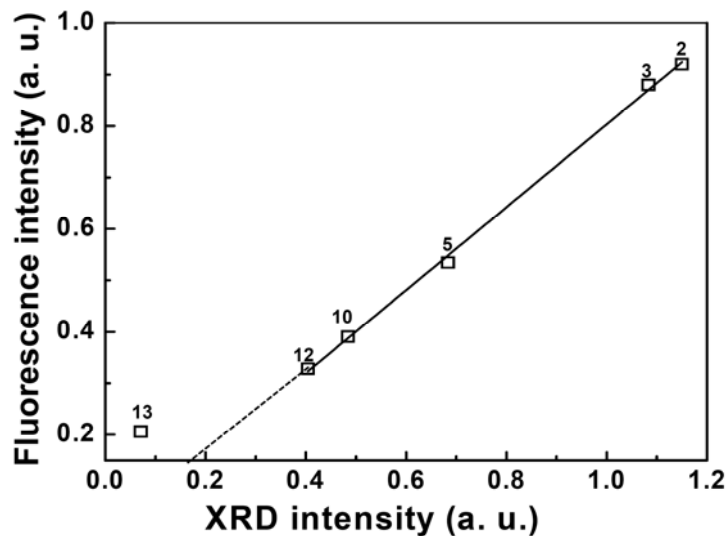


Figure 3.37: Variation in fluorescence intensity at 390 nm and the (200) peak intensity normalized with respect to that of (220) for films obtained with different cooling rates.

against the XRD intensity corresponding to the (200) plane. The plot shows a linear variation up to the cooling rate 12 °C/ min, indicating a dependence of the fluorescence emission on the preferred orientation of the film on the glass surface. The preferred orientation is along (200) planes at slower cooling rates while the orientation is along (220) plane at higher cooling rates.

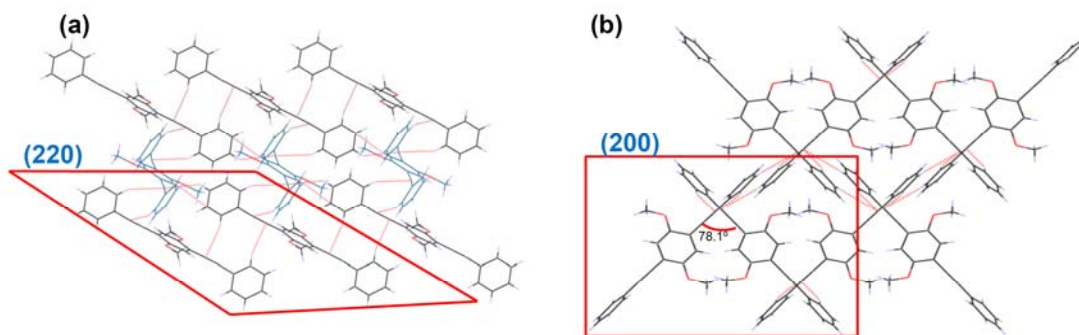


Figure 3.38: Packing of molecule C1 in crystallographic planes (220) and (200).

In order to understand the variation in the fluorescence intensity with the preferred orientation, an insight into the molecular packing along (200) and (220) planes is desirable. In the projection of the (220) plane, the molecules arrange in such a way that they form J-aggregate pairs as in the case of the crystals grown from solution, whereas along (200), the molecules form comprise a non-interacting pairs (see Figure 3.38). Hence, the emission peaks at 425 and 444 nm originate from the (220) oriented regions, whereas that observed at 390 nm arises due to crystallites oriented along the (200) plane. It is interesting to note that the 390 nm peak is even lower than what was seen in the case of solution phase spectrum (401 nm) (see Figure 3.20). The non planar conformation of molecule in crystals can be the reason for the blue shifted emission in the (200) oriented crystallites with respect to the monomeric emission in the solutions.

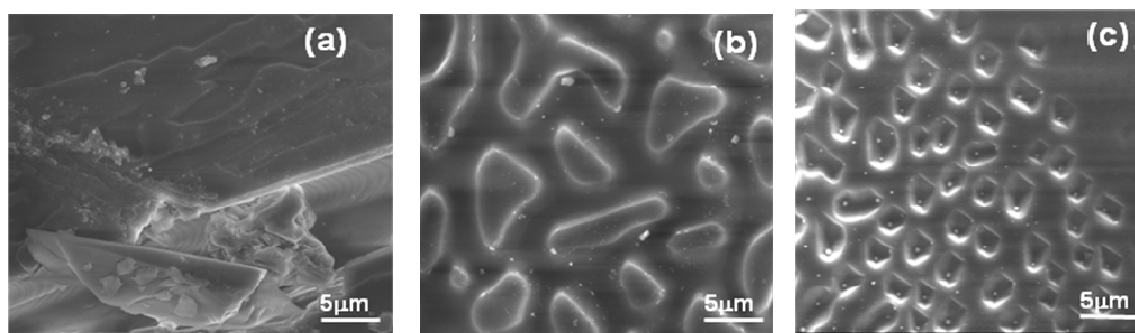


Figure 3.39: Scanning electron microscope image showing features on the films formed at different cooling rate (a) 3°C/min. (b) 10°C/min. (c) 13°C/min.

In order to understand the film morphology with different cooling rates, a scanning electron microscopy (SEM) was carried out. Figure 3.39 shows film the morphology at three different cooling rates. The film formed at a cooling rate of 3 °C/min

shows flakes, while that at 10 °C/min shows the presence of domain structures. On further increase in the cooling rate to 13°C/min, a reduction in the domain size is observed as shown in the Figure 3.39c. The difference in the observed film morphology with respect to the change in the cooling rates of the melt can be attributed to the cooling rate dependent preferential wetting of the surface.

Investigations have also been carried out to understand the nature of the film formed by cooling the melt rapidly. The rapid cooled film (>15°C/min) shows a broad fluorescence emission centered on 465 nm along with various shoulders and the film is transparent as shown in Figure 3.40. The broad emission of the rapid cooled film can be attributed to the presence of molecules in various orientations in the melt. On leaving the film for 12 hours at room temperature, the emission spectrum shows a shoulder at 500 nm with maximum retained at 465 nm. When the same film was annealed at 70 °C, the emission spectrum exhibited a blue shift resembling the emission of crystals grown from solution.

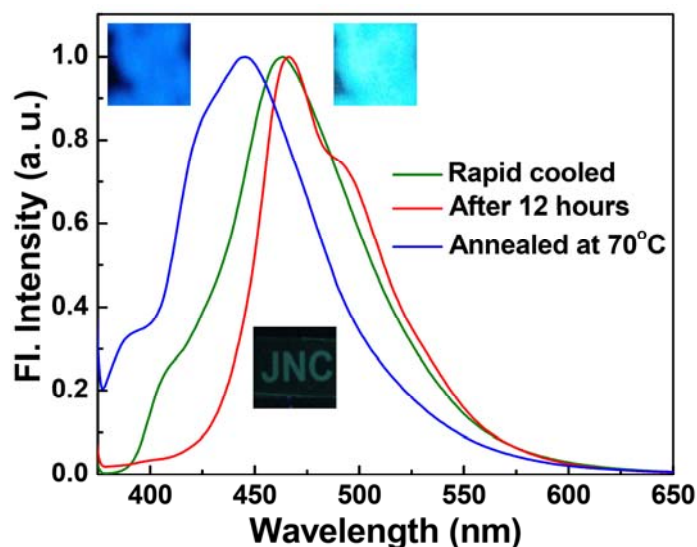


Figure 3.40: Fluorescence emission (excitation 360 nm) for a rapid cooled film.

The excitation spectra (see Figure 3.41) of the rapid cooled film show maxima at 405 nm with two more peaks at 369 and 335 nm. When the film is left for 12 hours at room temperature, it shows a change in the spectral features with maxima at 418 nm along with lower wavelength peak at 340 nm and a broad absorption at higher wavelength side. The excitation spectrum recorded after annealing the film at 70 °C

shows the maxima on 369 nm along with blue shifted and red shifted peaks centered on 330 and 405 nm respectively. The variations in the excitation spectra of the film clearly indicate that the nature of the absorbing species changes with annealing.

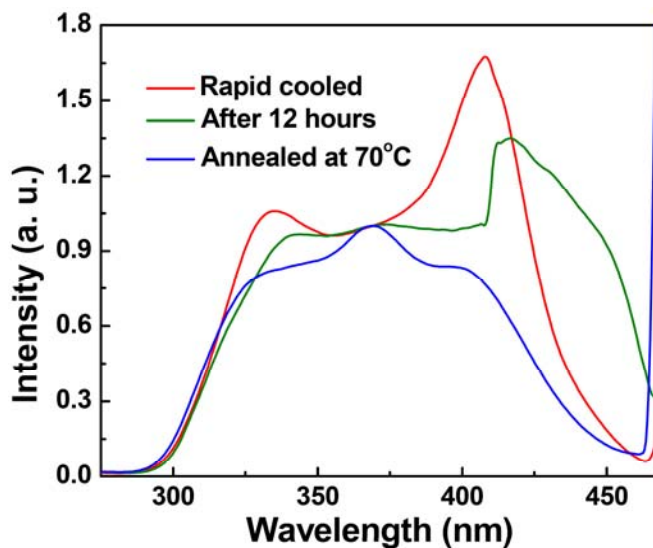


Figure 3.41: Excitation spectra recorded for a rapid cooled film (emission collected at 480 nm).

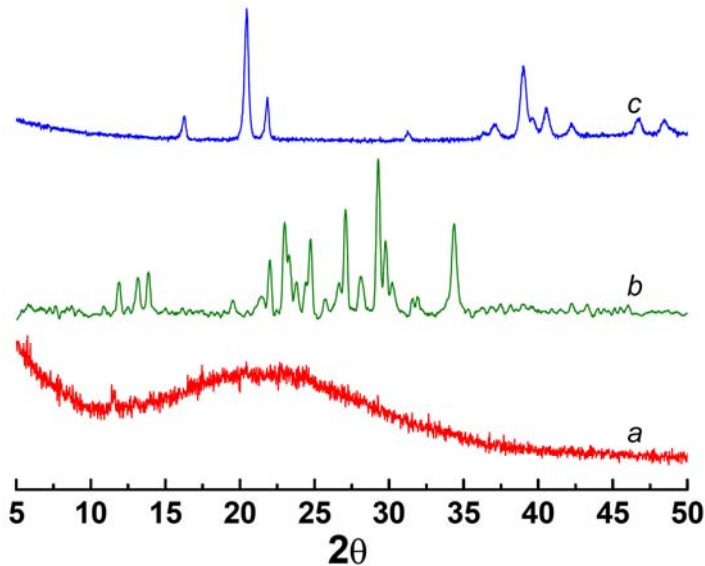


Figure 3.42: (a) Powder XRD patterns collected for (a) rapid cooled film a. Immediately after film formation, (b) After 12 hours and (c) on heat annealing after 12 hours

In order to understand the crystalline nature of the rapid cooled film, XRD patterns have been recorded (see Figure 3.42). A rapidly cooled film does not show any peak in XRD indicating that it is amorphous in nature. The pattern recorded after 12 hours

contained various peaks due to evolution of crystallinity but the XRD pattern does not show any similarity with the simulated powder pattern of the single crystal XRD data of **C1** (see Figure 3.35). On annealing the film at 70 °C, the XRD pattern shows a large difference with that recorded for the film left for 12 hours in the room temperature as well as with that of the simulated pattern.

To elucidate the structure of the molecules in the film formed by rapid cooling of the melt, detailed analysis has been carried out using IR-spectroscopy. Figure 3.43 shows the carbon-carbon triple bond stretching frequency for the films left for 12 hours (curve 'a') at room temperature and that for the thermal annealed (70 °C) film (curve 'b'). The spectrum 'a' shows two peaks at 2195 and 2214 cm^{-1} , of which the former corresponds to the molecules in the planar form. In planar form, the molecule is more conjugated which in turn gives rise to lower stretching frequency. The same film after annealing at 70 °C shows a single peak at 2217 cm^{-1} indicating that all the molecules go back to the thermodynamically stable phase from the kinetically trapped state.

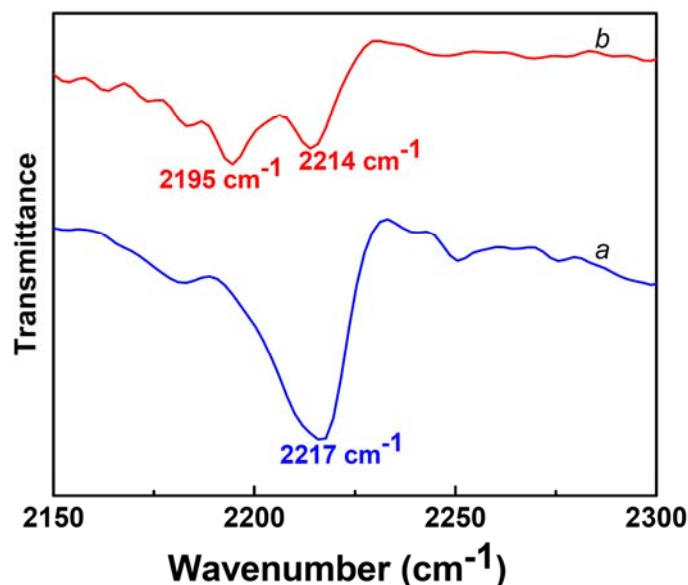


Figure 3.43: IR spectra showing C-C triple bond stretching: (a) Fast cooled film after 12 hours and (b) after heat annealing upto 70°C.

The melt cooling experiments of the molecules can be summarized as given in the Table 3.7. The observed photophysical property of **C1** is clearly born out of the structure of the film as seen by X-ray diffraction. At very small cooling rate i.e., less than 1°C/min, the melt would solidify on the substrate with molecules lying flat in extended lamellar

structures. This way low cooling rate allows complete wetting of the substrate surface by the molecules. The emission is broad and is red shifted, clearly due to possible strong aggregate formation. At slightly increased cooling rate such as 2°C/min, the crystallization process sets in, overriding the wetting property. Thus, we find large flaky domains with preferred (200) ordering. The aggregate interaction is, however, weak giving rise to predominant peak at 390 nm accompanied by 425 and 444 nm peaks. As the cooling rate increases further (3°C/min and above), there is increased dewetting of the film and a higher tendency to show the polycrystalline nature. Thus, small sized domains are seen with the (220) preferred orientation. This effect is more pronounced at higher cooling rates (upto 13°C/min), where only polycrystalline phase gets formed. An even

Table 3.7 Summary of the melt cooling experiments for the molecule 1,4-bis(phenylethynyl)-2,5-bis(methoxy)benzene, **C1**.

	Rate of cooling			
Cooling rate	1°C/min.	2 to 12 °C/min	13 to 14 °C/min	>15 °C/min
Structure	Lamellar Polymorph I	Preferred orientation (200) Plane ←→ (220) Plane	Polycrystalline Polymorph II	Glassy
Wetting	Complete (in equilibrium)	Dewetting → (semi equilibrium)	No wetting No interactions	Complete (non equilibrium)
Fluorescence	Highly red shifted	Blue emission ← 390 nm peak → 425 nm → 444 nm	Crystal emission	Red shifted
Aggregate	Cofacial	78.1° tilted dimer and J-aggregate ↑	J-aggregate etc.	Cofacial 70 °C

higher cooling rate takes the system into a glassy state which exhibits an extremely slow reversal to the crystalline phase. Accordingly, maximum aggregate interaction and hence highly red shifted peak may be expected in the glassy phase, which reverts to the crystalline phase gradually upon annealing at room temperature with characteristic emission at 444 nm. This reversal can be accelerated by holding the substrate at a slightly

elevated temperature i.e., 70°C. This observation unequivocally proves the glassy nature of the fast cooled melt.

3.5 Conclusions

This study presents the structure, weak interactions and the solid state photophysical properties of 1,4-bis(phenylethynyl)-2,5-bis(alkyloxy)benzenes. The structural analysis of the molecules using single crystal X-ray diffraction has shown that all the molecules show various types of deformation in the geometry. The structural deformations in the molecules are classified into mainly three types. These are rotation of the phenyl rings, in-plane lifting of the phenyleneethynylene backbone and the bending of the single-triple bond linker between the two phenyl rings. The molecule with methoxy substitution (**C1**), shows maximum deviation from planarity ($\sim 80^\circ$) while the molecule with dodecyloxy substitution (**C12**) shows a minimum deviation ($\sim 0.50^\circ$). On increasing the alkyloxy chain length the molecules show a tendency for the planarization of the phenyl rings which is attributed to the buildup of weak intermolecular interactions such as C-H... π and chain-chain interactions involving the alkyloxy chains. Other differences such as in-plane lifting of the phenyleneethynylene backbone and the bending of the single-triple bond linker is maximum in molecule **C4** (butyloxy substitution) due to a unique C-H...O arising from terminal phenyl ring. Both the aromatic rings and the alkyl chain hydrogens serve as donors while the triple bond and aromatic π -density are the potential acceptors. Interestingly, the acceptor nature of the triple bond is best expressed in molecules and with high deviation from planarity (**C1**, **C2**, **C4**) perhaps due to the charge localization resulting from limited conjugation.

All the molecules showed interesting photophysical properties in both the solution as well as in solid state. In the dilute solutions, the fluorescence peak positions (401 nm) and quantum yields (~ 0.9) are similar in all cases. The fluorescence behavior is quite different in the solid state. The fluorescence spectra showed varied peak maxima from 444 to 515 nm with hardly any noticeable trend with respect to the chain length. Further, the quantum yields were also varied, 0.3 to 0.8. The packing analysis using single crystal data showed that the molecules in the crystals form J-aggregate pairs, hence the red shifted emission. Interestingly, the red shift in emission could be linearly related to the

parallel spacing between the interacting pair of molecules in the J-aggregates. In another study, the molecule **C1** showed a cooling rate dependent emission behavior in the film sandwiched between two glass cover slips. The dependence of the fluorescence emission of the molecule **C1** with the rate of cooling of the melt has been attributed to the preferred orientation of the crystallites on the substrate and which in turn is related to the temperature dependent wetting nature of the substrate. This behavior is unique to molecule **C1**.

References

1. (a) T. A. Skotheim, J. R. Reynolds, *Handbook of Conducting Polymers*, Third Edition, Conjugated Polymers: Processing and Applications, C R C Publishers, USA, (b) W. Brütting, *Physics of Organic Conductors*, Wiley-VCH, Berlin, Germany (2005) (c) F. C. Spano, *Ann. Rev. Phys. Chem.*, (2006), **57**, 217.
2. (a) S. Suramitr, T. Kerdcharoen, T. Sriksirin, S. Hannongbua, *Synth. Met.*, (2005), **155**, 27; (b) S. Fratiloiu, F. C. Grozema, L. D. A. Siebbeles, *J. Phys. Chem. B*, (2005), **109**, 5644; (c) F. C. Grozema, L. D. A. Siebbeles, G. H. Gelinck, J. M. Warman, *Top. Curr. Chem.*, (2005), **257**, 1436; (d) G. D. Scholes, G. Rumbles, *Nat. Mater.* (2006), **5**, 683; (e) (d) A. Ajayaghosh, S. J. George, *Chem. Eur. J.*, (2005), **5**, 593.
3. (a) G. Voskerician, C. Weder, *Electronic Properties of PAEs*, Advances in polymer science, Springer, Berlin, Germany (2005); (b) J. C. Collings, A. C. Parsons, L. Porrès, A. Beeby, A. S. Batsanov, J. A. K. Howard, D. P. Lydon, P. J. Low, I. J. S. Fairlamb, T. B. Marder, *Chem. Commun.*, (2005), 2666; (c) J. Kim, *Pure Appl. Chem.*, (2002), **74**, 2031; (d) J. Kim, T. M. Swager, *Nature*, (2001), **411**, 1030.
4. (a) P. Puschnig, K. Hummer, C. A. Draxl, G. Heimel, M. Oehzelt R. Resel, *Phys. Rev. B*, (2003), **67**, 235321; (b) S. Tasch, A. Niko, G. Leising, U. Scherf, *Appl. Phys. Lett.*, (1996), **68**, 1090; (c) G. Leising, S. Tasch, F. Meghdadi, L. Athouel, G. Froyer, U. Scherf, *Synth. Met.*, (1996), **81**, 185.
5. (a) G. Gigli, O. Inganäs, M. Anni, M. De Vittorio, R. Cingolani, G. Barbarella, L. Favaretto, *Appl. Phys. Lett.* (2001), **78**, 1493; (b) T. Otsubo, Y. Aso, K. Takimiya, *Bull. Chem. Soc. Jap.*, (2001), **74**, 1789.
6. (a) G. Barbarella, M. Melucci, G. Sotgiu, *Adv. Mater.*, (2005), **17**, 1581; (b) L. De. Cole, *Molecular Wires from Design to Properties*, Springer, Berlin, Germany, (2005); (c) Y. M. Sun, K. Xiao, Y. Q. Liu, J. L. Wang, J. Pei, G. Yu, D. B. Zhu, *Adv. Funct. Mater.*, (2005), **15**, 818; (d) I. N. Hulea, S. Russo, A. Molinari, A. F. Morpurgo, *App. Phys. Lett.*, (2006), **88**, 113512.

7. (a) H. A. Al Attar, A. P. Monkman, M. Tavasli, S. Bettington, M. R. Bryce, *App. Phys. Lett.* (2005), **86**, 121101; (b) X. Gong, S. Wang, D. Moses, G. C. Bazan, A. J. Heeger, *Adv. Mater.* (2007), **17**, 2053; (c) C. J. Tonzola, A. P. Kulkarni, A. P. Gifford, W. Kaminsky, S. A. Jenekhe, *Adv. Mater.* (2007), **17**, 874.
8. (a) W. Ma, C. Yang, X. Gong, K. Lee, A. J. Heeger, *Adv. Funct. Mater.*, (2005), **15**, 1617; (b) J. Y. Kim, K. Lee, N. E. Coates, D. Moses, T. Q. Nguyen, M. Dante, A. J. Heeger, *Science*, (2007), **317**, 222.
9. (a) B. Kirtman, B. Champagne, *Int. Rev. Phys. Chem.*, (1997) **16**, 389; (b) S. K. Park, J. Y. Do, J. J. Ju, S. Park, M. Kim, M. H. Lee, *Mater. Lett.*, (2005), **59**, 2872; (c) Y. Kawabe, H. Ikeda, T. Sakai, K. Kawasaki, *J. Mater. Chem.*, 1992, **2**, 1025; (d) A. Mathy, K. Ueberhofen, R. Schenk, H. Gregorius, R. Garay, K. Müllen, C. Bubeck, *Phys. Rev. B*, (1996), **53**, 4367.
10. (a) S. Y. Hong, *Bull. Korean Chem. Soc.*, (1999), **20**, 42; (b) T. Mitsumori, I. M. Craig, I. B. Martini, B. J. Schwartz, F. Wudl, *Macromolecules*, (2005) **38**, 4698. (c) A. A. Argun, P. H. Aubert, B. C. Thompson, I. Schwendeman, C. L. Gaupp, J. Hwang, N. J. Pinto, D. B. Tanner, A. G. MacDiarmid, J. R. Reynolds, *Chem. Mater.*, (2004), **16**, 4401; (d) T. Jiu, Y. Li, H. Liu, J. Ye, X. Liu, L. Jiang, M. Yuan, J. Li, C. Li, S. Wang, D. Zhu, *Tetrahedron*, (2007) **63**, 3168; (e) J. M. Hancock, S. A. Jenekhe, *Macromolecules*, (2008), **41**, 6864.
11. (a) A. Salomon, D. Cahen, S. Lindsay, J. Tomfohr, V. B. Engelkes, C. D. Frisbie, *Adv. Mater.*, (2003), **15**, 1881; (b) W. Haiss, C. Wang, I. Grace, A. Batsanov, D. J. Schiffrin, S. J. Higgins, M. R. Bryce, C. J. Lambert, R. J. Nichols, *Nature Mater.*, (2006), **5**, 995.
12. (a) S. Lakshmi, S. K. Pati, *J. Chem. Phys.*, (2004), **121**, 11998; (b) J. M. Seminario, A. G. Zacarias, P. A. Derosa, *J. Phys. Chem. A*, (2001), **105**, 791; (c) Y. Karzazi, J. Cornil, J. L. Brédas, *Nanotechnology*, (2003), **14**, 165; (d) J. D. Le, Y. He, T. R. Hoye, C. C. Mead, R. A. Kiehl, *Appl. Phys. Lett.*, (2003), **83**, 5518; (e) S. Lakshmi, S. K. Pati, *Phys. Rev. B*, (2005), **72**, 193410.
13. J. Chen, M. A. Reed, A. M. Rawlett, J. M. Tour, *Science*, (1999), **286**, 1550.

14. (a) Z. J. Donhauser, B. A. Mantooth, K. F. Kelly, L. A. Bumm, J. D. Monnell, J. Stapleton, D. W. Price Jr., A. M. Rawlett, D. L. Allara, J. M. Tour, P. S. Weiss, *Science* (2001), **292**, 2303; (b) S. I. Khondaker, Z. Yao, L. Cheng, J. C. Henderson, Y. Yao, J. M. Tour, *Appl. Phys. Lett.* (2004), **85**, 645; (c) N. Li, K. Jia, S. Wang, A. Xia, *J. Phys. Chem. A*, (2007), **111**, 9393.
15. (a) E. Tekin, D. A. M. Egbe, J. M. Kranenburg, C. Ulbricht, S. Rathgeber, E. Birckner, N. Rehmann, K. Meerholz, U. S. Schubert, *Chem. Mater.*, (2008), **20**, 2727; (b) R. Davis, N. P. Rath, S. Das, *Chem Commun.*, (2004), 74; (c) R. Davis, N. S. Saleesh Kumar, S. Abraham, C. H. Suresh, N. P. Rath, N. Tamaoki, S. Das, *J. Phys. Chem. C*, (2008), **112**, 2137.
16. (a) H. Li, R. West, *Macromolecules*, (1998), **31**, 2866; (b) H. Li, D. R. Powell, R. K. Hayashi, R. West, *Macromolecules*, (1998), **31**, 52; (c) K. Yoosaf, P. V. James, A. R. Ramesh, C. H. Suresh, K. G. Thomas, *J. Phys. Chem. C*, (2007), **111**, 14933.
17. U. H. F. Bunz, *Chem. Rev.*, (2000), **100**, 1605.
18. (a) M. Levitus, K. Schmieder, Holly Ricks, K. D. Shimizu, U. H. F. Bunz, M. A. Garcia-Garibay, *J. Am. Chem. Soc.*, (2001), **123**, 4259; (b) P. Samorí, V. Francke, K. Müllen, J. P. Rabe, *Chem. Eur. J.*, 1999, **5**, 2312; (c) B. G. Sumpter, P. Kumar, A. Mehta, M. D. Barnes, W. A. Shelton, R. J. Harrison, *J. Phys. Chem. B*, (2005), **109**, 7671.
19. H. Meier, D. Ickenroth, U. Stalmach, K. Koynov, A. Bahtiar, C. Bubeck, *Eur. J. Org. Chem.*, (2001), 4431.
20. S. M. Dirk, D. W. Price, S. Chanteau, D. V. Kosynkin, J. M. Tour, *Tet. Lett.*, (2001), **57**, 5109.
21. A. I. Vogel, A. R. Tatchell, B. S. Furnis, A. J. Hannaford, P. W. G. Smith, *Vogel's Textbook of Practical Organic Chemistry (5th Edition)*, ELBS-Longman, Singapore publishers, Singapore (1989).
22. M. Muccini, M. Murgia, C. Taliani, A. D. Esposti, R. Zamboni, *J. Opt. A: Pure Appl. Opt.*, (2000), **2**, 577–583.
23. H. Mattoussi, H. Murata, C. D. Merritt, Y. Iizumi, J. Kido, Z. Kafaf, *J. Appl. Phys.*, (1999), **86**, 2642.

24. S. W. Watt, C. Dai, A. J. Scott, J. M. Burke, R. L. Thomas, J. C. Collings, C. Viney, W. Clegg, T. B. Marder, *Angew. Chem. Int. Ed.*, (2004), **43**, 3061.
25. P. Sykes, *Guide Book to Organic Reactions Mechanisms*, Longman group, London (1975).
26. H. Suezawa, S. Ishihara, Y. Umezawa, S. Tsuboyama, M. Nishio, *Eur. J. Org. Chem.*, (2004), 4816.
27. P. V. James, P. K. Sudeep, C. H. Suresh, K. G. Thomas, *J. Phys. Chem. A*, (2006), **110**, 4329.
28. Manual, Time Correlated Single Photon Counting, HORIBA Jovin Yvon Inc., (2006).
29. E. G. McRae, M. Kasha, *J. Chem. Phys.*, (1958) **28**, 721.

EXPERIMENTAL CHARGE DENSITY FOR DESCRIBING CONJUGATION IN 1,2-PHENYLACETYLENE AND 1,4- DIPHENYLBUTADIYNE*

Summary

This chapter deals with the analysis of experimental charge density in phenyleneethynylene prototypes 1,2-diphenylacetylene and 1,4-diphenylbutadiyne derived from high resolution X-ray diffraction data. The occurrence of two different geometries of the molecule in the crystal structure of 1,2-diphenylacetylene, one being planar and the other tilted by $\sim 6^\circ$, has been investigated in relation to the nature of the acetylene linker. 1,4-diphenylbutadiyne exists as a half molecule in the asymmetric unit. The experimental charge density analysis shows that the acetylene linker exhibits a non-cylindrical density reminiscent of the strong conjugation present in the 1,2-diphenylacetylene molecule whereas, that in 1,4-diphenylbutadiyne have triple bond character close to an ideal triple bond. This is in clear contrast to the situation 1,2-diphenylacetylene, where the charge density parameters resemble more closely those of a double bond due to extended conjugation. This is attributed to the mixed nature of the π -density in 1,4-diphenylbutadiyne thus diminishing the extended conjugation that was present in 1,2-diphenylacetylene. The π -orbitals of the acetylenic linker in 1,2-diphenylacetylene derived from DFT calculations, are found to sustain a variety of conjugation lengths between the phenyl rings, thereby giving flexibility to the molecule to arrange itself in various packing conformations in the crystal. It is interesting that the energy involved for such distortions is only $k_B T$, allowing several polymorphic forms of the crystal structure as reported in the literature.

*A paper based on above studies has appeared in J. Phys. Chem. B (2005) and another has been submitted to Pramana (2008)

4.1 Introduction

Conjugated organic molecules have been well studied in literature in view of their potential applications in electronic and photonic devices. These include molecular wire or one-dimensional conductors,¹ electronic controllers,² logic gates,³ FET (field effect transistors),⁴ photo-responsive systems⁵ and liquid crystalline devices.⁶ More often, these molecules consist of either fused aromatic ring systems or phenyl rings linked by ethylene or acetylene groups (phenylene vinylene systems and phenyl acetylene systems),¹⁻⁶ or polyacetylenes.⁷

During the last decade, the phenyl-acetylene based molecular conductors have raised a great deal of interest among researchers worldwide. This is primarily due to the ability to tune their electronic properties by changing functional groups and in turn the geometry. Various researchers have studied the electrical properties of these thiol functionalized oligomers using different techniques such as self assembly,⁸ mechanical break junction,⁹ cross wire junction,¹⁰ or by binding to the nanoparticle.¹¹ It is interesting to note that when these molecules are functionalized with donor, acceptor or donor-acceptor combinations give rise to fascinating properties such as rectification and Negative Differential Resistance (NDR) effects.¹² It has also been shown that, in addition to functional group effects, the change in the molecular geometry may also influence the electrical properties.¹³ The theoretical studies by Seminario et al,¹⁴ on thiotolane sandwiched between two gold electrode have shown that the switching of electronic state between conducting and non conducting by changing the angle between the phenyl ring. The possibility for such a variation in conducting states by changing the molecular geometry is offered by the cylindrical symmetry of triple bond.

Recently, there are some interesting reports on strength of conjugation and hyperconjugation in molecules such as 1,3-butadiene and 1,3-butadiyne.¹⁵ Unlike these molecules, in phenyleneethynylene based molecular conductors; the extent of conjugation critically depends on the degree of the planarity across the molecular length which is determined by the scope of phenyl ring rotation offered by the triple bond. Hence, triple bonds in phenyleneethynylenes play a major role in determining the conjugation in the molecules. In last few years, there have been a number of theoretical¹⁶ and experimental¹⁷ (spectroscopic) studies on alkyne groups. However, the triple bonds in conjugated

systems have received little attention, particularly in relation to the charge density distribution and electrical transport. In this context the method of electronic charge density analysis based on X-ray crystallography has to be well suited as it has been applied to study diverse aspects of molecular systems.¹⁸⁻²² The charge density $\rho(r)$ is a fundamental physical property which uniquely characterizes an electronic system.²³ Charge density of a chemical entity can be obtained theoretically from high level *ab initio* calculations and from high resolution X-ray diffraction experiments at low temperatures.^{18a} The topological analysis of $\rho(r)$ based on Bader's Atoms In Molecules (AIM) allows a quantitative description of bonds, non-bonding interactions, electronic structure and reactivity.²⁴

4.2 Scope of the Present Investigation

There are a number of reports in the literature dealing with the charge transport in phenyleneethynylenes and related compounds.⁸ There are also theoretical studies examining the frontier molecular orbitals and relating to the mechanism of the transport.¹⁴ However there are no reports on the electronic charge density distribution in this molecules in relation to the transport properties. The only charge density study is on *cis*-2,2'-ethynyldibenzoic acid²⁵ does not deal specifically with the above aspect. The present investigation is an attempt to understand the nature of charge distribution especially around the acetylenic linker and its influence in the molecular conjugation. For this purpose 1,2-diphenylacetylene and 1,4-diphenylbutadiyne were chosen. While 1,2-diphenylacetylene carries a triple bond and phenyl rings are linked by a single-triple-single bonds, the 1,4-diphenylbutadiyne carries an additional triple bond. This study also presents the results of the analysis of Cambridge Structural Data (CSD) to reason out the presence of two half molecule in the asymmetric unit of a highly symmetric molecule like 1,2-diphenylacetylene and which is supported by density functional (DFT) calculations. In particular, this study exemplify the role of the additional triple bond in 1,4-diphenylbutadiyne in the light of experimental charge density and *ab-initio* theoretical analysis.

4.3 Experimental Section

The title compounds 1,2-diphenylacetylene and 1,4-diphenylbutadiyne were synthesized following reported procedures.²⁶ Rod shaped crystals of these compounds were obtained from their methanolic solutions on slow evaporation at 4 °C and room temperature respectively. High quality crystals of the compounds were chosen after examination under an optical microscope. X-ray diffraction intensities were measured by ω scan using a Siemens three circle diffractometer attached with a CCD area detector, and graphite monochromator for the Mo K α radiation (50 kV, 40 mA). The crystals were cooled to 130 K on the diffractometer using a stream of cold nitrogen gas from vertical nozzle and the temperature maintained within 1 K throughout the data collection.

The unit cell parameters and the orientation matrix of the crystals were initially determined using ~80 reflections from 25 frames collected over a small ω scan of the 7.5° sliced at 0.3° intervals. A hemisphere data set of the reciprocal space was collected with 2 θ settings of the detector at 28° and 70°. Data reduction was performed using the SAINT program (Siemens, 1995)²⁷ and the orientation matrix along with the detector and cell parameters were refined over every 40 frames on all the measured reflections. The experimental details were listed on the Table 4.1. Absorption corrections were applied using the SADABS program (Siemens, 1995).²⁸ The crystal structure was first determined with a low-resolution data up to $\sin\theta/\lambda = 0.56\text{\AA}^{-1}$. The phase problem was solved by direct methods and the non-hydrogen atoms were refined anisotropically, by means of the full matrix least squares procedure using the SHELXTL program (Siemens, 1995).²⁹ All the hydrogen atom positions were located from difference Fourier map. The bond lengths and bond angles are comparable with the previous structure reports of 1,2-diphenylacetylene³⁰ and 1,4-diphenylbutadiyne.³¹ Detailed tables for bond lengths and bond angles along with isotropic displacement parameters are provided in Appendix Tables A4.1 to A4.4.

The charge density analysis was carried out on the basis of multipole expansion of the electron density centered at the nucleus of the atoms³² using XD package³³ A high-order refinement of the data was performed using reflections with $(\sin\theta)/\lambda \geq 0.4\text{\AA}^{-1}$ and $F_o \geq 5\sigma$. All the hydrogens were held constant throughout the refinement along with their

isotropic temperature factors. Multipolar refinement was carried out following the procedure discussed in the General experimental and related aspects section of Chapter 1. The parameters after the multipole refinement is provided in Table 4.1 (also see Appendix Tables A 4.5 onwards and related Figures).

4.4 Results and Discussion

4.4.1 Analysis of structure and weak interactions

Figure 4.1 shows the ORTEP plots of 1,2-diphenylacetylene and 1,4-diphenylbutadiyne with the asymmetric unit labeled. Crystal data and other experimental details are listed in Table 4.1. 1,2-diphenylacetylene and 1,4-diphenylbutadiyne crystallize in monoclinic space groups $P2_1/c$ and $P2_1/n$ respectively. The asymmetric unit of 1,2-diphenylacetylene contains two half molecules, where the acetylenic bond carries

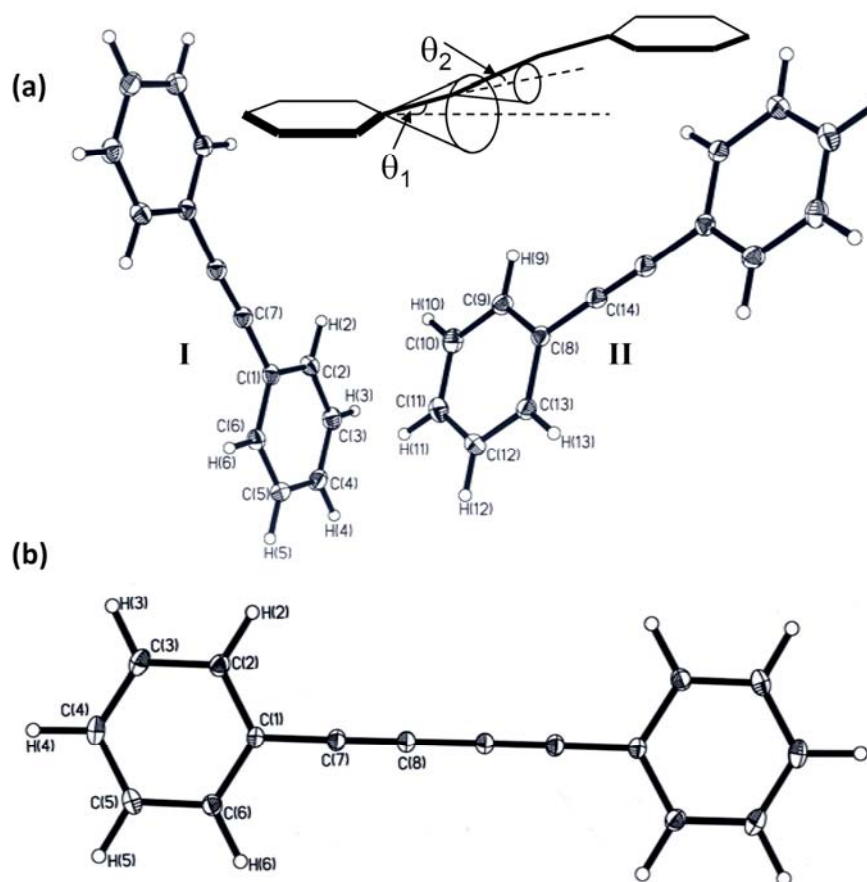


Figure 4.1: ORTEP plot at 50% probability (a) 1,2-diphenylacetylene (molecule I and molecule II) and (b) 1,4-diphenylbutadiyne: Schematic in the inset shows the deviation from planarity in molecule I of 1,2-diphenylacetylene.

Table 4.1 Crystal Structure data of 1,2-diphenylacetylene and 1,4-butadiyne

Chemical formula	C ₁₄ H ₁₀	C ₁₆ H ₁₀
Formula weight	178.22	202.24
Cell setting	Monoclinic	Monoclinic
Space group	P2 ₁ /c	P2 ₁ /n
a (Å)	15.2816(2)	6.5715(1)
b (Å)	5.7161(1)	6.0157 (1)
c (Å)	12.7546(2)	14.5092(3)
β(°)	113.764(1)	102.378(1)
ρ (g/cm ³)	1.161	1.199
μ, mm ⁻¹	0.066	0.068
Cell volume (Å ³)	1019.67(3)	560.25(2)
Crystal size (mm)	0.35 × 0.3 × 0.3	0.25 × 0.27 × 0.40
Z	4	2
F(000)	376	212
Radiation type	Mo K _α (0.71073 Å)	Mo K _α (0.71073 Å)
Crystal-detector distance (cm)	5.0	5.0
Temperature (K)	130 (1)	130 (1)
No. of measured reflections	15815	9186
No. of independent reflections	8839	4771
R _{int}	0.0503	0.0261
θ _{max} (°)sinθ/λ (Å ⁻¹)	1.46 to 49.34	2.87 to 49.36
Refinement		
Refinement on F ²		
R ₁	0.0711	0.0943
WR ₂	0.1846	0.1345
S	0.909	1.188
No. of reflections used in the	8839	4759
No. of parameters refined	167	93
After multipole refinement		
Weighting scheme	0.0853,	0.0952, 0.2146
R{F}	0.037	0.0396
R{F ² }	0.0596	0.0535
S	1.1447	1.003
No. of variables	246	208
N _{ref} /N _v	16.89	22.5240

a centre of inversion in both the molecules of 1,2-diphenylacetylene. The 1,4-diphenylbutadiyne consists of half a molecule with one triple bond where the inversion center lies in the geometric centre of the molecule. Molecule **II** in 1,2-diphenylacetylene is perfectly planar while molecule **I** is distorted along the length characterized by θ_1 , 2.1° and θ_2 , 3.2° with the phenyl rings being parallel (see schematic in Figure 4.1). In the

representation shown in Figure 4.1, θ_1 is the solid angle made by the single bond with the axis of the aromatic ring and θ_2 is that made by the triple bond with the single bond. The molecules of 1,4-diphenylbutadiyne are perfectly planar. The single bond ($sp^2(\text{aromatic})-sp$) in 1,4-diphenylbutadiyne is slightly elongated, 1.435(1) Å as compared to 1.424(1) Å in 1,2-diphenylacetylene, while for triple ($sp-sp$) bonds, it is the other way (1.205(2) as against 1.217(1) Å), both however being higher than the neutron value (1.189 Å).³⁴ (see Appendix Table A4.1 also). Interestingly in 1,4-diphenylbutadiyne, the single ($sp-sp$) bond connecting the two triple bonds is much shorter (1.363(2) Å). Thus, it is clear that in phenyleneethynylene molecules, the single bonds are noticeably shortened and the triple bonds are elongated compared to the ideal values, 1.54 Å and 1.18 Å respectively, but the extent is varied among the molecules. While the hybridization around the linker bonds present is similar in both the molecules, it is the degree of conjugation seems to be responsible for the observed bond lengths differences.

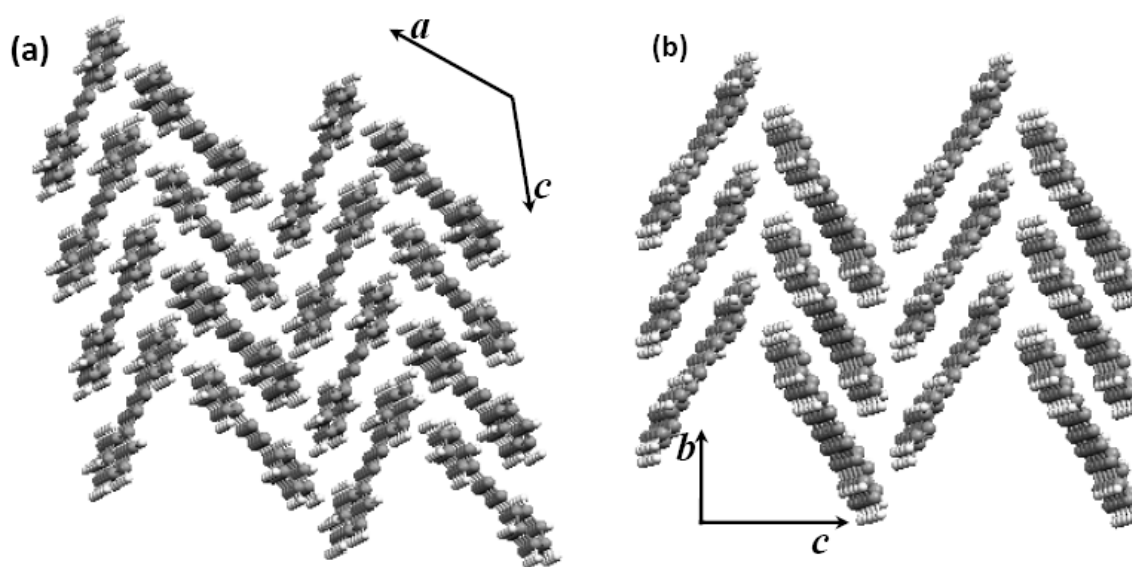


Figure 4.2. Molecular packing of (a) 1,2-diphenylacetylene (b) 1,4-diphenylbutadiyne.

Figure 4.2 shows the molecular packing in 1,2-diphenylacetylene and 1,4-diphenylbutadiyne molecules. Both 1,2-diphenylacetylene and 1,4-diphenylbutadiyne molecules pack in herringbone fashion along b and a axis respectively. In 1,2-diphenylacetylene each herringbone stack consist of alternating molecules **I** and **II** (see Figure 4.1) where the distance between mean plane passing through two parallel molecules being 2.504 Å.

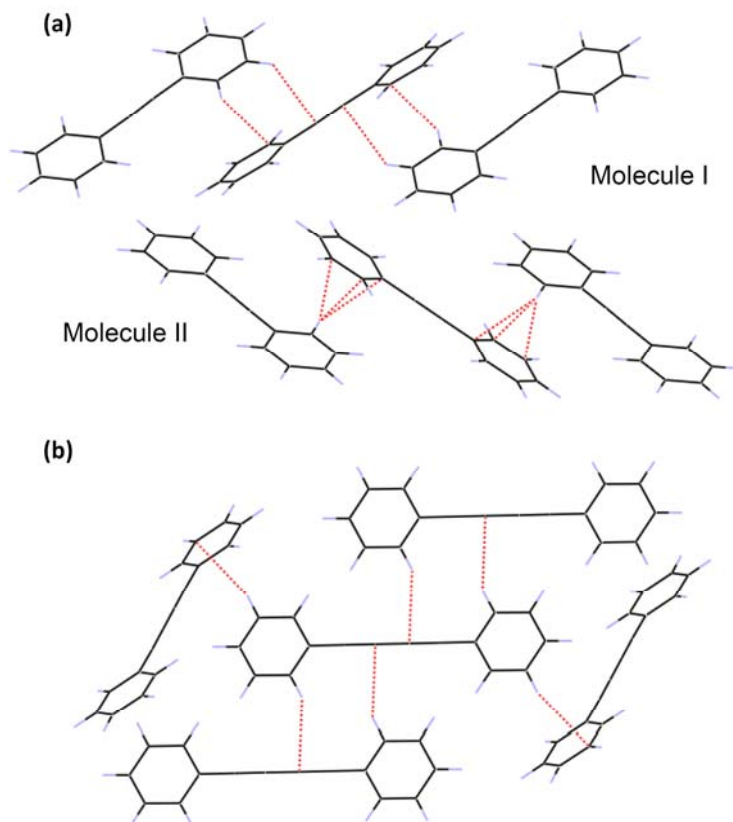


Figure 4.3: C-H... π interactions between the molecules 1,2-diphenylacetylene (a) molecule **I** (b) molecule **II** and (c) 1,4-diphenylbutadiyne.

Molecules of 1,2-diphenylacetylene pack in crystal lattice through various C-H... π interactions. It is interesting to note that these interactions are clearly between the molecules present in the individual stack and there are no such interactions between the successive molecular stacks. Importantly, individual herringbone stacks are built up of different C-H... π interactions exclusively either between the molecules **I** or **II**. The C-H... π interactions in the alternating stacks are clearly different in nature. Figure 4.3a shows the C-H... π interactions present in the stacks of molecules **I** and **II**. It is clearly evident from the Figure 4.3a that only one stack of molecules forms C-H... π interactions where both the triple bond as well as phenyl ring act as acceptor for C-H... π interactions. The H...A distance and D-H...A angle for the C-H... π interactions formed with the triple bond are 2.89(1) Å and 135.3(2) ° respectively while that formed with aromatic ring are 2.79(2) Å and 145.5(1) °. The C-H... π interactions in the molecular stack formed by the molecules of type **II** clearly originate from the hydrogen atom H13 where the π -density

at the C8, C12, C13 of the nearest molecule acts as an acceptor. The average distance and angle for these interactions are 2.852(1) Å and 155.24(2) ° respectively. The interactions in 1,4-diphenylbutadiyne consists of a pair of C-H... π interactions with aromatic ring (C5-H5... π C5) and triple bond (C2-H2... π C8) carbon atoms as acceptors with the distances 2.897(1) Å and 2.883(1) Å respectively. It is noteworthy that unlike 1,2-diphenylacetylene, the herringbone stacks in 1,4-diphenylbutadiyne are connected through C-H... π interaction C5-H5... π C5 (see Figure 4.3b)

4.4.2 Analysis of Experimental Charge Density

The method of experimental charge density has been used to derive a quantitative picture of the extent of conjugation in 1,2-diphenylacetylene and 1,4-diphenylbutadiyne. The topology of the charge density in the bonding regions is usually quantified by the critical point (CP) analysis.²⁴ The important bond parameters are the total density at the critical point (ρ_{BCP}) and its Laplacian, ($\nabla^2\rho_{\text{BCP}}$), and the ellipticity, ϵ . The value of ρ_{BCP} is a measure of the bond strength, where as the Laplacian signifies the extent of depletion or concentration of the bonding density. The ellipticity, which is related to the ratio of the curvatures along the minor and major principal axis perpendicular to the bond, measures the extent of conjugation and the π -character of the bond. Ellipticity values of ideal single, double and triple C-C bonds are 0.014, 0.298, 0.0 respectively.³⁵

The deformation density maps depict the bonding regions in these molecules (see Figures 4.4a and b). The contours show typical of covalent bonding present in the molecules 1,2-diphenylacetylene and 1,4-diphenylbutadiyne respectively, which is also clear from the Laplacian maps shown in Figure 4.5. Both deformation and Laplacian maps show a typical density distribution in the phenyl ring region. A similar observation can be made in the case of triple bond regions in 1,2-diphenylacetylene and 1,4-diphenylbutadiyne which is shown in Figures 4.5b and c respectively. The C-C ring bonds in the contours show a uniform distribution, where the atomic orbitals overlap give rise to a covalent bonding in the benzene ring. The average values of BCP (bond critical point) parameters, density and Laplacian in the aromatic ring regions for molecule **I** are 2.21 $e\text{Å}^{-3}$ and $-17.1 e\text{Å}^{-5}$ respectively and for molecule **II**, the values are not very different (2.18 $e\text{Å}^{-3}$ and $-16.4 e\text{Å}^{-5}$), where as in the case 1,4-

diphenylbutadiyne these values are $2.33(4) e\text{\AA}^{-3}$ and $18.2(1) e\text{\AA}^{-5}$ indicating that the phenyl ring region in both the molecules comparable. The ellipticity at the bond critical point for

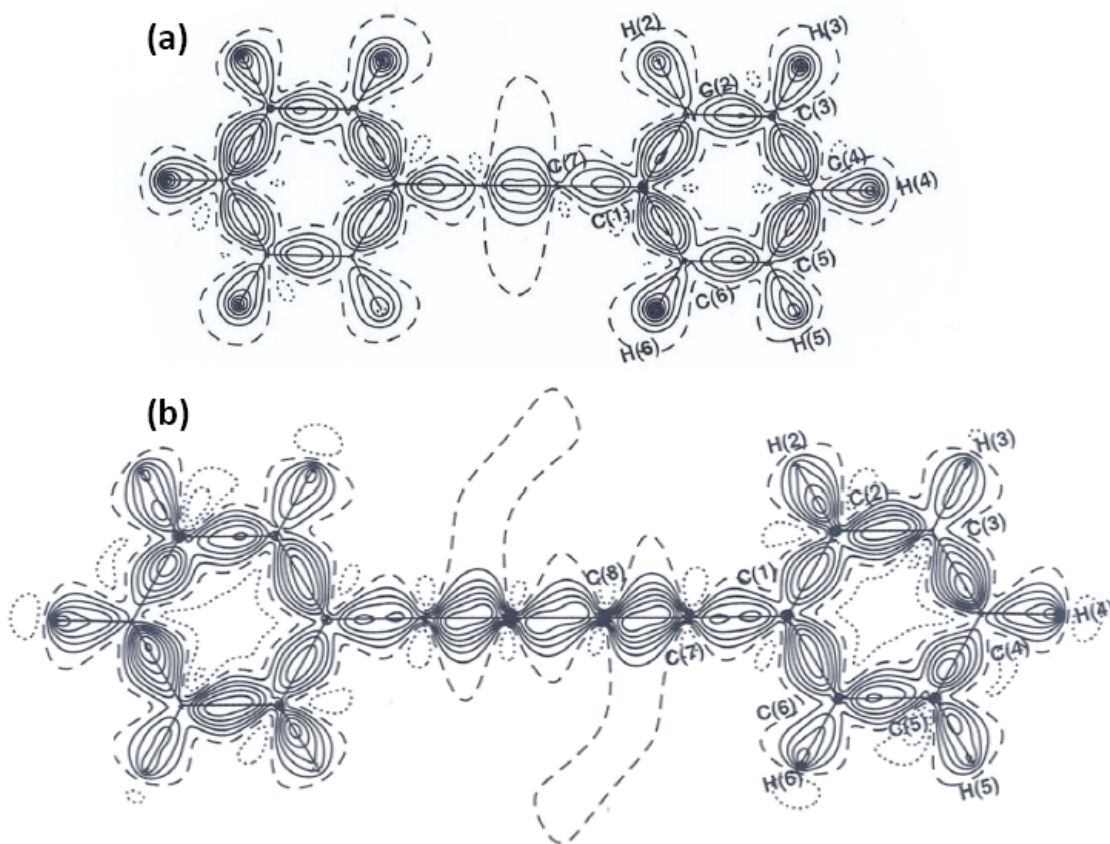


Figure 4.4: Deformation density maps for (a) 1,2-diphenylacetylene and (b) 1,4-diphenylbutadiyne.

the benzene ring bonds in the fragments are found to be 0.14 and 0.21 for molecules **I** and **II** respectively, which is less compared to the reported value (0.23) for a typical benzene ring bonds.³⁶ The ellipticity values for the aromatic carbon-carbon bonds in the case of 1,4- diphenylbutadiyne is 0.25 which is comparable with previous report.³⁵ Figure 4.5b shows the Laplacian map at the single and triple bond regions for a typical 1,2-diphenylacetylene molecules. Evidently, the contours are more closely packed in the triple bond regions of 1,2-diphenylacetylene compared to that of single bond region. The triple bond in 1,2-diphenylacetylene has a density of $2.79 e\text{\AA}^{-3}$, (see Table 4.2) considerably lower than that of an ideal triple bond ($2.82 e\text{\AA}^{-3}$).³⁶ Concomitantly, the Laplacian is also considerably reduced from the ideal value $-30.9 e\text{\AA}^{-5}$ to -21.0 and $-20.8 e\text{\AA}^{-5}$ respectively. It is interesting to see the contours in the region of the single bond (*sp-sp*) in 1,4-diphenylbutadiyne showing densely packed contours (Figure 4.5c), where this

unique single bond carries a Laplacian value of $-13.89(1) e\text{\AA}^{-5}$ much like an ideal double bond ($11.99 e\text{\AA}^{-5}$).³⁶ The triple bonds in 1,4-diphenylbutadiyne show a density and Laplacian values of $3.01(1) e\text{\AA}^{-5}$ and $24.1 e\text{\AA}^{-5}$ respectively. It is interesting to compare the cross sectional view of Laplacian at the critical point of triple bonds in 1,2-diphenylacetylene and 1,4-diphenylbutadiyne. Figure 4.5d, i and ii shows such a cross

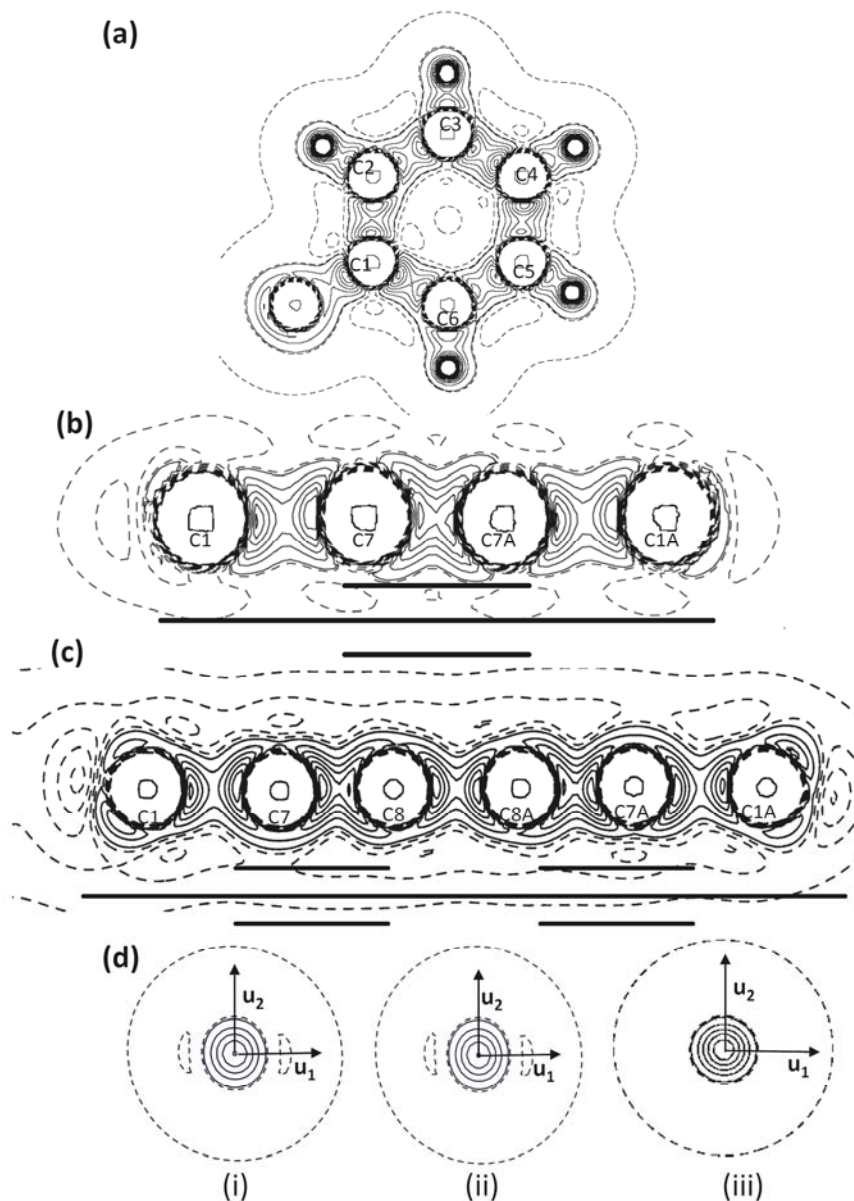


Figure 4.5: Laplacian maps (a) in the plane of a benzene ring. In the plane of the single and triple bonds of (b) 1,2-diphenylacetylene (c) 1,4-diphenylbutadiyne; (d) Laplacian map of the triple bond in the eigen plane spanned by eigen vectors u_1 (minor) and u_2 (major axis), 1,2-diphenylacetylene (i) molecule I and (ii) molecule II (iii) 1,4-diphenylbutadiyne.

Table 4.2 Bond critical point parameters in 1, 2-diphenylacetylene and 1, 4 - diphenylbutadiyne.

Molecule	Bond	$\rho(\text{\AA}^{-3})$	$\nabla^2\rho(e\text{\AA}^{-})$	$\lambda(e\text{\AA}^{-5})$	$\lambda(e\text{\AA}^{-5})$	$\lambda(e\text{\AA}^{-})$	ε
1,2-diphenylacetylene, Molecule I	C(1)-C(2)	2.31(4)	-18.2(1)	-17.83	-15.88	15.53	0.12
	C(2)-C(3)	2.02(4)	-13.3(1)	-14.85	-13.22	14.76	0.12
	C(3)-C(4)	2.27(4)	-17.7(1)	-19.18	-16.43	17.85	0.17
	C(4)-C(5)	2.38(4)	-20.4(1)	-18.86	-16.81	15.26	0.12
	C(5)-C(6)	2.07(4)	-14.9(1)	-16.04	-13.39	14.53	0.20
	C(6)-C(1)	2.24(4)	-17.9(1)	-18.11	-15.98	16.17	0.13
	C(1)-C(7)	1.93(3)	-12.9(1)	-14.46	-13.63	15.22	0.06
	C(7)-C(7)A	2.81(5)	-21.0(1)	-19.60	-15.71	14.32	0.25
	C(2)-H(2)	1.95(8)	-15.8(3)	-19.9	-19.28	23.35	0.03
	C(3)-H(3)	2.06(8)	-16.7(4)	-23.15	-22.30	28.76	0.04
	C(4)-H(4)	1.82(7)	-13.5(2)	-16.93	-15.48	18.93	0.09
	C(5)-H(5)	1.96(8)	-15.2(4)	-20.89	-20.04	25.79	0.04
	C(6)-H(6)	2.11(8)	-18.7(4)	-24.08	-22.58	-27.92	0.07
	1,2-diphenylacetylene, Molecule II	C(8)-C(9)	2.29(4)	-17.2(1)	-17.64	-15.37	15.85
C(9)-C(10)		1.99(4)	-13.8(1)	-15.49	-12.28	13.98	0.26
C(10)-C(11)		2.28(4)	-19.9(1)	-20.09	-16.00	16.24	0.26
C(11)-C(12)		2.36(4)	-19.1(1)	-18.70	-16.22	15.82	0.15
C(12)-C(13)		1.97(4)	-11.8(1)	-14.30	-11.73	14.20	0.22
C(13)-C(8)		2.22(4)	-16.4(1)	-18.68	-14.65	16.95	0.27
C(14)-C(8)		1.84(4)	-10.5(1)	-13.54	-11.51	14.59	0.18
C(14)-C(14)A		2.78(5)	-20.8(1)	-19.57	-16.31	15.10	0.20
C(9)-H(9)		1.94(7)	-15.6(2)	-19.16	-18.30	21.84	0.05
C(10)-H(10)		2.00(8)	-19.1(3)	-22.47	-20.70	24.11	0.09
C(11)-H(11)		1.84(8)	-15.6(3)	-18.53	-18.03	20.93	0.03
C(12)-H(12)		2.02(8)	-18.3(3)	-21.35	-20.82	23.85	0.03
C(13)-H(13)		1.95(8)	-13.2(4)	-23.07	-21.27	31.16	0.08
1,4-diphenylbutadiyne	C(1)-C(2)	2.12(3)	-15.3(1)	-17.48	-14.07	16.24	0.24
	C(2)-C(3)	2.33(3)	-19.3(1)	-20.09	-16.10	16.88	0.25
	C(3)-C(4)	2.33(4)	-18.4(1)	-19.89	-15.54	16.99	0.25
	C(4)-C(5)	2.10(4)	-14.8(1)	-17.14	-13.57	15.90	0.26
	C(5)-C(6)	2.22(3)	-17.4(1)	-18.71	-15.31	16.58	0.22
	C(6)-C(1)	2.28(4)	-16.5(1)	-19.05	-15.15	17.75	0.26
	C(1)-C(7)	2.04(3)	-11.5(1)	-15.70	-13.77	18.00	0.14
	C(7)-C(8)	3.01(4)	-24.1(1)	-21.45	-20.20	17.53	0.06
	C(8)-C(8)A	2.29(8)	-13.9(1)	-17.23	-16.43	19.78	0.05
	C(2)-H(2)	1.91(6)	-17.3(2)	-21.22	-18.94	22.86	0.12
	C(3)-H(3)	1.75(6)	-13.1(2)	-17.39	-16.56	20.85	0.05
	C(4)-H(4)	1.94(6)	-16.0(2)	-19.17	-17.72	20.85	0.08
	C(5)-H(5)	1.85(6)	-15.8(2)	-20.24	-17.96	22.36	0.13
	C(6)-H(6)	1.77(5)	-13.0(2)	-17.55	-16.08	20.71	0.09

sectional view of Laplacian in 1,2-diphenylacetylene. It is interesting to see that the contours in both i and ii are elliptical in nature indicating the deformation in the triple bond density due to charge migration which is an after effect of the extended conjugation present in the molecule. The Laplacian for the triple bond in 1,4-diphenylbutadiyne (Figures 4.5d(iii)) is more symmetric. The nature of this Laplacian map clearly indicates that the charge polarization is significantly less in 1,4-diphenylbutadiyne as compared to that in 1,2-diphenylacetylene.

The delocalization of electron density from the triple bond is apparent from the ellipticity values. The triple bonds in 1,4-diphenylbutadiyne exhibit values (0.06) that in spite being close to the ideal value (0.0), are distinctly finite. Compare this situation with that in 2,2'-ethynylendibenzoic acid,²⁵ where the two phenyl rings are twisted to an extent of 20°; here the middle triple bond behaves like an ideal triple bond with ellipticity of 0.01.²⁵ However, when compared to 1,2-diphenylacetylene (0.23), the value of 0.06 is considerably less. Thus, the charge delocalization in 1,4-diphenylbutadiyne is limited relative to that in 1,2-diphenylacetylene. It is clear that for effective delocalization, besides molecular planarity, the triple bond is to be linked on both the sides by phenyl rings, which is not the case in 1,4-diphenylbutadiyne and hence reduced conjugation.

4.4.3 Cambridge Crystallography Data (CSD) Analysis

Indeed, the presence of two non-identical geometries of 1,2-diphenylacetylene in the crystal structure is not unusual. A search through Cambridge Structural Database (CSD) provided 26 clear hits, out of which 8 are polymorphic forms,^{30,37} while the remaining 18 reports are cocrystals of 1,2-diphenylacetylene with either organic or metal organic complexes.³⁸ Interestingly, all the 8 polymorphs crystallize in monoclinic $P2_1/a$ or $P2_1/c$ space groups and their cell parameters vary in a narrow range (see Table 4.3). This is clearly due to the flexibility in the nature of the chemical bonds in the 1,2-diphenylacetylene molecule, as discussed in the theoretical section later. Earlier reports have attributed this observation to an increase in libration about the longitudinal axis of the molecule.³⁰ Of the 26 hits, 2 are duplicates and 3 do not contain 3D coordinates. Besides these, 1,2-diphenylacetylene in an orthorhombic lattice containing single planar molecule (CCDC ref. No: 606397) is also included in current study. However, as the crystal was unstable, it could not be used for charge density data collection. Including the

polymorph presented in this charge density analysis, the total number of structures used in CSD analysis will be 23.

Table 4.3 Cell parameters^a of the various structural reports on 1,2-diphenylacetylene^{30,37}

Sl no	CCDC refcode	a(Å)	b(Å)	c(Å)	β (°)	Volume (Å ³)
1	DPHACT	15.67	5.73	12.75	115.2	1035.856
2	DPHACT01	15.68	5.772	12.714	114.63	1045.989
3	DPHACT02	15.508	5.764	12.778	113.39	1048.34
4	DPHACT03	15.488	5.754	12.766	113.36	1044.426
5	DPHACT04	15.509	5.762	12.782	113.4	1048.292
6	DPHACT05 ^b	15.204	5.685	12.721	113.9	1005.255
7	DPHACT06 ^b	15.27	5.708	12.741	113.74	1016.55
8	DPHACT07	15.495	5.754	12.762	113.37	1044.492

^aCell settings have been made uniform for the purpose of comparison.

^bCrystal data collected at low temperatures.

The observed distortions in the non-planar molecules **I** from all the crystal structures in addition to the polymorph shown in the Figure 4.1a, are characterized in terms of angular rotations θ_1 and θ_2 as defined earlier (see schematic in Figure 4.1a). The analysis of geometric variations resulted in a range of θ_1 and θ_2 values varying from 0.58° to 2.24° and 1.11° to 3.73° for the polymorphs and 0.53° to 2.32° and 0.67° to 4° for the cocrystals respectively. However, as shown in Table 4.4, there are 4 cocrystals with large θ_1 and θ_2 values. Such large distortions in their molecular structure with unusual bond-lengths are due to solid state effects, namely OH- π interactions as in CCDC refcode *GAWLEV*,^{38l} π - π interactions as in *JOXLIR*^{38m} and regio constraints due to steric class of repulsions as in *BETDEJ*³⁸ⁿ and *EBAWUA*.^{38o} This study investigates how 1,2-diphenylacetylene molecule can incorporate such small distortions. It is noteworthy that even in the presence of the tilt in the molecular geometry; the single bond lengths in the two molecules are comparable. This is suggestive of a high degree of conjugation present in these molecules. On the other hand, the comparable bond lengths in the various structures of 1,2-diphenylacetylene molecules reported in CCDC indicate that the 1,2-diphenylacetylene molecules can accommodate smaller distortions on packing the molecules in the crystal lattice without disrupting the conjugation.

Table 4.4: Various reports on 1,2-diphenylacetylene in CCDC with varying geometry defined by θ_1 and θ_2 , δE represents the energy change between the planar molecule.^{30,37,38}

Sl. No.	CCDC refcode	Single bond(Å)	Triple bond(Å)	θ_1 (°)	θ_2 (°)	δE (eV)
1	Asijer	1.439	1.190	1.75	1.75	0.01742
2	Cepnoa	1.455	1.255	0.53	2.63	0.00327
3	Cifwuj	1.437	1.199	1.4	1.17	0.00574
4	Dphact01a*	1.416	1.223	2.23	3.73	0.01872
4	Dphact01b*	1.395	1.221	2.24	1.33	0.01461
5	Dphact02a*	1.437	1.199	0.92	1.55	0.00301
5	Dphact02b*	1.436	1.205	2.52	4.93	0.029
6	Dphact03a*	1.439	1.192	1.91	1.88	0.01135
6	Dphact03b*	1.435	1.191	1.4	1.11	0.00569
7	Dphact05a*	1.425	1.211	2.27	2.42	0.01649
7	Dphact05b*	1.425	1.211	0.58	1.74	0.00188
8	Dphact06a*	1.428	1.210	2.23	2.31	0.01580
8	Dphact06b*	1.433	1.205	0.66	1.7	0.00209
9	Dphact07a*	1.440	1.198	2.16	1.9	0.000526
9	Dphact07b*	1.435	1.197	0.93	2.04	0.00329
10	Hamhuy	1.415	1.216	2.27	2.51	0.01665
11	Ocayia	1.438	1.201	0.88	0.67	0.00207
12	Puzbiv	1.438	1.189	1.12	1.12	0.00014
13	Ukolip	1.435	1.199	1.14	1.81	0.00463
14	Xobyao	1.457	1.155	2.32	4.00	0.02052
15	Yalsot	1.437	1.198	1.17	1.71	0.004689
16	Zoqwux	1.444	1.178	1.20	2.53	0.00624
17	Joxlir [#]	1.420	1.240	3.36	5.84	0.064
18	Gawlev [#]	1.376	1.174	8.57	23.55	
19	Silvue	1.425	1.186	1.6	0.36	0.0092
20	Betdej [#]	1.423	1.132	3.01	5.53	0.041
21	Ebawua [#]	1.593	1.787	23.64	6.65	
22	CCDC606397	1.435	1.201	0.38	0.50	0.0010
23	CCDC606396	1.4348	1.206	2.1	3.2	0.019

*Polymorphs,

[#]The cocrystals with high θ_1 and θ_2 have large δE and are left blank. Note the unusual bond length in these cases. On the other hand, Sl. Nos. 17 and 20 have $\theta_2 > 5$ and have δE little above $k_B T$ (At room temperature).

4.4.4 Theoretical Results

In order to understand the conformational variation in the solid state and the existence of the two dissimilar molecules in the crystal structure of 1,2-diphenylacetylene a detailed theoretical analysis have been carried out. Previous theoretical studies by Seminario et al,¹⁴ on α,ω - thiol functionalized 1,2-diphenylacetylene molecules showed that the molecular conformation is crucial in determining their conducting properties. This is primarily due to the localization brought about by the geometry change. However, for a better understanding of the exact nature of this triple bond linker between the aromatic rings at the molecular level, an optimization of 1,2-diphenylacetylene molecule have been carried out using the hybrid Becke 3 Lee–Yang– Parr (B3LYP) gradient corrected approximate density functional procedure at the 6-31G(d) basis set level available in the Gaussian set of codes.³⁹ The molecule was then distorted through variation in the angles θ_1 and θ_2 (as described before). It is well known that for an isolated triple bond, as in acetylene, sp-hybridization of carbon gives rise to the degeneracy in the frontier bonding orbitals, the HOMO and HOMO-1, each representing electrons in the degenerate $2p_y$ and $2p_z$ lobes. When this bond acts as a linker between two aromatic rings, the conjugated nature of the rings affects the nature of these frontier occupied orbitals. The planar nature of the rings ensures preference for electrons in one bonding orbital over the other, depending on the nature of the p lobes in the conjugated ring. The energy difference between these highest bonding orbitals is maximum when both the rings are planar, and reduces with increase in θ_1 and θ_2 , as the preference for one p orbital over the other is gradually evened out. From the theoretical calculations it can be observed that for large values of θ_1 ($>40^\circ$) and θ_2 ($>50^\circ$), the energies of the HOMO and HOMO-1 approach each other gradually resulting in degenerate frontier orbitals resembling an ideal triple bond. Hence, with varying values of the distortion angle, the highest bonding orbitals with contribution from the triple bond are the HOMO and HOMO-n where $n=3$ for $0 < \theta_1 < 40^\circ$ and $0 < \theta_2 < 50^\circ$ and $n=1$ for larger angles, as can be seen in Figure 4.6. A detailed analysis of the frontier filled orbitals for a range of distortion angles shows that for small distortion angles, the energy gap between these frontier orbitals is so large that orbitals localized only on the aromatic rings appear in between (HOMO-1 and HOMO-2), while the triple bond characteristic orbital is pushed below.

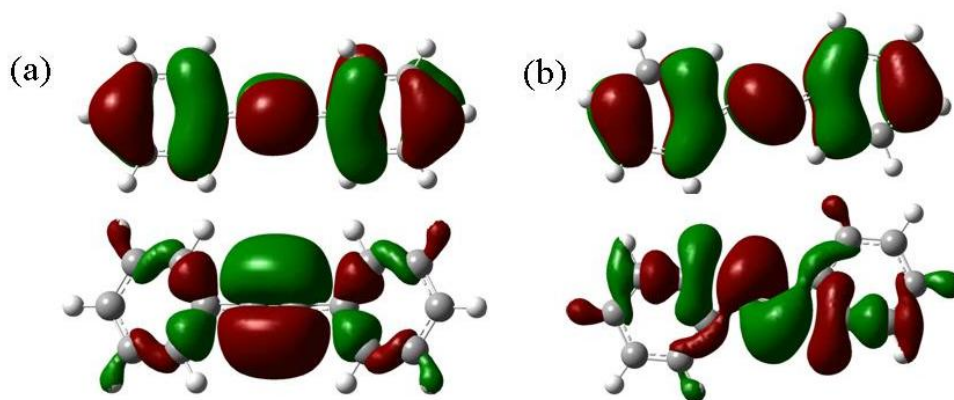


Figure 4.6: Orbital plot: (a) HOMO and HOMO-3 plots of the molecule for the planar molecule (b) HOMO and HOMO-1 plots of the molecule for $\theta_1 = 40^\circ$ and $\theta_2 = 50^\circ$

A comparison with calculations performed at the MP2 level shows larger energy differences as compared to DFT, but the qualitative nature of the orbitals do not change much. In the case of the planar molecule, in fact, the energy difference becomes larger, allowing a third bonding orbital to appear between the highest bonding orbitals with contribution from the triple bond. The distorted molecule, on the other hand, shows similar character in both cases. Also, analysis of an order parameter, like bond-order for the triple bond shows that it increases with the θ_1 and θ_2 values, reflecting its tendency to behave more and more like an isolated triple bond. Similarly, the charge density at the carbon atoms neighboring the triple bond increases with increase in distortion angles. These results confirm that while planarity increases π -conjugation, it in turn reduces the triple bond formation probability. Only when the distortion increases to reduce the conjugation that the triple bond approaches towards an ideal isolated triple bond.

As discussed, in the experimental section of 1,2-diphenylacetylene, there are two types of molecules in the crystal, one perfectly planar while the other is slightly distorted with respect to the planar conformation. Various other crystals of the same molecule are also known in the literature, with varying deviations from planarity.^{30,37,38} In order to account for the diverse crystallographic structures in nature, a single point energy calculations have been performed at the same level of theory mentioned before with varying angles of θ_1 and θ_2 (see schematic in Figure 4.1). Figure 4.7, shows a surface plot of energy (in kcal/mol) against θ_1 and θ_2 values. As can be seen, with increase in θ_1 and

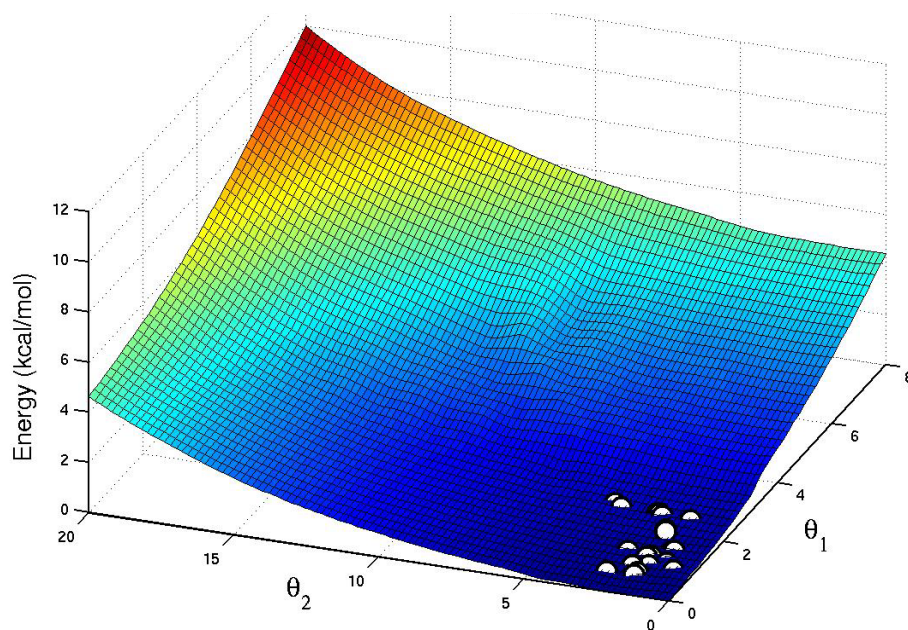


Figure 4.7: Plot showing change in energy (kcal/mol) with various values of solid angles θ_1 and θ_2 . The white dots stand for the energy values derived for various experimental structures.

θ_2 values, the energy of the molecule increases due to increase in strain from its planar minimum energy conformation. The calculated energies for all molecular geometries retrieved from CCDC^{30,37,38} are shown as points in the same figure (Figure 4.7, white dots). As can be clearly seen from the surface plot, all their energies fall within the thermal activation energy, $k_B T$, (0.58 kcal/mol at room temperature) available for the molecule. Thus, the molecules are able to pack into crystals accommodating small distortions.

4.5 Conclusions

This study reports the results of an experimental charge density study on 1,4-diphenylbutadiyne in comparison to 1,2-diphenylacetylene. Unlike in 1,2-diphenylacetylene where the triple bond is covered on either side by the π -density from the phenyl rings, in 1,4-diphenylbutadiyne, it is linked to a phenyl ring only on one side (the other side being linked to another triple bond). Accordingly, triple bonds in 1,4-diphenylbutadiyne molecule shows density and Laplacian values more typical of an ideal triple bond. The ellipticity value is 0.06 (ideal, 0.0) indicating a reduction in the deformation of charge density of the triple bonds of 1,4-diphenylbutadiyne. The higher

ellipticity values of the triple bonds in 1,2-diphenylacetylene (0.23) are due to the extended conjugation present in this molecule, where the triple bonds are directly connected to two phenyl rings. Theoretical calculations in 1,2-diphenylacetylene, in conjunction with the experimental findings, have shown that the π -orbitals of the triple bond can give enough scope to the molecule to sustain a range of conjugation lengths. Such a variation in effective conjugation in turn gives some flexibility to the molecule to be arranged in various packing conformations in the crystal with varying degrees of distortion. Interestingly, this costs only $k_B T$ energy as evidenced in diverse crystal structures involving the molecule. This is an important outcome of this study, most relevant to molecular electronics, particularly in the low-bias regime where various molecular features can be probed.

References

1. (a) C. Zhou, M. R. Deshpande, M. A. Reed, L. Jones II, J. M. Tour, *Appl. Phys. Lett.*, (1997), **71**, 611; (b) L. A. Bumm, J. J. Arnold, M. T. Cygan, T. D. Dunbar, T. P. Burgin, L. Jones II, D. L. Allara, J. M. Tour, P. S. Weiss, *Science*, (1996), **271**, 1705; (c) J. M. Tour, *Acc. Chem. Res.*, (2000), **33**, 791.
2. J. Chen, L. Xu, J. Lin, Y. Geng, L. Wang, D. Ma, *Appl. Phys. Lett.* (2006), **89**, 083514-3; (b) J. M. Seminario, R. A. Araujo, L. Yan, *J. Phys. Chem. B*, (2004), **108**, 6915.
3. A. P. de Silva, N. D. McClenaghan, *Chem. Eur. J.*, (2004), **10**, 574.
4. (a) P. W. M. Blom, M. C. J. M. Vissenberg, *Phys. Rev. Lett.*, (1998), **80**, 3819; (b) H. C. F. Martens, P. W. M. Blom, H. F. M. Schoo, *Phys. Rev. B.*, (2000), **61**, 7489.
5. (a) L. M. Herz, C. Daniel, C. Silva, F. J. M. Hoeben, A. P. H. J. Schenning, E. W. Meijer, R. H. Friend, R. T. Phillips, *Phys. Rev. B*, (2003), **68**, 045203; (b) S. J. George, A. Ajayaghosh, *Chem. Eur. J.*, (2005), **11**, 3217.
6. (a) P. T. Lin, S.T. Wu, C. Y. Chang, C. S. Hsu, *Mol. Cryst. Liq. Cryst.*, (2004), **411**, 243; (b) S. T. Wu, J. D. Margerum, H. B. Meng, L. R. Dalton, C. S. Hsu, S. H. Lung, *Appl. Phys. Lett.*, (1992), **61**, 630.
7. (a) C. K. Chiang, C. R. Fincher, Jr. Y. W. Park, A. J. Heeger, H. Shirakawa, E. J. Louis, S. C. Gau, A.G. MacDiarmid, *Phys. Rev. Lett.*, (1977), **39**, 1098; (b) M. A. Butler, D. S. Ginley, J. W. Bryson, *Appl. Phys. Lett.*, (1986), **48**, 1297.
8. (a) A. Salomon, D. Cahen, S. Lindsay, J. Tomfohr, V. B. Engelkes, C. D. Frisbie, *Adv. Mater.*, (2003), **15**, 1881; (b) W. Haiss, C. Wang, I. Grace, A. Batsanov, D. J. Schiffrin, S. J. Higgins, M. R. Bryce, C. J. Lambert, R. J. Nichols, *Nature Mater.*, (2006), **5**, 995.
9. M. A. Reed, C. Zhou, C. J. Muller, T. P. Burgin, J. M. Tour, *Science*, (1997), **278**, 252.
10. J. G. Kushmerick, J. Naciri, J. C. Yang, R. Shashidhar, *Nano. Lett.*, (2003), **3**, 897.

11. (a) J. S. Na, J. Ayres, K. L. Chandra, C. Chu, C. B. Gorman, G. N. Parsons, *Nanotechnology*, (2007), **18**, 035203; (b) V. V. Agrawal, R. Thomas, G. U. Kulkarni, C. N. R. Rao, *Pramana*, (2005), **65**, 769.
12. (a) S. Lakshmi, S. K. Pati, *J. Chem. Phys.*, (2004), **121**, 11998; (b) J. M. Seminario, A. G. Zacarias, P. A. Derosa, *J. Phys. Chem. A*, (2001), **105**, 791; (c) Y. Karzazi, J. Cornil, J. L. Brédas, *Nanotechnology*, (2003), **14**, 165; (d) J. D. Le, Y. He, T. R. Hoye, C. C. Mead, R. A. Kiehl, *Appl. Phys. Lett.*, (2003), **83**, 5518; (e) S. Lakshmi, S. K. Pati, *Phys. Rev. B*, (2005), **72**, 193410.
13. a) Z. J. Donhauser, B. A. Mantooth, K. F. Kelly, L. A. Bumm, J. D. Monnell, J. J. Stapleton, D. W. Price Jr., A. M. Rawlett, D. L. Allara, J. M. Tour, P. S. Weiss, *Science*, (2001), **292**, 2303; (b) S. I. Khondaker, Z. Yao, L. Cheng, J. C. Henderson, Y. Yao, J. M. Tour, *Appl. Phys. Lett.*, (2004), **85**, 645; (c) I. Kratochvilova, M. Kocirik, A. Zambova, J. Mbindyo, T. E. Mallouk, T. S. Mayer, *J. Mater. Chem.*, (2002), **12**, 2927; (d) J. Cornil, Y. Karzazi, J. L. Brédas, *J. Am. Chem. Soc.*, (2002), **124**, 3516-3517.
14. J. M. Seminario, A. G. Zacarias, J. M. Tour, *J. Am. Chem. Soc.*, (1998), **120**, 3970.
15. (a) D. W. Rogers, N. Matsunaga, A. A. Zavitsas, F. J. McLafferty, J. F. Liebman, *Org. Lett.*, (2003), **5**, 2373. (b) P. D. Jarowski, M. D. Wodrich, C. S. Wannere, P. v. R. Schleyer, K. N. Houk, *J. Am. Chem. Soc.*, (2004), **126**, 15036. (c) G. B. Kistiakowsky, J. R. Ruhoff, H. A. Smith, W. E. Vaughan, *J. Am. Chem. Soc.*, (1936), **58**, 146. (d) I. Fernández, G. Frenking, *Chem. Eur. J.*, (2006), **12**, 3617.
16. (a) A. Shimojima, H. Takahashi, *J. Phys. Chem. B*, (1993), **97**, 9103; (b) D. Cremer, E. Kraka, A. Wu, W. Luttko, *ChemPhysChem*, (2004), **5**, 349.
17. (a) M. Rubin, A. Trofimov, V. Gevorgyan, *J. Am. Chem. Soc.*, (2005), **127**, 10243; (b) A. Beeby, K. S. Findlay, P. J. Low, T. B. Marder, P. Matousek, A. W. Parker, S. R. Rutter, M. Towrie, *Chem. Commun.*, (2003), 2406.
18. (a) T. S. Koritsanszky, P. Coppens, *Chem. Rev.*, (2001), **101**, 1583; (b) G. U. Kulkarni, R. S. Gopalan, C. N. R. Rao, *J. Mol. Struct., (THEOCHEM)* (2000), **500**, 339.

19. (a) T.; Koritsanszky, R. Flaig, D. Zobel, H.-G. Krane, W. Morgenroth, P. Luger, *Science*, (1998), **279**, 356; (b) S. Dahaoui, V. Pichon-Pesme, J. A. K. Howard, C. Lecomte, *J. Phys. Chem. A*, (1999), **103**, 6240.
20. (a) R. Flaig, T. Koritsánszky, R. Soyka, L. Häming, P. Luger, *Angew. Chem, Int. Ed.*, (2001), **40**, 355; (b) D. E. Hibbs, J. Overgaard, S. T. Howard, T. H. Nguyen, *Org. Biomol. Chem.*, (2005), **3**, 441; (c) G. A. Jeffrey, J. F. Piniella, *The Application of Charge Density Research to Chemistry and Drug Design*; Plenum Publishing: New York, **1991**.
21. (a) A. Fkyerat, A. Guelzim, F. Baert, J. Zyss, A. Perigaud, *Phys. Rev. B.*, (1996), **53**, 16236; (b) R. S. Gopalan, G. U. Kulkarni, C. N. R. Rao, *ChemPhyChem.*, (2000), **1**, 127; (c) G. K. H. Madsen, F. C. Krebs, B. Lebech, F. K. Larsen, *Chem. Eur. J.*, (2000), **6**, 1797; (d) H. B. Bürgi, S. C. Capelli, A. E. Goeta, J. A. K. Howard, M. A. Spackman, D. S. Yufit, *Chem. Eur. J.*, (2002), **8**, 3512; (e) A. Ranganathan, G. U. Kulkarni, *J. Phys. Chem. A*, (2002), **106**, 7813.
22. (a) A. Volkov, T. Koritsanszky, X. Li P. Coppens, *Acta Crystallogr. Sect. A*, (2004), **60**, 638; (b) A. Volkov, H. F. King, P. Coppens, L. J. Farrugia, *Acta Crystallogr. Sect. A*, (2006), **62**, 400; (c) X. Li, A. V. Volkov, K. Szalewicz, P. Coppens, *Acta Crystallogr. Sect. D*, (2006), **62**, 639.
23. Hohenberg, P.; Kohn, W. *Phys. Rev. B*, (1964), **136**, 864.
24. R. F. W. Bader, *Atoms in Molecules: A quantum theory*; Clarendon Press: Oxford, U.K., 1990.
25. G. T. Smith, J. A. K. Howard, J. D. Wallis, *Phys. Chem. Chem. Phys.*, (2001), **3**, 4503.
26. (a) K. Sonogashira, Y. Tohda, N. Hagihara, *Tet. Lett.*, (1975), **16**, 4467; (b) R. Ziessel, J. Suffert, M. T. Youinou, *J. Org. Chem.*, (1996), **61**, 6535.
27. Siemens Analytical X-ray Instruments Inc., Madison, Wisconsin, USA 1995.
28. SADABS, SGI version, Siemens Analytical X-ray Instruments Inc., Madison, Wisconsin, USA, 1995.
29. SHELXTL, SGI version, Siemens Analytical X-ray Instruments Inc., Madison, WI, USA 1995.
30. (a) A. A. Espiritu, J. G. White, *Z. Krist.*, (1978), **147**, 177; (b) A.V.Abramenkov, A. Almenningen, B. N. Cyvin, S. J. Cyvin, T. Jonvik, L.S. Khaikin, C. L.

- Romming, V. Vilkov, *Acta. Chem. Scan. A*, (1988), **42**, 674. (c) A. Mavridis, I. Moustakali-Mavridis, *Acta Crystallogr. B*, (1977), **33**, 3612.
31. F. R. Fronczek, M. S. Erickson, *J. Chem. Cryst.*, (1995) **25** 737.
32. N. K. Hansen, P. Coppens, *Acta. Cryst. A*, (1978), **34** 909.
33. T. Koritsanszky, S. T. Howard, T. Richter, P. R. Mallinson, Z. Su, N. K. Hansen, XD, A computer program package for multipole refinement and analysis of charge densities from diffraction data. Cardiff, Glasgow, Buffalo, Nancy, Berlin, (1995).
34. F. H. Allen, O. Kennard, D. G. Watson, L. Brammer, A.G. Orpen, R. Taylor, *J. Chem. Soc., Perkin Trans. II*, (1987), S1-S19.
35. P.L.A. Popelier, *Atoms in Molecule: An Introduction*, Prentice Hall: London, 2000.
36. D. Cremer, E. Kraka, *Croat. Chem. Acta*. (1984), **57**, 1259.
37. (a) V. D. Samarskaya, R. M. Myasnikova, A. I. Kitaigorodskij, *Kristallografiya (Russ)*, (1968), **13**, 616; (b) Y. P. Ivanov, M. Y. Antipin, A. I. Pertsin, *Kristallografiya (Russ.)*, (1982), **27**, 1982; (c) I. E. Zanin, M. Y. Antipin, Y. T. Struchkov, *Kristallografiya(Russ.)*, (1991), **36**, 411.
38. (a) C. E. Smith, P. S. Smith, R. L. Thomas, E. G. Robins, J. C. Collings, Chaoyang Dai, A. J. Scott, S. Borwick, A. S. Batsanov, S. W. Watt, S. J. Clark, C. Viney, J. A. K. Howard, W. Clegg, T. B. Marder, *J. Mater. Chem.*, (2004), **14**, 413; (b) S. A. MacLaughlin, N. J. Taylor, A. J. Carty, *Organometallics*, (1984) **3**, 392; (c) L. Pasimeni, C. Corvaja, D. A. Clemente, *Mol. Cryst. Liq. Cryst.*, (1984), **104**, 231; (d) M. P. Byrn, C. J. Curtis, Yu. Hsiou, S. I. Khan, P. A. Sawin, S. K. Tendick, A. Terzis, C. E. Strouse *J. Am. Chem. Soc.*, (1993), **115**, 9480; (e) J. C. Collings, A. S. Batsanov, J. A. K. Howard, T. B. Marder, *Acta Crystallogr. C*, (2001), **57**, 870; (f) J. C. Barnes, J. A. Chudek, *Acta Crystallogr. E*, (2002), **58**, 703; (g) F. Montilla, A. Galindo, E. Carmona, E. Gutierrez-Puebla, A. Monge, *J. Chem. Soc. Dalton Trans.*, (1998), 1299; (h) M. Gdaniec, W. Jankowski, M. J. Milewska, T. Polonski, *Angew. Chem. Int. Ed.*, (2003), **42**, 3903; (i) N. Burford, J. A. C. Clyburne, J. A. Wiles, T. S. Cameron, K. N. Robertson *Organometallics*, (1996), **15**, 361; (k) A. A. Pasynskii, F. S. Denisov, A. N. Grechkin, I. V.

- Skabitskii, Y. V. Torubayev, Z. V. Dobrokhotova, G. G. Aleksandrov, K. A. Lyssenko, *Organometallics*, (2001), **46**, 1984; (l) M. Westerhausen, H. D. Hausen, W. Schwarz, *Z. Anorg. Allg. Chem.*, (1992), **618**, 121; (m) W. J. Evans, M. A. Hozbor, S. G. Bott, G. H. Robinson, J. L. Atwood, *Inorg. Chem.*, (1988), **27**, 1990; (n) D. Wolff von Gudenberg, I. Sens, U. Muller, B. Neumuller, K. Dehnicke, *Z. Anorg. Allg. Chem.*, (1992), **613**, 49; (o) T. W. Graham, J. Kickham, S. Courtenay, P. Wei, D. W. Stephan, *Organometallics*, (2004), **23**, 3309.
39. M. J. Frisch, G. W. Trucks, H. B. Schlegel, G. E. Scuseria, M. A. Robb, J. R. Cheeseman, J. A. Montgomery, Jr., T. Vreven, K. N. Kudin, J. C. Burant, J. M. Millam, S. S. Iyengar, J. Tomasi, V. Barone, B. Mennucci, M. Cossi, G. Scalmani, N. Rega, G. A. Petersson, H. Nakatsuji, M. Hada, M. Ehara, K. Toyota, R. Fukuda, J. Hasegawa, M. Ishida, T. Nakajima, Y. Honda, O. Kitao, H. Nakai, M. Klene, X. Li, J. E. Knox, H. P. Hratchian, J. B. Cross, C. Adamo, J. Jaramillo, R. Gomperts, R. E. Stratmann, O. Yazyev, A. J. Austin, R. Cammi, C. Pomelli, J. W. Ochterski, P. Y. Ayala, K. Morokuma, G. A. Voth, P. Salvador, J. J. Dannenberg, V. G. Zakrzewski, S. Dapprich, A. D. Daniels, M. C. Strain, O. Farkas, D. K. Malick, A. D. Rabuck, K. Raghavachari, J. B. Foresman, J. V. Ortiz, Q. Cui, A. G. Baboul, S. Clifford, J. Cioslowski, B. B. Stefanov, G. Liu, A. Liashenko, P. Piskorz, I. Komaromi, R. L. Martin, D. J. Fox, T. Keith, M. A. Al-Laham, C. Y. Peng, A. Nanayakkara, M. Challacombe, P. M. W. Gill, B. Johnson, W. Chen, M. W. Wong, C. Gonzalez, and J. A. Pople, Gaussian 03, Revision B.05, Gaussian, Inc., Pittsburgh PA, (2003).

**CHARGE DENSITY ANALYSIS OF PROTON TRANSFER
COMPLEXES: UNDERSTANDING HYDROGEN BONDING AND
DETERMINATION OF IN-CRYSTAL DIPOLE MOMENTS***

Summary

This chapter describes the results of an experimental charge density study on two proton-transfer complexes exhibiting nonlinear optical (NLO) properties - melaminium L-tartrate monohydrate and L-asparaginium picrate, employing high-resolution X-ray diffraction at 100 K. Both the complexes crystallize in noncentric space group $P2_1$ and the structures exhibit interesting patterns of N-H...O and O-H...O hydrogen bonding. Experimental determination of the dipole moment (μ) for the asymmetric unit reveals that for both the crystals, there is a large cooperative enhancement in the crystalline μ arising essentially due to hydrogen bond mediated charge transfer between the melaminium ion and the L-tartrate in one case, and between the L-asparaginium ion and the picrate in the other complex. In order to understand the effect of hydrogen bonding among the molecules, an analysis of the charge density at the hydrogen-bond critical point has been carried out. The analysis showed that in melaminium L-tartrate monohydrate the bonding is stronger compared to that present in L-asparaginium picrate, where hydrogen bonding resulted in the redistribution of the electron density.

*The paper based on this study has been accepted for publication in *J. Chem. Sci.* (2008).

5.1 Introduction

Last few decades have witnessed a tremendous interest in molecular materials and soft condensed matter. Such materials include organic solids,¹⁻⁴ polymers,⁵ thin-films,⁶ micelles⁷ and biomaterials⁸ which occupy a central-stage for both basic and applied research. These materials are being actively used for the design of smart devices such as organic light emitting diodes,⁹ hybrid organic-inorganic nanoporous materials¹⁰ those are important in gas-sensing, hydrogen storage and bio-mimetic applications.¹¹ However, the optimization and fine-tuning of the properties of molecular materials is dually challenging. It calls for a sound understanding of the properties at the molecular level, which in turn demands an understanding of the intermolecular forces that glue the molecules in a material. In most systems, the intermolecular interactions are the weak supramolecular forces involving hydrogen bonding^{12,13} and π -stacking¹⁴. Thus, a basic understanding of the factors that control the intermolecular interactions in an aggregate is of fundamental interest for the proper design and fabrication of smart materials.^{15,16}

An important class of organic materials is the nonlinear optically (NLO) active molecular crystals.¹⁷⁻¹⁹ A very stringent requirement for a material to exhibit non-zero second harmonic generation (SHG) is that the crystal has to exist in a non-centrosymmetric point group. In fact, most molecules (like parnitroaniline) which show very large SHG at the molecular scale due to charge transfer (CT) from the donor to the acceptor (NH_2 to NO_2), crystallize in a centrosymmetric lattice due to predominating anti-parallel π -stacking between the aromatic rings as a consequence of dipolar interactions.^{20,21} However, weak intermolecular forces like hydrogen bonding due to their directional nature can orient molecules in a head-to-tail manner thereby avoiding centrosymmetric packing and thus lead to enhanced SHG.²²⁻²⁵

The topological analysis of $\rho(r)$ based on Baders atoms-in-molecule (AIM) theory allows a quantitative description of bonds, non-bonding interactions, electronic structure and reactivity of a molecular system.²⁷ Recent literature covers numerous experimental charge density studies on NLO active crystals.²⁹ The advantage with the experimental charge density method is that it can provide complete estimation of the in-crystal

molecular properties. This becomes particularly important when the said property such as SHG arises only because of the crystal packing.

5.2 Scope of the Present Investigation

This study is intended for a proper understanding of the role of hydrogen bonding in controlling molecular packing and return the SHG response of the molecular crystals. Present study analyzes the distribution of experimental charge density ($\rho(r)$) in the crystal lattices of two proton transfer complexes - melaminium-L-tartrate monohydrate (**MELT**) and L-asparaginium picrate (**LASP**) within the framework of Baders atoms-in-molecule (AIM) theory.²⁶ The complexes chosen for the present study are known to exhibit SHG activities of 1.2 (**MELT**)³⁰ and 66 (**LASP**)³¹ times of KDP. In view of the previous report on enhancement of the molecular dipole moment in the non-centric crystal field in NLO systems,^{29a} this study is an effort to understand how the hydrogen bond mediation in such complexes help to enhance the in-crystal dipole moments in a noncentric crystal field.

5.3 Experimental Section

Crystals of **MELT** and **LASP** were grown respectively from aqueous and acetone-aqueous solutions respectively by slow evaporation at room temperature. High quality crystals were separated under an optical microscope. The crystal data were collected on a Siemens three circle diffractometer attached with a CCD area detector and a graphite monochromator for the Mo K α radiation (50 kV, 40 mA). The crystals were cooled to 100 K on the diffractometer using a stream of cold nitrogen gas from a vertical nozzle and the temperature was maintained within 1 K throughout the data collection. The experimental details of the system are listed in Table 5.1.

The unit cell parameters and the orientation matrix of the crystal were initially determined using 45 and 53 reflections from 25 frames collected over a small ω scan of 12.5° sliced at 0.5° interval **MELT** and **LASP** respectively. (see general experimental and related aspects in Chapter 1) A hemisphere of data of the reciprocal space with similar 2θ settings was collected. Data reduction was performed using the SAINT program³² (Bruker, 2002) matrix along the detector and the cell parameters were refined

for every 40 frames on all the measured reflections. The experimental details for the system are listed in Table 5.1. Absorption correction was applied on the data using the SADABS program.³³ The crystal structure was first determined with the low-resolution data up to $\sin(\theta/\lambda) = 0.56 \text{ \AA}^{-1}$. The phase problem was solved by direct methods and the

Table 5.1 Refinement table for the complexes melaminium L-tatrate monohydrate (**MELT**) and L-asparaginium picrate (**LASP**).

Compound	MELT	LASP
Chemical formula	C ₇ H ₁₄ N ₆ O ₇	C ₁₀ H ₁₁ N ₅ O ₁₀
Formula weight	294.24	361.24
Cell setting	Monoclinic	Monoclinic
Space group	P2 ₁	P2 ₁
a (Å)	4.9727(1)	10.2441(4)
b (Å)	21.7273(1)	5.1147(2)
c (Å)	5.5789(1)	13.0587(5)
β (°)	103.580(2)	94.129(1)
ρ (mg/m ³)	1.668	1.758
μ, mm ⁻¹	0.148	0.160
Cell volume (Å ³)	585.92(2)	682.44(5)
Crystal size (mm)	0.30 x 0.20 x 0.20	0.25 x 0.20 x 0.20
Z	2	2
F(000)	308	212
Radiation type	Mo K _α (0.71073 Å)	MoK _α (0.71073 Å)
Crystal-detector distance (cm)	5.0	5.0
No. of measd reflns	9711	31898
No. of ind reflns	7282	14978
No. of obsd reflns	5479	14968
Resolution (Å)	0.35	0.35
R _{merge}	0.0607	0.0354
R _{int}	0.0284	0.0297
R ₁	0.0461	0.0360
wR2	0.1106	0.0977
S	1.019	1.1070
No. of parameters refined	237	270
After multipole refinement		
Weighting scheme	0.0459, 0.0869	0.0390, 0.0765
R{F}	0.0309	0.0277
R{F ² }	0.0509	0.0382
S	1.180	1.1264
N _{ref} /N _v	11.23	35.2212

non-hydrogen atoms were refined anisotropically, by means of the full-matrix least-squares procedure using the SHELXTL program.³⁴ All the hydrogens were located using the difference Fourier method. All bond lengths and bond angles along with atom coordinates and isotropic displacement parameters for both the complexes are given in Appendix Tables A5.1 to A5.4.

The charge density analysis was carried out on the basis of multipole expansion of the electron density centered at the nucleus of the atoms³⁵ using XD package³⁶ (see Chapter 1 general experimental and related aspects). A high-order refinement of the data was performed using reflections with $\sin(\theta/\lambda) \geq 0.5 \text{ \AA}^{-1}$ and $F_o \geq 5\sigma$. All the hydrogens were held constant throughout the refinement along with their isotropic temperature factors. Multipolar refinement for the charge density analysis was carried out using the XDLSM routine of the XD package, and the details are given in Table 5.1. The XDPROP routine was used to calculate the total electron density, $\rho(r)$, Laplacian, $\nabla^2\rho$ and the ellipticity, ϵ , at the bond critical points (BCPs) as well as the electrostatic potential, $\phi(r)$ profile. The deformation density maps have been plotted using the XDGRAPH routine. The electrostatic potential surface was plotted using MolIso program.³⁷ The multipole populations, residual density maps and other related tables and figures for the complexes **MELT** and **LASP** are given in the Appendix for the Chapter 5.

5.4 Results and Discussion

Figure 5.1 shows the asymmetric units of the molecular complexes **MELT** and **LASP** with atom labeling scheme. The asymmetric unit of **MELT** contains one diprotonated melaminium ion and one tartrate ion along with a molecule of water, whereas that of **LASP** consists of a picrate ion and a monoprotonated L-asparaginium ion. The refinement details of the complexes are given in Table 5.1. Both the molecular complexes crystallize in a noncentric monoclinic space group $P2_1$. In melaminium L-tartrate monohydrate, the C-O bond lengths of bond indicate that the tartaric acid molecule exists in a doubly ionized form with two carboxylate groups. The carboxylate protons from the tartaric acid is transferred to the two nitrogens (N5 and N6) of the melamine, hence the melamine ring exists in a doubly protonated form. In the case of asparaginium picrate, the carboxyl group of the asparagine is protonated by the proton

transferred from the picric acid. The L-asparagine molecule lost its zwitter ionic nature and exists as positively charged species. Complete list of bond lengths and bond angles are provided in Appendix Table A5.1.

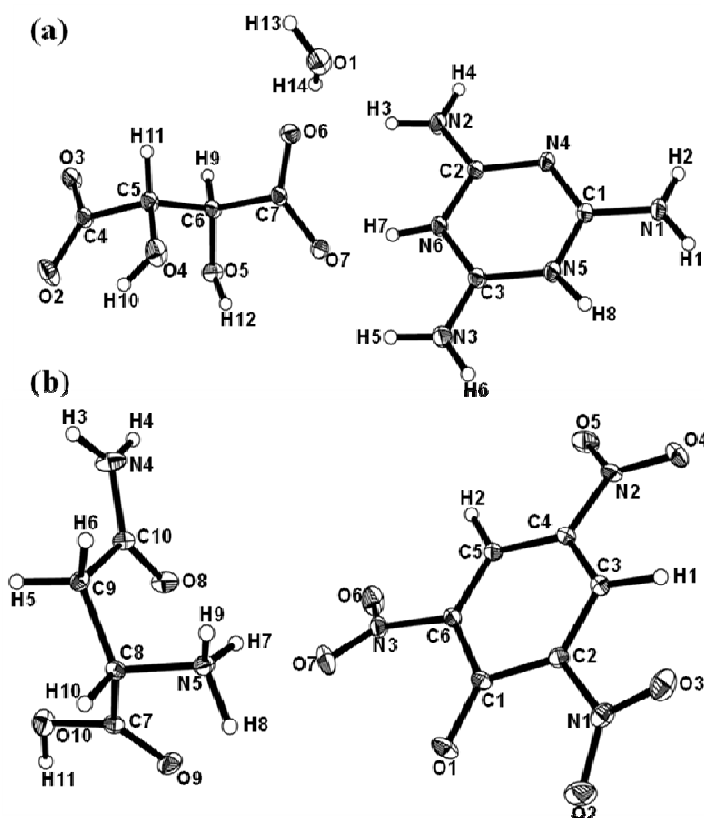


Figure 5.1: ORTEP representation of the molecular complexes (a) melaminium tartrate monohydrate (**MELT**) (b) L-asparaginium picrate (**LASP**). Displacement ellipsoids are drawn at a 50% probability level.

The molecular complex formed by melamine and tartaric acid displays a variety of hydrogen bonds within the three molecules of the asymmetric unit. The hydrogen bonds are either O-H...O or N-H...O type. The unique hydrogen-bonding patterns observed in the crystal structures are shown in Figure 5.2. It is noteworthy that the water molecule in the crystal of melaminium L-tartrate (Figure 5.2a) is located in between the two highly ionic species and engaged in a tetrahedral hydrogen-bonding environment via two N-H...O (N2-H4...O1 and N3-H5...O1) and two O-H...O (O1-H13...O4 and O1-H14...O6) interactions (see Table 5.2). All the carboxylic acid and hydroxyl oxygen atoms of the tartaric acid participate in various N-H...O and O-H...O interactions and play an important role in directing the crystal structure. The interaction between the

melaminium residue and the tartrate includes two pairs of N-H...O hydrogen bonds, (N5-H8...O2 and N3-H6...O3; N2-H3...O6 and N6-H7...O7) which are formed between the tartrate oxygens and hydrogens from melamine. In addition, the tartrate ion forms an internal O-H...O interaction (O5-H12...O6, not shown), involving the carboxylate oxygen and one of the hydroxyl groups

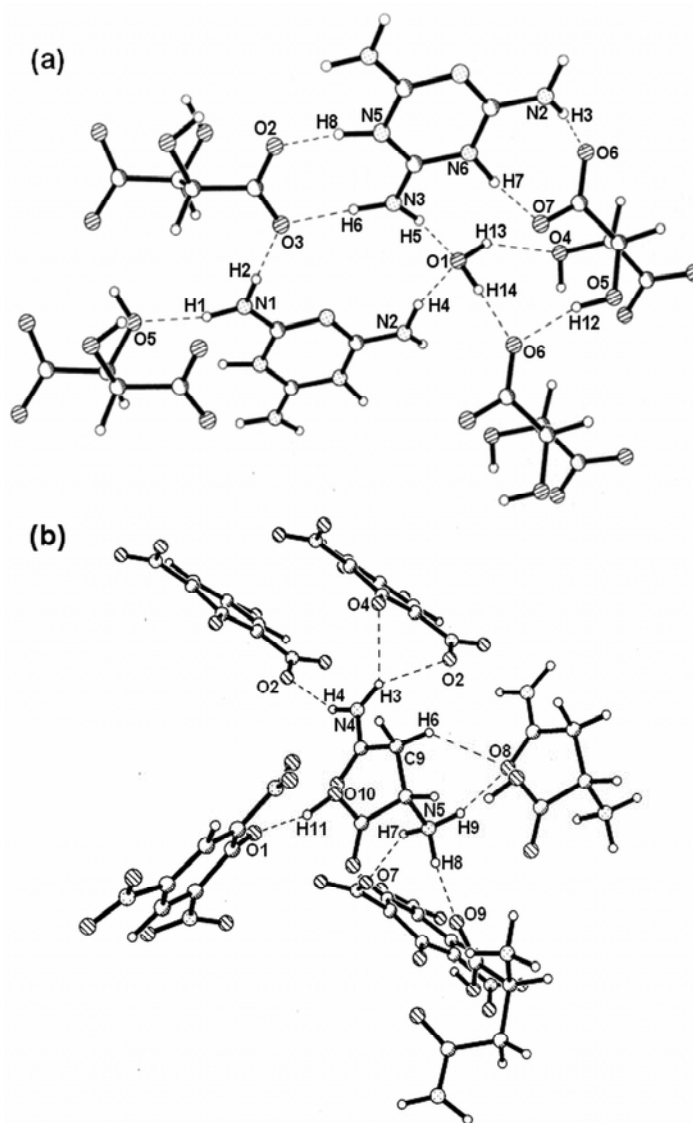


Figure 5.2: Unique set of hydrogen bonds observed in the molecular complexes (a) MELT (b) LASP.

The molecular complex of L-asparagine with picric acid also shows interesting hydrogen bonding pattern (Figure 2b) and these interactions are mainly N-H...O type. The N-H...O interactions originate from either the amide or the amino group of the L-

Table 5.2 Unique hydrogen bond interactions in **MELT** and **LASP**.

Compounds	Bonds	H...A(Å)	D...A(Å)	D-H...A(°)
MELT	N(1)-H(1)...O(5)	1.8902	2.8866	168.80
	N(1)-H(2)...O(3)	1.9202	2.9289	178.82
	N(2)-H(3)...O(6)	1.8801	2.8816	171.42
	N(2)-H(4)...O(1)	1.8428	2.8346	166.90
	N(3)-H(5)...O(1)	1.8879	2.8894	171.38
	N(3)-H(6)...O(3)	1.8345	2.8399	174.08
	N(6)-H(7)...O(7)	1.5776	2.5869	164.26
	N(5)-H(8)...O(2)	1.5673	2.5924	170.88
	O(4)-H(10)...O(2)	1.9491	2.5726	120.01
	O(5)-H(12)...O(6)	1.8125	2.7512	162.88
	O(1)-H(13)...O(4)	2.1211	2.9915	142.61
O(1)-H(14)...O(6)	1.7647	2.7741	172.54	
LASP	N(4)-H(3)...O(1)	2.2952	3.0943	135.28
	N(4)-H(3)...O(2)	2.3599	3.1552	135.05
	N(4)-H(4)...O(2)	2.1329	3.0727	154.19
	N(5)-H(7)...O(7)	2.1387	3.0691	148.83
	N(5)-H(8)...O(9)	1.7903	2.8144	170.81
	N(5)-H(9)...O(8)	2.0121	2.8673	138.39
	O(10)-H(11)...O(1)	1.5731	2.5611	163.16
C(9)-H(6)...O(8)	2.4935	3.2245	123.31	

asparaginium ion. The N-H...O interactions are in the range of 1.790 - 2.360Å with bond angles 170.8 - 135.3° (see Table 5.2). In addition to this, there exists a strong O-H...O (O10-H11...O1) hydrogen bond, which is formed by the phenolate oxygen of picrate and the carboxylic group of the L-asparagine. A C-H...O interaction (C9-H6...O8) is also formed between two asparaginium ions.

Analysis of experimental charge density

In order to correlate the structure and charge density distribution to property, a detailed analysis of experimental charge density on both the crystals of molecular complexes **MELT** and **LASP** have been carried out and the density and Laplacian values are listed in Tables 5.3 and 5.4 respectively. In **MELT**, the bond critical point parameters of melaminium ion indicate the variation in charge delocalization on protonation of the ring nitrogen (see Table 5.3). A comparison of the bond critical point properties of the protonated melamine ring with that of the previously reported melamine molecule has been made.³⁸ The density at the bond critical point is slightly decreased and it is in the range of 2.22(7) to 2.59(6) $e\text{Å}^{-3}$ whereas in the pristine melamine ring, the values are in

the range, 2.4(2) to 2.62(2) $e\text{\AA}^{-3}$. The Laplacian of the density shows larger variations, where these values are in the range, -18.2(2) to -32.0(3) $e\text{\AA}^{-5}$ and -21.1(2) to -25.5(3) $e\text{\AA}^{-5}$ for protonated and non-protonated

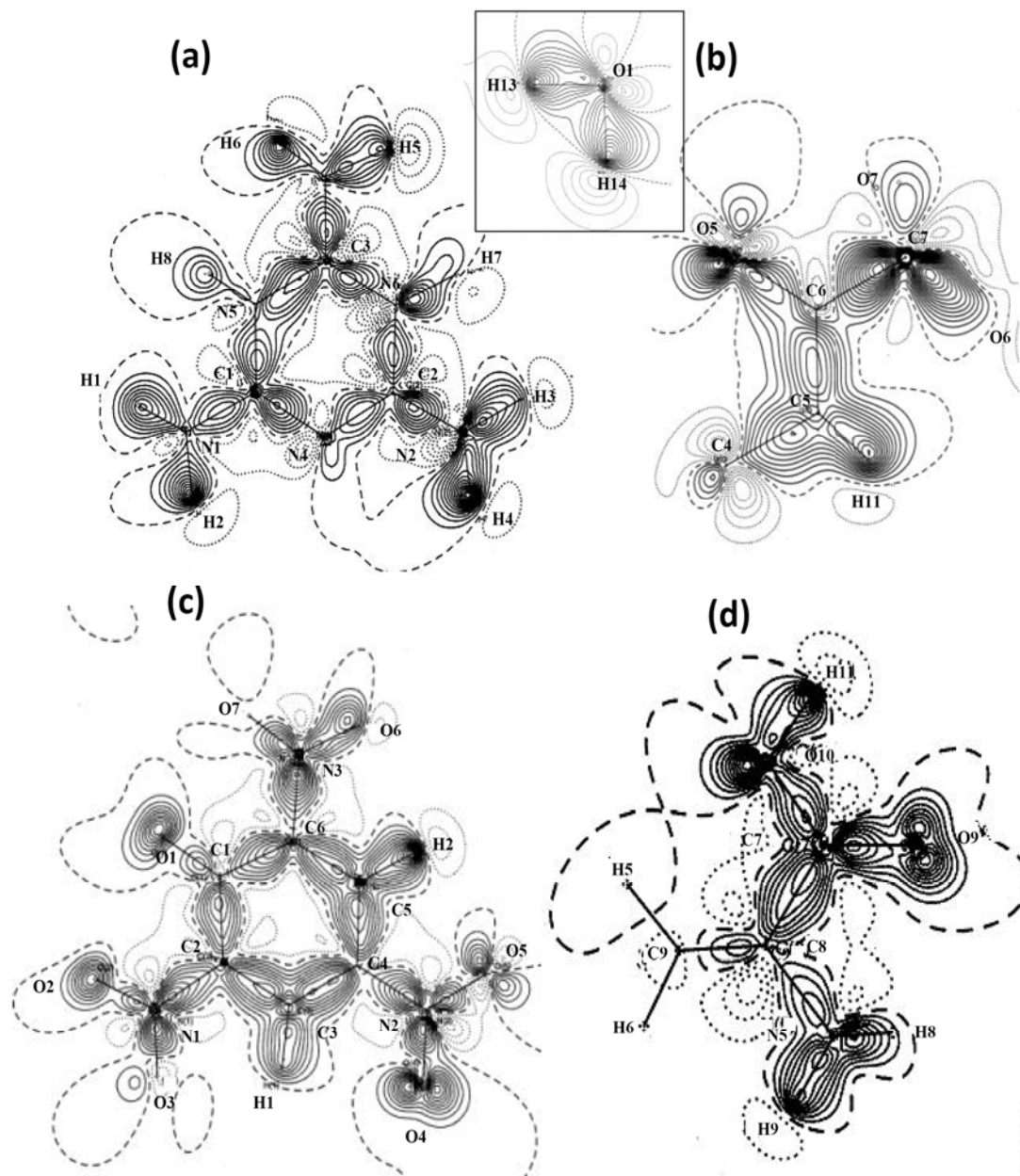


Figure 5.3: Static deformation density maps in the main molecular planes (a) melaminim ion through the atoms N1, N2 and N3 (c) tartrate ion through atoms C(5), C(7) and O(5). Inset shows the deformation density in the bonding regions of water molecules. (c) picrate ion through ring atoms N(1), N(2) and N(3) (d) aspraginium ion through atoms N(6), O(9) and O(10). Contour intervals at $0.1e\text{\AA}^{-3}$; positive contours are represented as solid lines while; zero and negative contours are represented dashed lines.

rings respectively. The variation of the Laplacian is interesting in the case of the protonated ring, where the values are higher for the bonds, which involve the protonated nitrogen atoms. The density and Laplacian in the bonding regions of the carboxylate ion of the tartrate are in the ranges, 3.08(8)- 2.65(9) $e\text{\AA}^{-3}$ and -51.9(4) - -17.10(2) $e\text{\AA}^{-5}$ respectively. In the case of **LASP** (see Table 5.4), the density and Laplacian for the C-C bonds in picrate anion are typical of an aromatic system, 1.87(3) to 2.34(4) $e\text{\AA}^{-3}$ and -15.5(1) to -20.0(1) $e\text{\AA}^{-5}$, respectively and that for the C-N bonds are in the range, 1.79(4) to 1.93(4) $e\text{\AA}^{-3}$ and -11.8(1) to -13.0(1) $e\text{\AA}^{-5}$. In L-asparaginium ion, the C-C charge

Table 5.3 Bond critical point parameters of melaminium L-tartrate monohydrate.

Bond	$\rho(\text{\AA}^{-3})$	$\nabla^2\rho(e\text{\AA}^{-5})$	$\lambda(e\text{\AA}^{-5})$	$\lambda(e\text{\AA}^{-5})$	$\lambda(e\text{\AA}^{-5})$	ϵ
C(1) - N(5)	2.31(6)	-22.7(2)	-20.61	-16.60	14.52	0.24
N(5) - C(3)	2.45(7)	-32.0(3)	-23.54	-19.44	10.99	0.21
C(3) - N(6)	2.32(6)	-16.2(2)	-21.51	-13.49	18.77	0.60
N(6) - C(2)	2.22(7)	-24.9(2)	-20.98	-15.51	11.63	0.35
C(2) - N(4)	2.41(7)	-31.4(3)	-22.46	-18.55	9.56	0.21
N(4) - C(1)	2.46(6)	-18.2(2)	-21.75	-16.05	19.64	0.36
C(1) -N(1)	2.29(9)	-31.2(5)	-22.93	-18.20	9.91	0.26
C(2) - N(2)	2.59(6)	-21.23(2)	-24.43	-15.47	18.67	0.58
C(3) - N(3)	2.59(7)	-29.7(2)	-25.61	-18.02	13.95	0.42
C(4) - O(2)	2.65(9)	-32.8(5)	-29.83	-23.32	20.32	0.28
C(4) - O(3)	2.69(7)	-17.10(2)	-22.46	-19.46	24.82	0.15
C(5) - O(4)	1.62(8)	-12.9(4)	-12.17	-10.93	10.17	0.11
C(6) - O(5)	2.02(6)	-12.7(2)	-15.91	-13.95	17.14	0.14
C(7) - O(6)	3.08(8)	-51.9(4)	-33.99	-28.25	10.34	0.20
C(7) - O(7)	2.70(9)	-33.5(5)	-29.18	-27.31	22.98	0.07
C(5) - H(9)	2.41(2)	-33.9(8)	-32.69	-32.15	30.98	0.02
C(6) - H(11)	1.69(9)	-14.3(1)	-16.65	-16.51	18.89	0.01
O(1) - H(13)	1.94(1)	-18.4(3)	-17.30	-17.01	15.93	0.02
O(1) - H(14)	2.20(2)	-21.4(8)	-29.01	-27.77	35.35	0.04
O(4) - H(10)	2.20(1)	-34.9(3)	-37.34	-35.66	38.15	0.05
O(5) - H(12)	2.65(1)	-33.1(7)	-36.27	-35.79	38.97	0.01
N(1) - H(1)	2.46(1)	-34.0(8)	-32.83	-31.54	30.36	0.04
N(1) - H(2)	2.16(1)	-24.2(6)	-28.36	-25.62	29.75	0.11
N(2) - H(3)	2.02(1)	-29.0(8)	-27.82	-27.38	26.24	0.02
N(2) - H(4)	2.27(1)	-20.8(7)	-30.14	-27.81	37.14	0.08
N(3) - H(5)	2.04(1)	-23.3(6)	-26.01	-24.83	27.50	0.0
N(3) - H(6)	2.06(1)	-18.3(8)	-26.52	-25.15	33.35	0.05
N(6) - H(7)	1.49(2)	-15.3(7)	-20.45	-19.61	24.79	0.04
N(5) - H(8)	1.74(2)	-11.3(8)	-22.13	-20.88	31.80	0.06

Table 5.4 Bond critical point parameters of L-asparaginium picrate.

Bond	$\rho(\text{\AA}^{-3})$	$\nabla^2\rho(e\text{\AA}^{-5})$	$\lambda(e\text{\AA}^{-5})$	$\lambda(e\text{\AA}^{-5})$	$\lambda(e\text{\AA}^{-5})$	ε
C(1)-C(2)	1.92(3)	-15.5(1)	-15.85	-12.05	12.44	0.32
C(2)-C(3)	2.24(3)	-19.1(1)	-17.82	-14.24	12.96	0.25
C(3)-C(4)	2.34(4)	-20.0(1)	-18.72	-14.94	13.65	0.25
C(4)-C(5)	2.15(3)	-18.4(1)	-17.68	-13.28	12.57	0.33
C(5)-C(6)	2.20(3)	-20.0(1)	-17.97	-14.13	12.11	0.27
C(6)-C(1)	1.87(3)	-15.5(1)	-15.37	-11.82	11.70	0.30
C(1)-O(1)	2.62(4)	-29.5(2)	-25.00	-20.70	16.17	0.21
C(2)-N(1)	1.93(4)	-12.5(1)	-16.17	-12.62	16.27	0.28
C(3)-H(1)	2.06(8)	-18.7(3)	-20.19	-20.01	21.47	0.01
C(4)-N(2)	1.80(4)	-13.0(1)	-14.61	-11.46	13.07	0.27
C(5)-H(2)	2.05(10)	-18.9(2)	-19.42	-17.60	18.17	0.10
C(6)-N(3)	1.79(4)	-11.8(1)	-14.85	-10.97	14.05	0.35
N(1)-O(2)	3.15(4)	0.7(1)	-29.06	-24.65	54.39	0.18
N(1)-O(3)	3.43(4)	-5.3(1)	-32.78	-29.32	56.82	0.12
N(2)-O(4)	3.41(4)	-7.9(1)	-34.11	-29.33	55.59	0.16
N(2)-O(5)	3.35(1)	-11.1(2)	-34.54	-29.29	52.69	0.18
N(3)-O(6)	3.47(5)	-7.3(1)	-34.95	-29.20	56.83	0.20
N(3)-O(7)	3.57(4)	-8.9(1)	-35.6	-30.76	57.45	0.16
C(7)-C(8)	1.82(3)	-13.3(1)	-13.83	-12.26	12.83	0.13
C(8)-C(9)	1.62(3)	-10.37(6)	-11.56	-10.91	12.10	0.06
C(9)-C(10)	1.77(3)	-10.4(1)	-13.26	-10.67	13.55	0.24
C(8)-N(5)	1.65(3)	-8.4(1)	-12.59	-11.13	15.32	0.13
C(10)-N(4)	2.38(4)	-23.3(1)	-20.73	-17.53	14.98	0.18
C(10)-O(8)	2.87(5)	-32.2(3)	-26.97	-23.17	17.95	0.16
C(7)-O(9)	2.93(5)	-33.8(3)	-30.93	-25.70	22.84	0.20
C(7)-O(10)	2.40(4)	-26.7(2)	-22.53	-20.04	15.88	0.12
N(4)-H(3)	2.15(10)	-27.9(7)	-30.78	-28.81	31.73	0.07
N(4)-H(4)	2.17(10)	-30.39(5)	-29.41	-27.66	26.68	0.06
N(5)-H(7)	2.18(10)	-24.2(5)	-26.36	-25.16	27.30	0.05
N(5)-H(8)	2.09(9)	-21.9(4)	-26.61	-26.15	30.88	0.02
N(5)-H(9)	2.24(1)	-26.7(5)	-29.19	-28.34	30.81	0.03
O(10)-H(11)	2.12(11)	-15.5(5)	-27.29	-26.24	38.02	0.04
C(8)-H(10)	1.75(9)	-17.1(3)	-17.94	-17.76	18.65	0.01
C(9)-H(5)	1.75(6)	-14.7(2)	-17.05	-15.62	17.96	0.09
C(9)-H(6)	1.82(9)	-15.6(3)	-18.46	-17.38	20.28	0.06

density and the Laplacian values indicate the single bond nature of the bonds. The density values for the two carboxylic acid C-O bonds are 2.93(5) and 2.40(4) $e\text{\AA}^{-3}$ with the corresponding Laplacian values of $-33.8(3)$ and $-26.7(2)$ $e\text{\AA}^{-5}$. The proton transfer from the picric acid gives rise to a carboxylic acid group (in place of a carbolyate ion) resulting in two unequal C-O bonds. The density and Laplacian for the C(8)-N(5) are

1.65(3) $e\text{\AA}^{-3}$ and $-8.4(1) e\text{\AA}^{-5}$ respectively. This indicates a decrease in the bond strength due to the ionic nature of the nitrogen atom.

In order to quantify the effect of the hydrogen bonding in the complexes a charge density analysis of the various hydrogen bonds in the crystal structure has been carried out. In Figure 5.4, shows typical deformation density maps for some of the representative hydrogen bonds in both complexes MELT and LAST. The maps clearly reveal significant features such as hydrogen bond regions and lone-pair (non-bonding) regions. There is an accumulation of charge density in the bonding region between the donor atom and the hydrogen atom resulting in a shared interaction. On the other hand, in the hydrogen bond (H...A) region, there is depletion of charge density between the two nuclei. This is due to the closed-shell interaction. Accordingly, small densities along with small and positive Laplacians are to be expected at the bond critical points. The details of the density distribution are given in Table 5.5. It is worthwhile to understand the variation in density and Laplacian of the density with respect to the hydrogen bond strength, measured in terms of the H...A distance and the D-H...A angle. For the N-H...O interactions in

Table 5.5 Hydrogen bond critical point parameters

Compounds	Bonds	$\rho(\text{\AA}^{-3})$	$\nabla^2\rho(e\text{\AA}^{-5})$
MELT	N(1)-H(1)...O(5)	0.11(5)	2.95(2)
	N(1)-H(2)...O(3)	0.13(5)	2.96(2)
	N(2)-H(3)...O(6)	0.13(6)	3.13(4)
	N(2)-H(4)...O(1)	0.27(5)	3.53(3)
	N(3)-H(5)...O(1)	0.15(5)	3.08(3)
	N(3)-H(6)...O(3)	0.24(5)	3.16(3)
	N(6)-H(7)...O(7)	0.40(1)	4.1(2)
	N(5)-H(8)...O(2)	0.50(9)	4.31(1)
	O(4)-H(10)...O(2)	0.18(4)	2.96(1)
	O(5)-H(12)...O(6)	0.10(5)	3.5(3)
LASP	O(1)-H(13)...O(4)	0.03(2)	0.86(1)
	O(1)-H(14)...O(6)	0.18(7)	4.06(6)
	N(4)-H(3)...O(1)	0.08(1)	1.14(3)
	N(4)-H(3)...O(2)	0.07(1)	1.05(4)
	N(4)-H(4)...O(2)	0.07(1)	1.05(4)
	N(5)-H(7)...O(7)	0.04(2)	1.01(3)
	N(5)-H(8)...O(9)	0.16(4)	3.65(3)
	N(5)-H(9)...O(8)	0.07(2)	1.97(4)
	O(10)-H(11)...O(1)	0.30(6)	7.19(8)
	C(9)-H(6)...O(8)	0.05(8)	0.77(4)

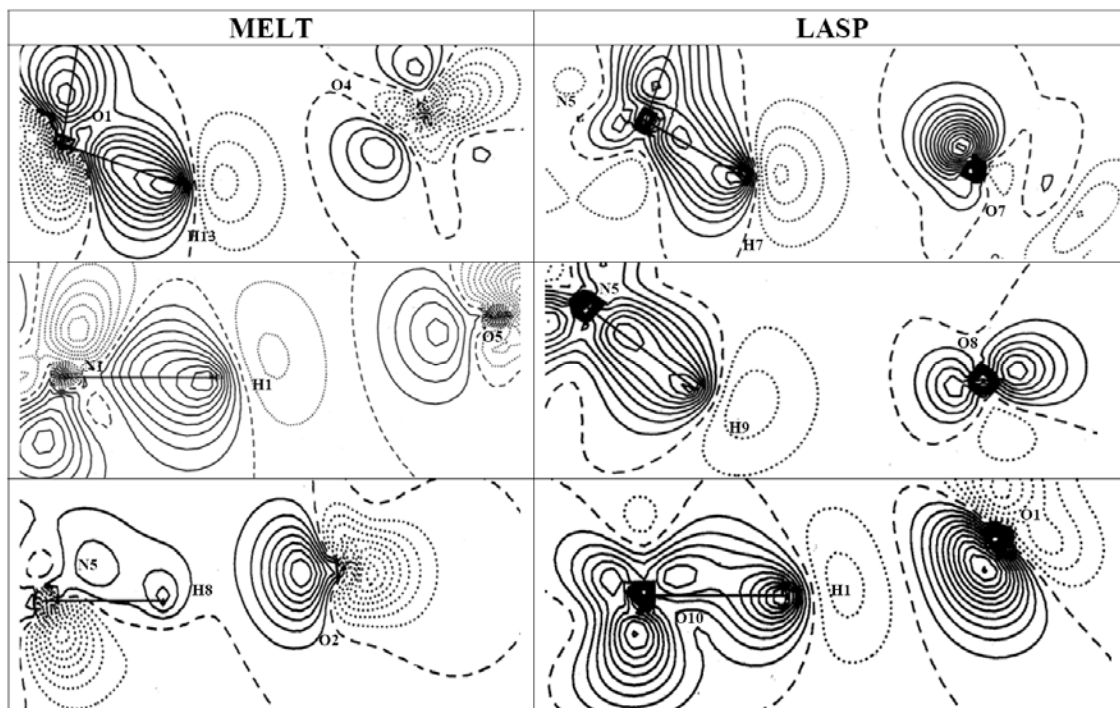


Figure 5.4: Static deformation density plots (at contour intervals of $0.1 e\text{\AA}^{-3}$) in the hydrogen bond plane for representative hydrogen bonding interactions in complexes **MELT** and **LASP**.

MELT crystals, the density and Laplacian values fall in the range of $0.11(5)$ to $0.50(9) e\text{\AA}^{-3}$ and $2.95(2)$ to $4.31(1) e\text{\AA}^{-5}$ respectively. These values are in good agreement with the standard values³⁸ expected for a strong N-H...O hydrogen bond, with short H...A distances and angles beyond 170° (see Table 5.5). Conversely, the O-H...O interactions in **MELT** carry a density and Laplacian values in the range of $0.10(5)$ to $0.18(7) e\text{\AA}^{-3}$ and $0.86(1)$ to $4.06(6) e\text{\AA}^{-5}$ respectively, indicating that these interactions are moderately strong. It is clear that in this complex, the dominant interactions are through N-H...O hydrogen bonds. The charge density analysis on the hydrogen bonding interaction in **LASP** also has been carried out (see Table 5.5). The density and Laplacian for N-H...O hydrogen bonds in these systems are in the range $0.04(2)$ to $0.16(4) e\text{\AA}^{-3}$ and $1.01(3)$ to $3.65(3) e\text{\AA}^{-5}$, respectively, somewhat low for a standard N-H...O interaction. On the other hand, the values for the O-H...O interaction ($0.30(6) e\text{\AA}^{-3}$ and $7.19(8) e\text{\AA}^{-5}$) indicate that this corresponds to a strong interaction. In general, it is clear from Tables 5.5 that the hydrogen bonding interactions in **LASP** are comparatively weaker than those existing in **MELT**.

A useful application of the multipole model of the electron density is the ability to derive the molecular electrostatic potential for an isolated molecule in the crystalline environment, and hence to evaluate contributions of electrostatics to intermolecular interactions and on molecular property.³⁹ Figure 3a and b show the electrostatic potential on the iso electron density surface at $\rho = 0.5 \text{ e}\text{\AA}^{-3}$, in **MELT** and **LASP** respectively. The maps indicate the donor acceptor sites for hydrogen bonding present in both the proton-transfer complexes. It is interesting to note that in **MELT**, (Figure 5.5a) the L-tartrate carries most of the negative potential (red) whereas the surface over melaminium ion is with positive values (green and blue) clearly implying proton transfer between these molecules. In the perspective given in Figure 5.5a, the water molecule is seen carrying negative lobes (red) corresponding to the lone-pair. A similar observation can be made in the **LASP** where the negative potential surface (red) is over the picrate ion and positive

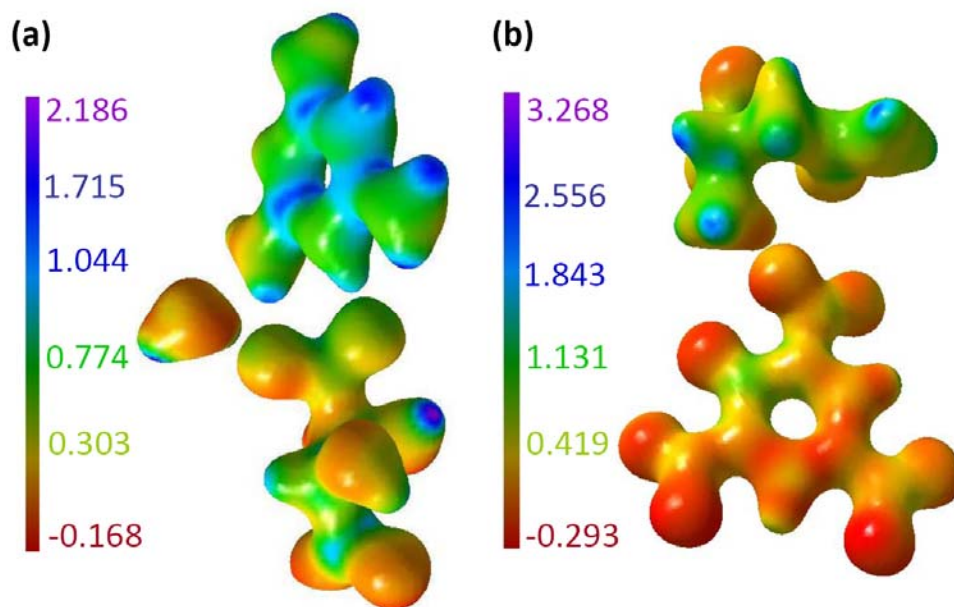


Figure 5.5: Experimental electrostatic potential of (a) **MELT** (b) **LASP** on the $0.5 \text{ e}\text{\AA}^{-3}$ isodensity surface. A colour gradient is applied to show the change from electronegative (towards red) to electropositive (towards blue) regions.

surface (green and blue) on the L-asparaginium ion, hence the charge transfer (see Figure 5.5a), this case being more vivid than for **MELT** in Figure 5.5b. Thus **LASP** presents a case of proton transfer where the charge transfer is almost complete with the prevailing hydrogen bonds being relatively weaker.

The dipole moments of the asymmetric units have been estimated with respect to the center of mass as the origin, although the values themselves are independent of the choice of origin as the asymmetric unit as a whole is neutral.⁴⁰ The values for **MELT** and **LASP** are 22.1(5) and 40.6(7) D respectively (see Figure 5.6a and 5.6b respectively). The charge separation in **LASP** being distinct, a high value of dipole moment is rather expected. The dipole moments of the various molecular partners within the two

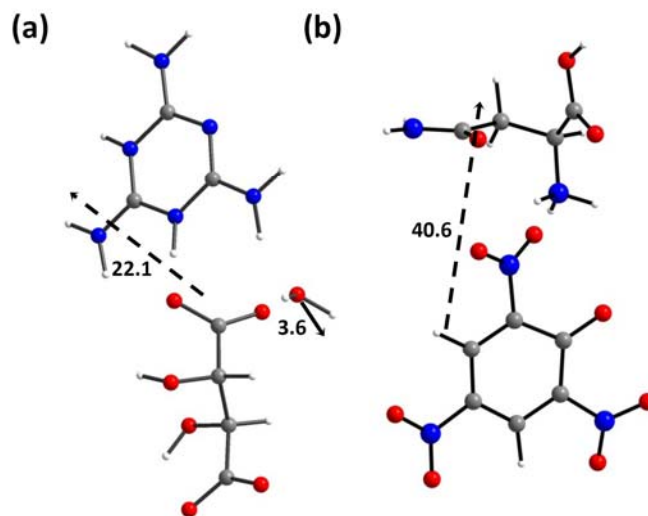


Figure 5.6: The dipole moments of the asymmetric unit are shown: (c) melaminium tartrate monohydrate and (d) asparaginium picrate. Note the dipole moment of water, (3.6 D) in (c).

asymmetric units are ill-defined quantities as they are charged species (except water molecule). It is interesting to note that the dipole moment in water molecule in the former is doubled in this ionic crystalline environment (gas-phase dipole-moment of water=1.84 D)⁴¹. Coppens et al⁴² have reported an enhancement in the water dipole-moment in non-centro symmetric crystal field. Previous theoretical calculations by Batista et al⁴³ in hexagonal ice structure have shown that the dipole-moment of water can reach as high as 3.09 D. The present study reports the experimental value of 3.6 D.

5.5 Conclusions

Based on the experimental and charge density studies on the crystals of melaminium-tartrate monohydrate and L-asparaginium-picrate molecular complexes, the charge-transfer characteristics of the hydrogen bonding interactions between the

molecules have been determined. The origin of the large enhancement in the crystal dipole moments in both the crystals is attributed to the presence of charge transfer interactions between the constituent molecules, facilitated through the hydrogen bonds. Interestingly, the dipole moment of the water of crystallization in melaminium-tartrate monohydrate determined to be twice as large as that in the gas-phase, which is again a consequence of the charge transfer interactions within the monomer that create a local charging environment for the water molecule. The present study provides a comprehensive understanding of the intermolecular forces prevalent in these important non-linear optical materials.

References

1. P. Batail, *Chem. Rev.*, (2004), **104**, 4887.
2. S. K. Pal, M. E. Itkis, R. W. Reed, R. T. Oakley, A. W. Cordes, F. S. Tham, T. Siegrist, R. C. Haddon, *J. Am. Chem. Soc.*, (2004), **126**, 1478.
3. A. Zelichenok, V. Burtman, N. Zenou, S. Yitzchaik, S. D. Bella, G. Meshulam, Z. Kotler, *J. Phys. Chem. B*, (1999), **103**, 8702.
4. K. Nakatani, J. A. Delaire, *Chem. Mater.*, (1997), **9**, 2682.
5. N. Tessler, N. T. Harrison, R. H. Friend, *Adv. Mater.*, (1998), **10**, 64; M. Ahlheim, F. Lehr, *Macromol. Chem. Phys.*, (1994), **195**, 361.
6. S. Lukas, D. Pascal, B. Mila, L. Kirsten, H. J. Mathieu, M. Manfred, V. Horst, *Angew. Chem. Int. Ed.*, (1999), **38**, 696.
7. S. Nagano, Y. Matsushita, Y. Ohnuma, S. Shinma, T. Seki, *Langmuir*, (2006), **22**, 5233.
8. H. Yan, S. H. Park, G. Finkelstein, J. H. Reif, T. H. LaBean, *Science*, (2003), **301**, 1882.
9. T. Mori, H. Tsuge, T. Mizutani, *J. Phys. D: Appl. Phys.*, (1999), **32**, L65.
10. C. N. R. Rao, S. Natarajan, R. Vaidhyanathan, *Angew. Chem. Int. Ed.*, (2004), **43**, 1466.
11. S. Hecht, J. M. J. Frechet, *Angew. Chem. Int. Ed.*, (2001), **40**, 74.
12. T. Steiner, *Angew. Chem. Int. Ed.*, (2002), **41**, 48.
13. G. R. Desiraju, *Angew. Chem. Int. Ed. Engl.*, (1995), **34**, 2311.
14. B. R. Kaafarani, B. Wex, A. G. Oliver, J. A. K. Bauer, D. C. Neckers, *Acta Cryst. E*, (2003), **59**, 227.
15. J. Ellena, A. E. Goeta, J. A. K. Howard, G. Punte, *J. Phys. Chem. A*, (2001), **105**, 8696.
16. H. S. Choi, K. M. Huh, T. Ooya, N. Yui, *J. Am. Chem. Soc.*, (2003), **125**, 6350.
17. H. Zhao, Y. H. Li, X. S. Wang, Z. R. Qu, L. Z. Wang, R.G. Xiong, B. F. Abrahams, Z. Xue, *Chem. -Eur. J.*, (2004), **10**, 2386.
18. L. Bogani, L. Cavigli, K. Bernot, R. Sessoli, M. Gurioli, D. Gatteschi, *J. Mater. Chem.*, (2006), **26**, 2587.
19. M. Ravi, P. Gangopadhyay, D. N. Rao, S. Cohen, I. Agranat, T. P. Radhakrishnan, *Chem. Mater.*, (1998), **10**, 2371.

20. S. C. Abrahams, J. M. Robertson, *Acta Cryst.*, (1948), **1**, 252.
21. J. Donhue, K. N. Trueblood, *Acta Cryst.*, (1956), **9**, 960.
22. A. Datta, S. K. Pati, *Chem. Soc. Rev.*, (2006), **35**, 1305; A. Datta, S. K. Pati, *Chem. -Eur. J.*, (2005), **11**, 4961.
23. A. Datta, D. Davis, K. Sreekumar, S. K. Pati, *J. Phys. Chem. A*, (2005), **109**, 4112.
24. A. Datta, S. K. Pati, *J. Phys. Chem. A*, (2004), **108**, 320.
25. A. Datta, S. K. Pati, *J. Chem. Phys.*, (2003), **118**, 8420.
26. R. F. W. Bader, *Atoms in Molecules A Quantum theory*; Clarendon Press: Oxford, U.K., (1990).
27. T. Koritsanzsky, Coppens, P. *Chem. Rev.*, (2001), **101**, 1583.
28. (a) T. Koritsanzsky, R. Flaig, D. Zobel, H. -G. Krane, W. Morgenroth, P. Luger, *Science*, (1998), **279**, 356; (b) A.V. Vokov, T. Koritsanzsky, P. Coppens, , *J. Phys. Chem. A*, (2004), **108**, 4283; (c) P. R. Mallinson, G. T. Smith, C. C. Wilson, E. Grech, K. Wozniak, *J. Am. Chem. Soc.*, (2003), **125**, 4259; (d) K. Wozniak, P. R. Mallinson, C. C. Wilson, E. Hovestreydt, E. Grech, *J. Phys. Chem. A.*, (2002), **106**, 6897; (e) A. Wagner, R. Flaig, B. Dittrich, H. Schmidt, T. Koritsanzsky, P. Luger, *Chem. -Eur. J.*, (2004), **10**, 2977; (f) B. Dittrich, T. Koritsanzsky, P. Luger, *Angew. Chem. Int. Ed.*, (2004), **43**, 2718; (g) A. Ranganathan, G. U. Kulkarni, C. N. R. Rao, *J. Phys. Chem. A.*, (2003), **107**, 6073.
29. (a) R. S. Gopalan, G. U. Kulkarni, C. N. R. Rao, *Chemphyschem*, (2000), **1**, 127; (b) J. M. Cole, R. C. B. Copley, G. J. McIntyre, J. A. K. Howard, *Phys. Rev. B*, (2002), **65**, 125107; (c) J. M. Cole, *Phil. Trans. R. Soc. Lond. A*, (2003), **361**, 2751; (d) J. M. Cole, A. E. Goeta, J. A. K. Howard, G. J. McIntyre, *Acta Cryst. B*, (2002), **58**, 690; (f) M. A. Spackman, P. Munshi, B. Dittrich, *Chemphyschem*, (2007), **8**, 2022.
30. M. K. Marchewka, J. Baran, A. Pietraszko, A. Haznar, S. Debrus and H. Ratajczak, *Sol. Stat. Sci.*, (2003), **5**, 509.
31. P. Srinivasan, T. Kanagasekaran, R. Gopalakrishnan, G. Bhagavannarayana, P. Ramasamy, *Cryst. Growth. Des.*, (2006), **6**, 1663.
32. Bruker AXS, SAINT Software Reference Manual v. 6.23, Madison, WI, (2002).

-
33. SADABS, SGI version, Siemens Analytical X-ray Instruments Inc., Madison, Wisconsin, USA, (1995).
 34. G. M. Sheldrick: SHELXS-97: Crystal Structure Solution, Version 97-1, Institut Anorg. Chemie, University of Gottingen, Germany: (1990).
 35. N. K. Hansen, P. Coppens, *Acta. Cryst. A*, (1978), **34**, 909.
 36. T. S. Koritsanszky; S. Howard; P. Macchi; C. Gatti; L. J. Farrugia; P. R. Mallinson, A. Volkov; Z. Su; T. Richter and N. K. Hansen, XD, A Computer Program Package for Multipole Refinement and Analysis of Electron Densities from Diffraction Data, version 4.10; Free University of Berlin: Berlin; University of Wales: Cardiff, U. K.; Università di Milano: Milano, Italy; University of Glasgow: Glasgow, U. K.; State University of New York: Buffalo, NY; University of Nancy: Nancy, France, (2003).
 37. C. B. Hubschle, P. Luger, *J. Appl. Crystallogr.*, (2006), **39**, 901.
 38. A. Ranganathan, G. U. Kulkarni, C. N. R. Rao, *J. Mol. Str.*, (2003), **656**, 249.
 39. Z. Su, P. Coppens, *Acta. Crystallogr. Sect. A*, (1997), **48**, 188.
 40. Users manual XD program version 4.10, (2003).
 41. P. W. Atkins, Physical Chemistry, Oxford University Press, 7th Edition, (2002).
 42. Y. A. Abramov, A. V. Volkov, P. Coppens, *Chem. Phys. Lett.*, (1999), **311**, 81.
 43. E. R. Batista, S. S. Xantheas, and H. Jónsson, *J. Chem. Phys.*, (1998), **109**, 4546.

EXPERIMENTAL CHARGE DENSITY DISTRIBUTION IN CARBAMAZEPINE AND OXCARBAZEPINE: POTENTIAL ANTIEPILEPTIC DRUGS*

Summary

Experimental charge density distribution in potential antiepileptic drugs carbamazepine, [*5H*-dibenz(b,f)azepine-5-carboxamide], (**CBZ**) and oxcarbazepine, [10-oxo-10,11-dihydro-5*H*-dibenz(b,f)azepine-5-carboxamide], (**OCBZ**) have been determined employing high resolution single crystal X-ray diffraction data measured at 100K. The molecules **CBZ** and **OCBZ** crystallize in monoclinic space groups $P2_1/n$ and $P2_1/c$ respectively with a full molecule in the asymmetric unit. Molecules **CBZ** and **OCBZ** show structural similarity with an exception in the region of additional $-C=O$ group in **OCBZ**. Analysis of hydrogen bonding in both the compounds has shown that **CBZ** form stronger interactions compared to **OCBZ**. The density and Laplacian in phenyl ring bonds show similar trends whereas that in amide groups show a large difference in these values. The electrostatic potential of both the molecules show a noticeable difference, where one of the phenyl rings in **OCBZ** is accumulated with negative potential and also indicates the potential binding sites on these molecules. The calculation of in-crystal dipole moment has shown that molecule **OCBZ** is more polar compared to **CBZ**. The difference observed in the strength of hydrogen bond and the other molecular properties such as electrostatic potential and dipole moment are related to the reported bioavailability and specificity of **OCBZ** over **CBZ**.

*A manuscript based on this work is under preparation.

6.1 Introduction

The complexity of the problem of drug–receptor recognition is not only to represent the molecular mechanism of drug binding to the specific receptor, but also to explain how a drug avoids ‘traps’ on the part of non-specific acceptors.¹ The main parameters of a molecule which determine the interaction of molecules with a receptor is the molecular structure, electron density and molecular electrostatic potential (MEP).² It is well known that a molecule forms an electrostatic field around itself, depending on atomic charges. Polar substituents that can be included in a molecule may greatly change its electrostatic potential, so the possibility of the binding and mutual orientation of a ligand molecule and the receptor vary due to the so-called field effect.¹ A modification of the substituting groups may change molecular electrostatic potential by both magnitude and sign at a distance of eight to ten carbon-carbon ordinary bonds’ distance from this group.³ In this respect the molecular electrostatic potential derived from the atomic charges can be a scaling factor which determines interactions and the functional groups effects in a molecular recognition processes.

Electronic charge density method of X-ray crystallography is being successfully employed to understand the diverse aspects of various organic and inorganic molecular systems. Studies in literature includes the bond properties of covalent and ionic bonding of various systems,⁴ understanding of non-bonding interactions like various hydrogen bonds⁵ and other electrostatic interactions,⁶ in-crystal molecular properties related to nonlinear optical activity,⁷ pyroelectricity⁸ and molecular magnetism,⁹ single molecular properties like aromaticity and conjugation.¹⁰ In addition to this there are quite a few reports on charge density evaluation of biomolecular functionality.¹¹

Recent literature covers some of the interesting results on charge density analysis of biologically important small molecules.¹² These studies provide a better understanding of the electronic structure of these molecules and also derive a relation between electron density distribution and the electrostatics involved in the intermolecular interactions. Recent reports on experimental and theoretical analysis of charge density by Destro¹³ and Soave et al¹⁴ on Angiotensin II provides an insight in to the understanding of charge density distribution to explain the electrostatics involved in the drug-receptor interaction.

These studies point out the importance of experimentally derived charge density in molecular systems for a precise understanding of the molecular properties. In addition to this there are some important studies on drug molecules of regular use like ibuprofen¹⁵ and zinc complex of aspirin¹⁶ to give a detailed understanding of structure and topology of electron density towards the understanding of these systems at molecular level. All these reports highlight the application of experimentally derived charge density for a better understanding of the intermolecular interactions.

6.2 Scope of the Present Investigation

Anticulsants or antiepileptic drugs are compounds which are found to help in control of epileptic seizure.¹⁷ Carbamazepine [5H-dibenz(b,f)azepine-5-carboxamide], **CBZ** is one of the most commonly used drugs in epileptic treatment, which is found to have a very less bioavailability¹⁸ and side effects. Carbamazepine is also well known for its polymorphism¹⁹ in addition to its ability to form cocrystals and solvates with various other molecules.²⁰ The compound oxcarbazepine [10-oxo-10,11-dihydro-5H-dibenz(b,f)azepine-5-carboxamide], **OCBZ** also satisfy same clinical purpose and found to be much effective and have fewer side effects in comparison to carbamazepine.²¹ Hence, it is interesting to compare the structure, electron density distribution and electrostatic potential in these molecules to the known difference in bioavailability and specificity of **OCBZ** to **CBZ**.¹⁸ This study investigates the experimental charge density and its topology in carbamazepine and oxcarbazepine molecules including the analysis of non-bonding interactions in these molecules in the crystals within the platform of Bader atoms in molecules (AIM) theory.²²

6.3 Experimental Section

The title compounds carbamazepine and oxcarbazepine were obtained from commercial suppliers and the crystals were grown from respective methanolic solutions by slow evaporation at room temperature. High quality crystals were separated under an optical microscope and covered with epoxy. The crystal data were collected on a Bruker-Nonius diffractometer with Kappa geometry attached with an APEX - II-CCD area detector and a graphite monochromator for the Mo K α radiation (50 kV, 40 mA).

The crystals were cooled to 100 K on the diffractometer using a stream of cold nitrogen gas from a vertical nozzle and the temperature was maintained within 1 K throughout the data collection.

Table 6.1 Crystal Structure and multipole refinement for the compounds **CBZ** and **OCBZ**.

Compound name	Carbamazipine	Oxcarbazipine
Chemical formula	C ₁₅ H ₁₂ N ₂ O	C ₁₅ H ₁₂ N ₂ O ₂
Formula weight	236.27	252.27
Cell setting	Monoclinic	Monoclinic
Space group	<i>P</i> 2 ₁ / <i>n</i>	<i>P</i> 2 ₁ / <i>c</i>
<i>a</i> (Å)	7.4831(2)	5.2052(1)
<i>b</i> (Å)	11.0335(3)	9.2586(2)
<i>c</i> (Å)	13.7570(4)	24.7809(6)
β (°)	92.942(1)	95.2660(10)
ρ (g/cm ³)	1.383	1.409
μ , mm ⁻¹	0.089	0.096
Cell volume (Å ³)	1134.35(5)	1189.22(4)
Crystal size (mm)	0.4 × 0.4 × 0.3	0.40x0.35x0.25
<i>Z</i>	4	4
F(000)	496	528
no. of measured reflections	9135	14504
no. of independent reflections	9135	6472
<i>R</i> _{merge}	0.0207	0.0237
<i>R</i> _{int}	0.0321	0.0292
<i>Refinement on F</i> ²		
<i>R</i> (<i>F</i>)	0.0367	0.0423
<i>wR</i> (<i>F</i> ²)	0.1110	0.1211
<i>S</i>	1.075	1.070
no. of reflections used in the	9135	6472
no. of parameters refined	211	220
weighting scheme	0.0317, 0.0627	0.0323, 0.0637
<i>After multipole refinement</i>		
<i>R</i> { <i>F</i> }	0.0263	0.0259
<i>R</i> { <i>F</i> ² }	0.0639	0.0378
<i>S</i>	1.1865	1.0927

The unit cell parameters and the orientation matrix of the **CBZ** and **OCBZ** crystals were initially determined using 138 and 125 reflections respectively from 75 frames collected over a small ω scan of 12.5° sliced at 0.5° interval with three ϕ (0, 120, 240) settings where the values of 2θ and ω are at 30° and -45°. A hemisphere data of the reciprocal space is collected with a strategy generated with COSMO program.²³ The data

collection and structure solution have been carried out following the procedure discussed in the experimental and related aspects section of Chapter 1. A high-order refinement of the data was performed using reflections with $\sin\theta/\lambda \geq 0.44 \text{ \AA}^{-1}$ and $F_o \geq 4\sigma$. All the hydrogens were held constant throughout the refinement along with their isotropic temperature factors. The complete list of bond lengths and bond angles in both **CBZ** and **OCBZ** are given in the Appendix Table A6.1 and A6.2 respectively and the atom coordinates along with the isotropic displacement parameters are given Table A6.3 and A6.4.

Multipolar refinement for the charge density analysis was carried out using the XDLSM routine of the XD package,²⁷ and the details are given in Table 6.1. The XD refinement strategy adopted for **CBZ** and **OCBZ** are also similar to previously discussed molecules (see Experimental and related aspects section of Chapter 1). The residual maps in different planes of the molecule were featureless (see Appendix Figure A6.3 and A6.4). Additional information related to experimental charge density analysis is given in the Appendix of Chapter 6.

6.4 Results and Discussion

The symmetric unit of both the compounds **CBZ** and **OCBZ** with atom labeling is shown in Figure 6.1 and crystal data and other experimental details are listed in Table 6.1. The asymmetric units of **CBZ** and **OCBZ** consist of a full molecule and both the compounds crystallize in monoclinic space groups $P2_1/n$ and $P2_1/c$ respectively. The main structural difference between the compounds **CBZ** and **OCBZ** are centered around the carbon atoms C(13) and C(14), where the former has double bond between these two atoms whereas the latter is an oxo derivative of **CBZ** with a keto group on carbon atom C(14). Both the molecules **CBZ** and **OCBZ** contain three rings. The two rings in **CBZ** are aromatic whereas heterocyclic heptameric ring is anti-aromatic and also participate in conjugation. **OCBZ** contain two aromatic rings and a non-aromatic heterocyclic heptameric ring, as in the case of **CBZ**. The main functional group in both the compounds are an amide group projecting out from the nitrogen atom N(1) of the heptameric ring. Except in the region of C13 and C14 carbon atoms both the molecules show structural similarity with slight deviation in bond lengths and bond angles. (see

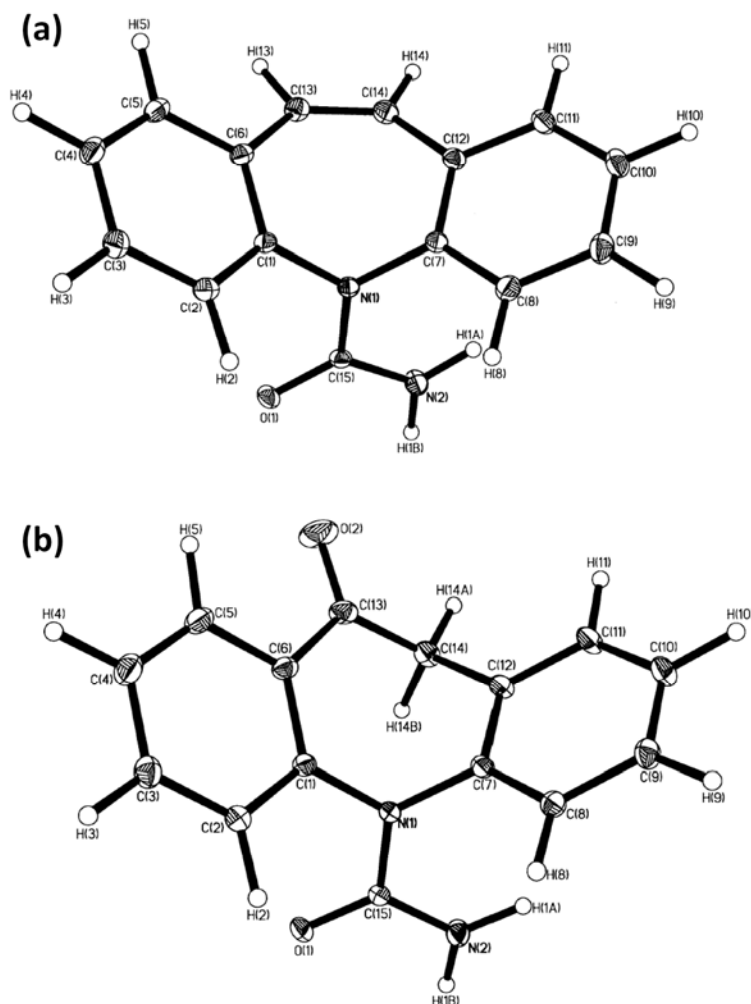


Figure 6.1: ORTEP representation of the molecules (a) Carbamazepine, **CBZ** (b) Oxcarbazepine, **OCBZ** indicating the atom numbering scheme used. Displacement ellipsoids are drawn at a 50% probability level.

Appendix Table A6.1 and A6.3) The average carbon - carbon bond lengths in phenyl rings of both the compounds are given by 1.396 Å. The bond C13-C14 in **CBZ** shows a length of 1.351 Å, which is the typical for a double bond, whereas that in **OCBZ** is given by 1.516 Å. Similar observation can be made in the case of bond angles; where the bond angle also show a deviation in the case of carbon atoms C13 and C14.

CBZ and **OCBZ** show few interesting non-bonding interactions such as N-H...O and C-H...O hydrogen bonds (see Figure 6.2). The hydrogen bonding interaction in **CBZ** molecule include a dimeric N-H...O (H1A...O1, 2.04(1) Å) and a C-H...O (H14...O1, 2.50(1) Å) where the N-H...O interaction is quite strong in nature and the respective

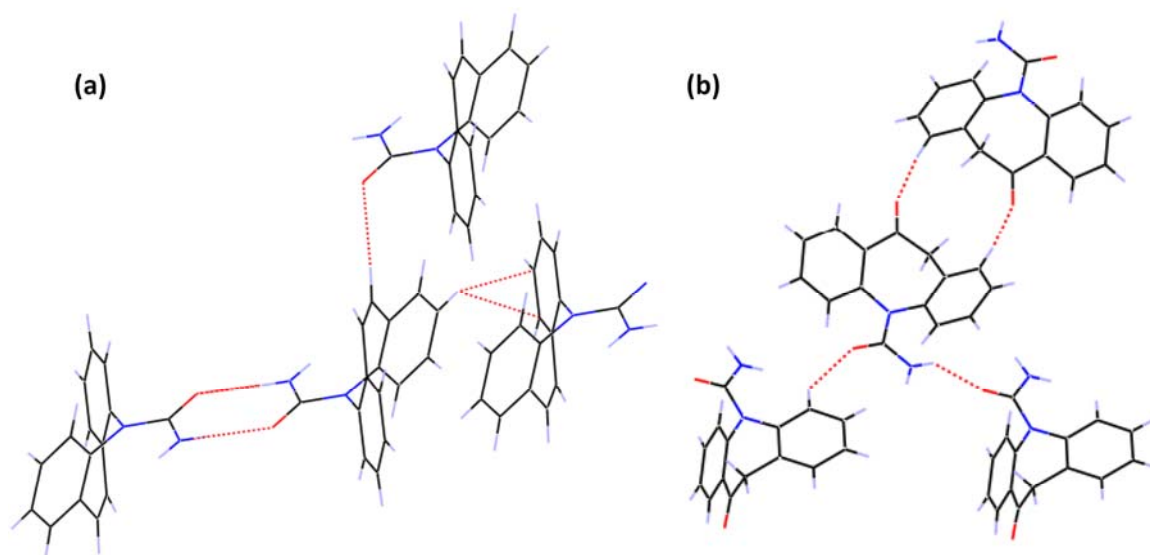


Figure 6.2: Hydrogen bonding in molecules (a) **CBZ** and (b) **OCBZ**.

hydrogen bond angles are given by 177 and 167°. In addition to these hydrogen bonds there exists a C-H... π interaction involving C10...H10 and one of the phenyl rings (atoms C1 to C10) in the molecules with the interaction distance and angle of 2.58 (1) Å and 136° respectively. **OCBZ** also shows a similar type of non-bonding interactions such as hydrogen bonding and C-H... π interactions. **OCBZ** molecules involve in one N-H...O and two C-H...O hydrogen bonds. The N-H...O (H1A...O1, 2.05(1) Å) interaction observed in this molecule is comparatively weaker than that observed in **CBZ** with a H...O distance of 2.05(1) Å (H1A...O1,) and D-H-O angle of 136°. The C-H...O interactions in this molecule are C-H...O (H8...O1, 2.50 (1) Å) and C-H...O (H11...O2, 2.50(1) Å) with angles 137 and 155°. From the analysis of hydrogen bonds it is clear that the **CBZ** form strong non-bonding interactions compared to that formed by **OCBZ**. The non preferential binding of **CBZ** over **OCBZ** can be understood on the basis of the tendency of **CBZ** molecule to form strong non bonding interactions.

In order to understand the effect of additional carbonyl group on molecule **OCBZ**, a comparative study of experimental charge density derived from high-resolution single crystal X-ray diffraction data of both compounds **CBZ** and **OCBZ** have been carried out. The representative deformation density maps of the benzene rings from both the compounds and the amide bond regions are shown in Figure 6.3. The contour depicts

typical covalent bonding present in both the molecules. The average density of the carbon-carbon bonds in the phenyl rings in **CBZ** is given by $2.12 e\text{\AA}^{-3}$, whereas that in

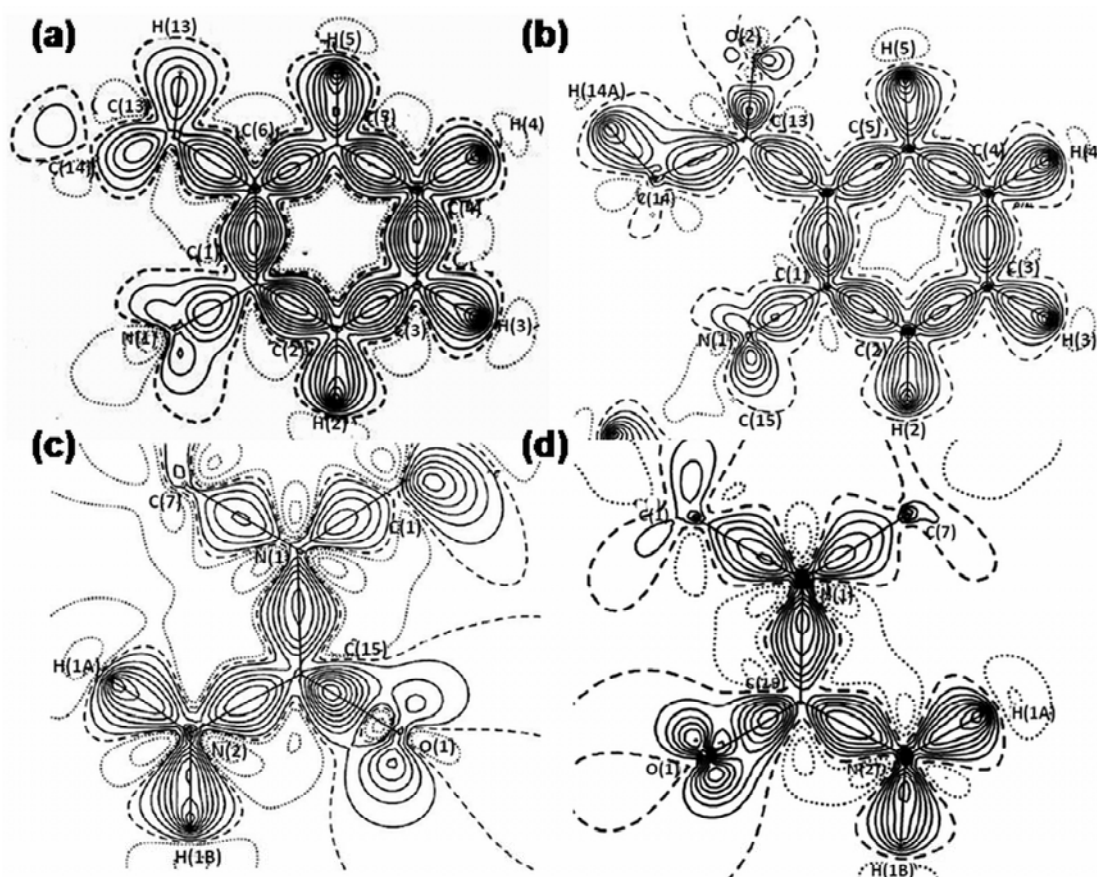


Figure 6.3: Static deformation density maps from the molecules **CBZ** and **OCBZ** (a) representative phenyl ring from **CBZ** (b) representative phenyl ring from **CBZ**. (c) amide group from **CBZ** (d) amide group from **OCBZ**. Contour intervals at $0.1e\text{\AA}^{-3}$; positive contours are represented as solid lines while zero and negative contours are represented as dashed lines.

OCBZ is given by $2.14 e\text{\AA}^{-3}$ which indicate that the carbonyl group on **OCBZ** is not influencing phenyl ring densities. The density of the C-N bonds, which is a part of the heterocyclic ring, is 1.89 and $1.90 e\text{\AA}^{-3}$ in **CBZ** while that for **OCBZ** is 1.97 and $1.83 e\text{\AA}^{-3}$ respectively. These values clearly indicate the extended conjugation in **CBZ** and the isolated ring part of the **OCBZ**. It is interesting to note that the density of the C15-N1 bonds in both the molecules is given by $2.22 e\text{\AA}^{-3}$, indicating that the bond is not affected by the carbonyl group in **OCBZ**. Similarly, the density of bonds in amide group present in both **CBZ** and **OCBZ** are comparable.

The Laplacian of the density at the bond critical point will give an idea about the charge polarization in the bonding regions in a molecule. Unlike density the variations of Laplacian values in **CBZ** and **OCBZ** molecules are interesting (see Tables 6.2 and 6.3). The average Laplacian for the aromatic bonds in the phenyl rings of **CBZ** are given by -19.2 and $-19.4 e\text{\AA}^{-5}$, whereas that for **OCBZ** is given by -17.5 and $-18.0 e\text{\AA}^{-5}$ indicating that in **OCBZ** the phenyl rings have undergone less charge polarization due to the diminished conjugation. The Laplacian values for C1-N1 (-14.2 and $-14.3 e\text{\AA}^{-5}$) and C7-N1 (-13.3 and $-9.9 e\text{\AA}^{-5}$) bonds in **CBZ** and **OCBZ** are comparable. A similar observation can be made in the case N1-C15 bond and the values are given by -20.4 and $-22.03 e\text{\AA}^{-5}$. It is interesting to note that the carbonyl bond in the amide group shows a considerable difference in the Laplacian values indicating that this bond in **CBZ** has undergone a higher polarization. The Laplacian values for these bonds are $-36.5(1)$ and $-27.7(1) e\text{\AA}^{-5}$ for **CBZ** and **OCBZ** respectively. The Laplacian of the C15-N2 bonds in **CBZ** and **OCBZ** shows very close values ($24.1 e\text{\AA}^{-5}$ and $-24.4 e\text{\AA}^{-5}$) suggesting that this bond is not affected by the functional group change and conjugation. The carbonyl group

Table 6.2 Bond critical point parameters of **CBZ**.

Bond	$\rho(\text{\AA}^{-3})$	$\nabla^2\rho(e\text{\AA}^{-5})$	$\lambda_1(e\text{\AA}^{-5})$	$\lambda_2(e\text{\AA}^{-5})$	$\lambda_3(e\text{\AA}^{-5})$	ε
C(1) - C(2)	2.190(5)	-19.982(15)	-17.42	-13.75	11.19	0.27
C(2) - C(3)	2.099(5)	-18.984(15)	-16.25	-13.41	10.68	0.21
C(3) - C(4)	2.154(5)	-19.438(15)	-16.71	-13.82	11.09	0.21
C(4) - C(5)	2.155(5)	-19.840(15)	-16.91	-13.68	10.75	0.24
C(5) - C(6)	2.030(5)	-17.775(15)	-15.48	-12.88	10.58	0.20
C(6) - C(1)	2.151(5)	-19.392(15)	-17.01	-13.63	11.25	0.25
C(1) - N(1)	1.895(6)	-14.301(20)	-13.96	-13.34	13.00	0.05
C(7) - N(1)	1.888(6)	-14.225(19)	-14.46	-13.36	13.60	0.08
C(7) - C(8)	2.085(5)	-19.122(15)	-16.81	-12.71	10.40	0.32
C(8) - C(9)	2.091(5)	-19.232(15)	-16.51	-13.18	10.45	0.25
C(9) - C(10)	2.143(6)	-20.190(16)	-17.18	-13.69	10.69	0.25
C(10) - C(11)	2.122(5)	-19.862(16)	-16.66	-13.67	10.47	0.22
C(11) - C(12)	2.016(5)	-17.313(15)	-15.56	-12.44	10.68	0.25
C(7) - C(12)	2.183(5)	-20.431(16)	-17.89	-13.72	11.18	0.30
C(6) - C(13)	1.872(5)	-14.557(14)	-13.98	-12.04	11.46	0.16
C(13) - C(14)	2.234(6)	-21.111(17)	-17.74	-13.51	10.14	0.31
C(14) - C(12)	1.860(5)	-14.145(13)	-13.45	-12.01	11.32	0.12
C(15) - N(1)	2.225(6)	-22.031(22)	-19.44	-15.51	12.92	0.25
C(15) - N(2)	2.276(6)	-24.127(26)	-20.00	-15.95	11.82	0.25
C(15) - O(1)	2.887(7)	-36.453(33)	-27.15	-24.17	14.87	0.12

present in the **OCBZ** molecule shows a density and Laplacian of $2.97(1) e\text{\AA}^{-3}$ and $-32.8(1) e\text{\AA}^{-5}$ respectively, which is comparable to that theoretically reported for a carbonyl bond.²⁸ The single bonds connecting double bond with the phenyl ring in **CBZ** show a higher density and Laplacian compared to the C6-C13 and C14-C12 in **OCBZ** indicating that in **CBZ** more density has flown from the phenyl ring and double bond. It is interesting to note that the bond C6-C13 in **OCBZ** shows more density and Laplacian values compare to C14-C12 indicating that this former bond is more conjugated due to

Table 6.3 Bond critical point parameters of **OCBZ**.

Bond	$\rho(\text{\AA}^{-3})$	$\nabla^2\rho(e\text{\AA}^{-5})$	$\lambda_1(e\text{\AA}^{-5})$	$\lambda_2(e\text{\AA}^{-5})$	$\lambda_3(e\text{\AA}^{-5})$	ε
C(1) - C(2)	2.153(5)	-18.279(15)	-16.78	-13.84	12.34	0.21
C(2) - C(3)	2.155(5)	-17.634(16)	-16.36	-13.82	12.55	0.18
C(3) - C(4)	2.146(5)	-17.410(15)	-16.19	-13.90	12.68	0.16
C(4) - C(5)	2.200(5)	-18.772(16)	-17.06	-14.26	12.55	0.2
C(5) - C(6)	2.119(5)	-16.543(16)	-15.96	-13.60	13.02	0.17
C(6) - C(1)	2.097(5)	-16.310(15)	-15.98	-13.11	12.79	0.22
C(6) - C(13)	1.792(5)	-12.126(12)	-13.32	-11.75	12.94	0.13
C(13) - C(14)	1.729(5)	-10.145(13)	-12.04	-11.02	12.92	0.09
C(14) - C(12)	1.688(5)	-10.066(12)	-11.81	-10.67	12.41	0.11
C(7) - C(8)	2.183(5)	-19.184(15)	-17.47	-13.92	12.20	0.25
C(8) - C(9)	2.072(5)	-17.565(15)	-16.44	-13.05	11.92	0.26
C(9) - C(10)	2.144(5)	-18.235(16)	-17.06	-13.44	12.26	0.27
C(10) - C(11)	2.129(5)	-18.428(16)	-16.65	-13.92	12.14	0.2
C(11) - C(12)	2.058(5)	-16.619(16)	-15.95	-12.77	12.09	0.25
C(12) - C(7)	2.167(5)	-18.129(16)	-17.37	-13.25	12.50	0.31
C(1) - N(1)	1.965(5)	-13.330(19)	-15.54	-13.81	16.01	0.13
C(7) - N(1)	1.826(6)	-9.902(19)	-13.26	-12.52	15.88	0.06
N(1) - C(15)	2.226(6)	-20.364(22)	-20.05	-15.70	15.39	0.28
C(15) - O(1)	2.911(7)	-27.730(27)	-26.40	-23.74	22.42	0.11
C(15) - N(2)	2.402(6)	-24.351(23)	-21.97	-17.51	15.13	0.25
C(13) - O(2)	2.967(7)	-32.802(30)	-27.12	-23.61	17.93	0.15

the presence of the carbonyl group nearby (see Table 6.2 and 6.3). A Similar trend is observed in the case of bond ellipticity as in the case of density and Laplacian. The average ellipticity of aromatic bonds in **CBZ** are in the range of 0.23 - 0.27, whereas that in **OCBZ** is 0.19 - 0.26 (see table 1 and 2). All the bond ellipticity values in these molecules are comparable with the theoretical values.

Any distribution of charge in a molecule creates an electrostatic potential in the surrounding space, which at any given point represents the potential of the molecule interacting with the electrical charge at that point.²⁹ The multipole description of electron density enables the calculation of the molecular electrostatic potential for an isolated molecule,^{4c} though the refined multipole parameters implicitly contain crystal field effects. All the previous experimental^{12-14, 30} and theoretical studies³¹ on various drug molecules have highlighted the importance of electrostatic potential to understand the possible interactions with receptor. The three dimensional display of this electrostatic potential have been widely used to compare the properties of various drugs and their homologues towards the rational design of new drugs with appreciable properties.³² This study investigate some of the features of the experimental molecular electrostatic potential based on the appearance of the $0.5 \text{ e}\text{\AA}^{-1}$ isodensity surfaces of **CBZ** and **OCBZ** given in the Figure 6.4.³³ The color gradient applied is to show the variation in electrostatic potential from electronegative regions

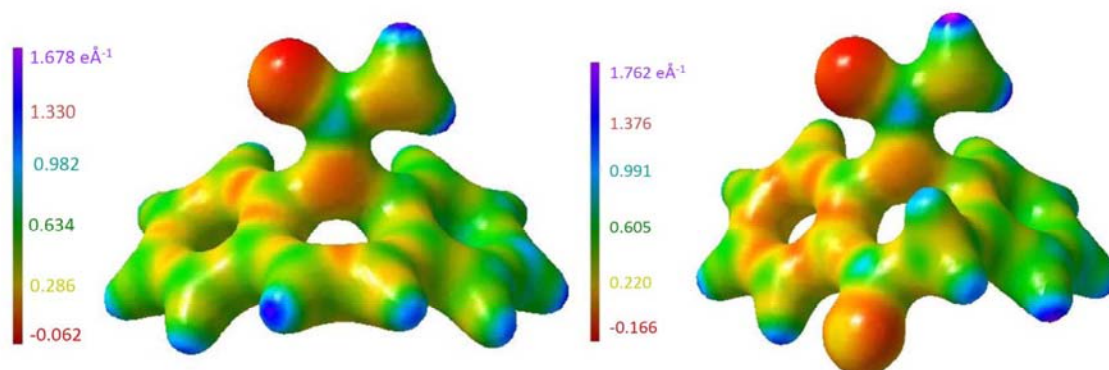


Figure 6.4: Experimental electrostatic potential of (a) **CBZ** (b) **OCBZ** on the $0.5 \text{ e}\text{\AA}^{-3}$ isodensity surface. A colour gradient is applied to show the change from electronegative regions (red) over neutral (green) to electropositive (blue).

(red) over neutral (green) to electropositive (blue). It is interesting to compare the electrostatic potential of the molecules **CBZ** and **OCBZ** as it shows some well-defined features. It is clear from the Figure 6.4 that the phenyl ring close to the -C=O possess more negative electrostatic potential compared to the other phenyl ring and its counterparts in **CBZ**. Similar observation can be made in the case of oxygen atom of the -C=O in amide group, where the negative potentials are $-0.62 \text{ e}\text{\AA}^{-1}$ and $-0.139 \text{ e}\text{\AA}^{-1}$ for **CBZ** and **OCBZ** respectively. The electrostatic potential for the protons of -NH_2 group

in **OCBZ** is at a higher side with a value of $1.776 \text{ e}\text{\AA}^{-1}$. Thus the comparison of the isodensity surfaces of both the molecules bring about some of the interesting features, which can be used to understand the possible interactions with the receptor molecules. It is noteworthy that the oxygen atoms as well as the phenyl ring of the **OCBZ** can make stronger interactions with the receptor with comparable electropositive sites. Similarly, the protons of the amide group in **OCBZ** can also make stronger interactions with the respective electronegative sites of the receptor.

This study also presents a comparison of multipole derived in-crystal dipole moments in molecules **CBZ** and **OCBZ**. Molecule **OCBZ** showed a large difference in dipole moment compared to **CBZ**, with a value of 12.5 (1) D, while **CBZ** showed a value of 7.1(1) D. The increase in the dipole moment of **CBZ** clearly born out from the effect of additional carbonyl functionality present in **OCBZ**. The higher dipole moment of the molecule **OCBZ** can be a reason for the higher bioavailability due to the improved solubility in polar body fluids.

6.5 Conclusions

Analysis of experimental charge density in two antiepileptic drugs, carbamazepine and its oxo derivative oxcarbazepine, has been carried out. The additional functional group present in oxcarbazepine brings about a noticeable difference in the molecular geometry with changes in bond lengths and bond angles. Analysis of density at the bond critical points of these molecules shows that the density and Laplacian values for the phenyl ring bonds in both of these molecules are comparable. Bearing an additional carbonyl group, the bonds in amide moiety of **OCBZ** molecule, especially –C=O group show a large variation in Laplacian values. Noticeable variations in these two molecular systems are observed in the case electrostatic potential, where the **OCBZ** shows an accumulation of the negative charge in the phenyl ring close to the carbonyl group in the molecule and also indicate the acidic nature of amide protons of **OCBZ**. Analysis of the structural and charge density features, especially electrostatic potential suggest that in addition to molecular geometry, the local charge polarizations in the immediate vicinity can play a key role in the specificity of the **OCBZ** over **CBZ**. The

calculations of the in-crystal dipole moments indicate that the polar nature of the **OCBZ** can be one of the reasons for the higher bioavailability of the compound.

Reference

1. F. S. Dukhovich, M. B. Darkhovskii, *J. Mol. Recognit.*, (2003), **16**, 191.
2. L. D. Gribov, S. P. Mushtakova, *Quantum Chemistry*, Gardariki, Moscow, (1999), 197.
3. G. A. Jeffrey, J. F. Piniella, *The Application of Charge Density Research to Chemistry and Drug Design*; Plenum Publishing: New York, 1991.
4. (a) T. Koritsanzsky, P. Coppens, *Chem. Rev.*, (2001), **101**, 1583; (b) G. U. Kulkarni, R. S. Gopalan, C. N. R. Rao, *J. Mol. Str.: THEOCHEM*, (2000), **500**, 239; (c) P. Coppens, *X-ray Charge Densities and Chemical Bonding*; Oxford Science Publishing: Oxford, U. K., 1997; (d) V. G. Tsierelson, R. P. Ozerov, *Electron Density and Bonding in Crystals*; Institute of Publishing: Bristol, U. K., 1996.
5. (a) A. Ranganathan, G. U. Kulkarni, C. N. R. Rao, *J. Phys. Chem. A.*, (2003), **107**, 6073; (b) D. Chopra, T. S. Cameron, J. D. Ferrara and T. N. G. Row, *J. Phys. Chem. A.*, (2006), **110**, 10465; (c) A. Ranganathan, G. U. Kulkarni, and C. N. R. Rao, *J. Mol. Str.*, (2003), **656**, 249; (d) E. Espinosa and E. Molins, *J. Chem. Phys.*, 2000, **113**, 5686. (e) A. Bach, D. Lentz and P. Luger, *J. Phys. Chem. A*, (2001), **105**, 7405; (f) E. Espinosa, C. Lecomte and E. Molins, *Chem. Phys. Lett.*, (1999), **300**, 745; (g) M. A. Spackman, *Chem. Phys. Lett.*, 1999, **301**, 425; (h) E. Espinosa, E. Molins, C. Lecomte, *Chem. Phys. Lett.*, (1998), **285**, 170.
6. (a) X. Li, G. Wu, Y. A. Abramov, A. V. Volkov and P. Coppens, *Proc. Nat. Acad. Sci.*, (2002), **99**, 12132; (b) P. Coppens, Y. Abramov, M. Carducci, B. Korjov, I. Novozhilova, C. Alhambra and M. R. Pressprich, *J. Am. Chem. Soc.*, (1999), **121**, 2585; (c) N. Bouhaida, N. E. Ghermani, C. Lecomte, and A. Thalal, *Acta Cryst. A*, (1999), **55**, 729.
7. (a) R. S. Gopalan, G. U. Kulkarni and C. N. R. Rao, *Chem. Phys. Chem.*, (2000), **1**, 127; (b) J. M. Cole, R. C. B. Copley, G. J. McIntyre and J. A. K., Howard, *Phys. Rev. B*, (2002), **65**, 125107; (c) J. M. Cole, *Phil. Trans. R. Soc. Lond. A* (2003), **361**, 2751.
8. (a) G. H. K. Madsen, F. C. Krebs, B. Lebech and F. K. Larsen, *Chem. Eur. J.*, 2000, **6**, 1797; (b) N. K. Hansen, P. Fertey and R. Guillot, *Acta Cryst. A* (2004), **60**, 465.
9. S. Pillet, M. Souhassou and C. Lecomte, *Acta Cryst. A*, (2004), **60**, 455.
10. (a) A. Ranganathan and G. U. Kulkarni, *J. Phys. Chem. A*, (2002), **106**, 7813; (b) T. S. Cameron, B. Borecks and W. Kwiatkowski, *J. Am. Chem. Soc.*, (1994), **116**, 1211;

- (c) H. –B. Burgi, S. C. Capelli, A. E. Goeta and J. A. K. Howard, M. A. Spackman and D. S. Yufit, *Chem. Eur. J.*, (2000), **8**, 3512.
11. (a) W. D. Arnold, L. K. Sanders, M. T. McMahon, A.V. Volkov, G. Wu, P. Coppens, S. R. Wilson, N. Godbout and E. Oldfield, *J. Am. Chem. Soc.*, (2000), **122**, 4708; (b) Y. A. Abramov, A. Volkov, G. Wu and P. Coppens, *J. Phys. Chem. B*, (2000), **104**, 2183; (c) L. Chęcińska, S. Mebs, C. B. Hübschle, D.; Förster, W. Morgenroth and P. Luger, *Org. Biomol. Chem.*, (2006), **4**, 3242; (d) R. Flaig, T. Koritsánszky, J. Janczak, H. G. Krane, W. Morgenroth and P. Luger, *Angew. Chem. Int. Ed.*, (1999), **38**, 1397.
12. (a) J.; Overgaard and D. E. Hibbs, *Acta Cryst. A*, (2004), **60**, 480; (b) A. Wagner, R. Flaig, B. Dittrich, H. Schmidt, T. Koritsánszky and P. Luger, *Chem. Eur. J.*, (2004), **10**, 2977; (c) D. E. Hibbs, C. J. A. Woods, J. A. Platts, J. Overgaard and P. Turner, *Chem. Eur. J.*, (2003), **9**, 1075; (d) M. P. Waller, S. T. Howard, J. A. Platts, R. O. Piltz, D. J. Willock and D. E. Hibbs, *Chem. Eur. J.*, (2006), **12**, 7603.
13. R. Destro, R. Soave, M. Barzaghi, L. L. Presti, *Chem. Eur. J.*, 2005,**11**, 4621.
14. R. Soave, M. Barzaghi and R. Destro, *Chem. Eur. J.*, (2007), **13**, 6942.
15. N. Bouhaida, M. Dutheil, N. E. Ghermani and P. Becker, *J. Chem. Phys.*, (2002), 116, 6196.
16. A. Spasojevic-de Bire, N. Bouhaida, A. Kremenovic, G. Morgant and N. E. Ghermani, *J. Phys. Chem. A.*, (2002), **106**, 12170.
17. D. B. Smith and J. DeToledo, *Diagnosis and Management of Seizure Disorders*, R. P. Lesser, Ed. Demos, New York, 1991.
18. Y. Kobayashi, S. Ito, K. Yamamoto, *Int. J. Pharm.*, (2000), **124**, 14834.
19. A. L. Grzesiak, M. Lang, K. Kim and A. J. Matzger, *J. Pharm. Sci.*, (2003), **92**, 2260.
20. (a) S. G. Fleischman, S. S. Kuduva, J. A. McMahon, B. Moulton, R. D. B. Walsh, N. R. Hornedo and M. J. Zaworotko, *Cryst. Grow. Des.*, (2003), **3**, 909; (b) T. Gelbrich and M. B. Hursthouse, *CrystEngComm*, (2006), **8**, 449.
21. D. E. Dietrich, S. Kropp and H. M. Emrich, *Pharmacopsychiatry*, (2001), **34**, 242.
22. R. F. W. Bader, *Atoms in Molecules A Quantum theory*; Clanderon Press: Oxford, U.K., 1990.
23. COSMO, Bruker suit programs, Germany,
24. Bruker AXS, SAINT Software Reference Manual v. 6.23, Madison, WI, 2002.
25. SORTAV, Wingx suit programs, Glasgo, UK, 2003

-
26. G M Sheldrick, **SHELXS-97**: Crystal Structure Solution, Version 97-1, Institut Anorg. Chemie, University of Gottingen, Germany: 1990.
 27. T. Koritsanszky, P. R. Mallinson, S. T. Howard, A. Volkov, P. Macchi, Z. Su, C. Gatti, T. Richter, L. J. Farrugia and N. K. Hansen, *XD, A computer program package for multipole refinement and analysis of charge densities from diffraction data*. v. 4.10, 2003.
 28. D. Cremer, E. Kraka, *Croat. Chem. Acta*, (1984), **57**, 1259.
 29. P. Politzer, P. R. Laurence and K. Jayasuriya, *Environ. Health. Perspect.*, (1985), **61**, 191.
 30. D. E. Hibbs, J. Overgaard, S. T. Howard and T. H. Nguyen, *Org. Biomol. Chem.*, (2005), **3**, 441.
 31. (a) J. S. Murray, F. A. Awwad, P. Politzer, L. C. Wilson, A. S. Troupin and R. E. Wall, *Int. J. Quant. Chem.*, (1998), **70**, 1137. (b) P. Politzer, J. S. Murray and Z. P. Inga, *Int. J. Quant. Chem.*, (2001), **85**, 676.
 32. G. R. Marshall and C. B. Naylor, *Comprehensive Medicinal Chemistry, Vol. 4 Quantitative Drug Design, Chapter 20.2*, Pergamon Press plc, Oxford, England, 2005.
 33. C. B. Hubschle and P. Luger, *J. Appl. Crystallogr.*, (2006), **39**, 901.